Research on the decomposition characteristics and biosafety of C5F10O/N2/O2 mixed insulating gas

Yalong Li

▶ **To cite this version:**

Yalong Li. Research on the decomposition characteristics and biosafety of C5F10O/N2/O2 mixed insulating gas. Plasmas. Université d'Orléans; Université de Wuhan (Chine), 2023. English. NNT : 2023ORLE1050 . tel-04533699

HAL Id: tel-04533699

https://theses.hal.science/tel-04533699

Submitted on 5 Apr 2024

HAL is a multi-disciplinary open access archive for the deposit and dissemination of scientific research documents, whether they are published or not. The documents may come from teaching and research institutions in France or abroad, or from public or private research centers.

L'archive ouverte pluridisciplinaire **HAL**, est destinée au dépôt et à la diffusion de documents scientifiques de niveau recherche, publiés ou non, émanant des établissements d'enseignement et de recherche français ou étrangers, des laboratoires publics ou privés.

Université de Wuhan

UNIVERSITÉ D'ORLÉANS

ÉCOLE DOCTORALE Energie – Matériaux – Sciences de la Terre et de l'Univers
Laboratoire GREMI / School of Electrical Engineering

THÈSE

présentée par :

Yalong LI

soutenue le : **21 Décembre 2023**

pour obtenir le grade de **Docteur de l'Université d'Orléans et de l'Université de Wuhan**

Discipline/Spécialité : Sciences et Technologies Industrielles. Energétique.

Research on the Decomposition Characteristics and Biosafety of $C_5F_{10}O/N_2/O_2$ Mixed Insulating Gas

THÈSE dirigée par :

M. BAUCHIRE Jean-Marc	Professeur, Université d'Orléans
M. ZHANG Xiaoxing	Professeur, Université de Wuhan

RAPPORTEURS :

M. TEULET Philippe	Professeur, Université Toulouse
M. LI Lee	Professeur, Huazhong University of Science and Technology, China

---

JURY :

M. TEULET Philippe	Professeur, Université Toulouse
M. LI Lee	Professeur, Huazhong University of Science and Technology, China
M. BAUCHIRE Jean-Marc	Professeur, Université d'Orléans
M. HONG Dunpin	Professeur, Université d'Orléans, Président du jury
Mme. TIAN Shuangshuang	Associate Professor, Hubei University of Technology, China

Research on the Decomposition Characteristics and Biosafety of $C_5F_{10}O/N_2/O_2$ Mixed Insulating Gas

Yalong LI

Abstract

Sulfur hexafluoride (SF_6) has been widely used in gas insulated equipment due to its excellent insulation and arc extinguishing properties. However, SF_6 gas has an extremely strong greenhouse effect. Its global warming potential is 23,500 times that of CO_2, and the natural lifespan in the atmosphere of about 3,200 years. In order to solve the environmental problems brought by the extensive use of SF_6 from the source, the research and development of eco-friendly insulating gases and equipment is urgently required. In recent years, perfluoropentanone ($C_5F_{10}O$) gas mixture is expected to replace SF_6 as insulation dielectric in medium and low-voltage gas insulated equipment due to its excellent environmental protection and insulation properties. However, the decomposition characteristics and biosafety of $C_5F_{10}O$ gas mixture under different conditions have not been comprehensively studied. In this manuscript, experimental and theoretical studies are carried out on the decomposition characteristics of $C_5F_{10}O/N_2/O_2$ gas mixture at the gas-solid interface of metal materials and under the discharge and thermal action, and the feasibility and safety of its application are evaluated in combination with the biosafety of $C_5F_{10}O$ gas and arc decomposition products of $C_5F_{10}O/N_2/O_2$.

Considering the long-term contact between $C_5F_{10}O/N_2/O_2$ gas mixture and the internal materials of the equipment during normal operation, the gas-solid interaction stability of $C_5F_{10}O/N_2/O_2$ gas mixture with commonly used metal copper, aluminum and silver inside the equipment is evaluated, and the mechanism of gas-solid interface interaction between $C_5F_{10}O$ gas mixture and metal materials is clarified. The stability experiments of $C_5F_{10}O/N_2/O_2$ with metal copper, aluminum and silver at different temperatures are carried out on the gas-solid interface stability experimental platform. And the decomposition of $C_5F_{10}O$, the surface morphology, element composition and valence state changes of metal materials are analyzed, and the stability optimization scheme of silver-plated protective layer on copper surface is proposed for metal copper material with poor gas-solid stability. Combined with the structural characteristics of $C_5F_{10}O$ molecules, the interaction models of $C_5F_{10}O$ and three metal materials are constructed, and the adsorption energy, charge transfer and differential charge density of the interaction system between $C_5F_{10}O$ and metal interface are analyzed. It is revealed that the copper material mainly interacts with the carbonyl oxygen atom of $C_5F_{10}O$ through the Top site to form chemical bonds, while the interaction between $C_5F_{10}O$ and silver and aluminum

materials belongs to physical adsorption, and the interaction mechanism between $C_5F_{10}O$ gas mixture and metal material gas-solid interface is revealed from the microscopic level.

Discharge and thermal fault may also occur during the long-term operation of the equipment. The failure decomposition mechanism of $C_5F_{10}O/N_2/O_2$ gas mixture is studied through experiments and simulations. The typical discharge and thermal fault decomposition characteristics of $C_5F_{10}O/N_2/O_2$ gas mixture containing different concentrations of oxygen are revealed. The composition and generation rules of decomposition products of the gas mixture under the fault of AC breakdown, partial discharge and partial over-thermal are obtained, and the correlation between the types and contents of characteristic decomposition products and the fault types, as well as the regulation of oxygen to $C_5F_{10}O$ gas mixture decomposition products and the inhibition mechanism of solid product precipitation are analyzed. The characteristic products characterizing the discharge and thermal fault of $C_5F_{10}O/N_2/O_2$ gas mixture are extracted, which provided a reference for the on-line fault monitoring based on the decomposition components. The discharge and thermal fault-induced $C_5F_{10}O/N_2/O_2$ gas dissociation and product generation systems are constructed. Based on density functional theory and transition state theory, the relaxation structure, energy, vibration frequency and other parameters of each particle are calculated, and the thermal and kinetic parameters of the relevant reaction paths, as well as the influence of oxygen and micro-water on the decomposition reaction are obtained, which combined with the experimental results to clarify the fault decomposition mechanism of $C_5F_{10}O$ gas mixture.

In order to ensure the application safety of $C_5F_{10}O$ gas insulated equipment, the biosafety study of $C_5F_{10}O$ and arc decomposition products of $C_5F_{10}O/N_2/O_2$ is carried out, and the LC50 of $C_5F_{10}O$ gas is 7461ppm (female) and 8724ppm (male), and the LC50 of decomposition products is 2300ppm (female and male). The effects of $C_5F_{10}O$ and its decomposition products on various organs and vital signs of mice are clarified by pathological and hematological experiment and analysis. Based on the relevant results, the application safety of $C_5F_{10}O/N_2/O_2$ gas mixture is evaluated, and targeted safety protection measures and suggestions are proposed.

This manuscript systematically reveals the stability of gas-solid interface interaction and discharge and thermal fault decomposition characteristics of $C_5F_{10}O/N_2/O_2$ gas mixtures through extensive theoretical and experimental studies, and experiments the biosafety of $C_5F_{10}O/N_2/O_2$ gas mixture and its arc decomposition products. The relevant research results provide an important reference for the engineering application and operation and maintenance of $C_5F_{10}O/N_2/O_2$ gas mixture.

Keywords: $C_5F_{10}O/N_2/O_2$ gas mixture, Eco-friendly insulating gas, Gas-solid interface stability, Discharge decomposition, Thermal decomposition, Biosafety

Recherche sur les caractéristiques de décomposition et la biosécurité du gaz isolant mixte $C_5F_{10}O/N_2/O_2$

Yalong LI

Résumé

L'hexafluorure de soufre (SF_6) a été largement utilisé dans les équipements à isolation gazeuse en raison de ses excellentes propriétés d'isolation et d'extinction d'arc. Cependant, le gaz SF_6 a un puissant effet de serre. Son potentiel de réchauffement de la planète est 23 500 fois supérieur à celui du CO_2 et sa durée de vie naturelle dans l'atmosphère est d'environ 3 200 ans. La recherche et le développement de gaz et d'équipements d'isolation respectueux de l'environnement peuvent résoudre les problèmes environnementaux liés à l'utilisation généralisée des gaz SF_6. Ces dernières années, on s'attend à ce que le mélange gazeux de C5 perfluoroketone ($C_5F_{10}O$) remplace le SF_6 comme diélectrique d'isolation dans les équipements isolés au gaz de moyenne et basse tension en raison de ses excellentes propriétés de protection de l'environnement et d'isolation. Cependant, les caractéristiques de décomposition et la biosécurité du mélange gazeux $C_5F_{10}O$ dans différentes conditions n'ont pas été étudiées de manière exhaustive. Dans cet manuscrit, des études expérimentales et théoriques sont menées sur les caractéristiques de décomposition du mélange gazeux $C_5F_{10}O/N_2/O_2$ à l'interface gaz-solide des matériaux métalliques et sous la décharge. L'action thermique et la faisabilité et la sécurité de son application sont évaluées en combinaison avec la biosécurité du gaz $C_5F_{10}O$ et les produits de décomposition de l'arc de $C_5F_{10}O/N_2/O_2$.

Compte tenu du contact à long terme entre le mélange gazeux $C_5F_{10}O/N_2/O_2$ et les matériaux internes de l'équipement pendant le fonctionnement normal, la stabilité de l'interaction gaz-solide du mélange gazeux $C_5F_{10}O/N_2/O_2$ avec les métaux cuivre, aluminium et argent couramment utilisés à l'intérieur de l'équipement est évaluée, et le mécanisme d'interaction de l'interface gaz-solide entre le mélange gazeux $C_5F_{10}O$ et les matériaux métalliques est clarifié. Les expériences de stabilité de $C_5F_{10}O/N_2/O_2$ avec les métaux cuivre, aluminium et argent à différentes températures sont réalisées sur la plateforme expérimentale de stabilité de l'interface gaz-solide. La décomposition de $C_5F_{10}O$, la morphologie de la surface, la composition des éléments et les changements d'état de valence des matériaux métalliques sont analysés, et un schéma d'optimisation de la stabilité de la couche protectrice argentée sur la surface du cuivre est proposé pour les matériaux en cuivre métallique présentant une mauvaise stabilité gaz-solide. En combinaison avec les caractéristiques structurelles des molécules de $C_5F_{10}O$, les modèles d'interaction de $C_5F_{10}O$ et de trois matériaux métalliques sont construits, et l'énergie d'adsorption, le transfert de charge et la densité de charge différentielle du système d'interaction entre $C_5F_{10}O$ et l'interface métallique sont analysés. Il s'avère que le matériau cuivre interagit principalement avec l'atome d'oxygène carbonyle de

$C_5F_{10}O$ via le site Top pour former des liaisons chimiques, tandis que l'interaction entre $C_5F_{10}O$ et les matériaux argent et aluminium appartient à l'adsorption physique, et le mécanisme d'interaction entre le mélange gazeux $C_5F_{10}O$ et l'interface gaz-solide du matériau métallique est révélé au niveau microscopique.

Une décharge et un défaut thermique peuvent également se produire pendant le fonctionnement à long terme de l'équipement. Le mécanisme de décomposition de la défaillance du mélange gazeux $C_5F_{10}O/N_2/O_2$ est étudié par des expériences et des simulations. Les caractéristiques typiques de décharge et de décomposition par défaut thermique du mélange gazeux $C_5F_{10}O/N_2/O_2$ contenant différentes concentrations d'oxygène sont révélées. La composition et les règles de génération des produits de décomposition du mélange gazeux sous l'effet d'une panne de courant alternatif, d'une décharge partielle et d'une surchauffe partielle sont obtenues, et la corrélation entre les types et le contenu des produits de décomposition caractéristiques et les types de défaut, ainsi que la régulation de l'oxygène vers les produits de décomposition du mélange gazeux $C_5F_{10}O$ et le mécanisme d'inhibition de la précipitation des produits solides sont analysés. Les produits caractéristiques de la décharge et du défaut thermique du mélange gazeux $C_5F_{10}O/N_2/O_2$ sont extraits, ce qui a fourni une référence pour la surveillance en ligne des défauts basée sur les composants de décomposition. Les systèmes de dissociation des gaz $C_5F_{10}O/N_2/O_2$ et de génération de produits induits par une décharge et un défaut thermique sont construits. Sur la base de la théorie de la fonction de la densité et de la théorie de l'état de transition, la structure de relaxation, l'énergie, la fréquence de vibration et d'autres paramètres de chaque particule sont calculés, et les paramètres thermiques et cinétiques des voies de réaction pertinentes, ainsi que l'influence de l'oxygène et des traces d'humidité sur la réaction de décomposition sont obtenus, ce qui, combiné aux résultats expérimentaux, permet de clarifier le mécanisme de décomposition par décharge et par défaut thermique du mélange gazeux $C_5F_{10}O$.

Afin d'assurer la sécurité d'application des équipements isolés au gaz $C_5F_{10}O$, l'étude de biosécurité du $C_5F_{10}O$ et des produits de décomposition de l'arc $C_5F_{10}O/N_2/O_2$ est réalisée. La concentration létale 50 (CL50) du gaz $C_5F_{10}O$ est de 7461ppm (femelle) et 8724ppm (mâle), et la CL50 des produits de décomposition est de 2300ppm (femelle et mâle). Les effets du $C_5F_{10}O$ et de ses produits de décomposition sur divers organes et signes vitaux des souris sont clarifiés par des expériences et des analyses pathologiques et hématologiques. Sur la base des résultats pertinents, la sécurité d'application du mélange gazeux $C_5F_{10}O/N_2/O_2$ est évaluée, et des mesures de protection ciblées et des suggestions sont proposées.

Cet manuscrit révèle systématiquement la stabilité de l'interaction entre l'interface gaz-solide et les caractéristiques de décomposition de la décharge et du défaut thermique des mélanges gazeux $C_5F_{10}O/N_2/O_2$ par le biais d'études théoriques et expérimentales approfondies, et expérimente la biosécurité du mélange gazeux $C_5F_{10}O/N_2/O_2$ et de ses produits de décomposition de l'arc. Les résultats de ces recherches constituent une référence importante pour l'application technique, l'exploitation et la maintenance du mélange gazeux $C_5F_{10}O/N_2/O_2$.

Mots clés: Mélange gazeux $C_5F_{10}O/N_2/O_2$, gaz isolant écologique, stabilité de l'interface gaz-solide, décomposition par décharge, décomposition thermique, biosécurité

Contents

1 Introduction

1.1 Research Background and Significance

With the rapid development of China's economy and accelerating urbanization, the land available in cities is becoming increasingly scarce, and electricity, as the driving force of urban development, is closely related to people's life and economic development. Therefore, the demand and stability requirements of electricity in cities are increasing. Gas Insulated Equipment (GIE) has a series of advantages, such as small footprint and space volume, long maintenance cycle, convenient maintenance, low electromagnetic pollution, and high operational reliability not affected by bad weather and climate. It is the main equipment in power network transmission and substation system at all levels. GIE includes gas insulated switchgear (GIS), gas circuit breaker (GCB), gas insulated transmission line (GIL), gas insulated cabinet (GIC), and gas insulated transformer (GIT), etc., all of which have closed gas chambers inside, and usually the gas chamber is filled with sulfur hexafluoride (SF_6) gas higher than atmospheric pressure (0.13MPa~0.6MPa) as insulation or arc extinguishing dielectric. SF_6 has excellent physical and chemical properties and electrical properties. Its insulation performance is about 2.5 times that of air at atmospheric pressure, and the arc extinguishing performance is about 100 times that of air under the same conditions. With the extremely stable chemical properties, it is an ideal insulation and arc extinguishing dielectric, and is currently the most widely used insulation dielectric in gas insulated equipment [1, 2]. However, SF_6 gas has an extremely strong greenhouse effect and an extremely long atmospheric lifetime. Its global warming potential (GWP) is 23,500 times that of CO_2 (in 100 years), and the natural lifespan in the atmosphere of about 3,200 years [3, 4]. The Kyoto Protocol, signed as early as 1997, has identified methane, carbon dioxide, hydrofluorocarbons, nitrous oxide, perfluorocarbons, and sulfur hexafluoride as the six categories of greenhouse gases that require emission limitations [5, 6].

The Global Monitoring Laboratory Earth System Research Laboratories (GMLERL) has been recording changes in atmospheric SF_6 concentrations since December 1994 as shown in Figure 1.1a. The global mean concentration of SF_6 has risen from 3.67 ppt (part per trillion) in December 1994 to 10.89 ppt (297% increase) in September 2021. The annual growth rate is about 0.24 ppt per year, and the recent growth rate of SF_6 has been increasing, with the global mean concentration of SF_6 in the atmosphere increasing by 44.49% over the last 10 years [7].

Currently, more than 80% of SF_6 produced annually worldwide is used in the power industry [8]. According to the "Research Report on Alternative Technology of Sulfur Hexafluoride in the Electric Power Industry" issued by China Energy Research Society in 2019 [9], the statistics and analysis of SF_6 gas usage in China's main electrical equipment found that the usage of SF_6 in 2018 has reached 7,000 tons, and with the continuous advancement of China's economic transformation and industrial upgrading, the use of SF_6 will show a trend of continuous growth (As shown in Figure 1.1b). The large-scale use of SF_6 gas will inevitably produce a large amount of SF_6 exhaust gas, which will bring major hidden dangers to the environment. Some countries and organizations have introduced many policies and measures to reduce the use of SF_6 gas and limit its direct emissions [10]. The EU's F-gas Regulation

proposes that by 2030 the EU's F-gas emissions will be reduced by two-thirds compared to 2014 [11]. Since the end of the last century, the EU member states of Denmark, Finland, the Netherlands, Norway and Sweden have been implementing carbon tax policies. At present, the tax rate levied by Denmark is $26.9/ton CO_2 equivalent; Finland's carbon tax is about $71.1/ton CO_2 equivalent; Sweden's carbon tax is as high as $129.7/ton CO_2 equivalent, and this tax rate is gradually increasing. Japan, Boulder, Colorado (USA) and Quebec (Canada) have also developed carbon tax policies to reduce greenhouse gas emissions, and the revenue from the tax can be used to fund environmental projects [12]. China has also actively participated in the formulation and implementation of greenhouse gas emission reduction measures. President Xi proposed at the general debate of the 75th United Nations General Assembly that China's CO_2 emissions will peak by 2030 and strive to achieve carbon neutrality by 2060. The power industry is a pillar industry of the national economy and a key industry for carbon emissions, and carbon peaking in the power industry plays an important role in accomplishing the carbon peaking target in China [13].

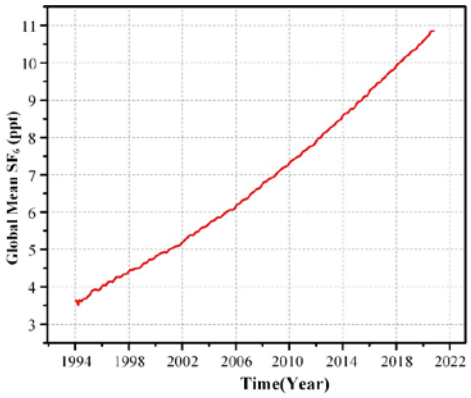

(a) Global mean SF_6 concentration in atmosphere

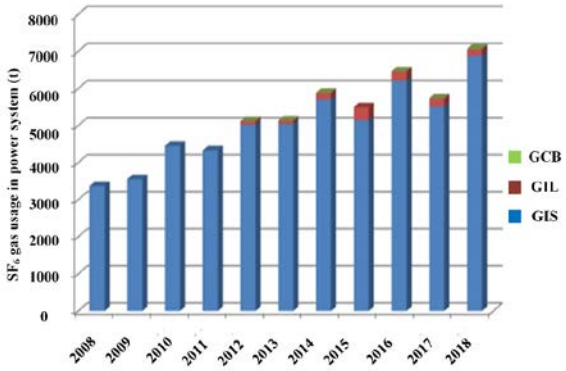

(b) SF_6 usage in electrical equipment from 2008 to 2018

Figure 1.1 Changes in the Global mean SF_6 concentration in atmosphere and SF6 usage in electrical equipment in China

In response to the call for energy saving and emission reduction, researchers in the power industry around the world are also working on solutions to reduce the greenhouse effect caused by SF_6 gas emissions from different directions. At present, the idea of SF_6 gas emission reduction in the power industry mainly revolves around recycling SF_6 exhaust gas for purification and reuse, degrading and transforming SF_6 exhaust gas and using low greenhouse effect insulation gas to reduce or prohibit the use of SF_6 gas.

The use of low greenhouse effect eco-friendly insulating gas to replace SF_6 gas as insulation dielectric can solve the greenhouse effect brought by SF_6 gas from the source. At present, electric power research institutions and electric power equipment manufacturers in many countries around the world are actively carrying out research on eco-friendly insulating gases. In recent years, $C_5F_{10}O$ (1,1,1,3,4,4,4-heptafluoro-3-(trifluoromethyl)-2butanone) has attracted the attention of scholars with its excellent environmental protection and insulation properties, and is considered to be promising alternative to SF_6 gas as insulation dielectric in electrical equipment of low and medium voltage grades. The GWP value of $C_5F_{10}O$ is less than 1, the ozone depletion potential (ODP) is 0, and the atmospheric lifetime is about 15 days. $C_5F_{10}O$ gas also has high insulation properties, and the relative dielectric strength of $C_5F_{10}O$

gas is 1.4 times that of SF_6. The main physicochemical properties of $C_5F_{10}O$ are shown in Table 1.1. Due to its high liquefaction temperature (26.9 °C under normal pressure), it is necessary to mix air components (CO_2, N_2 or dry air) with lower liquefaction temperature as buffer gas to reduce the dew point temperature of $C_5F_{10}O$ gas mixture to meet the temperature requirements in engineering applications. The use of $C_5F_{10}O$ gas mixture as an insulating dielectric for electrical equipment can reduce the greenhouse effect caused by the use of SF_6 in the power industry by more than 99.99% [15]. ABB has already carried out a trial run in Switzerland in 2015 for grid-connected $C_5F_{10}O$ gas insulated equipment at 170 kV and 24 kV voltage grades [16], and has received an order from the German grid company to install the world's first high-voltage $C_5F_{10}O$ gas insulated equipment at 380 kV voltage grade in 2026 [17].

Table 1.1 Key physicochemical properties of $C_5F_{10}O$ [14]

	Characteristics
Chemical Formula	$CF_3C(O)CF(CF_3)_2$
Molecular Weight (g/mol)	266
Burning Point	Non-flammable
Freezing Point (°C)	-110
Boiling Point (°C)	26.89
Critical Temperature (°C)	146.11
Critical Pressure (MPa)	2.14
Saturated vapor pressure at 25°C (kPa)	93.77
LC50	>10000ppm（Rat 4h）
Dielectric Strength at 0.1MPa, disk electrodes 2.5mm in gap (kV)	18.4
Atmospheric Lifetime (years)	0.04
GWP (100-yr ITH, IPCC 2013 method)	<1
ODP（CFC-11=1）	0

Although $C_5F_{10}O$ gas has excellent environmental protection and insulation properties, the evaluation of $C_5F_{10}O$ engineering application reliability also needs to include gas-solid material interface stability, electrothermal stability, arc extinguishing performance, decomposition characteristics, biosafety and many other aspects. The ideal insulating dielectric should be able to keep the electrical equipment stable under complex operating conditions and even under fault conditions, without a large amount of decomposition. GIE has high working voltage grade and works in strong electromagnetic environment for a long time, which is prone to hidden faults such as partial discharge (PD) and partial over-thermal fault (POF) [18, 19]. At the same time, electrical equipment may produce insulation defects such as burrs during production, installation, operation and maintenance, and may cause PD during equipment operation. PD is a long-term, slowly developing process. If the potential fault cannot be found in time, the high-energy particles generated by the PD ionization will diffuse into the surrounding gas and undergo physical and chemical processes such as collision ionization and adsorption with other molecules, further aggravating the intensity of PD, which will lead to the decomposition of the insulating dielectric inside the GIE and eventually lead to an insulation failure accident [20, 21]. In addition, the high-voltage contacts inside the equipment may also increase the contact resistance between contacts due to poor contact, damage and oxidation of the silver-plated layer on the surface, which can lead to abnormal heating during operation due

to the thermal effect of the current [22]. GIE can only dissipate heat through internal gas exchange, while normal operation of the equipment may also generate temperature increases of up to 70 °C on the busbar due to normal temperature rise effects. When the POF occurs inside the equipment, the partial temperature inside the equipment will rise to a higher level. High temperature may lead to decomposition of the insulating gas and corrosion of the metal conductor surface. The long-term contact between the insulating gas and the metal conductor, and the chemical reaction at the gas-solid interface, when the temperature rises, may lead to the decomposition of the insulating gas, which will threaten the service life and operational stability of the equipment. In addition, the recovery characteristics of the gas insulating dielectric after decomposition, and the biosafety of the gas itself and its decomposition products are also critical to examining whether the insulating gas is suitable for application.

At present, the research on the stability of gas-solid material interaction, electrothermal decomposition characteristics and biosafety of $C_5F_{10}O$ GIE under normal operating conditions and fault conditions is still insufficient, and the macroscopic characteristics are not fully grasped and the microscopic reaction mechanism is not clear. Therefore, it is necessary to carry out systematic research on the decomposition characteristics and mechanism of $C_5F_{10}O$ gas mixture, and comprehensively evaluate the feasibility and potential of its engineering application in combination with biosafety, as well as to provide basic data reference for operation and maintenance technology based on component analysis method, so as to promote the green upgrading and healthy development of China's transmission and distribution gas insulation equipment industry.

1.2 Current Status of Research on Eco-friendly Insulating Gases

Since the large-scale application of electricity, with the increase of electricity consumption and the increase of power transmission distance, the transmission voltage has gradually increased. As the initial insulating dielectric, air insulation can no longer meet the needs of insulation, and related researchers have also begun to search for a better insulating dielectric. Since SF_6 gas was synthesized in the laboratory in 1900, it has become the third-generation insulating dielectric after air and oil due to its excellent insulation and arc extinguishing properties, and has been widely used in power systems[23, 24]. Because SF_6 gas has nearly perfect insulation and arc extinguishing properties, the early exploration of SF_6 alternative gas is mainly to solve the problem of high liquefaction temperature of SF_6 gas. General Electric analyzed the insulation properties and saturated vapor pressure characteristics of 35 potential SF_6 alternative gases, and found that only CF_3CN has a dielectric strength higher than SF_6 at a pressure of 0.6MPa (liquefaction temperature of -25°C). When the gas pressure is 0.2MPa (the liquefaction temperature is -25°C), the insulation properties of CF_3CCCF_3, CF_2ClCF_3 and C_2F_5CN are better than SF_6. When the gas pressure is ≤0.2MPa, those gases with better insulation properties than SF_6 have more economic advantages [25]. After the "Kyoto Protocol" signed in 1997 identified SF_6 as one of the six greenhouse gases where usage needs to be restricted, the greenhouse effect of SF_6 has attracted the attention of relevant researchers at home and abroad, and the research on eco-friendly insulating gases has gradually become a hot spot[26, 27, 28].

Eco-friendly insulating gases mainly include conventional air component gases (N_2, CO_2 and dry air), SF_6 gas mixtures (SF_6/N_2, SF_6/CO_2, SF_6/CF_4) and fluorocarbon insulating gases

(perfluorocarbon, CF_3I, perfluoronitrile, perfluoroketone, etc.) [29]. As shown in Table 1.2, the basic parameters of insulating gases that have received more attention are given.

Table 1.2 Basic properties of common insulating gases

Gases	GWP	Atmospheric Lifetime (years)	Insulation performance relative to SF_6	Boiling Point (°C)	LC50 (ppm)
SF_6	23500	3200	1	-63.9	800000
N_2	-	∞	0.40	-196	-
O_2	-	-	0.33	-183	-
Air	≈0	∞	0.39	<-183	-
CO_2	1	-	0.35	-78.5	-
CF_4	6630	50000	0.41	-128	-
C_2F_6	11100	10000	0.73	-78	-
C_3F_8	8900	2600	0.86	-39	-
c-C_4F_8	9540	3200	1.27	-6	-
CF_3I	0.4	0.005	1.2	-21.8	160000
C_4F_7N	2090	22	2.2	-4.7	<15000
$C_5F_{10}O$	<1	0.04	1.4	26.9	20000
$C_6F_{12}O$	1	0.014	2.7	49	>10000
HFO-1234ze(E)	6	0.005	0.85	-19.4	>207000
HFO-1336mzz(E)	18	0.06	>1	7.5	-

Conventional air component gases are as chemically stable as SF_6 and have a much lower liquefaction temperature than SF_6. The insulation dielectric itself is derived from air and does not pose environmental and biosafety problems, and has the advantages of low cost, easy availability and low greenhouse effect. Conventional air component gases were also the gas initially used for insulation, but air component gases such as N_2, O_2 and CO_2 have relatively low insulation strength and need to increase gas pressure and insulation distance when used in electrical equipment, which leads to problems such as increasing the size of the equipment and are gradually discarded. In the process of looking for eco-friendly insulating gases, conventional air component gases have once again attracted the attention of relevant researchers. At present, they are mainly used as buffer gases to reduce the dew point temperature of gas mixtures and solve the problem of high liquefaction temperature of single insulating gas.

SF_6 gas mixtures are using SF_6 and buffer gas with low liquefaction temperature, low greenhouse effect but low insulation strength. In order to ensure the gas mixture has high insulation performance, the SF_6 content is generally above 30%. As early as 2001, Siemens has carried out the trial operation of GIL with SF_6/N_2 gas mixture in Switzerland [30]. The State Grid Corporation of China has also carried out related research on SF_6 gas mixture and carried out on-grid operation [31]. Compared with pure SF_6, SF_6 gas mixture has lower liquefaction temperature, which makes it more suitable for use in alpine regions, and can reduce the greenhouse effect caused by SF_6, but SF_6 gas mixture also faces the problem that the waste gas is not easy to handle, and cannot solve the environmental problems caused by SF_6 from the source.

Fluorocarbon insulating gases are considered to be the most promising gases to replace

SF_6 as the insulating dielectric by virtue of their excellent insulation properties. Initially, studies on fluorocarbon gases focused on perfluorocarbon gases, such as C_2F_6, C_3F_8, and c-C_4F_8, but perfluorocarbon gases still have high GWP values and long atmospheric lifetimes, with insulation properties comparable to SF_6 but with higher liquefaction temperatures, and thus have low application potential [32, 33, 34, 35]. CF_3I gas has very low GWP value (only 0.4) and 1.2 times the insulation performance of SF_6, but it is a carcinogenic, mutagenic and reprotoxic (CMR) substance, and CF_3I is easily decomposed during discharge to produce solid iodine, which reduces the insulation performance of the mixed gas, so it cannot be applied in engineering practice [36, 37, 38]. Subsequently, perfluoronitrile and perfluoroketone gases have received extensive attention from relevant researchers at home and abroad. The main focus of research on perfluoronitrile gases is C_4F_7N, whose GWP value is 2090, its insulation performance is more than twice that of SF_6, and its liquefaction temperature is -4.7°C [39, 40]. C_4F_7N is mainly used in medium and high voltage insulation equipment, but the GWP value of C_4F_7N is also higher than that of perfluoroketone gases, and the biotoxicity of C_4F_7N decomposition products is high, and there is biosafety risk when gas decomposition and leakage are caused by faults during equipment operation [41]. $C_5F_{10}O$ and $C_6F_{12}O$ in perfluoroketone gases are the main research objects of the researchers. The GWP values of $C_5F_{10}O$ and $C_6F_{12}O$ are both less than 1, and the insulation performance is also better than that of SF_6. The liquefaction temperature of both is high, and the liquefaction temperature of $C_6F_{12}O$ under normal pressure is as high as 49 °C [42, 43, 44]. Therefore, it is necessary to use mixed buffer gases together in the application. In addition, some researchers are also conducting tests on the refrigerants HFO-1234ze(E) and HFO-1336mzz(E) to analyze their potential for application in insulation equipment [45, 46].

In summary, the research on eco-friendly insulating gases has experienced a gradual trend from conventional air component gases to SF_6 gas mixtures to fluorocarbon insulating gases. The current research focus is on the mixed insulating dielectric solution of high dielectric strength fluorocarbon insulating gas as the main insulating dielectric and buffer gas used to reduce the dew point temperature.

The insulation level of GIE of low and medium voltage grades is relatively low, the technical difficulty is small, and the equipment usage is large. Therefore, carrying out research on the application of eco-friendly insulating gas in electrical equipment of low and medium voltage grades has the advantages of wide application range, low technical difficulty, and at the same time, it can greatly reduce the power industry's dependence on SF_6 gas and the greenhouse effect it brings. Currently, some achievements have been made in the research on the insulation properties, arc extinguishing properties, electrothermal decomposition properties and biosafety of $C_5F_{10}O$ and its gas mixtures at home and abroad. The existing research shows that $C_5F_{10}O$ gas has great application prospects in low and medium voltage grades GIE.

1.2.1 Insulation Performance of $C_5F_{10}O$ Gas Mixture

The current research on the insulation properties of $C_5F_{10}O$ and its gas mixtures mainly focuses on its breakdown characteristics and lightning impulse characteristics at the macro level. In 2014, J.D. Mantilla of ABB first tested the insulation properties of $C_5F_{10}O$ gas mixture. Under the same gas pressure, the dielectric strength of $C_5F_{10}O$ gas mixture is only slightly lower than that of SF_6. The dielectric strength can be improved by increasing the gas pressure

or increasing the concentration of $C_5F_{10}O$. The U50% of the $C_5F_{10}O$/air gas mixture with the total gas pressure of 0.7 MPa and the concentration of 5% is comparable to that of 0.4 MPa pure SF_6 gas, and the synergistic effect similar to that of SF_6/N_2 gas mixture is observed between $C_5F_{10}O$ and synthetic air. In addition, the breakdown voltage of $C_5F_{10}O$/air gas mixture is slightly higher than that of $C_5F_{10}O/CO_2$ gas mixture [47]. Subsequently, P.Simka et al. of ABB used $C_5F_{10}O$/air gas mixture to test the DC breakdown field strength at step voltage under a quasi-uniform electric field, and set up a comparative experiment by changing the roughness of the electrode, and obtained the breakdown field strength of the gas under different gas pressures with 20mm gap. Studies have shown that the pressure-reduced electric breakdown field of pure $C_5F_{10}O$ is about twice that of SF_6, the pressure-reduced electric breakdown field of the gas mixture containing 5.2% $C_5F_{10}O$ at 0.7MPa is equivalent to 95% of that of pure SF_6 at 0.45MPa. The critical field strength of $C_5F_{10}O$/air gas mixture at 0.1-0.2 MPa is equal to or even greater than that of SF_6 at 0.45-0.6 MPa. Through the study of the influence of electrode roughness on its critical field strength, it is found that the sensitivity of $C_5F_{10}O$/air gas mixture to electrode roughness is higher in high gas pressure environment than in low gas pressure environment [48]. In 2017, Rong Mingzhe et al. of Xi'an Jiaotong University studied the saturated vapor pressure characteristics of $C_5F_{10}O/CO_2$ gas mixture and the breakdown characteristics in inhomogeneous fields. The results shown that mixing 20 kPa and 40 kPa of $C_5F_{10}O$ into the gas mixture with a total pressure of 0.2 MPa can make the power frequency discharge voltage of the gas mixture reach 61.89% and 81.99% of that of SF_6 gas under the same conditions, respectively. By increasing the content of $C_5F_{10}O$, the dielectric strength of the gas mixture can be effectively improved. When the gas pressure increases, the positive polarity breakdown voltage increases, while the negative polarity breakdown voltage becomes saturated [49]. Due to the large height and volume of some GIE, gas stratification will occur when the height of the gas mixture is too high. The calculation shows that in the gas mixture whose temperature is 20℃, the total gas pressure is 0.2MPa, and the concentration of $C_5F_{10}O$ is 10%, the change of the mixing ratio is 0.52% when the height of the gas mixture is 20 meters, and the concentration of the gas mixture with height is not significant. In engineering applications, the concentration change caused by the height of the equipment is small and does not affect the electrical characteristics of the gas mixture [50]. Wang Xiaohua et al. tested the AC and lightning impulse performance of $C_5F_{10}O/CO_2$ gas mixture under different partial pressures, and analyzed its possibility as SF_6 alternative gas. The experimental results show that the gas mixture has the hump effect under the gas pressure of 0.3MPa in the lightning impulse test. Increasing the content of $C_5F_{10}O$ gas in the gas mixture or increasing the gas pressure can improve its AC voltage tolerance. $C_5F_{10}O/CO_2$ gas mixture with $C_5F_{10}O$ partial pressure of 40 kPa and total gas pressure of 0.8 MPa is expected to replace the SF_6 gas in 0.5 MPa GIS [51]. Zhang Xiaoxing of Wuhan University also tested the AC breakdown voltage of $C_5F_{10}O/N_2$ and $C_5F_{10}O$/air mixtures with different pressures and concentrations. When the partial pressure of $C_5F_{10}O$ in the gas mixture is greater than 15kPa, the AC breakdown voltage of $C_5F_{10}O$/air gas mixture increases with the increase of the concentration of $C_5F_{10}O$, and its growth rate is similar to that of $C_5F_{10}O/N_2$ gas mixture. With increasing $C_5F_{10}O$ concentration, the relative dielectric strength of $C_5F_{10}O$ gas mixture is not significantly improved by increasing the total gas pressure, and the dielectric strength of the gas mixture is mainly determined by the concentration of $C_5F_{10}O$ [52].

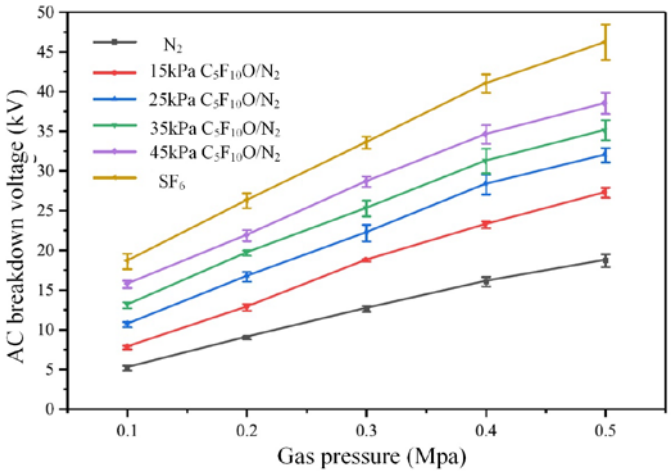

(a) AC breakdown voltage of $C_5F_{10}O/N_2$ gas mixture

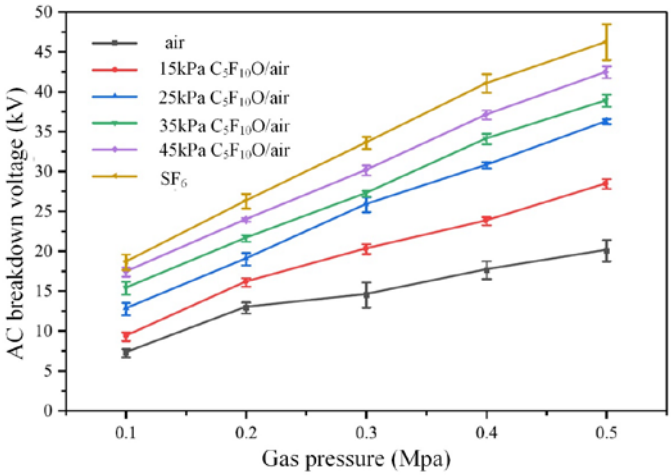

(b) AC breakdown voltage of $C_5F_{10}O$/air gas mixture

Figure 1.2 AC breakdown voltage of $C_5F_{10}O/N_2$ and $C_5F_{10}O$/air gas mixtures

The study on the electron avalanche parameters and critical breakdown field strength of $C_5F_{10}O$ gas mixture from the microscopic level can provide insight into the insulation properties and discharge mechanism of $C_5F_{10}O$ gas. A. Chachereau et al. calculated electron velocities and transport coefficients in pure $C_5F_{10}O$, $C_5F_{10}O/N_2$, and $C_5F_{10}O/CO_2$ gas mixtures, and gave estimates of total electron attachment for $C_5F_{10}O$. Studies have shown that there is a synergistic effect in $C_5F_{10}O/CO_2$ and $C_5F_{10}O/N_2$ gas mixtures, resulting in a relatively high critical electric field for higher gas pressure mixtures even at lower $C_5F_{10}O$ concentrations, but $C_5F_{10}O$ gas mixture at the same gas pressure cannot provide the same critical electric field as SF_6. Therefore, compared with SF_6 insulation equipment, it is necessary to increase gas pressure or insulation distance for $C_5F_{10}O$ gas mixture insulation equipment. The electron attachment on $C_5F_{10}O$ mainly occurs when the electron energy is higher than the thermal energy. The electron attachment cross section of $C_5F_{10}O$ has only one main attachment peak at 1.3 eV at low energy, while a large number of attachments are observed in the range of 3–11 eV [53, 54]. Wang Feng from Hunan University used the binary-encounter-Bethe (BEB) method to calculate the total electron impact ionization cross sections (Q_{ion}) of $C_5F_{10}O$. The results show that the Q_{ion} values calculated by MP2 function for other tested molecules are in good agreement with the experimental results, and the regression analysis shows that there is a

certain correlation between Q_{ion} and E_r. The maximum Q_{ion} value can also be used as a new predictor variable to estimate the dielectric strength of the potential insulating gas of SF_6 [55]. Li Xingwen et al. used the Deutsch–Märk (DM) formula and the modified formula to calculate the electron impact ionization cross sections, geometric optimization and electron population of $C_5F_{10}O$ gas. The modified DM formula was established by changing the weight factor of atoms, and the obtained electron impact ionization cross sections was in good agreement with the experimental data in terms of peak value and curve shape [56].Wang Xiaohua et al. of Xi'an Jiaotong University proposed a method of DM combined with BEB to calculate the electron impact ionization cross sections of $C_5F_{10}O$ gas molecule using double S-type functions and found that the 2p shells of carbon, nitrogen or oxygen atoms in the molecule dominated the electron impact ionization, while the shells of fluorine atoms has no significant effect on the ionization process [57]. Märt Aints determined the effective Townsend ionization coefficient (αeff/N) of $C_5F_{10}O$ and its gas mixture with air using the steady-state non-self-sustaining Townsend discharge formed by the UV-irradiated cathode, which varies with the decrease of the electric field strength E/N. The critical electric field strength of pure $C_5F_{10}O$ gas is (770±25)Td, which is about twice the corresponding value of SF_6. The critical electric field strength of the 7.6% $C_5F_{10}O$/92.4%air gas mixture with the total pressure of 0.14MPa is more than twice that of air, and is about 2/3 of that of pure SF_6 [58]. Egüz et al. used the pulse Townsend experiment to study the group parameters of $C_5F_{10}O/CO_2/O_2$ and $C_5F_{10}O/N_2/O_2$ gas mixtures, and found that the effective ionization rate coefficient of the mixed gas will not be changed when the oxygen concentration added to the $C_5F_{10}O/CO_2$ gas mixture is lower than 10%. Oxygen mainly plays a role in reducing the formation of CO and solid carbon soot when the charged part of the GIS is discharged. The effective ionization rate coefficient and drift velocity of the gas mixture when oxygen is added to the $C_5F_{10}O/N_2$ gas mixture are significantly increased near the critical electric field. The dielectric strength of $C_5F_{10}O/N_2$ mixture is 6.5% higher than that of $C_5F_{10}O$/air mixture under the same conditions, which is due to the opposite electronic regulation properties of N_2 compared with CO_2 and O_2 [59].

At present, the research on the insulation performance of $C_5F_{10}O$ gas mixture has confirmed that it has excellent insulation performance as an insulating dielectric from multiple dimensions such as breakdown characteristics, lightning impulse characteristics test, ionization parameters, and critical breakdown field strength simulation, and has the potential to be used as an insulating dielectric in GIE.

1.2.2 Decomposition Characteristics of $C_5F_{10}O$ Gas Mixture

The decomposition of $C_5F_{10}O$ gas mixture is mainly caused by electron collision, space photoionization and thermal dissociation under the action of discharge and thermal faults to induce $C_5F_{10}O$ molecules to dissociate to form various particles, and the particles will recombine to form $C_5F_{10}O$ molecules or other gas molecules. The factors that may cause the decomposition of $C_5F_{10}O$ gas mixture in GIE mainly include decomposition caused by discharge and thermal failures and decomposition caused by the gas-solid interface of materials inside the equipment.

(1) Discharge Decomposition Characteristics

In 2015, Maik et al. first studied the decomposition characteristics of $C_5F_{10}O$ gas mixture under the action of arc. Studies have shown that the energy of the arc will cause the temperature

around the arc core to rise sharply, and the $C_5F_{10}O$ gas molecules located around the arc core will decompose. Both $C_5F_{10}O$ and SF_6 decomposition during arc fault can produce trace amounts of hydrogen fluoride (HF), while gases such as CO_2 and CO will be produced. $C_5F_{10}O$ will not produce harmful substances such as S_2F_{10} because it does not contain S elements [60]. ABB's Ranjan et al. also tested the arc extinguishing performance and the decomposition products of $C_5F_{10}O$/air gas mixture load break switch (LBS). Since the main component in $C_5F_{10}O$/air gas mixture is still air, the addition of $C_5F_{10}O$ did not significantly change the arc extinguishing performance of the mixtures. After the arc extinguishing experiment was completed, the gas composition detection found that only a small part of $C_5F_{10}O$ decomposed and produced some non-toxic decomposition by-products, such as CF_4, CO_2, C_2F_6, C_3F_8, C_3F_6, C_4F_{10} and C_3HF_7 [61]. ABB also tested the arc extinguishing performance and decomposition products of $C_5F_{10}O$/air and $C_5F_{10}O/CO_2$ mixtures. Only small amounts of heptafluoropropane (C_3HF_7), CF_4, CO_2, C_2F_6, C_3F_8, and C_4F_{10} were produced during the arc extinguishing process. Part of the decomposed components produced by $C_5F_{10}O$ may be absorbed by the zeolite desiccant in the GIS during arc burning or after arc extinguishing [62]. Tatarinov et al. used Gas Chromatography-Mass Spectrometry (GC-MS) to detect the decomposition products of $C_5F_{10}O/N_2$ and $C_5F_{10}O$/air mixtures in dielectric barrier discharge, and found that C_4F_{10}, C_6F_{14}, C_3F_6 and C_5F_{12} were produced, and pointed out that the addition of air accelerated the decomposition of $C_5F_{10}O$ [63, 64]. Zhang Xiaoxing et al. firstly analyzed the stability and possible decomposition paths of $C_5F_{10}O$ from the microscopic level using density functional theory (DFT), and used GC-MS to analyze the gas components of $C_5F_{10}O/N_2$ and $C_5F_{10}O$/air mixtures before and after AC breakdown. By calculating the three main decomposition paths of $C_5F_{10}O/N_2$, it is found that the formation of CF_3CO, C_3F_7, C_3F_7CO and CF_3 radicals is the most likely to occur, and various radicals formed during the discharge process will combine to generate CF_4, C_2F_6, C_3F_8, C_3F_6, C_4F_{10}, C_5F_{12}, and C_6F_{14}, and these decomposition products have high dielectric strength [65, 66]. In the study of $C_5F_{10}O$/air gas mixture, it was found that C_4F_7O, CF_3, C_3F_7 and CO radicals were formed mainly through two decomposition paths in the process of discharge decomposition, and the radicals further reacted to generate the decomposition products such as CF_4, C_2F_6 and C_3F_8. In the experiment, it was found that with the increase of AC breakdown times, the breakdown voltage of the gas mixture decreased slightly, and the main decomposition products after breakdown were CF_4, C_2F_6, C_3F_8, C_3F_6, C_4F_{10} and CF_2O [67]. At the same time, Zhang also found that OH and H radicals generated by H_2O in the micro-water environment can catalyze the decomposition of $C_5F_{10}O$. $C_5F_{10}O$ decomposes in micro-water environment to produce decomposition products such as CF_4, C_2F_6, C_3F_6, C_3F_8, C_4F_{10}, C_5F_{12}, C_6F_{14}, C_3F_7COH, C_3F_7OH, CF_3COH, C_3HF_7 and CF_3OH [68, 69]. Wang Xiaohua et al. of Xi'an Jiaotong University used DFT to calculate the possible decomposition pathways and types of decomposition products of $C_5F_{10}O$, and proposed a decomposition process including 6 decomposition pathways and 48 important intermediate products (including all reactants, products and transition states) [70, 71]. Han Dong et al. studied the decomposition characteristics of $C_5F_{10}O$ gas mixture under corona discharge. It was found that the decomposition products of $C_5F_{10}O/N_2$ and $C_5F_{10}O$/air mixtures were mainly CO, CO_2, CF_4, C_2F_4, C_2F_6, C_3F_6 and C_3F_8. The content of decomposition products is positively correlated with $C_5F_{10}O$ concentration and corona discharge voltage [72].

Currently, the research on the characteristics of $C_5F_{10}O$ gas mixture discharge

decomposition shows that arc, AC breakdown and corona discharge can lead to the decomposition of $C_5F_{10}O$ gas and produce a variety of fluorocarbons. However, most of the existing studies are qualitative decomposition studies of single experimental variable, and there is lack of systematic studies on the evolution law of $C_5F_{10}O$ gas mixture discharge decomposition products for different discharge types and discharge energy.

(2) Thermal Decomposition Characteristics

Zhang Xiaoxing et al. of Wuhan University used reactive molecular dynamics theory to calculate the decomposition reaction of $C_5F_{10}O$ gas and found that the chemical bond between the carbonyl oxygen atom in $C_5F_{10}O$ molecule and the adjacent carbon atom is weak and has high reactivity. The main decomposition components generated by the decomposition of $C_5F_{10}O/CO_2$ gas mixture above 2600 K are CF_3^*, CO, $C_3F_7CO^*$, CF^*, CF_2^*, $C_3F_7^*$, F^*, CF_3^* and C^* [73]. Zeng Fuping et al. have studied the decomposition characteristics of $C_5F_{10}O/CO_2$ gas mixture under POF through experiments. The study found that $C_5F_{10}O/CO_2$ gas mixture began to decompose at about 375 ℃, and C_3F_8 and C_3F_6 were first produced. When the temperature is higher than 500 °C, C_2F_6 and CF_4 are generated, and components such as C_2F_4, C_5F_{12}, CF_2O, CO, and CO_2 will also be generated at higher temperatures [74].

Based on the thermal decomposition pathway and reaction rate constant, Li Xingwen et al. conducted chemical kinetic calculations for the decomposition of $C_5F_{10}O$ thermal decomposition products C_3F_4O and C_4F_7O. The results show that the thermal decomposition relaxation time of C_3F_4O is temperature dependent. The relaxation time for C_3F_4O decomposition is close to 5 s at 500 K and only 10^{-4} s at 2000 K. C_3F_4O gradually decomposes with the increase of temperature. When the temperature is lower than 600K, there is a large difference between the calculation results of the LTE method and the chemical kinetics method due to the existence of the barrier energy of the reaction. When the temperature is greater than 600K, the LTE is in good agreement with the chemical kinetic composition [75]. After calculating the decomposition path and radical recombination process of $C_5F_{10}O$ at 400℃~700℃, it was found that $C_5F_{10}O$ began to decompose at about 400℃, and only 4% of $C_5F_{10}O$ decomposed at 400℃. The decomposition of $C_5F_{10}O$ was intense at 600℃, and the main decomposition products were CO, CF_4, C_2F_4, C_2F_6, C_3F_6, C_3F_8 and CF_2O, while the radicals CF_2^*, CF_3^*, $C_2F_5^*$, $C_3F_5^*$, $C_2F_3O^*$, $C_3F_4O^*$ and $C_3F_7^*$ were produced. At 700 °C, 96% of $C_5F_{10}O$ decomposed to produce decomposition products such as CO, C_2F_4, C_2F_6 and C_3F_6 [76]. Wang Baoshan et al. of Wuhan University used Monte Carlo annealing method to optimize the ReaxFF parameters, and used the optimized parameters to predict the geometry, relative reaction energy and bond stretching curve of $C_5F_{10}O$, and simulated the thermal decomposition of $C_5F_{10}O$ in the temperature range of 300-5000 K. The results showed that the apparent activation energy of $C_5F_{10}O$ was 40.10±1.27 kcal/mol. In the initial stage of $C_5F_{10}O$ decomposition, the C-C bond is cleaved earlier than other bonds, and the main decomposition products are CF_4, C_2F_4, C_2F_6, C_3F_6, C_3F_8, C_4F_8, CO, CF_2O, CO_2. Wang Baoshan et al. also pointed out that the decomposition of insulating gas under humid conditions will produce the characteristic decomposition product of corrosive gas HF [77]. Wang Xiaohua et al. established a chemical kinetic model to study the temperature change characteristics of $C_5F_{10}O$ decomposition components at 300K~3500K, and then calculated the molar fractions of $C_5F_{10}O$ decomposition products under different temperature decreasing curves and pressures. The results show that the molar fractions of $C_5F_{10}O$ is about 1 when the temperature is decreased

to 1500 K, and the temperature decreasing rates has similar effect on the relaxation time of the reaction to generate $C_5F_{10}O$. High pressure can promote the recombination of decomposition products to form $C_5F_{10}O$ by increasing the molar fractions of $C_5F_{10}O$ decomposition components [78]. In the calculation of the reaction rate constants for the decomposition of $C_5F_{10}O$ at different temperatures, it was found that most of $C_5F_{10}O$ decomposition reactions are absorb heat. Due to the different activation energies between different reactions, their reaction rate constants are quite different. At 1500 K and above, most of the reaction rate constants are in the range of 10^{-15} to 10^{30} $cm^3mole^{-1}s^{-1}$ (or s^{-1}), so the corresponding reactions in $C_5F_{10}O$ plasma model are not negligible. In addition, the reaction of $C_5F_{10}O$ decomposition to generate C_2F_4 and CO is the main reason for the degradation of $C_5F_{10}O$ insulation and arc extinguishing performance [79]. Xiao Dengming et al. calculated the plasma behavior of $C_5F_{10}O/N_2$ gas mixture in the temperature range of 300 K ~ 30000 K and gas pressure range of 0.1 MPa ~ 0.8 MPa and found that when the temperature is less than 7500 K, the enthalpy of the gas mixture increases with the increase of the concentration of $C_5F_{10}O$, while when the temperature exceeds 7500 K, the result is opposite. This is because in pure N_2, the specific heat has two peaks around 7500 K and 15000 K, which are related to the dissociation reaction of N_2 and the ionization reaction of N, respectively. After the addition of $C_5F_{10}O$, the dissociation reaction of CO and CN mainly occurred at temperatures below 7500 K, and the first peak shifted to a lower temperature. The ionization energy of F (17.45 eV) is greater than that of N (14.53 eV) due to the decrease of the partial pressure of N atoms and the increase of the partial pressure of F atoms, and the second peak shifted from 15000 K to 16000 K [80].

In summary, the research on the thermal decomposition characteristics of $C_5F_{10}O$ gas mixture is mainly based on simulation, and the related research uses chemical kinetic models to construct the dissociation paths and decomposition product types of $C_5F_{10}O$ molecules in different temperature ranges, but the relevant experimental data are relatively lacking.

(3) Interfacial Decomposition Characteristics of Gas-solid Materials

In 2015, Maik et al. studied the decomposition characteristics of $C_5F_{10}O$ gas mixture under the action of arc and found that the micro-water contained in the equipment would cause the decomposition of $C_5F_{10}O$ gas to produce HF, which would corrode the internal equipment surface and produce powdery products that seriously threaten the safety of equipment and staff. Due to the long-term contact between solid materials and insulating gas in GIS, the insulating gas should be able to exist stably for a long time without chemical reactions. Experiments show that some polymers need to be replaced by new materials [60]. Zhang Xiaoxing et al. studied the gas-solid interface stability of $C_5F_{10}O$ gas mixture with EPDM rubber sealing materials inside electrical equipment, and found that $C_5F_{10}O$ reacted with EPDM under thermally accelerated aging conditions, causing the decomposition of $C_5F_{10}O$ to produce C_3F_6, C_3F_6O, and C_3HF_7. At the same time, a large number of crystal particles will be precipitated on the surface of EPDM rubber and an oily film will be formed, which will reduce its mechanical properties and accelerate aging [81]. Li Xingwen et al. also studied the stability of the decomposition products of $C_5F_{10}O$ and $C_5F_{10}O$/air gas mixture with copper and aluminum under thermal decomposition and partial discharge conditions. It was found that $C_5F_{10}O$ had good thermal stability at 300 °C, and $C_5F_{10}O$ decomposed at 500 °C to produce CO, CO_2, C_2F_6, C_2F_4, C_3F_8, C_3F_6, C_4F_{10}, C_4F_8 and CHF_3, of which CO_2, C_3F_6, and C_4F_{10} were the main components. CF_4, C_3F_6, CF_2O, CHF_3 and C_3HF_7 in the decomposition products have good stability on copper and aluminum surfaces,

while the interaction of $C_2F_6O_3$ on copper and aluminum surfaces is chemisorption [82].

In summary, the research on the gas-solid interface stability of $C_5F_{10}O$ gas mixture with gas-solid materials such as metal materials, various non-metal materials and adsorbents in the equipment is relatively scarce. Relevant research is also mainly based on experimental tests, and there is a lack of systematic research on the mechanism of gas-solid interface interaction of solid materials in equipment.

Currently, some progress has been made in the research on the decomposition characteristics of $C_5F_{10}O$ gas mixture, including the decomposition characteristics of electrical, thermal and metal interfaces. The relevant simulation studies mainly focus on the decomposition path construction and the calculation of reaction thermodynamic parameters, and the experimental studies mainly based on analysis and testing, lacking systematic studies on the interaction mechanism between $C_5F_{10}O$ gas mixture and solid materials in the equipment and the electrothermal decomposition characteristics and decomposition mechanism of $C_5F_{10}O$ gas mixture under different conditions.

1.2.3 Biosafety of $C_5F_{10}O$ Gas Mixture

The biosafety of $C_5F_{10}O$ gas and its decomposition products is of great significance to its application safety. Carrying out biosafety research before its engineering application is the premise to ensure the safety of relevant workers. The material safety data sheet (MSDS) [17, 83] given by Minnesota Mining and Manufacturing (3M) points out that the 4h lethal concentration 50% (LC50) of $C_5F_{10}O$ is 14000 ppm (parts per million)-20000 ppm (rat), and the 8-hour time weighted average (TWA) occupational exposure limits (OEL) of $C_5F_{10}O$ is set to 225 ppm [84]. Christophe et al. found that the LC50 (rat, 4 h) value of $C_5F_{10}O$/air gas mixture (liquefaction temperature of -15°C) used in load switches is10%. After the load switch is subjected to a current breaking test, the LC50 of the gas mixture decreased to 3000 ppm [85]. ABB company has evaluated the environment and safety of its insulating equipment codenamed AirPlus, the insulating gas inside the equipment is $C_5F_{10}O$/air gas mixture. The results indicate that there is no serious environmental or personal safety risk for operators operating AirPlus insulation equipment. Even in the event of a fault condition resulting in the leakage of insulating gas, the $C_5F_{10}O$ concentration does not exceed the threshold 225ppm of the TWA-OEL. In the process of arc burning, equipment using air, SF_6 or $C_5F_{10}O$/air gas mixture as insulating dielectric all produce toxic gases. The concentration of toxic decomposition products produced by $C_5F_{10}O$/air gas mixture is slightly higher than that of air, but significantly lower than that of SF_6. AirPlus insulation equipment is not only more eco-friendly than SF_6 equipment, but also safer in normal operation and failure [86].

As a new type of insulating gas that has attracted much attention in recent years, $C_5F_{10}O$ gas is extremely scarce in its biosafety research. However, biosafety research is an indispensable part before the large-scale application of new gases, especially in today's society, which pays more and more attention to public safety. Therefore, the acute inhalation toxicity test of $C_5F_{10}O$ and its decomposition products is carried out to obtain the clinical symptoms and pathological characteristics of organisms after acute inhalation, and to clarify the biosafety of $C_5F_{10}O$ gas mixture, which can provide an important guiding basis for the formulation of relevant operation specifications and protective measures.

1.2.4 $C_5F_{10}O$ Gas Mixture Engineering Application Cases

The high-voltage equipment developed by ABB with $C_5F_{10}O/CO_2/O_2$ gas mixture as insulating dielectric passed all type tests, and eight high-voltage GIS of 170 kV and 50 medium-voltage GIS of 24 kV were installed in 2015 at the Elektrizitätswerke Zürich substation in the city of Zurich. Gas samples collected after three months of substation operation showed no detectable changes in $C_5F_{10}O$ concentration, indicating that $C_5F_{10}O$ gas does not decompose during normal operation of the equipment [15, 87]. ABB also installed four AirPlus ring main units (RMUs) at the Leander network in Flevoland, the Netherlands, in November 2015 for a 3-year field experience project. Gas samples are collected several times a year for analysis, and equipment is visually inspected during site visits. By the end of the field experience project in 2018, an inspection of the equipment recovery found no significant changes in gas composition analysis and measurements since the RMUs were installed and energized [88]. ABB has received an order of about $40 million from the German grid operator for upgrading high-voltage substations. As one of the components of the upgrade, the world's first 380kV GIS with an industry-standard $C_5F_{10}O$ gas mixture as an alternative to SF_6 is expected to be installed in Germany in 2026 [16].

Although foreign electrical equipment manufacturers such as ABB have designed, manufactured and tested equipment using $C_5F_{10}O$ gas mixture as the insulating dielectric, they are still in the testing and optimization stage. The main significance is to verify the feasibility of engineering applications, and China currently lacks the design experience of eco-friendly GIE. In order to break through the technical barriers and realize the independent production and manufacture of eco-friendly GIE, it is necessary to carry out systematic research on the stability, decomposition characteristics and biological safety of $C_5F_{10}O$ gas mixture, and comprehensively evaluate its application feasibility. In this manuscript, the decomposition characteristics and biosafety of $C_5F_{10}O/N_2/O_2$ gas mixture as an insulating dielectric are systematically studied. N_2 and O_2 are chosen as buffer gases because $C_5F_{10}O$ has a stronger synergistic effect with N_2 than CO_2 gas and N_2 has better environmental protection properties compared to CO_2 gas. The role of O_2 is to inhibit the decomposition of $C_5F_{10}O$ gas under discharge conditions to produce solid carbon. The research results of this manuscript provide important theoretical and practical support for the design, material selection, manufacturing, and optimization of electrical equipment with $C_5F_{10}O$ as the insulating dielectric, so as to reduce SF_6 emissions in the power industry and contribute to curbing global warming and environmental protection of power gas insulation equipment manufacturing.

1.3 Research Content and Chapter Arrangement

1.3.1 Main Research Content

At present, the research on the insulation properties of $C_5F_{10}O$ gas mixture by domestic and foreign researchers has confirmed its application potential, but further systematic research is urgently needed on its electrothermal decomposition mechanism, interface decomposition characteristics with commonly used metal materials and biosafety. This manuscript focuses on the decomposition characteristics and biological safety of $C_5F_{10}O/N_2/O_2$ gas mixture. Firstly, the stability of $C_5F_{10}O/N_2/O_2$ gas mixture with the metal materials in the equipment is tested.

Then, the electrothermal decomposition characteristics of $C_5F_{10}O/N_2/O_2$ gas mixture under typical electrothermal faults are studied, and the decomposition mechanism and gas-solid interface interaction mechanism of $C_5F_{10}O$ are studied based on density functional theory and transition state theory, and the decomposition mechanism of $C_5F_{10}O/N_2/O_2$ gas mixture under different conditions is obtained. Finally, the biosafety of $C_5F_{10}O$ and $C_5F_{10}O/N_2/O_2$ arc decomposition products is tested, and targeted protective measures and suggestions are put forward. The main research contents are as follows:

1) Evaluate the interfacial stability of $C_5F_{10}O/N_2/O_2$ gas mixture with metal materials, and propose optimized solutions for metal materials with poor gas-solid stability. Combined with the molecular structure characteristics of $C_5F_{10}O$, the gas-solid interface interaction model between $C_5F_{10}O$ and metal conductive materials commonly used in equipment is constructed, and the interaction mechanism between $C_5F_{10}O$ and metal interface is obtained based on density functional theory.

2) Reveal the discharge and thermal faults decomposition characteristics of $C_5F_{10}O/N_2/O_2$ gas mixture containing different concentrations of oxygen, and analyze the relationship between the types and contents of $C_5F_{10}O/N_2/O_2$ gas mixture decomposition products and the failure types, and the regulation mechanism of oxygen on $C_5F_{10}O/N_2/O_2$ gas mixture decomposition products.

3) Consider the influence of oxygen and micro-water to construct the decomposition path of $C_5F_{10}O/N_2/O_2$ gas mixture and the composite path of decomposition products. The structural properties, reaction enthalpy and activation energy of each decomposition product and intermediate product are calculated based on density functional theory and transition state theory, and the decomposition mechanism of $C_5F_{10}O$ is clarified by combining the experimental results.

4) Carry out experiments to test the acute inhalation toxicity of $C_5F_{10}O$ and $C_5F_{10}O/N_2/O_2$ arc decomposition products, obtain the changes of physiological characteristics and clinical symptoms of mice after exposure. Based on pathological and hematological detection and analysis methods, the influence of $C_5F_{10}O$ and its decomposition products on various organs and vital signs of mice is clarified, and the application safety of $C_5F_{10}O/N_2/O_2$ gas mixture is evaluated based on the experiment results.

1.3.2 Research Ideas and Technical Route

The technical roadmap used in this manuscript is shown in Figure 1.3, and the specific research ideas are as follows:

For the study of the interaction stability of $C_5F_{10}O/N_2/O_2$ gas mixture and metal materials, it is planned to carry out the gas-solid interface decomposition characteristics experiment of $C_5F_{10}O/N_2/O_2$ with the conductive metal materials copper, aluminum and silver inside the equipment under different temperature conditions, and obtain the decomposition of $C_5F_{10}O$ and the physical and chemical changes of the metal surface during the interaction process. Combined with the molecular structure of $C_5F_{10}O$ and the distribution of active sites on the surface of metal materials, the gas-solid interface interaction model between $C_5F_{10}O$ and metal materials such as copper, aluminum and silver are constructed. The parameters of adsorption energy, differential charge density and charge transfer of gas on solid surface are calculated based on density flooding theory. The stability of the interaction between $C_5F_{10}O/N_2/O_2$ gas

mixture and metal materials is evaluated by a combination of experiments and simulations, and optimization suggestions are given.

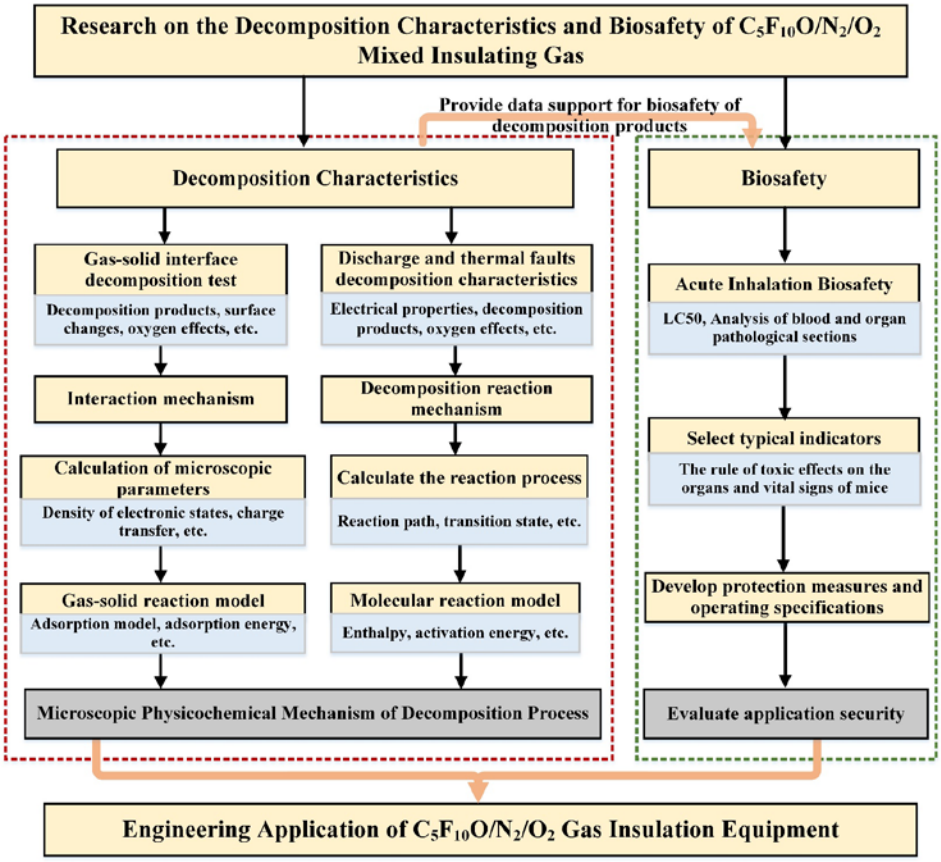

Figure 1.3 The technical roadmap of this manuscript

For the study of the electrothermal decomposition characteristics of the $C_5F_{10}O/N_2/O_2$ gas mixture, the types and contents of decomposition products of $C_5F_{10}O/N_2/O_2$ gas mixture under different test conditions are obtained through AC breakdown, PD and POF tests using gas chromatography-mass spectrometry, and the relationship between external conditions and the types and contents of decomposition products is summarized. Combining the molecular structure characteristics of $C_5F_{10}O$, O_2 and H_2O, the decomposition reaction path is constructed based on density functional theory and transition state theory, and the decomposition mechanism of $C_5F_{10}O/N_2/O_2$ gas mixture is clarified by calculating the activation energy and enthalpy of different decomposition reaction paths that satisfy the energy minimum principle.

For the biosafety study of $C_5F_{10}O/N_2/O_2$ gas mixture and its decomposition products, it is planned to build a biosafety experimental platform for $C_5F_{10}O$ and $C_5F_{10}O/N_2/O_2$ decomposition products, and evaluate the biosafety of $C_5F_{10}O/N_2/O_2$ gas mixture and its arc decomposition products by using mice as experiment subjects. Based on the experiment results, make targeted recommendations for the protection of relevant personnel. Finally, combined with the decomposition characteristics and biosafety results of $C_5F_{10}O/N_2/O_2$ gas mixture, the feasibility and application safety of $C_5F_{10}O/N_2/O_2$ gas mixture to replace SF_6 gas as an insulating dielectric in medium- and low-voltage voltage grade equipment are evaluated.

1.3.3 Thesis Structure and Chapter Arrangement

This manuscript mainly includes the following six chapters:

In Chapter 1, firstly introduces the research background and significance of eco-friendly insulating gas, and summarizes its research status. The research progress of insulation performance, decomposition characteristics and biosafety of $C_5F_{10}O$ gas mixture is mainly introduced and summarized, and the main research content and technical route of this manuscript are proposed.

In Chapter 2, the gas-solid interface stability of $C_5F_{10}O/N_2/O_2$ gas mixture with copper, aluminum and silver is tested considering the long-term contact of $C_5F_{10}O$ with metal conductive materials (copper, aluminum and silver) inside the equipment. The stability of the interaction of $C_5F_{10}O/N_2/O_2$ gas mixture with metal materials is evaluated by analyzing the gas composition, metal surface morphology and chemical composition changes, and the optimization scheme is proposed.

Chapter 3 tests the decomposition characteristics of $C_5F_{10}O/N_2/O_2$ gas mixture under typical electrothermal faults. The decomposition characteristics of $C_5F_{10}O/N_2/O_2$ gas mixture are tested by electrothermal decomposition experiments under different conditions, and the correlation between the external conditions and the types and contents of the decomposition products and the regulation mechanism of oxygen on the decomposition products of $C_5F_{10}O/N_2/O_2$ gas mixture are obtained.

In chapter 4, the gas-solid interface model of $C_5F_{10}O$ and copper, aluminum and silver are constructed, and the gas-solid interaction is studied based on density functional theory. The decomposition pathways of $C_5F_{10}O$, O_2 and H_2O are constructed by combining their molecular structure properties, and the parameters such as enthalpy and activation energy of the relevant reaction pathways are calculated. The gas-solid interaction mechanism and decomposition mechanism of $C_5F_{10}O$ are clarified with the experimental results in the previous manuscript.

Chapter 5 studies the biosafety of $C_5F_{10}O/N_2/O_2$ gas mixture and its arc decomposition products with mice as the experiment object. Combined with the electrothermal decomposition characteristics and biosafety results of $C_5F_{10}O/N_2/O_2$ gas mixture, the feasibility and safety of its engineering application are evaluated, and relevant safety protection measures and suggestions are put forward.

Chapter 6 summarizes the main research content of this manuscript and gives an outlook to the follow-up research work.

2 Experimental Research on Interface Decomposition Characteristics of $C_5F_{10}O/N_2/O_2$ Gas Mixture with Metal Materials

GIE has a long service life and maintenance period, and the operating gas pressure is also high, and the insulating gas is in direct contact with the materials inside the equipment for a long time under normal operating conditions. The physical and chemical properties of $C_5F_{10}O$ gas are quite different from SF_6 gas. The gas-solid interface interaction between the $C_5F_{10}O/N_2/O_2$ gas mixture and the materials in the equipment accompanies the entire life cycle of GIE, so it puts forward higher requirements for its material compatibility, which is also a prerequisite for its engineering application. Compared with non-metallic insulating materials such as rubber sealing materials and epoxy resins in the equipment, the chemical properties of the metal conductive materials are more active, and the maximum temperature rise caused by the thermal effect of the current during the normal operation of the equipment can lead to metal current-carrying busbar to working in a temperature environment of 100~120 °C (the working temperature is much higher than the insulating material at the equipment shell). Therefore, it is necessary to carry out the interface decomposition characteristics experiment of $C_5F_{10}O/N_2/O_2$ gas mixture and metal materials in the equipment at different temperatures to obtain the stability of gas-solid interaction under thermally accelerated aging conditions.

This chapter takes copper, aluminum and silver commonly used in GIE as the research objects, and builds a gas-solid interface interaction experimental platform for $C_5F_{10}O/N_2/O_2$ gas mixture and metal materials. The gas-solid interface decomposition characteristics of $C_5F_{10}O/N_2/O_2$ gas mixture with copper, aluminum and silver materials in the range of 120~220℃ is tested, and the stability of the gas-solid interface is evaluated by testing the gas composition, metal surface morphology and chemical changes.

2.1 Metal Material Gas-solid Interface Stability Experimental Platform and Method

2.1.1 Experimental Platform

The experiment platform shown in Figure 2.1 mainly comprises a heating system and a temperature feedback monitoring control system. The heating system includes a heat source and a copper outer casing outside of the heat source, whereas the heat source transfers heat to the surface of the heating device through the copper outer casing. The copper shell has the same material as the experiment copper sheet sample, whereas the air chamber shell is made from stainless steel. To prevent the heating device from transmitting high temperature to the inner wall of the air chamber, the heating device does not directly contact the air chamber wall, thereby avoiding stainless steel interference during the experiments. The temperature feedback monitoring control system includes a temperature sensor and a proportional-integral-derivative (PID) controller. The copper sample and temperature sensor for the PID controller feedback control are fixed on the copper casing to monitor the temperature of the copper sample in real time and to control the experiment process. The $C_5F_{10}O$ gas used in the experiments are provided by 3M Company, with a purity of ≥99.5%. Metal materials include copper, aluminum

and copper with a protective silver plating on the surface. To facilitate the characterization of the samples after the experiment, the metal materials used in the experiment are uniformly cut into 0.2×5×100 mm thin slices. Use ethanol solution to clean and remove the possible stains on the surface of sample after cutting, then the residual ethanol on the surface is washed by distilled water, and the sample is placed in a dry box and dried at 35°C for 1 hour.

The metal sample is fastened to the surface of the metal casing before the experiment, so that the sample can be close to the heat source during the experiment (In order to control the experiment variables, in the gas-solid interface decomposition characteristic experiment of different metals, the metal shell covered on the outside of the heat source is replaced with a metal of the same material as the test metal). Before the experiment, the pre-prepared sample is fixed on the heat source, and then the vessel is vacuum-washed three times with N_2 gas to eliminate interference from other gaseous impurities. After the completion of the scrubbing, the vessel is evacuated to a vacuum by a vacuum pump. First, the vessel is filled with 22.5 kPa of $C_5F_{10}O$, and then charged with N_2 and O_2 to a total gas pressure of 0.3 MPa (absolute pressure). After the aeration is completed, the reactor is allowed to stand for 24 h to ensure gases are evenly mixed. The concentrations of oxygen in $C_5F_{10}O/N_2/O_2$ gas mixture used in the experiment are 0 and 20%, respectively. Relevant regulations stipulate that the maximum ambient temperature for the safe and stable operation of the equipment is 40°C, and the maximum allowable temperature rise of the equipment is 70°C. Considering the normal operation and thermal fault conditions of the current-carrying bus in the equipment, this manuscript selects three experiment temperatures of 120°C, 170°C and 220°C for the 8h thermally accelerated aging experiment. After the experiment, the gas in the gas chamber is collected and analyzed by GC-MS. After the gas is exhausted, the metal samples are tested and analyzed by scanning electron microscope (SEM) and X-ray Photoelectron Spectrometer (XPS).

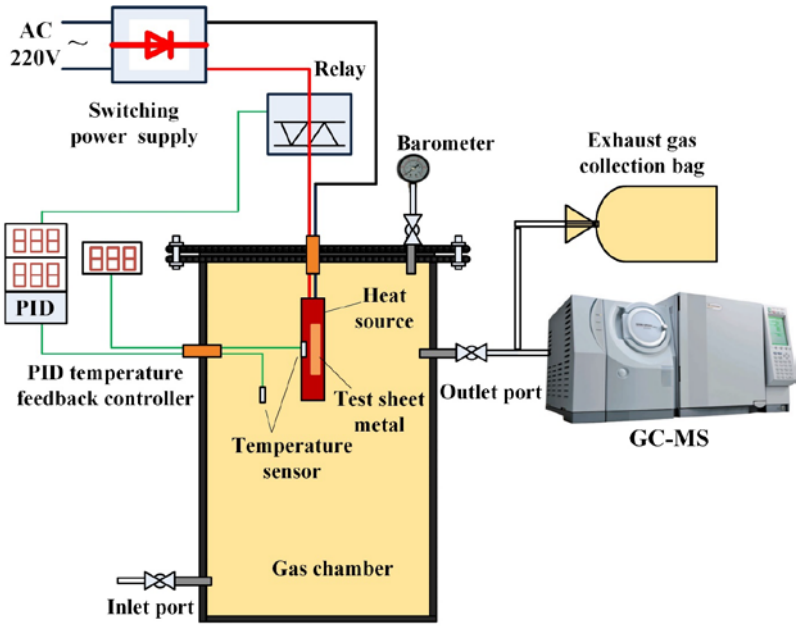

Figure 2.1 Experimental platform for decomposition characteristics of metal gas-solid interface

2.1.2 Decomposition Products Detection Method

1 Detection Method of Gas Decomposition Products

The molecular structure of SF_6 gas is a space-symmetric regular octahedral structure consisting of a centrally located S atom and six F atoms with six identical S-F bonds. The main decomposition products of SF_6 during the chemical reaction are SO_2F_2, SOF_2, SOF_4, SO_2, HF and CS_2 [89], with a small variety of products. However, the $C_5F_{10}O$ molecule is a fluorine ketone gas composed of five carbon atoms, and many small carbon-containing organic compounds can be produced during the decomposition process, which greatly increases the difficulty of detecting the decomposed gas. GC-MS detection method is currently a popular method that can simultaneously detect the types and contents of various gases in gas mixture.

The decomposition products of $C_5F_{10}O/N_2/O_2$ gas mixture in this manuscript are detected by GC-MS (SHIMADZU GCMS-QP2010 Ultra shown in Figure 2.2). The column type, film thickness, length, inner diameter, column temperature, inlet temperature, and mass ion source temperature are CP-SIL 5 CB, 8 μm, 60 m, 0.32 mm, 32 ° C, 200 ° C, and 200 ° C, respectively.

Figure 2.2 GC-MS

Since the decomposition components of $C_5F_{10}O/N_2/O_2$ gas mixture are complex, and the decomposition products under different conditions are different, the chromatograms of all the decomposition products of $C_5F_{10}O$ gas are firstly obtained using the SCAN full scan mode of GC-MS. Then, the similarity search is carried out with reference to the standard mass spectrum of the National Institute of Science and Technology (NIST) Standard Reference Database 14.0 to preliminarily determine the gas types of the decomposition products of the $C_5F_{10}O$ gas mixture, and the separation time and characteristic particle mass-to-charge ratio (m/z) of each decomposition product. The chromatogram and mass spectrum of the decomposition products of $C_5F_{10}O/N_2/O_2$ gas mixture are obtained by scanning again in the Selective Ion Monitoring (SIM) mode for quantitative detection of the decomposition products. Based on the standard gas samples to confirm and calibrate the decomposition products, a quantitative detection program for the decomposition products of $C_5F_{10}O/N_2/O_2$ gas mixture is developed using the external standard method. Finally, the gas samples of the decomposition products of $C_5F_{10}O/N_2/O_2$ gas mixture under different experiment conditions are detected and analyzed to determine the type and content of the decomposition products, which are used to assist in the analysis of the decomposition law of $C_5F_{10}O$ gas under different experiment conditions. It should be specially pointed out that for the decomposition products (such as CF_2O) for which no standard gas is available or not readily available, semi-quantitative detection is performed

by using the area external standard method to integrate the peak area of characteristic ions.

Figure 2.3 shows the chromatogram and mass spectrum of the decomposition products of $C_5F_{10}O/N_2/O_2$ gas mixture obtained by the above method after multiple AC breakdowns. It can be seen that the detection program developed in this manuscript can identify the decomposition components such as CF_4, C_2F_4, C_2F_6, C_3F_6, C_3F_8, C_4F_{10}, CO, CO_2, CF_2O and C_3HF_7 (The characteristic ion mass-to-charge ratio m/z of each gas is shown in Table 2.1). Most of the decomposition products are fluorocarbons containing -CF_3 groups (m/z=69). Therefore, in order to avoid the problem of interference in quantitative detection caused by the overlapping of mass spectral peaks of m/z=69 produced by different gases, different characteristic ions are used for quantitative research on gases with overlapping mass spectral peaks of m/z=69.

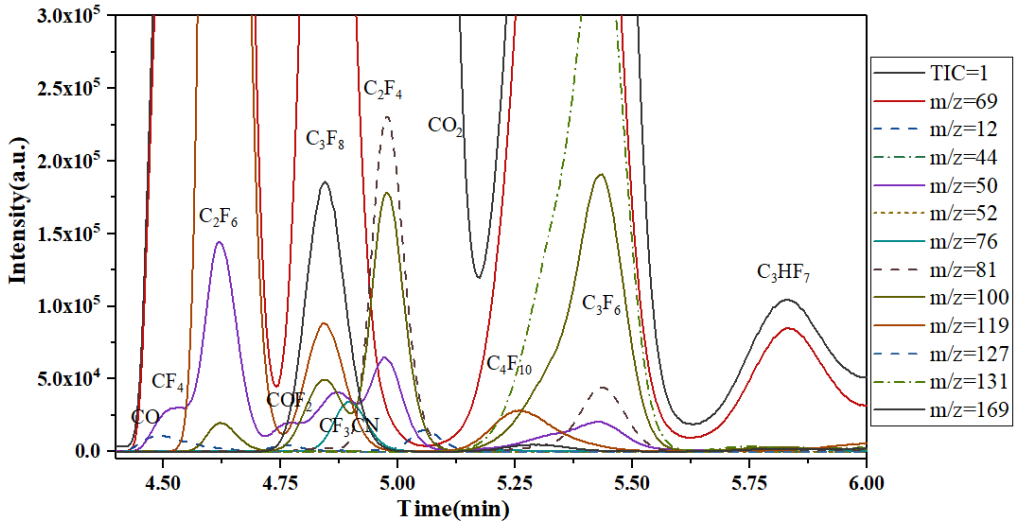

(a) Mass spectrum of decomposition products

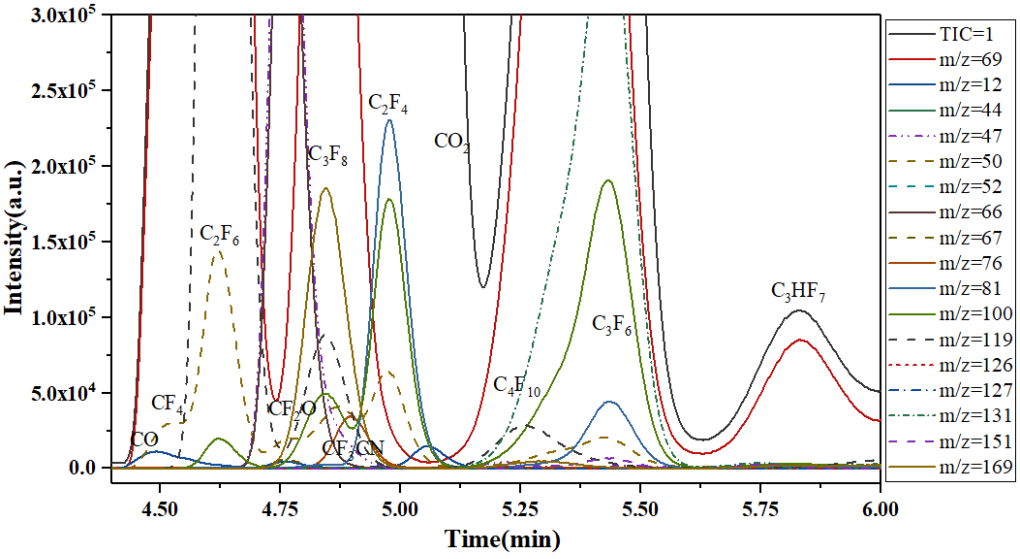

(b) Partial magnification of the mass spectrum of the decomposition products

Figure 2.3 Mass spectrum of $C_5F_{10}O/N_2/O_2$ gas mixture and its decomposition products

2 Solid Surface Detection Methods

The detection of solid surfaces mainly characterizes the microscopic physical and chemical changes of solids from two aspects: surface morphology and elemental analysis. The microscopic surface morphology analysis is observed by SEM, and the elemental analysis

could be analyzed by SEM with Energy Dispersive Spectroscopy (EDS) and XPS.

1) SEM

SEM is mainly used to obtain high-resolution topography of surface micro-regions of material samples. The thermal field emission scanning electron microscope is used in this study, and its main parameters are: acceleration voltage range 0.1~30kV, resolution 1.3nm@20kV, 1.5nm@15kV or 2.3nm@1kV. EDS needs to be used together with SEM. It can scan the line distribution and surface distribution of elements on the surface of the sample material, and use the characteristic X-rays excited by the electron beam of the SEM to determine the type and distribution of surface elements.

2) XPS

The basic principle of XPS is to use X-rays to irradiate the surface of the sample, so that the substances in the sample are in an excited state by the photoelectric effect, thereby generating photoelectron emission. The energy analyzer in XPS has the function of measuring the kinetic energy of photoelectrons, and the binding energy (B.E.) of the excited electrons can be obtained by calculation. XPS can quantitatively detect all elements except hydrogen and helium. The detection sensitivity of XPS used in this manuscript is 0.1% to 1% atomic concentration ratio, the optimal spatial resolution is better than 20 μm, and the imaging spatial resolution is better than 3 μm. XPS can determine the chemical state and characteristic chemical bond of the compound by detecting the photoelectron spectrum curve generated after the solid substance is excited, and can be employed to analyze the chemical composition and material composition of the sample surface.

Table 2.1 Characteristic mass-to-charge ratio m/z of $C_5F_{10}O/N_2/O_2$ gas mixture decomposition products

Gas type	Mass-to-charge ratio (m/z)
CF_4	**69**
C_2F_4	50、**81**、100
C_2F_6	50、69、**100**、119
C_3F_6	50、69、**81**、100、131、150
C_3F_8	69、100、119、**169**
CO	**12**
CO_2	**44**
C_3HF_7	51、**69**、151
C_4F_{10}	69、100、**119**、131、169
CF_2O	47、**66**

2.2 Experiment on Interface Decomposition Characteristics of $C_5F_{10}O/N_2/O_2$ with Copper and Aluminum

By means of the experimental platform shown in Figure 2.1, the metal shell and metal samples are made of copper (or aluminum) material to carry out the gas-solid interface decomposition characteristics experiment of $C_5F_{10}O/N_2$ and $C_5F_{10}O/N_2/O_2$ gas mixtures with copper (or aluminum). The test results obtained are as follows:

2.2.1 Gas Composition

(1) Gas Decomposition Products at the Copper Interface

Some chemical reactions at the gas-solid interface of copper materials may cause the decomposition of $C_5F_{10}O$, and these gas decomposition products can be detected and analyzed by GC-MS. After the experiment, a sampling bag is use of to collect gas samples inside the gas chamber for analysis. Since the composition of the decomposition products generated by the gas-solid interface interaction when $C_5F_{10}O/N_2/O_2$ gas mixture is in contact with copper is unknown, the SCAN mode is used to scan all possible decomposition products for qualitative analysis during the GC-MS analysis and testing process, as shown in Figure 2.4.

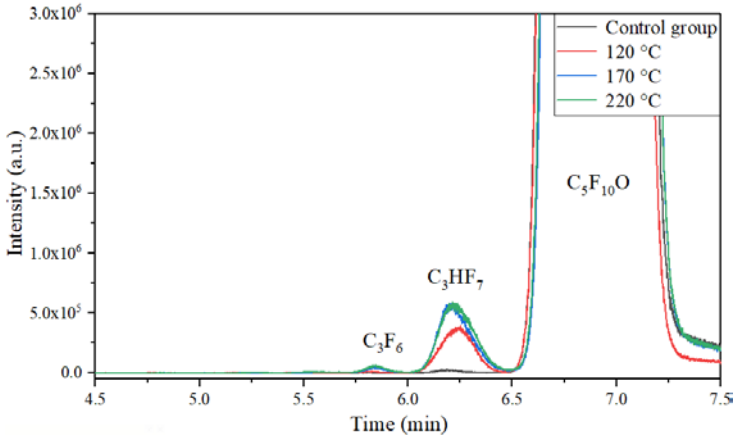

(a) Gas chromatograms of $C_5F_{10}O/N_2$ gas mixture before and after the experiment

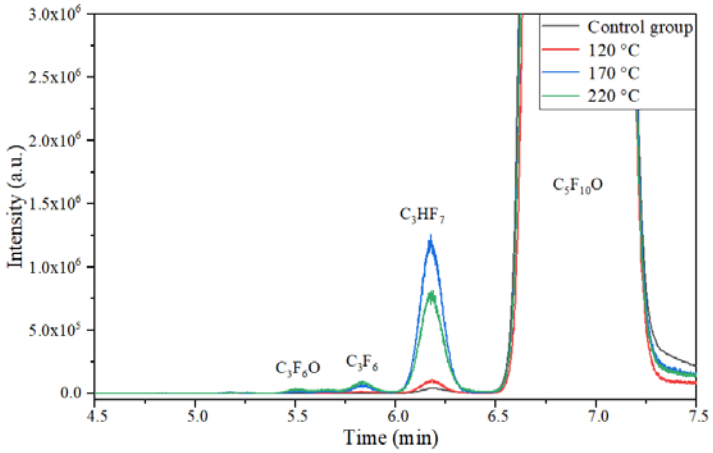

(b) Gas chromatograms of $C_5F_{10}O/N_2/O_2$ gas mixture before and after the experiment

Figure 2.4 Gas chromatogram of $C_5F_{10}O/N_2/O_2$ gas mixture

From Figure 2.4a, it can be seen that a trace amount of $C_5F_{10}O$ decomposed to produce C_3F_6 and C_3HF_7 in the experiment group. The reason why C_3HF_7, a product containing H element, is detected in the decomposition product is that although the interference of H_2O and air is eliminated as much as possible by means of air washing and drying in the experiment, the interior of the simulated gas chamber and sealing materials such as rubber still contain trace amounts of moisture, and the reaction activity of $C_5F_{10}O$ with H_2O is high, and a violent hydrolysis reaction will occur at room temperature [17]. Therefore, in the experiment of this manuscript, due to the increase of temperature, the material inside the gas chamber will slowly release the micro-water contained in it and participate in the decomposition reaction of $C_5F_{10}O$. However, the material in the gas chamber contains very little water, and the hydrolysis reaction stops after the reaction with $C_5F_{10}O$ is consumed, so the content of the decomposition products is very small, and the content of the decomposition products (the relative content can be judged

by the peak value and peak area) grows slightly with the increase of the experiment temperature. From Figure 2.4b, it can be seen that the $C_5F_{10}O$ in $C_5F_{10}O/N_2/O_2$ gas mixture experiment group undergoes decomposition similar to that in Figure 2.4a. The chromatographic column separated C_3F_6 and C_3HF_7 at the same time, with the difference that the decomposition product C_3F_6O is also detected.

(2) Gas Decomposition Products at the Aluminum Interface

Figure 2.5 shows the detection results of gas components after the interface decomposition experiment of $C_5F_{10}O/N_2/O_2$ gas mixture and aluminum. C_3HF_7, C_3F_6 and CHF_3 are detected in the decomposition products. These products are mainly produced by the hydrolysis reaction between the micro-water contained in the material inside the gas chamber and $C_5F_{10}O$. The content of decomposition products is also not related to the change of experiment temperature.

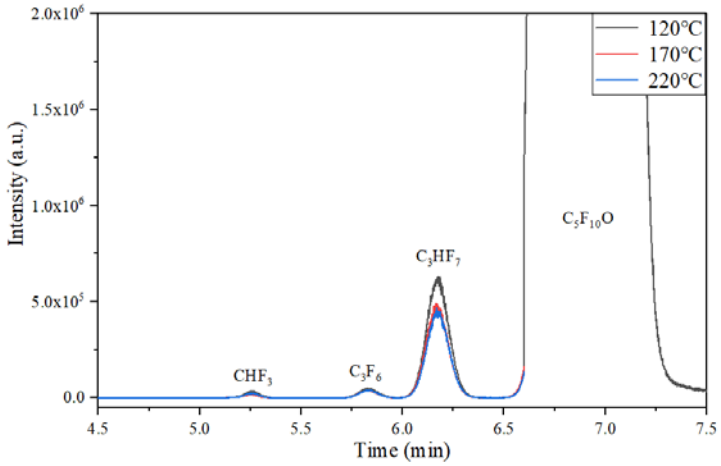

(a) Gas chromatograms of $C_5F_{10}O/N_2$ gas mixture before and after the experiment

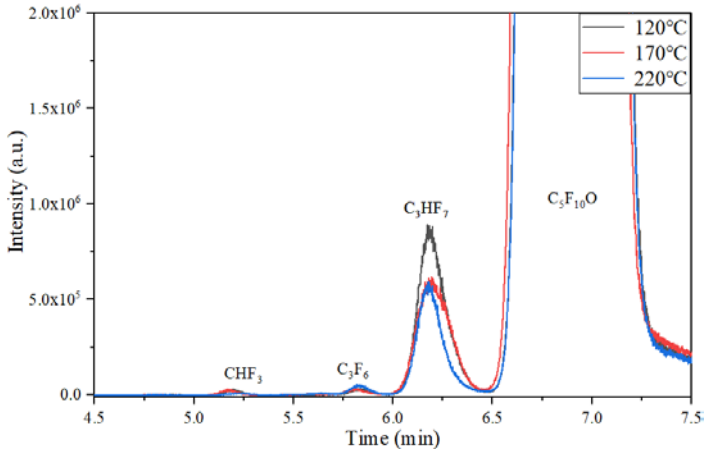

(b) Gas chromatograms of $C_5F_{10}O/N_2/O_2$ gas mixture before and after the experiment

Figure 2.5 Gas chromatogram of $C_5F_{10}O/N_2/O_2$ gas mixture

2.2.2 Metal Surface Morphology

(1) Copper Surface Morphology

A photo of the copper samples after $C_5F_{10}O/N_2$ gas mixture come in contact with the copper material under high temperature conditions is presented in Figure 2.6. The copper material in the control group before the experiment is purple–red and bright in color. When the experiment temperatures range between 120 °C and 170 °C, the copper surface color gradually

turns golden yellow. When the experiment temperature is 220 °C, the copper surface color turns pink.

(a) Control group (b) Experiment temperature 120 °C (c) Experiment temperature 170 °C (d) Experiment temperature 220 °C

Figure 2.6 Surface photo of copper before and after contact with $C_5F_{10}O/N_2$ gas mixture

Figure 2.7 shows the change in the color of the copper surface after the $C_5F_{10}O/N_2/O_2$ gas mixture comes in contact with the copper sample under different experiment temperature conditions. Figure 2.5d and Figure 2.6a show that $C_5F_{10}O/N_2/O_2$ gas mixture at a experiment temperature of 120 °C has a similar color to the copper surface of $C_5F_{10}O/N_2$ gas mixture experiment group at a experiment temperature of 220 °C. When the experiment temperature is 170 °C, the copper sheet fixed on the surface turns brown. When the experiment temperature is 220 °C, the surface color of the copper turns dark brown and a strong pungent odor is emitted. The change in the color of the copper surface is most obvious at this time.

(a) Experiment temperature 120 °C (b) Experiment temperature 170 °C (c) Experiment temperature 220 °C

Figure 2.7 Surface photo of copper before and after contact with $C_5F_{10}O/N_2/O_2$ gas mixture

The surface micro-morphology of the copper sample is characterized by SEM, and the surface micro-structure is shown in Figure 2.8 and Figure 2.9.

Figure 2.9 shows the surface morphology of copper in $C_5F_{10}O/N_2$ gas mixture experiment groups and the control group. In the control group, the copper surface is smooth and flat, while its structure is fine and compact. The small grooves appearing under the microstructure are inevitable due to the limitations of the manufacturing process. When the experiment temperature is 120 °C, corrosion spots appear on some parts of the copper surface. Figure 2.7b presents the morphology of the corrosion point, which in turn shows an island-like irregular distribution in the field of view and a flat crystal structure. When the experiment temperature is 170 °C, the distribution of the corrosion points gradually enhanced while its distribution

remains relatively uniform. The crystal structure of the corrosion points in the entire field of view becomes 3D, and the crystal exhibits a certain regularity. When the experiment temperature is 220 °C, the corrosion layer evenly covers the entire copper surface, and the density of the corrosion point increases. However, the corrosion layer remains in the shallow region of the copper surface during the experiment.

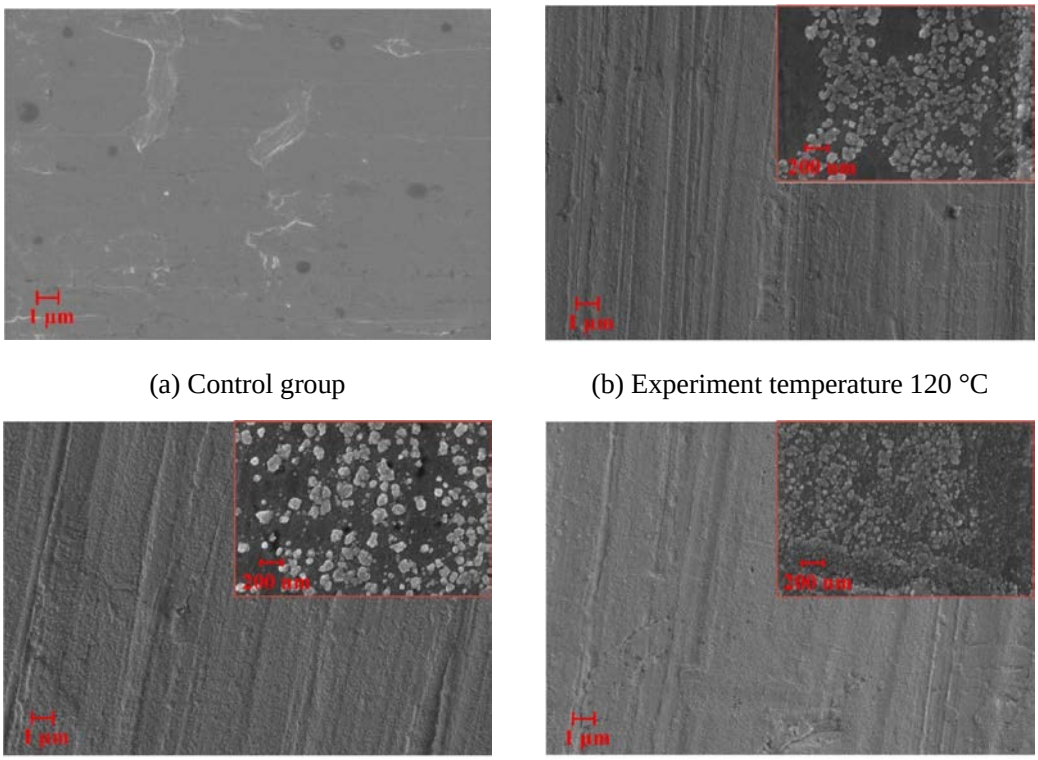

(a) Control group (b) Experiment temperature 120 °C

(c) Experiment temperature 170 °C (d) Experiment temperature 220 °C

Figure 2.8 SEM morphology of surface after contact of copper with $C_5F_{10}O/N_2$ gas mixture

When the copper surface temperature increases, the corrosion point is initially concentrated in the position where the copper surface has a small flaw. As the temperature increases, the corrosion point gradually spreads across the surface of the copper sample. The temperature further increases and the corrosion point becomes dense, thereby covering the entire copper surface.

Figure 2.9 shows the surface morphology of the copper in $C_5F_{10}O/N_2/O_2$ gas mixture experiment groups. When the experiment temperature of $C_5F_{10}O/N_2/O_2$ gas mixture experiment group is 120 °C, no obvious corrosion point is observed on the copper surface. The copper surface color of $C_5F_{10}O/N_2/O_2$ gas mixture experiment group at 120 °C becomes similar to that of $C_5F_{10}O/N_2$ gas mixture experiment group at a temperature of 220 °C. However, the micrograph does not show a similar morphology, thereby suggesting that the change in the color of the copper surface cannot accurately determine whether the copper is corroded. Therefore, FESEM testing must be applied on the copper samples. When the experiment temperature is 170 °C, a dense cubic block crystal appears on the copper surface, thereby suggesting a severe corrosion on the copper surface. Meanwhile, when the experiment temperature is 220 °C, a rough and uniform crystal is observed on the surface when viewed under a microscope, and a more serious degree of corrosion is recorded.

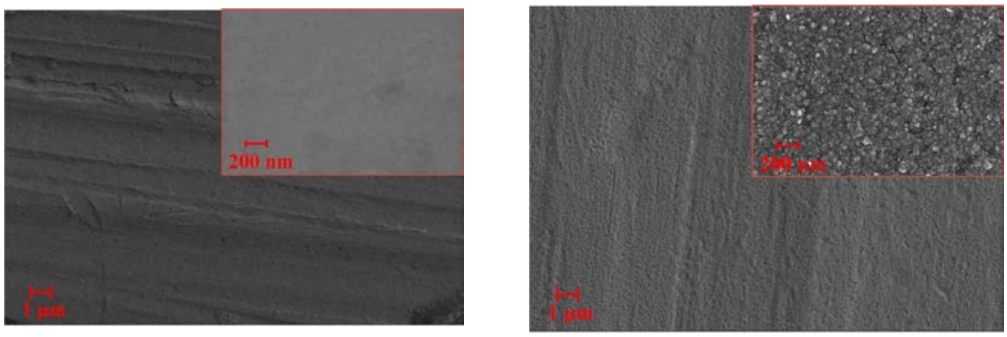

(a) Experiment temperature 120 °C (b) Experiment temperature 170 °C

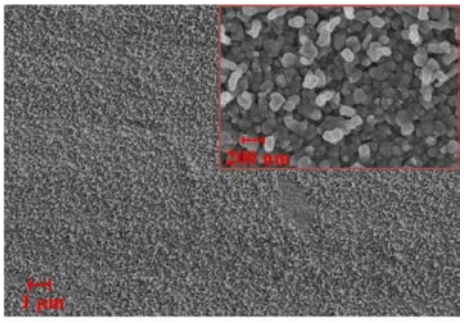

(c) Experiment temperature 220 °C

Figure 2.9 SEM morphology of surface after contact of copper with $C_5F_{10}O/N_2/O_2$ gas mixture

The above results show that $C_5F_{10}O/N_2$ and $C_5F_{10}O/N_2/O_2$ gas mixture have poor interaction stability with copper, and the surface needs to be treated with anti-corrosion. ABB researchers also proposed that in the equipment using $C_5F_{10}O/N_2/O_2$ gas mixture as the insulating dielectric, the contacts through which the primary current flows should be silver-plated according to the IEC 62271-200 standard [90]. As a buffer gas, N_2 has high stability and low liquefaction temperature. Under normal circumstances, it is inert in chemical properties and does not participate in the chemical reaction between $C_5F_{10}O$ and copper. Therefore, the change in the surface morphology of $C_5F_{10}O/N_2$ gas mixture in contact with copper at different experiment temperatures is mainly due to the slight corrosion of the surface of the copper sample by $C_5F_{10}O$ at high temperature. When $C_5F_{10}O/N_2/O_2$ gas mixture is experimented at 120 °C, the copper material has high chemical stability. Due to the low temperature, oxygen cannot oxidize copper. According to the experiment results, the presence of oxygen inhibits the corrosion of $C_5F_{10}O$ gas to copper, showing good stability at low temperature, but high temperature and high pressure will make copper react with oxygen to form metal oxides. Generally, the gas or equipment is mixed with micro-water, and the HF produced by the hydrolysis of $C_5F_{10}O$ gas is highly corrosive and will strongly corrode the copper material.

In conclusion, $C_5F_{10}O/N_2/O_2$ gas mixture with copper showed better stability than $C_5F_{10}O/N_2$ gas mixture at lower experiment temperatures. During the interaction between $C_5F_{10}O/N_2/O_2$ gas mixture and copper, the copper surface is seriously corroded and pungent gas is emitted. The electrical equipment using $C_5F_{10}O/N_2/O_2$ gas mixture instead of SF_6 as insulation medium in engineering applications should take special measures to protect against the corrosion of copper materials in the equipment caused by local overheating due to temperature rise and other reasons, which will threaten the safe and stable operation of the equipment and the health of on-site maintenance personnel.

(2) Aluminum Surface Morphology

The color of the aluminum surface does not change after $C_5F_{10}O/N_2$ and $C_5F_{10}O/N_2/O_2$ gas mixtures contact with the aluminum material under different experiment temperature conditions. The surface micro-morphology of the aluminum sample is characterized by SEM, and the surface micro-structure is shown in Figure 2.10 and Figure 2.11. The micro-morphology of the aluminum surface is relatively flat, and no morphology change is observed under the electron microscope before and after the reaction. Figure 2.11a shows the aluminum surface after the surface cleaning treatment before the experiment. The small grooves on the surface are caused by the limitation of the manufacturing process. In $C_5F_{10}O/N_2$ and $C_5F_{10}O/N_2/O_2$ gas mixtures experiment groups at temperatures of 120 °C, 170 °C and 220 °C, respectively, the surface morphology is consistent with the control group, and no corrosion points are found.

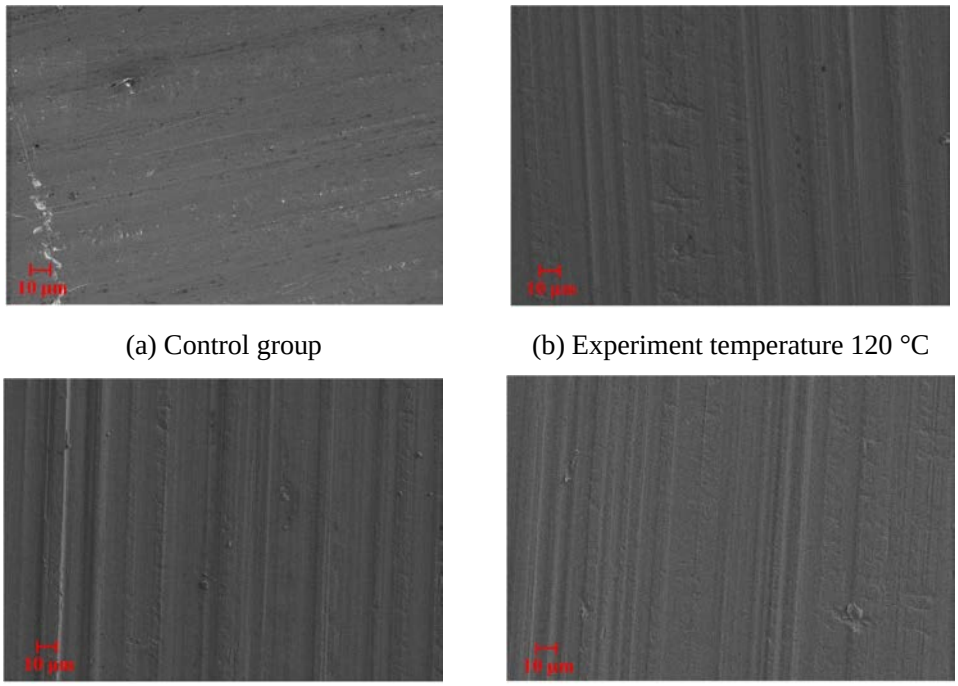

(a) Control group (b) Experiment temperature 120 °C

(c) Experiment temperature 170 °C (d) Experiment temperature 220 °C

Figure 2.10 SEM morphology of surface after contact of aluminum with $C_5F_{10}O/N_2$ gas mixture

2.2.3 Elemental Composition and Valence State of Metal Surface

(1) Elemental Composition and Valence State of Copper Surface

To further study the changes in the elements (Cu 2p, F 1s, C 1s, and O 1s) and materials on the surface of copper samples, an energy spectrum scanning test is performed on XPS. The track of the element being tested is selected according to internationally accepted test rules. After using the XPS Peak software to perform a Shirley-type fitting deduction on the energy spectrum background, the Gaussian algorithm is used for peak fitting, and the chemical state of the element is determined by using the NIST XPS database and previous studies as references [91].

Figure 2.12a presents the photoelectron spectroscopy curve of the 2p orbital of Cu element on the surface of a copper sample. After the peak photo-matching of the secondary photoelectron emission peak of the copper element, the five peaks with electron binding energies of 932.7, 934.6, 944.8, 952.5, and 952.7 eV are Cu_2O $2p_{3/2}$, CuO $2p_{3/2}$, CuO $2p_{3/2}$,

Cu_2O $_{2p1/2}$, and CuO $2p_{1/2}$, respectively. The secondary photoelectron emission peak at 954.90 eV in Figure 2.12a exceeds the photoelectron binding energy generated by the transition of the Cu element level. Therefore, this peak should be the photoelectron emission peak of the other elements. The change in CuO and Cu_2O content in Figure 2.12a corresponds to the change in the color of the copper surface. The copper energy spectrum scanning results indicate that the surface of the copper sample mainly contains CuO and Cu_2O produced via oxidation of the copper surface. Copper and $C_5F_{10}O/N_2$ gas mixtures react at high temperature to form CuF_2 (Figure 2.12b). The surface copper detection results recorded at 120 °C are consistent with the control group, thereby indicating that copper shows good interaction stability with the $C_5F_{10}O/N_2/O_2$ gas mixture at 120 °C (the XPS test results are consistent with the FESEM results). Some Cu participates in the reaction as the experimental temperature increases.

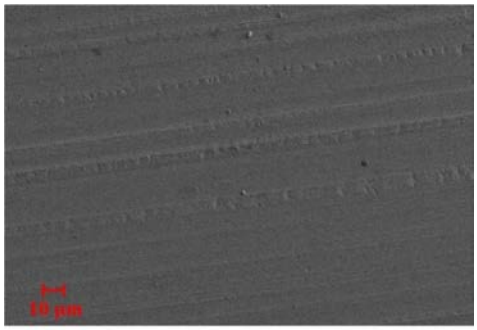

(a) Experiment temperature 120 °C

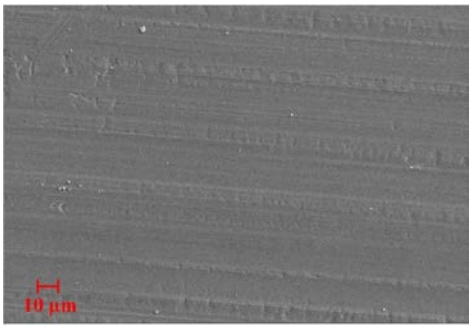

(b) Experiment temperature 170 °C

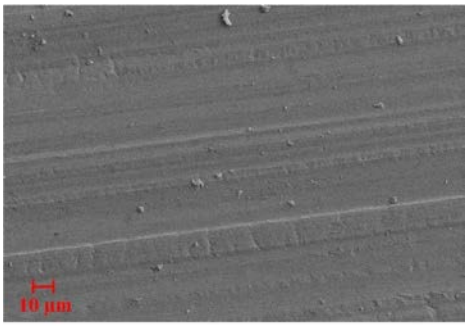

(c) Experiment temperature 220 °C

Figure 2.11 SEM morphology of surface after contact of aluminum with $C_5F_{10}O/N_2/O_2$ gas mixture

Figure 2.12b presents the photoelectron spectroscopy of the 1s orbital of the F element on the surface of the copper sample. No F element is detected in the control group, while the experiment group showed that some $C_5F_{10}O$ are decomposed on the copper surface at a high temperature, and CuF_2 and C-F bonds are detected at binding energies of 684.7 eV and 688.8 eV. The detected CuF_2 is a product of the reaction of $C_5F_{10}O$ molecules with CuO on the copper surface. CuF_2 and C-F bonds are detected in the $C_5F_{10}O/N_2$ experiment group, thereby suggesting that the $C_5F_{10}O/N_2$ gas mixture reacted with copper at an elevated temperature and that the relative content of CuF_2 and C–F bonds increased along with the experiment temperature. By contrast, $C_5F_{10}O/N_2/O_2$ gas mixture experiment group tended to decrease the relative content of CuF_2 and C–F bonds as the experiment temperature increased. CuF_2 is not detected at 220 °C, and the fluorine element on the copper surface is mainly present as a C–F bond. In the experiments group, the fluorine element mainly existed in the form of a C–F bond, a small amount of fluorine existed in the form of CuF_2, and the C–F bond does not show much differences across each experiment group. The C–F bond may be a $C_5F_{10}O$ molecule adsorbed

on the surface of a copper sample.

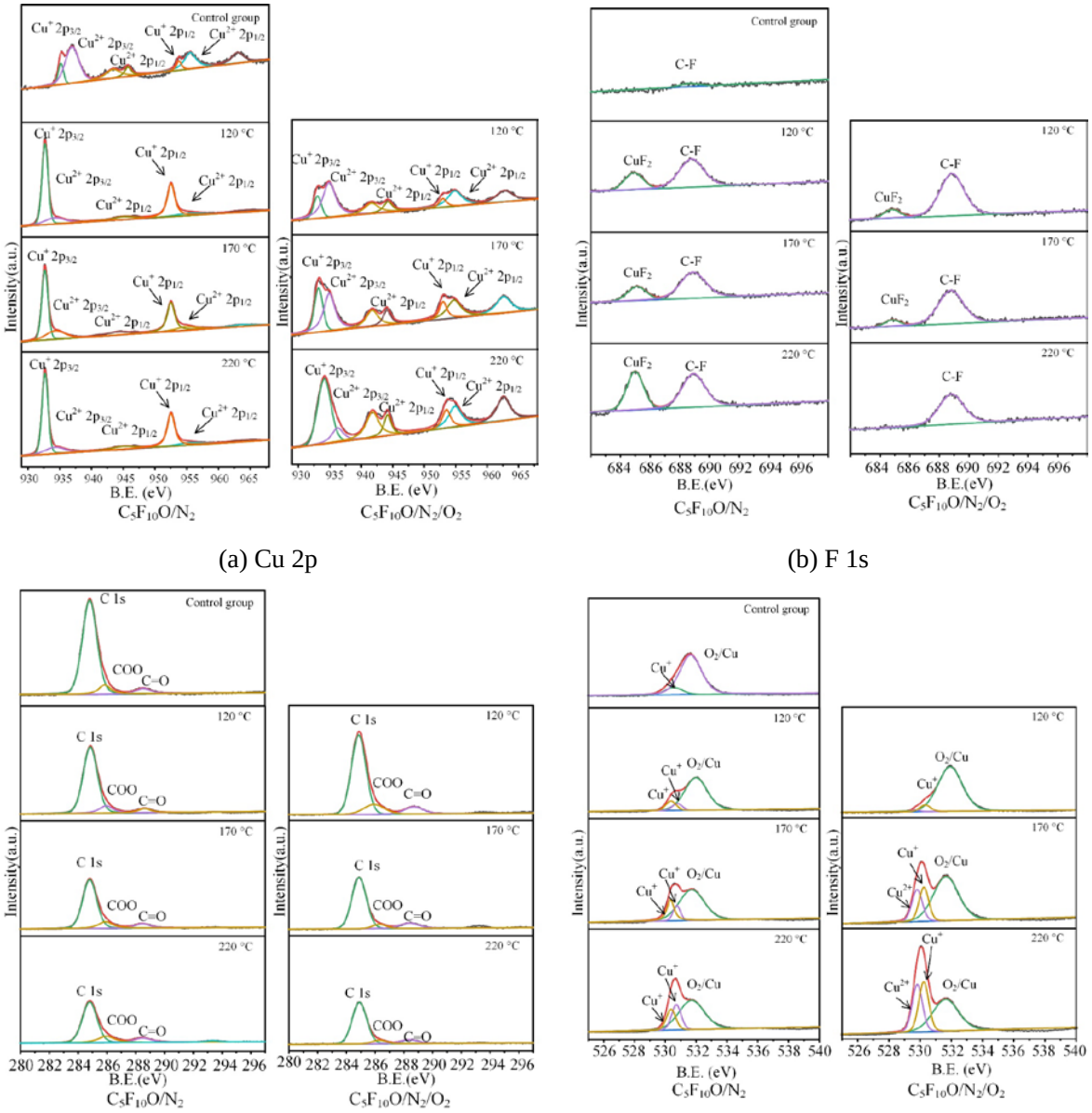

(a) Cu 2p (b) F 1s

(c) C 1s (d) O 1s

Figure 2.12 Copper surface element XPS energy spectrum

Figure 2.12c presents the photoelectron spectroscopy of the 1s orbital of the C element on the surface of the copper sample. The energy peaks detected at photoelectron binding energies of 284.70, 286.30, and 286.60 eV are C 1s, COO, and C=O, respectively. The peaks of COO and C=O do not differ between the control group and each experimental group, and the relative content of the C 1s peak is slightly reduced. Figure 2.12d presents the photoelectron spectroscopy of the 1s orbital of the O element on the surface of the copper sample. In $C_5F_{10}O/N_2/O_2$ gas mixture experiment groups，the three peaks with electron binding energies of 529.8, 530.3, and 531.8 eV are Cu^{2+}(CuO or CuF_2), Cu^{+}(Cu_2O), and O_2/Cu (oxygen on copper, O_2^-, O^{2-} or O^-), respectively. In other gas mixture experiment groups or control group, Cu^{+}(Cu_2O) is detected at photoelectron binding energies of 530.3 eV and 530.7 eV. O_2/Cu (oxygen on copper, O_2^-, O^{2-} or O^-) is detected at photoelectron binding energies of 531.8 eV and 532.9 eV. Cu^{2+}(or Cu^{+}) with different binding energies are copper oxide or cuprous oxide

crystals of different crystal types, and the oxygen on copper detected in the control group because oxygen in the air is adsorbed on the surface.

In summary, the gas-solid interface stability of $C_5F_{10}O/N_2/O_2$ gas mixture and copper material is poor. During the operation of GIE, $C_5F_{10}O/N_2/O_2$ gas mixture may corrode the copper surface during the long-term contact with the copper surface, increase its surface resistivity, and the cumulative thermal effect of the current is more significant. This will make the temperature rise of the equipment exceed the relevant standard limit, and the higher temperature will aggravate the corrosion of the copper surface, forming a vicious circle, which may eventually lead to serious failure of the equipment, threatening its safe and stable operation. Therefore, it is necessary to perform anti-corrosion treatment on the surface of the copper material.

(2) Elemental Composition and Valence State of Aluminum Surface

The energy spectrum scanning test results of the four elements (Al 2p, F 1s, C 1s and O 1s) that may exist on the aluminum surface are shown in Figure 2.13. The photoelectron spectroscopy of the 2p orbital of Al element detected Al_2O_3 and Al at the electron binding energies of 74.30 eV and 71.89 eV, respectively, and the Al element on the aluminum sample surface exists mainly in the Al_2O_3 state. The chemical properties of aluminum are active, but it shows high stability in the tests because the oxide layer (Al_2O_3) on the surface of the aluminum sample plays a protective role, preventing the reaction of aluminum with $C_5F_{10}O/N_2/O_2$ gas mixture. The content of F element on the surface of aluminum samples showed a different trend from that of copper samples. When the experiment temperature is 120°C, there is no accumulation of F element on the aluminum surface. When the experiment temperature exceeds 120°C, fluorine-containing gas ($C_5F_{10}O$) will be adsorbed on the surface of the aluminum sample, but no new products appeared, which should be a physical adsorption phenomenon. This also reflects the stability of the aluminum material, and the aluminum does not react like the copper material because of the protection of the surface oxide layer Al_2O_3. The contents of C and O elements showed similar regularities to those on the surface of the copper samples.

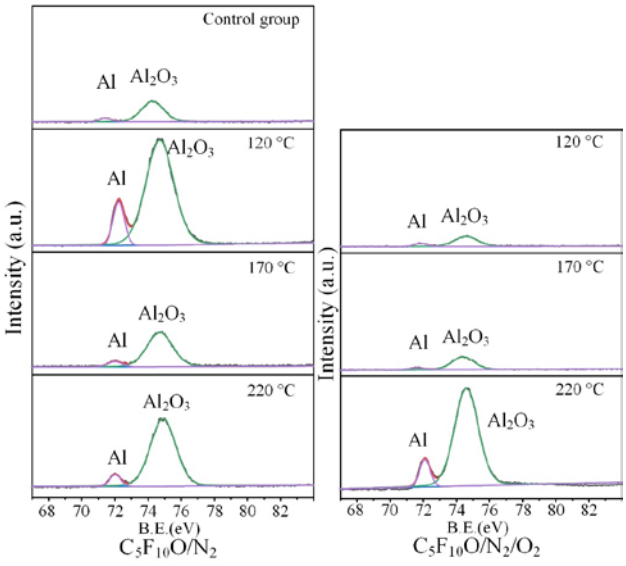

(a) Al 2p

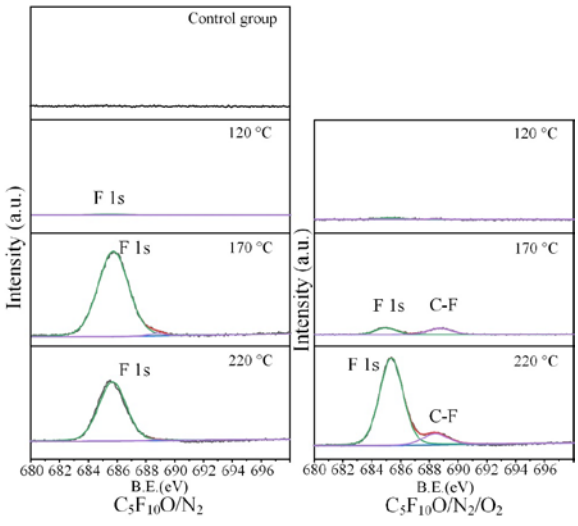

(b) F 1s

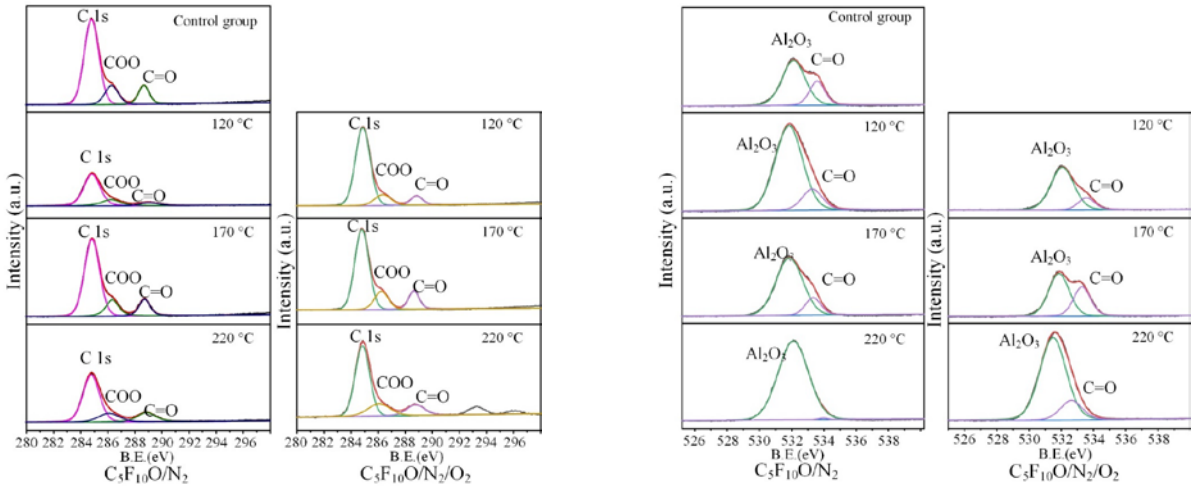

(c) C 1s (d) O 1s

Figure 2.13 Aluminum surface element XPS energy spectrum

2.3 Experiment on Interface Decomposition Characteristics of $C_5F_{10}O/N_2/O_2$ and Silver

In the experiment in Section 2.2, it is found that $C_5F_{10}O$ gas mixture and metal copper will react chemically at the gas-solid interface to corrode the copper surface, and it is necessary to carry out anti-corrosion treatment on the surface. At the same time, in order to ensure that the metal conductor has good electrical conductivity, the relevant standards for SF_6 GIE also recommend silver plating on the surface of the copper contacts. Therefore, in this section, the decomposition characteristics of the gas-solid interface with $C_5F_{10}O/N_2$ and $C_5F_{10}O/N_2/O_2$ gas mixtures after silver plating on the copper surface are studied. Before the experiment, the copper of the same material used in the experiment in Section 2.2 is plated with silver by electroplating, and then the experiment is continued using the experimental platform shown in Figure 2.1. The test results obtained are as follows:

2.3.1 Gas Composition

Figure 2.14 shows the detection results of gas components after the interface decomposition experiment of $C_5F_{10}O/N_2/O_2$ gas mixture and silver. Simple decomposition products such as C_3HF_7, C_3F_6, C_3F_6O and CHF_3 produced by the hydrolysis of $C_5F_{10}O$ are also detected in the decomposition products.

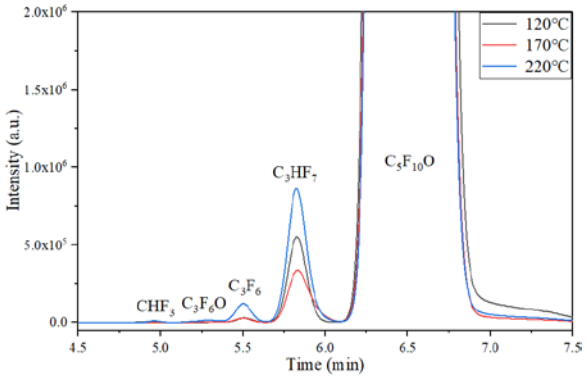

(a) Gas chromatograms of $C_5F_{10}O/N_2$ gas mixture before and after the experiment

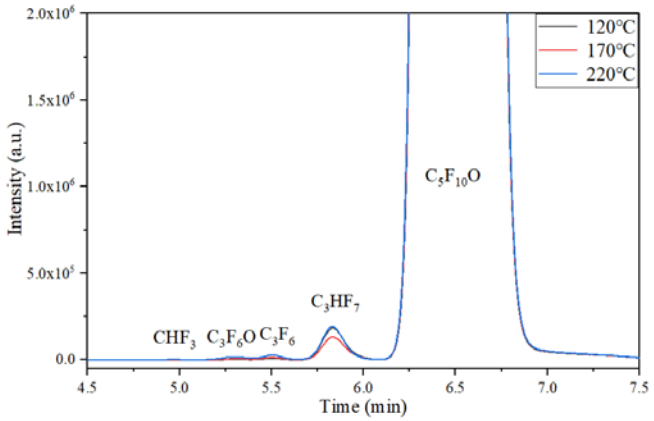

(b) Gas chromatograms of $C_5F_{10}O/N_2/O_2$ gas mixture before and after the experiment

Figure 2.14 Gas chromatogram of $C_5F_{10}O/N_2/O_2$ gas mixture

2.3.2 Silver Surface Morphology

The color of the silver surface is bright silver before and after the experiment, and the surface color does not undergo any obvious color change similar to that of the copper surface. The surface microstructure of the silver sample is shown in Figure 2.15 and Figure 2.16. No obvious change is observed under the electron microscope before and after the reaction of the microscopic morphology formed by electroplating on the silver surface (the highlighted part in the figure is formed by the adsorption of small particles of silver formed during the electroplating process on the surface). The surface morphology of silver in $C_5F_{10}O/N_2$ and $C_5F_{10}O/N_2/O_2$ gas mixture experiment groups is the same as that in the control group, and no corrosion points are found.

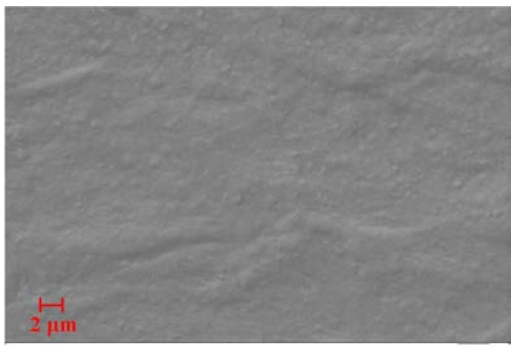

(a) Control group

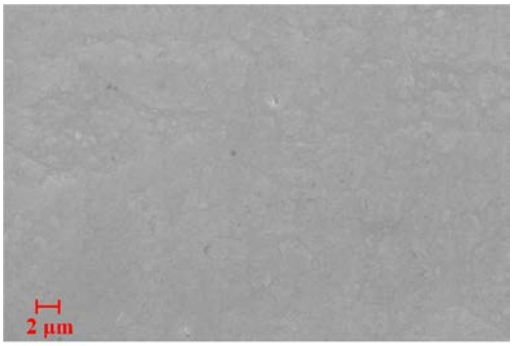

(b) Experiment temperature 120 °C

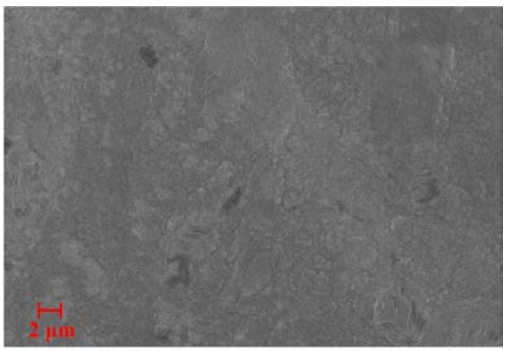

(c) Experiment temperature 170 °C

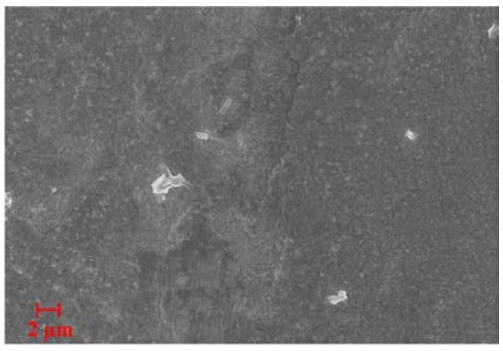

(d) Experiment temperature 220 °C

Figure 2.15 SEM morphology of surface after contact of aluminum with $C_5F_{10}O/N_2$ gas mixture

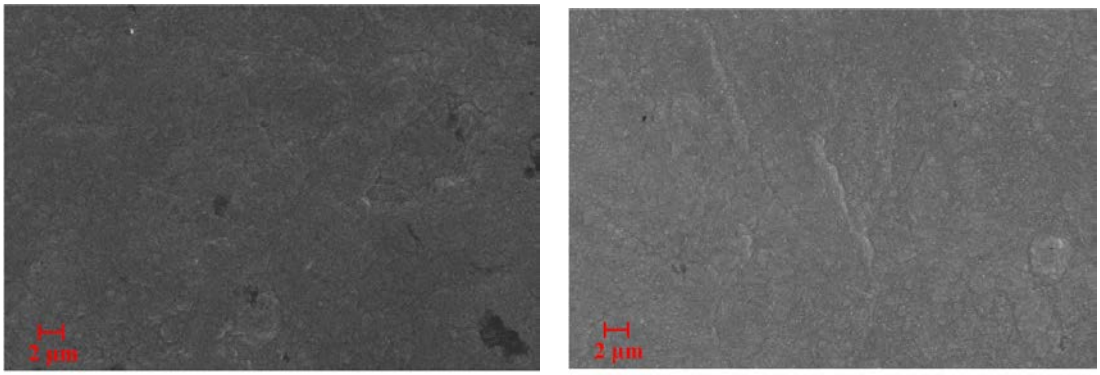

(a) Experiment temperature 120 °C (b) Experiment temperature 170 °C

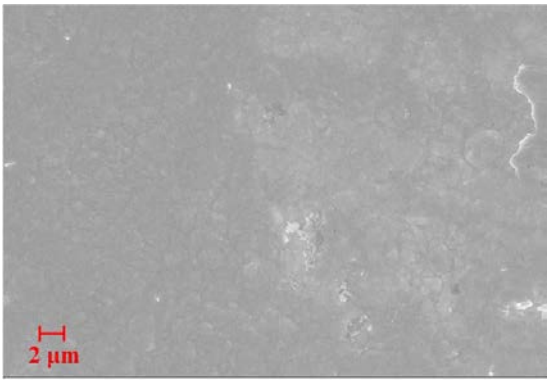

(c) Experiment temperature 220 °C

Figure 2.16 SEM morphology of surface after contact of aluminum with $C_5F_{10}O/N_2/O_2$ gas mixture

2.3.3 Elemental Composition and Valence state of Silver Surface

The energy spectrum scanning test results of the four elements (Ag 3d, F 1s, C 1s and O 1s) that may exist on the silver surface are shown in Figure 2.17. The photoelectron spectra of the 3d orbitals of element Ag detected two characteristic peaks of Ag 3d5/2 and Ag 3d3/2 at the electron binding energies of 374.34 eV and 368.52 eV, respectively, with no significant changes in both the experiment and control groups. The silver shows high stability during the contact with $C_5F_{10}O/N_2/O_2$ gas mixture, which could well protect the internal copper material. After the experiment, the F element accumulates on the silver surface, but no new decomposition products are detected. The F element on the silver surface should be caused by the adsorption of $C_5F_{10}O$ molecules on the silver surface.

On the whole, silver plating on the copper surface can well protect the internal copper and improve the poor stability of the gas-solid interface between copper and $C_5F_{10}O/N_2/O_2$ gas mixture. At the same time, silver plating can reduce the resistance of the conductor and improve the conductivity of the copper conductor. In engineering applications, it is necessary to check the integrity and corrosion of the silver-plated layer and the changes in surface resistance and thermal conductivity parameters in the maintenance plan to evaluate the protective effect of the silver-plated layer on the copper material, if the silver-plated layer is found to be damaged and corroded, it needs to be maintained in time to avoid serious accidents.

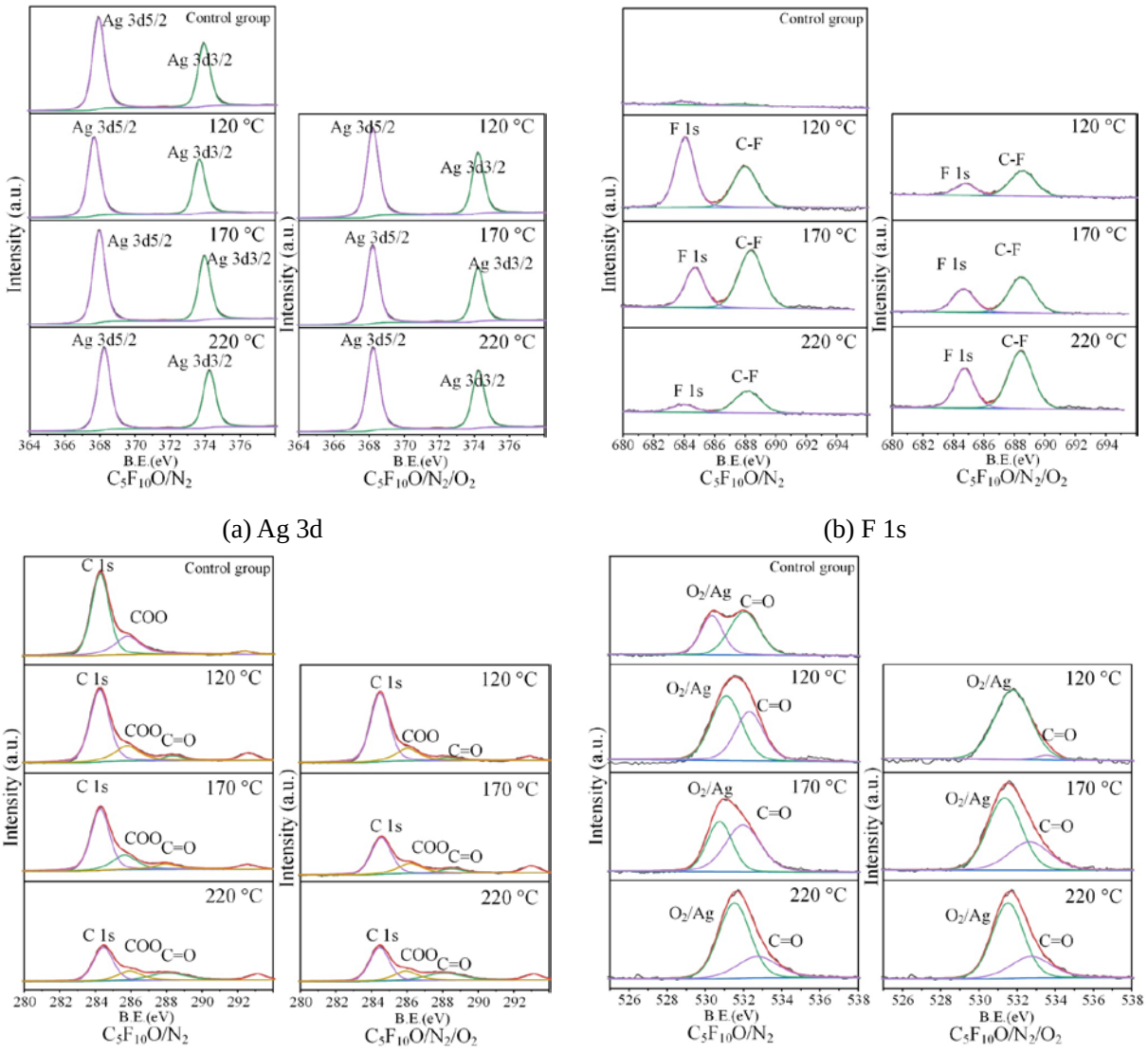

(a) Ag 3d (b) F 1s

(c) C 1s (d) O 1s

Figure 2.17 Silver surface element XPS energy spectrum

2.4 Chapter Summary

In this chapter, the gas-solid interface stability experiment of $C_5F_{10}O/N_2$ and $C_5F_{10}O/N_2/O_2$ gas mixtures and the conductive metal materials copper and aluminum in equipment is carried out through the gas-solid interface decomposition characteristics experimental platform. After finding that the stability of copper material with $C_5F_{10}O$ gas mixture at high temperature is poor, and it may cause potential failure hazards in engineering applications, a scheme of silver-plated protective layer on copper surface is proposed, and the gas-solid interface stability experiment of the silver-plated protective layer on the copper surface and $C_5F_{10}O$ gas mixture is carried out to verify the effectiveness of the silver-plated protective layer. The stability of the gas-solid interface during the long-term operation of $C_5F_{10}O$ gas mixture insulation equipment is preliminarily solved, and the following conclusions are obtained:

1) $C_5F_{10}O$ gas mixture has poor gas-solid stability with copper materials, which will cause corrosion of the copper surface to form CuO and Cu_2O at high temperatures. Oxygen in

$C_5F_{10}O/N_2/O_2$ gas mixture will aggravate the corrosion of the copper surface at high temperatures, while oxygen exhibits the opposite effect at lower experiment temperatures, and the copper surface needs to be treated with anti-corrosion. The surface of the aluminum material will naturally oxidize to form an Al_2O_3 oxide layer to protect the internal aluminum material, thus showing a high gas-solid interface stability.

2) The decomposition of $C_5F_{10}O$ gas is mainly caused by the hydrolysis reaction with the micro-water contained in the equipment and the decomposition caused by the interaction with the surface of the copper material. The main decomposition products are C_3HF_7, C_3F_6O, C_3F_6 and CHF_3. The content of the decomposition products mainly depends on the moisture content remaining in the solid material.

3) The chemical properties of the silver material are stable, and the silver-plated protective layer on the copper surface can protect the copper material. In order to prolong the service life and operation stability of the equipment, it is necessary to pay attention to the integrity of the silver protective layer in engineering applications, and if it is damaged, it needs to be maintained in time.

3 Experimental Research on Decomposition Characteristics of $C_5F_{10}O/N_2/O_2$ Gas Mixture under Typical Discharge and Thermal Faults

GIE may cause POF, PD and AC breakdown under long-term operating conditions. When a fault occurs, a series of chemical reactions may occur in the insulating gas due to discharge and thermal effects and various decomposition products may be produced. Because the molecular structure of SF_6 is simple and the insulating gas is a single component, most of its decomposition products are sulfuryl gases, while the molecular structure of $C_5F_{10}O$ gas is complex, and it needs to be mixed with buffer gas as an insulating gas, which will make its decomposition process more complicated. Therefore, it is necessary to carry out experimental research on the decomposition characteristics of $C_5F_{10}O$ gas under typical discharge and thermal faults. In addition, the interaction stability of $C_5F_{10}O/N_2$ gas mixture and copper is found to be better than that of $C_5F_{10}O/N_2/O_2$ gas mixture in the study of gas-solid interface interaction stability in Chapter 2. When the gas mixture does not contain oxygen, it is beneficial to its gas-solid stability, but $C_5F_{10}O/N_2$ gas mixture will produce black solid decomposition products when the discharge decomposition occurs, which will seriously affect the operational reliability of the equipment. Therefore, the effect of oxygen on the decomposition characteristics of $C_5F_{10}O/N_2$ gas mixture under typical discharge and thermal faults needs to be further studied.

In this chapter, the decomposition characteristics experiment of $C_5F_{10}O/N_2/O_2$ gas mixture is carried out by building the typical discharge and thermal faults simulation experimental platform, and the research on the influence of oxygen concentration on its decomposition characteristics is carried out. The decomposition law of $C_5F_{10}O/N_2/O_2$ gas mixture is obtained by testing its electrical characteristics and decomposition characteristics under different conditions, and the range of oxygen concentration to be added to $C_5F_{10}O/N_2$ gas mixture is suggested based on the experiment results.

3.1 AC Breakdown Decomposition Characteristics of $C_5F_{10}O/N_2/O_2$

AC breakdown (spark discharge) is a self-excited electrical phenomenon formed by the breakdown of the gas dielectric between the cold electrodes with small curvature by the strong electric field generated by the high voltage. The discharge channel is more tortuous and narrower than that of arc discharge, and is accompanied by photoacoustic phenomena such as sparks and gas pops [92]. Due to the high voltage between the two electrodes that generate the spark discharge, the insulation resistance between the electrodes will decrease during the discharge, resulting in a sharp increase in current, and the voltage between the electrodes decreases, causing the discharge to temporarily extinguish. After the discharge stops, the insulation resistance and voltage between the electrodes also gradually recover, and spark discharge occurs again after the voltage recovers. Spark discharge is an intermittent discharge phenomenon. During the discharge process, the ions generated by the ionization of gas molecules form conductive channels, which will cause the gas molecules to dissociate to form small ion fragments. After the discharge stops, the ions recombine to form new substances, which will lead to the decomposition of the insulating gas. Compared with SF_6 gas, the

molecular structure of $C_5F_{10}O$ is more complex, the types of ion fragments generated by ionization are also more, and there are more types of combinations of various ion fragments after the discharge is stopped, which will produce complex types of decomposition gases.

In this section, by building AC breakdown experimental platform, firstly, 100 AC breakdown discharge tests are carried out on $C_5F_{10}O/N_2$ and $C_5F_{10}O/N_2/O_2$ gas mixtures, and the decomposition products of $C_5F_{10}O$ gas mixture after AC breakdown are detected. The test found that $C_5F_{10}O/N_2$ gas mixture will produce solid decomposition products after discharge, but $C_5F_{10}O/N_2/O_2$ gas mixture experiment group containing oxygen does not produce solid decomposition products. Therefore, the effects of different concentrations of oxygen on the decomposition characteristics of $C_5F_{10}O/N_2/O_2$ gas mixture are investigated.

3.1.1 Experimental Platform and Method

The experimental platform is shown in Figure 3.1. The transformer used in the discharge experiment is an autotransformer. A low-voltage input terminal served as the control terminal, and its voltage adjustment range is 0–380 V. The output voltage range of the high-voltage controlled terminal and the rated capacity are 0–100 kV and 100 kVA, respectively. Protective resistor (10 kΩ) with current limit of 0.5A is used to limit the current flowing through the circuit to avoid damage to the experimental device due to excessive current. Capacitive voltage divider (500 pF, 100 kV) is used to measure the voltage applied to the high voltage side of the gas chamber. $C_5F_{10}O/N_2/O_2$ gas mixtures are tested in a closed simulated gas chamber. The electrodes used in the experiment are brass spheres with a diameter of 50 mm, and the gas gap between spheres is 2 mm. The spheres are washed with absolute ethanol and dried before each experiment. The chamber is cleaned three times with high purity N_2 before each experiment to eliminate interferences from other impurity gases. The total gas pressure used in this study is 140 kPa (absolute pressure), and the partial pressure of $C_5F_{10}O$ gas is 10.5 kPa (7.5% $C_5F_{10}O$ volume fraction, −25 °C mixture liquefaction temperature). The effect of changes in oxygen content on the discharge decomposition products of $C_5F_{10}O/N_2$ mixtures is investigated by changing the ratio of nitrogen and oxygen. In the experiments, the concentrations of oxygen are 4%, 8%, 12%, 16%, and 20% with a volume fraction of 4% as the gradient, and $C_5F_{10}O/N_2$ mixtures containing no oxygen are used as the control group. The gas used in the experiments is prepared according to Dalton's law of partial pressure, and $C_5F_{10}O$, oxygen and nitrogen are charged into the simulated gas chamber according to the requirements of the above experimental groups. After the gas is charged into the gas chamber, it is allowed to stand for 24 hours. The experiment began after the gas is sufficiently mixed [93]. In the experiments, the gradual voltage-rising method is used to increase the voltage between the two electrodes slowly until insulation breakdown occurred in the gas gap. After the gas gap is broken down, it is allowed to stand for 5 minutes until for the gas in the chamber spread evenly and cooled to room temperature before starting the next experiment. Each group of experimental gases is subjected to 100 breakdowns, and gas samples in the gas chamber are collected every 20 breakdowns experiments, and gas components are tested using a GC-MS.

3.1.2 Analysis of Solid Decomposition Products Produced by AC Breakdown

$C_5F_{10}O/N_2$ gas mixture produced black decomposition products after multiple discharge breakdown experiments. The black solids adhered to the upper and lower spheres of the brass

sphere surface, and more solid substances adhered to the surface of the lower sphere (Figure 3.2a) than to that of the upper sphere because the solids produced during the discharge process have a high density and naturally fall to the surface of the sphere after arc extinguishing via the influence of gravity. The deposition of decomposition products on the surface of the electrodes could distort the electric field inside the gas gap between electrodes, causing the gas gap to discharge at a low voltage, which is not conducive to the safe and stable operation of electrical equipment.

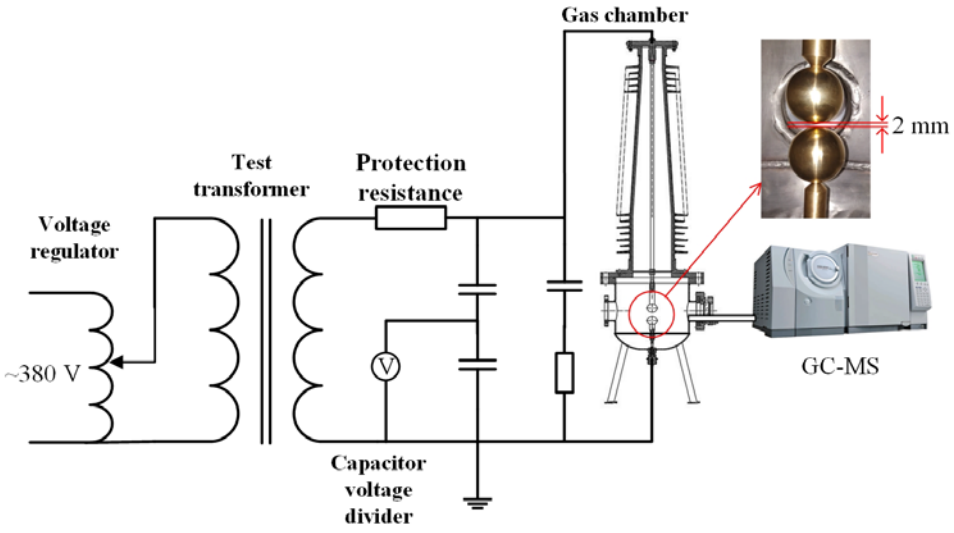

Figure 3.1 AC discharge experimental platform

Table 3.1 Concentration ratio of $C_5F_{10}O/N_2/O_2$ gas mixture

No.	Total gas pressure	Gas concentration (v/v)		
		$C_5F_{10}O$	O_2	N_2
1	0.14MPa	7.5%	0	92.5%
2	0.14MPa	7.5%	4%	88.5%
3	0.14MPa	7.5%	8%	84.5%
4	0.14MPa	7.5%	12%	80.5%
5	0.14MPa	7.5%	16%	76.5%
6	0.14MPa	7.5%	20%	72.5%

The black solids attached to the surface of the experimental sphere are collected and characterized via SEM and XPS to evaluate their surface topography and elemental composition, respectively. The relevant results are shown in Figure 3.3 and Figure 3.4.

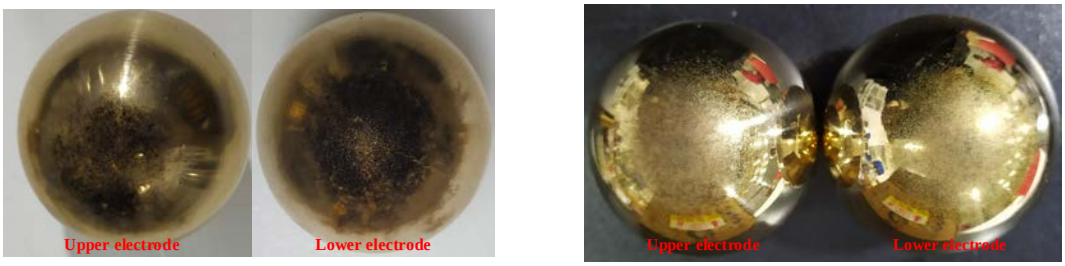

(a) $C_5F_{10}O$ /N_2 mixtures control group experimental sphere

(b) Experimental group sphere after adding oxygen

Figure 3.2 Brass ball electrode

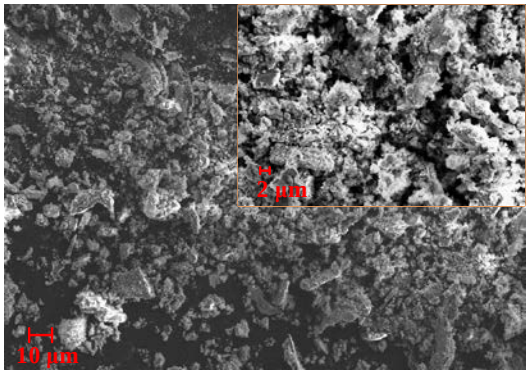

Figure 3.3 FESEM characterization results

The SEM micrographs obtained show that the black solids are irregularly fluffy and have a loose porous structure. The rough and loose structure of the black solids changes the original smooth structure of the electrode surface, thereby allowing its easy discharge at a low voltage and further causing dielectric breakdown. This phenomenon is caused by the natural deposition of the black solids during repeated breakdown of the gas gap. Each breakdown produces a trace amount of solid material, which is adsorbed on the surface of the ball electrode after arc extinguishing. As the number of breakdowns grows, the black solids gradually accumulate to deteriorate the insulation condition.

XPS detected C 1s, F 1s, O 1s, N 1s and Cu 2p in the black solids. After Shirley-type fitting deduction on the energy spectrum background, the Gaussian algorithm is used for peak fitting, and information on the chemical state, molecular structure and chemical bonds of the elements is determined by referring to the NIST XPS database and previous studies. The result shown in Figure 3.4. The XPS characterization results show that the total relative contents of C and F in the black solids are above 92%; specifically, the contents of C 1s and F 1s are 40.49% and 51.92%, respectively. The content of O 1s, which is mainly derived from the carbonyl group (−C=O−) in the C5-PFK molecules, is 4.72%. The relative content of N 1s is only 1.3%, which also indicates that in the absence of O_2, N_2 as the buffer gas is chemically stable in the case of discharge [94]. Even in the extreme case of discharge, N_2 cannot be decomposed. This feature is one advantage of using N_2 as buffer gas and indicates that N_2 can maintain the stability of the N molecular structure after the device breaks down due to insulation failure. The appearance of Cu is attributed to the composition of the experimental electrode, which is made of Cu.

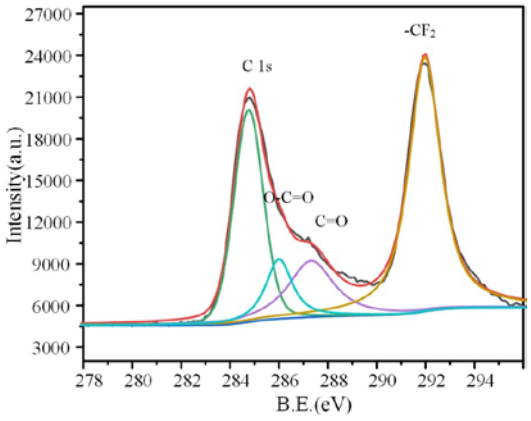

(a) C 1s photoelectron spectroscopy

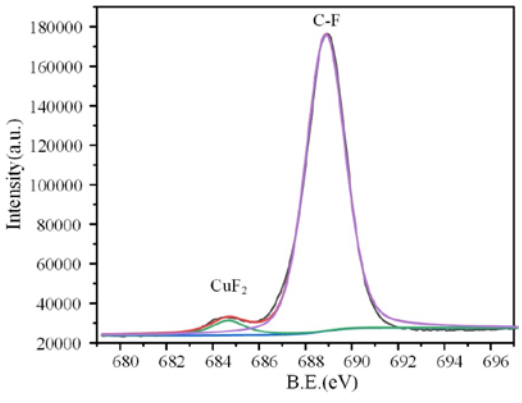

(b) F 1s photoelectron spectroscopy

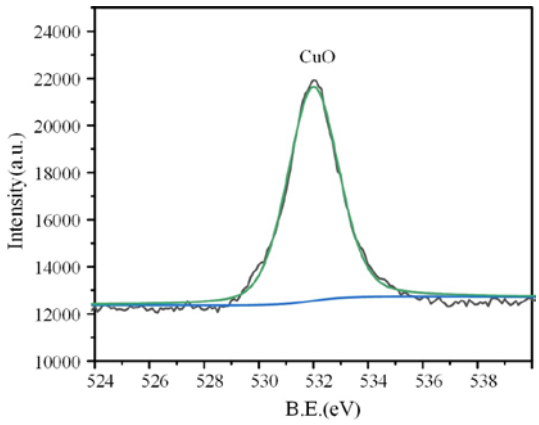

(c) O 1s photoelectron spectroscopy

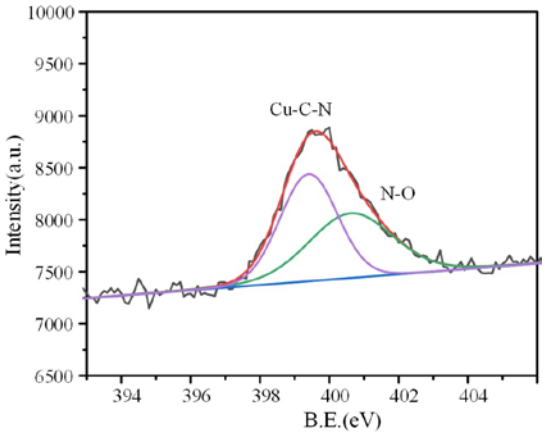

(d) N 1s photoelectron spectroscopy

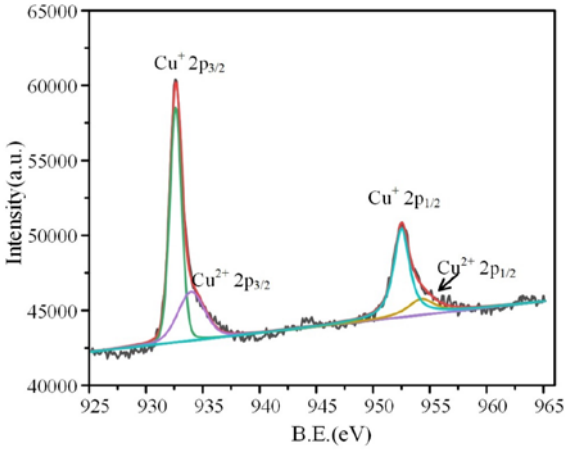

(e) Cu 2p photoelectron spectroscopy

Figure 3.4 XPS characterization results

The XPS spectrum of C 1s in Figure 3.4a reveals elemental C, COO, −C=O− and CF_2− at electron binding energies of 284.76, 286.00, 287.31, and 291.97 eV, respectively. Comparison of the individual peak areas in Fig. 4a indicates that the black solids contain some simple carbon substances; however, most of the identified C-containing materials are present as O- or F-containing compounds such as COO, −C=O−, and CF_2−. These substances are the decomposition products of $C_5F_{10}O$ molecules during discharge breakdown. The XPS spectrum of F 1s in Figure 3.4b reveals the characteristic bonds of CuF_2 and C–F at electron binding energies of 684.01 and 688.88 eV, respectively. Upon discharge, the arc center forms a plasma region with very high temperature, and the $C_5F_{10}O$ molecules in the arc center react with the Cu atoms on the electrode surface to form CuF_2. At the same time, the gas-solid interface stability experiment in Chapter 2 also shows that $C_5F_{10}O$ gas will react with copper to produce CuF_2 at high temperature. The XPS spectrum of O 1s in Figure 3.4c reveals the presence of CuO at an electron binding energy of 532.00 eV. CuO is formed by oxidation of the Cu electrode material, and its color is black, consistent with the color of solid products. The extreme condition of high temperature and pressure is generated when discharge occurs, and the contact of the Cu electrode participates by the decomposition reaction of $C_5F_{10}O$, which is also reflected in the detection of N and Cu elements. The XPS spectrum of N 1s reveals the characteristic bonds of Cu–C–N− and N–O at binding energies of 398.60 and 400.10 eV,

respectively. The XPS spectrum of Cu 2p reveals the presence of $Cu_2O2p_{3/2}$, $CuO2p_{3/2}$, $CuO2p_{3/2}$, $Cu_2O2p_{1/2}$, and $CuO2p_{1/2}$ at electron binding energies of 932.7, 934.6, 944.8, 952.5, and 952.7 eV, respectively. Cu_2O forms because only a small amount of O is available after the decomposition of $C_5F_{10}O$ molecules in during discharge. Cu is seriously deficient in O during the reaction, resulting in the incomplete oxidation of Cu to form Cu_2O.

3.1.3 Influence of Oxygen Concentration on AC Breakdown Voltage of $C_5F_{10}O/N_2/O_2$

The effect of different volume fractions of oxygen on the insulation breakdown voltage of $C_5F_{10}O/N_2/O_2$ gas mixture shown in Figure 3.5. The breakdown voltages of $C_5F_{10}O/N_2/O_2$ gas mixture grows slightly after addition of oxygen and continue to grow with increasing oxygen concentration. This increase indicates that the addition of oxygen can appropriately increase the breakdown voltage of $C_5F_{10}O/N_2/O_2$ gas mixture, thus enhancing the dielectric strength of the system.

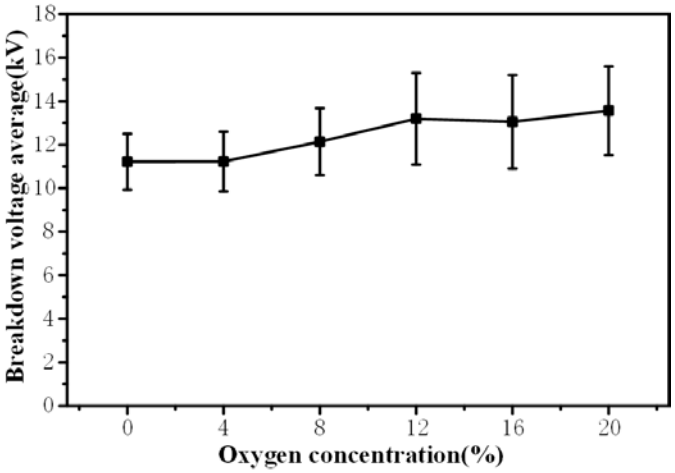

Figure 3.5 Effect of oxygen on the breakdown voltage of $C_5F_{10}O/N_2/O_2$ gas mixture

Gas breakdown voltage has a certain randomness due to factors such as uneven electric field affects the formation of the discharge channel [95]. The breakdown voltage of SF_6 and $C_5F_{10}O/N_2/O_2$ gas mixture shows a certain degree of dispersion can be characterized by the standard deviation (σ) of the breakdown voltage:

$$\sigma=\sqrt{\frac{\sum_{i=1}^{n}\left(x_i-\bar{x}\right)^2}{n}} \tag{3.1}$$

where n represents the total number of samples (n = 100), $\bar{x}$ represents the average value of breakdown voltage, and x_i represents the voltage value of the i-th breakdown of gas mixture.

The voltage amplitude for each AC breakdown of $C_5F_{10}O/N_2/O_2$ gas mixture is plotted in Figure 3.6. The overall trend of the breakdown voltage as a function of the number of breakdowns can be obtained by linear fitting (red line) and the parameters obtained by the fitting are shown in Table 3.2. It should be specially pointed out that the slope of the fitting curve of the breakdown voltage of $C_5F_{10}O/N_2/O_2$ gas mixture in some of the experimental groups with oxygen added is positive, which may due to the reason that most of the breakdown voltage values are close to the average value and only a small amount of breakdown voltage values deviate from the average value.

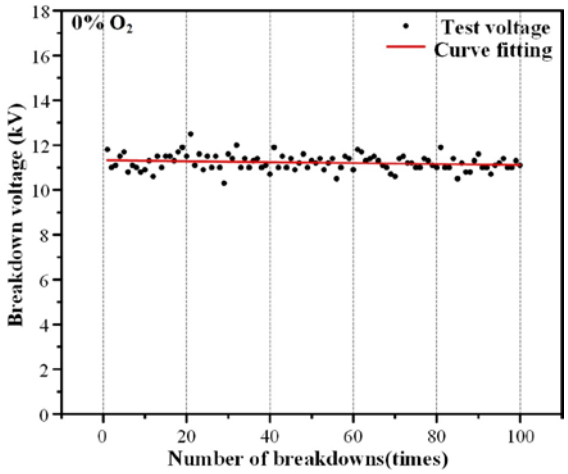

(a) Breakdown voltage of $C_5F_{10}O/N_2$ gas mixture

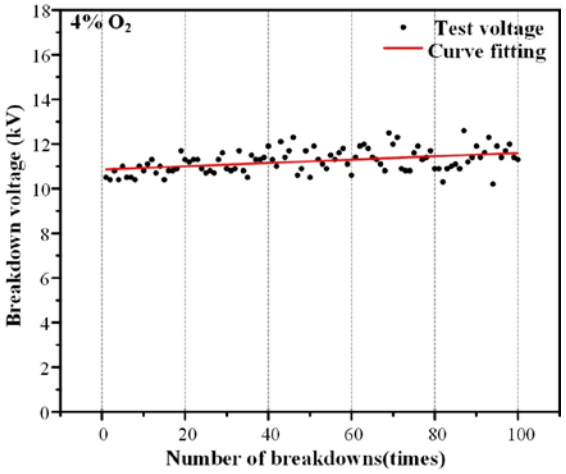

(b) Breakdown voltage of $C_5F_{10}O/N_2/O_2$ gas mixture containing 4% oxygen

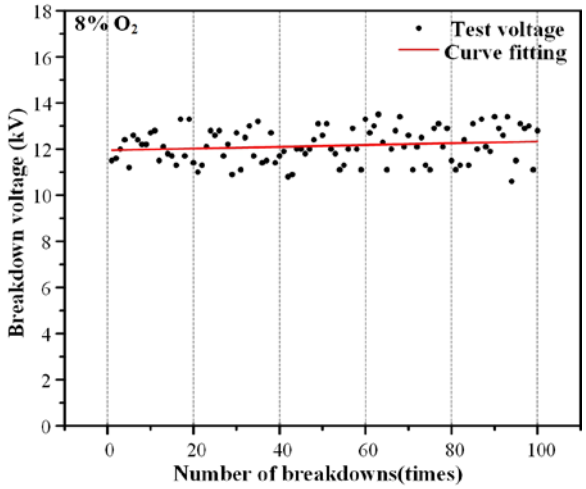

(c) Breakdown voltage of $C_5F_{10}O/N_2/O_2$ gas mixture containing 8% oxygen

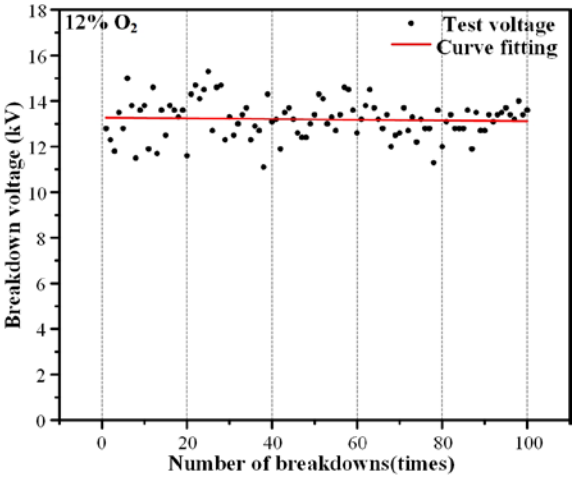

(d) Breakdown voltage of $C_5F_{10}O/N_2/O_2$ gas mixture containing 12% oxygen

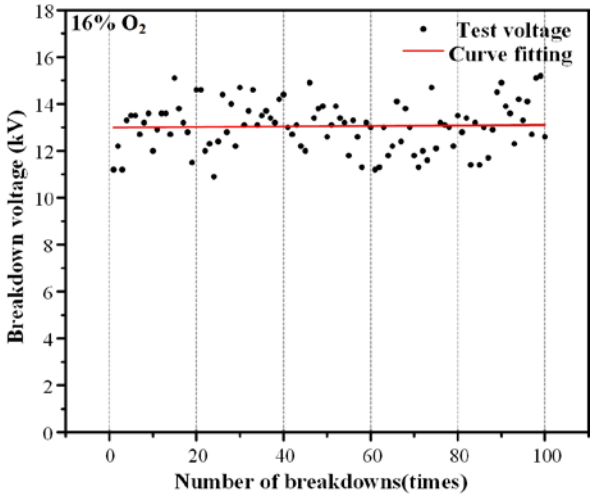

(e) Breakdown voltage of $C_5F_{10}O/N_2/O_2$ gas mixture containing 16% oxygen

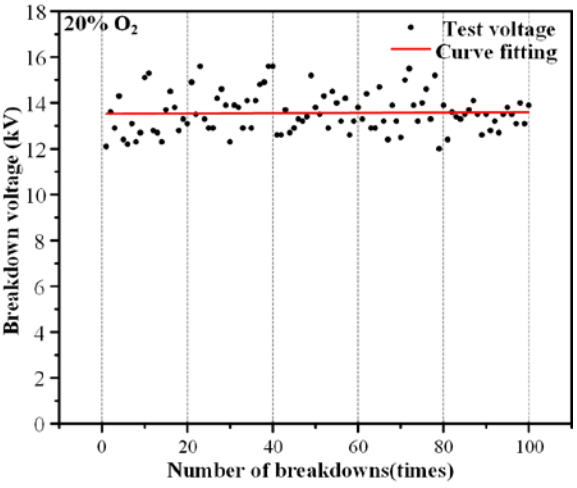

(f) Breakdown voltage of $C_5F_{10}O/N_2/O_2$ gas mixture containing 20% oxygen

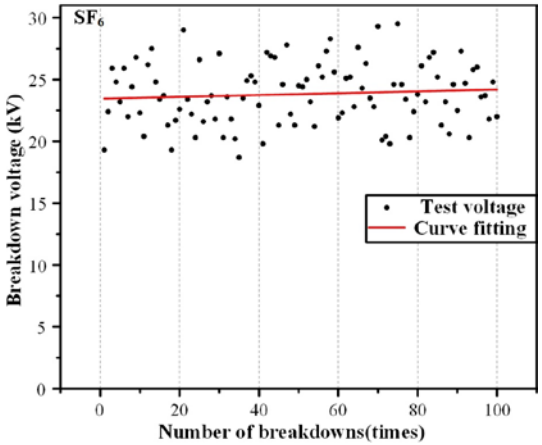

(e) Breakdown voltage of pure SF_6 gas

Figure 3.6 Effect of oxygen on breakdown voltage of $C_5F_{10}O/N_2/O_2$ gas mixture

Table 3.2 Fitting parameters of breakdown voltage of different gases

Gas type	Slope	Standard deviation
SF_6	0.00289	2.18
$C_5F_{10}O/N_2$	-0.00213	0.357
$C_5F_{10}O/N_2$/4% O_2	0.00748	0.525
$C_5F_{10}O/N_2$/8% O_2	0.00379	0.747
$C_5F_{10}O/N_2$/12% O_2	-0.00166	0.824
$C_5F_{10}O/N_2$/16% O_2	0.00116	1.02
$C_5F_{10}O/N_2$/20% O_2	-0.000669	0.869

The effect of oxygen concentration on the standard deviation of the breakdown voltage of $C_5F_{10}O/N_2/O_2$ gas mixture is shown in Figure 3.7. The slope and standard deviation of the fitting curve of the discharge voltage can reflect the change of the dielectric strength of $C_5F_{10}O$ gas mixture after AC breakdown. It can be seen that AC breakdown voltage of $C_5F_{10}O/N_2$ gas mixture is about 11.2kV, the dispersion of voltage amplitude during 100 discharges is small, and the discharge voltage has high stability. Adding oxygen to $C_5F_{10}O/N_2$ gas mixture will increase the standard deviation of AC breakdown voltage of the mixtures. With the increase of oxygen concentration, the standard deviation of the breakdown voltage of $C_5F_{10}O/N_2/O_2$ gas mixture showed a trend of first increasing and then decreasing, and the discharge voltage dispersion is the largest when the oxygen concentration is 16%. Excessive dispersion is detrimental to the insulation properties of the gas, and in some extreme cases, it may cause dielectric breakdown when the voltage is very low, causing equipment shutdown. When the oxygen concentration added to $C_5F_{10}O/N_2$ gas mixture is too high, it will enhance its dispersibility and reduce its insulation stability. It can be seen from Figure 3.6e that although AC breakdown voltage of $C_5F_{10}O/N_2/O_2$ gas mixture under the experiment conditions of this manuscript is lower than that of SF_6 gas, the dispersion of power frequency breakdown voltage of SF_6 gas is greater.

3.1.4 Effect of Oxygen Concentration on the Discharge Decomposition Characteristics of $C_5F_{10}O/N_2/O_2$

1 Qualitative Analysis of the Gas Products of $C_5F_{10}O/N_2/O_2$ Gas Mixture during Discharge

Decomposition

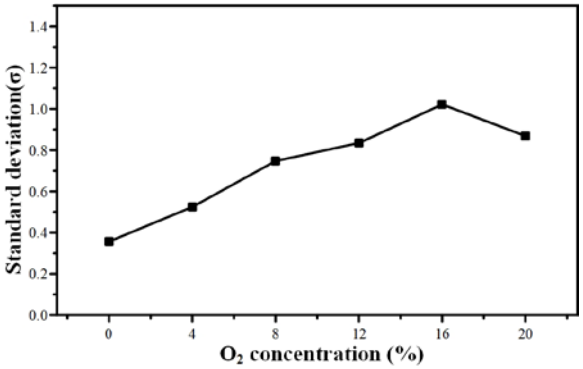

Figure 3.7 Standard deviation of breakdown voltage of $C_5F_{10}O/N_2/O_2$ gas mixture

The mass spectra of the decomposition products of $C_5F_{10}O/N_2/O_2$ ternary mixtures with 0%, 4%, 8%, 12%, 16%, and 20% O_2 after 20 and 100 discharges are revealed in Figure 3.8. According to the NIST14 database and standard gas test results, the decomposition products mainly included CO, CF_2O, CF_4, C_2F_4, C_2F_6, C_3F_6, C_3F_8, C_4F_{10} and C_3HF_7. The figure shows that the contents of CO, CF_2O, CF_4, C_2F_4, C_2F_6 and C_3F_8 increased in all experimental groups with increasing number of breakdowns, but the growth rules of each component differed. $C_5F_{10}O$ molecules are decomposed during each discharge breakdown. Some decomposition products participate in the decomposition reaction to generate new products during discharge, resulting in inconsistent growth rules among decomposition products. The separation times of C_3F_6 and C_4F_{10} are close; hence, their characteristic peaks overlapped, and their relative content could not be qualitatively analyzed. Using the SIM mode is necessary to identify the characteristic ions generated by gas for quantitative analysis. The content of C_3HF_7 mainly depends on the moisture content in the gas chamber, which is quickly consumed at the beginning of the experiment. As the number of breakdowns grows, H_2O is inadequate to provide the H required to generate C_3HF_7. Thus, the content of C_3HF_7 no longer increased.

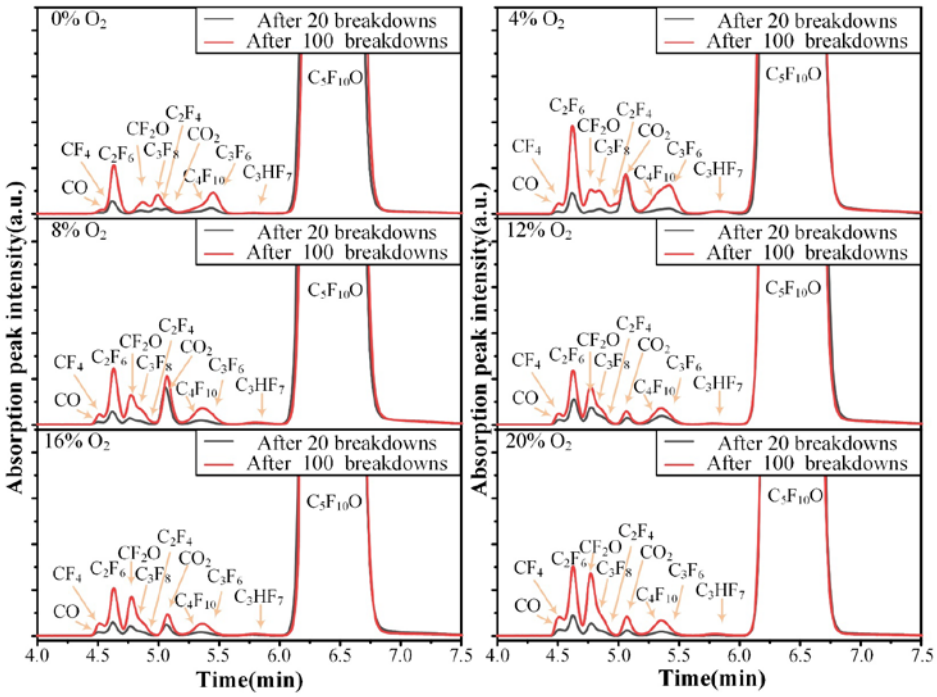

Figure 3.8 Qualitative analysis of $C_5F_{10}O$ discharge decomposition products

2 Quantitative Analysis of the Gas Products of $C_5F_{10}O/N_2/O_2$ Gas Mixture during Discharge Decomposition

The six main gas products are quantitatively analyzed using a standard gas as the reference and the internal peak integration method to further explore the specific contents of the six major decomposition products of CO, CF_4, C_2F_4, C_2F_6, C_3F_8, and C_3F_6 during discharge of $C_5F_{10}O/N_2/O_2$ gas mixture. In addition, due to the lack of the standard gas of CF_2O gas, the area external standard method is used to compare the peak area to indirectly study the change law of the content. The gas sampling obtained results after every 20 breakdowns of $C_5F_{10}O$ gas are analyzed via GCMS and the results are shown in Figure 3.9.

Figure 3.9 demonstrates that the contents of CO, CF_4, C_2F_4, C_2F_6, C_3F_8 and C_3F_6 grows with increasing number of breakdowns. However, in the horizontal comparison, the contents of C_3F_8, C_3F_6 and C_2F_4 gradually decreased with increasing of oxygen concentration; indeed, the decrease in C_2F_4 is the most evident among the products formed. When the concentration of added oxygen is at least 8%, the content of C_2F_4 in the decomposition products formed after 100 breakdowns of $C_5F_{10}O/N_2/O_2$ gas mixture is less than 1 ppm; further increases in oxygen content resulted in extremely low traces of C_2F_4. Compared with that of C_2F_4, the concentration of C_2F_6 only slightly changed in the horizontal comparison and the product is less affected by the change in oxygen content. The concentrations of CO and CF_4 grow with increasing oxygen concentration and are extremely sensitive to changes in oxygen concentration. Because CF_2O gas contains oxygen element, the generation amount in the process of AC breakdown depends on the oxygen content in the gas mixture. It can be seen from Figure 3.9g that $C_5F_{10}O/N_2$ gas mixture only generates a trace amount of CF_2O gas during the AC breakdown process, and the oxygen elements required to generate the CF_2O gas all come from the oxygen atoms in the $C_5F_{10}O$ gas molecules. However, the gas products containing oxygen elements produced by the decomposition of $C_5F_{10}O$ gas also include CO and CO_2, etc. Therefore, almost no CF_2O gas is produced when the gas mixture does not contain oxygen. $C_5F_{10}O/N_2/O_2$ gas mixture will generate more CF_2O gas under discharge conditions. With the increase of oxygen concentration or AC breakdown times, the production of CF_2O gas grows gradually. The oxygen element in the CF_2O gas produced by the decomposition of $C_5F_{10}O/N_2/O_2$ gas mixture mainly comes from the oxygen in the gas mixture.

Figure 3.9 reveal that every 20 breakdowns forms a group, and that $C_5F_{10}O$ gas mixture mixed with oxygen produce more decomposition products in the first 20 insulation breakdowns than in later breakdowns. With the increasing oxygen concentration in the first 20 breakdowns, the average content of CO and CF_4 produced after each breakdown reach 8 and 6 ppm, respectively. The gradient results of every 20 breakdowns indicate that the concentration of each decomposition product grows in an approximately linear manner. The increase in CO and CF_4 produced by the oxygen added $C_5F_{10}O/N_2$ gas mixture every 20 insulation breakdowns is above 30 ppm, and the average CO and CF_4 content per breakdown are greater than 1.5 ppm. The LC50 of rats within 4 hours is 1,807 ppm due to the high biological toxicity of CO. Electrical equipment with $C_5F_{10}O/N_2/O_2$ gas mixture as the insulation dielectric, similar to SF_6 GIE, could produce toxic decomposition products after insulation fault. Gas leaks in the electrical equipment or inadequate protection could harm the life and health of maintenance personnel. Therefore, limiting the concentration of the oxygen added to $C_5F_{10}O/N_2$ gas mixture is necessary.

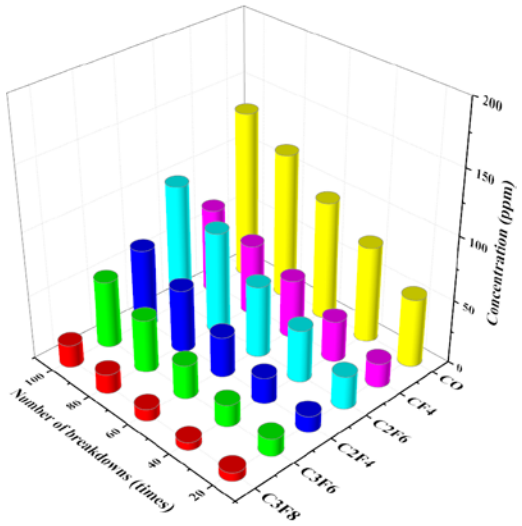

(a) $C_5F_{10}O/N_2$ gas mixture control group

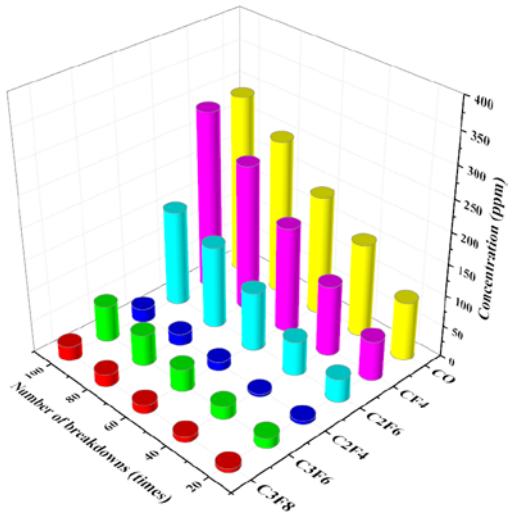

(b) $C_5F_{10}O/N_2/O_2$ gas mixture containing 4% O_2

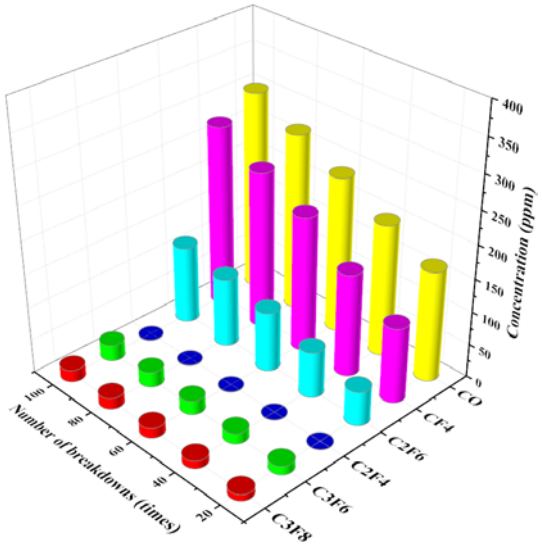

(c) $C_5F_{10}O/N_2/O_2$ gas mixture containing 8% O_2

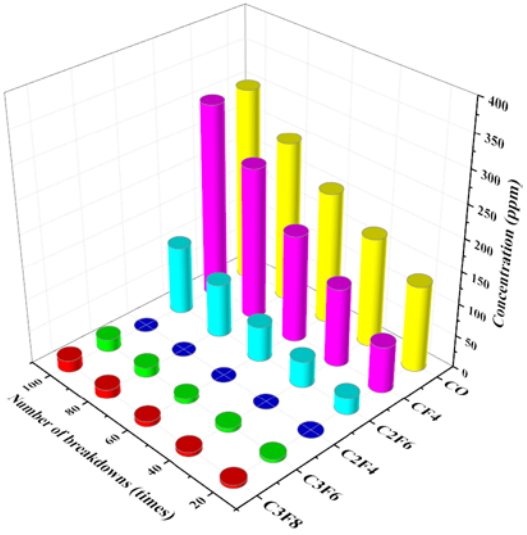

(d) $C_5F_{10}O/N_2/O_2$ gas mixture containing 12% O_2

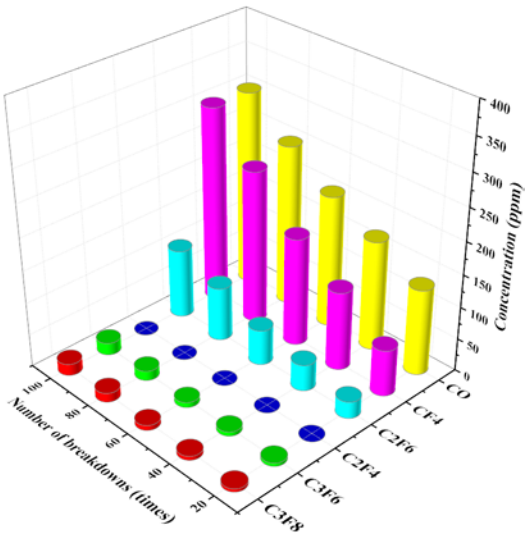

(e) $C_5F_{10}O/N_2/O_2$ gas mixture containing 16% O_2

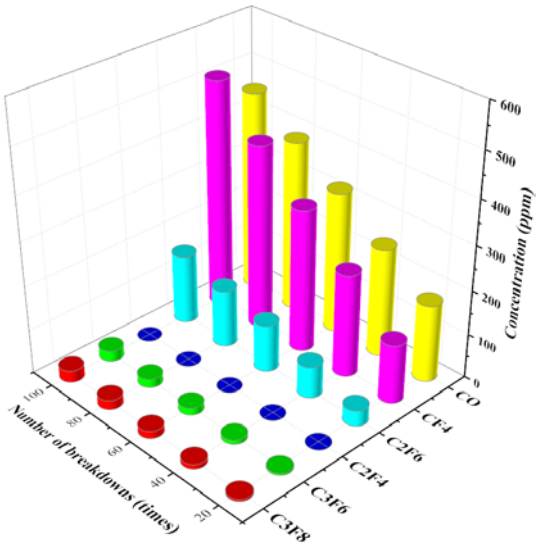

(f) $C_5F_{10}O/N_2/O_2$ gas mixture containing 20% O_2

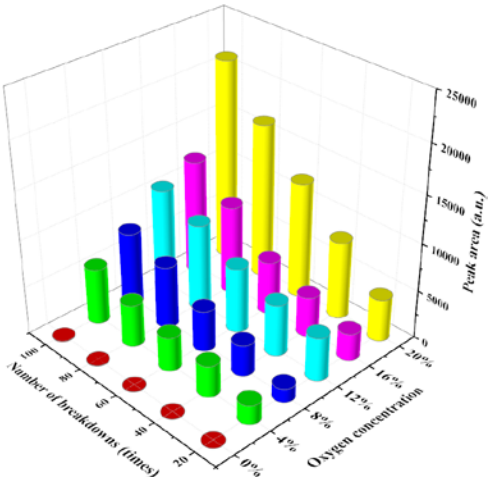

(g) CF_2O gas concentration

Figure 3.9 Quantitative analysis of $C_5F_{10}O$ discharge decomposition products

3.2 PD Decomposition Characteristics of $C_5F_{10}O/N_2/O_2$

PD (corona discharge) occurs near the electrode with a small radius of curvature, because the electric field near the electrode is extremely uneven. The local electric field strength exceeds the minimum electric field strength required for ionization of the insulating gas, resulting in ionization of the gas to form a local self-sustaining discharge phenomenon. The corona near the electrode will also produce light and sound phenomenon. With the increasing of voltage applied between the two electrodes, the frequency and amplitude of the pulse discharge generated by corona discharge gradually increases, the corona discharge will be transformed into glow discharge, and the further enhancement of voltage will result in streamer discharge, which will lead to insulation breakdown of the gap when the streamer discharge develops to connect two electrodes. Because of the low voltage between the electrodes producing PD, its discharge energy density is much smaller than the frequency breakdown.

PD is a relatively stable form of discharge, which can persist under the condition of constant voltage between electrodes. It is an early stage of development, causing insulation gap breakdown in uneven electric fields. Partial discharge is an important cause of dielectric breakdown in GIE, and it is also an significant sign of insulation deterioration of insulating dielectrics [96]. Therefore, the study of the PD characteristics of $C_5F_{10}O$ gas mixture is meaningful to clarify the discharge characteristics of $C_5F_{10}O$ GIE during early corona discharge. In this section, the experimental study of PD decomposition characteristics of $C_5F_{10}O/N_2/O_2$ gas mixture is carried out to clarify the characteristic quantities and products of PD in $C_5F_{10}O/N_2/O_2$ gas mixture under the influence of oxygen concentration changes on its electrical parameters and decomposition products in the process of PD, and to provide reference for online monitoring and fault identification of PD in $C_5F_{10}O$ GIE.

3.2.1 Effect of Oxygen Concentration on PD of $C_5F_{10}O/N_2/O_2$

1 PD Test Platform and Methods

The test platform for partial discharge decomposition characteristics of $C_5F_{10}O/N_2/O_2$ gas mixture is shown in Figure 3.1. The difference lies in that the spheres electrodes shown in Figure 3.1 needs to be replaced with the pin-plate electrodes shown in Figure 3.10 to simulate

the partial discharge caused by metal protrusion defects. The radius of the plate electrode is 35 mm with the thickness of 10 mm. And the radius of curvature of the pin electrode tip is 0.3 mm with the pin-plate spacing of 10 mm. The detection of the PD signal and the correction of the discharge magnitude are performed based on the pulse current method recommended by the IEC 60270: 2015 standard [97]. The gas mixture composition is the same as the gas conditions used in AC breakdown test in the previous section, and the gas composition for each group of tests is shown in Table 3.1. The total gas pressure is 0.14 MPa, the concentration of $C_5F_{10}O$ is fixed at 7.5%, and the concentrations of oxygen are 0, 4%, 8%, 12%, 16% and 20%, respectively. A step-up method is employed in the PD test to study the breakdown voltage, partial discharge inception voltage (PDIV) and the change of decomposition products of $C_5F_{10}O/N_2/O_2$ gas mixture under the extremely non-uniform electric field formed by the pin-plate electrode. In the course of the voltage rise, it is necessary to wait for 1 minute for each voltage ΔV increase across the pin-plate electrode after the PDIV signal is detected, and then use the oscilloscope to detect and record the local discharge signal after the signal has stabilized. To test PDIV, the trigger level of the oscilloscope needs to be set as low as possible, just above the level of the noise signal. The PDIV of $C_5F_{10}O/N_2/O_2$ gas mixture containing different concentrations of oxygen is always 11 kV. The difference in gas composition in different test groups denotes the change in the ratio of oxygen and nitrogen, and the dielectric strength of oxygen is not much different from that of nitrogen, so the oxygen content has little effect on the value of PDIV.

Figure 3.10 pin-plate electrode

In order to test the PD characteristics of $C_5F_{10}O/N_2/O_2$ gas mixture at different voltages, the breakdown voltage of $C_5F_{10}O/N_2/O_2$ gas mixture is first tested in this manuscript to avoid the insulation breakdown during the detection of the PD signal due to the high voltage applied to the pin-plate electrode. To prevent multiple breakdowns of the gas gap from causing ablation of the pin electrode and decomposition of $C_5F_{10}O$, which would lead to significant changes in the breakdown voltage of the pin-plate gap and reduce the confidence of the test results, the breakdown voltage is tested three times for each group of gases and averaged, as shown in Figure 3.11. The breakdown voltage of $C_5F_{10}O/N_2/O_2$ gas mixture in the extremely non-uniform electric field is about 22 kV. The PDIV value of $C_5F_{10}O/N_2/O_2$ gas mixture is about 1/2 of its breakdown voltage value under the same conditions. With the increase of oxygen concentration, the breakdown voltage of $C_5F_{10}O/N_2/O_2$ gas mixture under the extremely non-uniform electric field does not change much. The breakdown voltage of the gas mixture does not change significantly when the oxygen concentration alters from 0 to 8%, while the breakdown voltage of the gas mixture indicates a slightly decreasing trend with the increase of oxygen concentration when the oxygen concentration is greater than 8%. This rule is opposite to the effect of oxygen on the breakdown voltage of $C_5F_{10}O/N_2/O_2$ gas mixture at AC breakdown voltage.

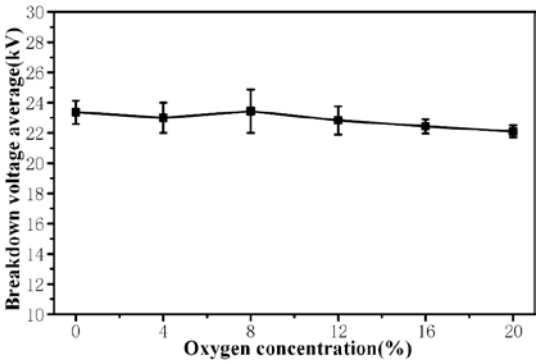

Figure 3.11 Breakdown voltage of $C_5F_{10}O/N_2/O_2$ gas mixture under extremely non-uniform electric field

2 Effect of Oxygen Concentration on PD of $C_5F_{10}O/N_2/O_2$ Gas Mixture

Figure 3.12 shows the typical PD signal waveforms of $C_5F_{10}O/N_2/O_2$ gas mixture and SF_6 gas. It can be seen that SF_6 gas is more likely to produce PD than $C_5F_{10}O/N_2/O_2$ gas mixture, and the amplitude and frequency of PD are higher. The reason is that SF_6 gas and $C_5F_{10}O$ gas are both strong electronegative gases. Although the insulation strength are high, corona discharge will most likely occur in the non-uniform electric field. The SF_6 gas used in the test is pure gas, while the $C_5F_{10}O$ gas mixture has nitrogen and oxygen in addition to $C_5F_{10}O$ gas, in which the electronegativity of F, O and N elements gradually decreases. The highest content in the $C_5F_{10}O$ gas mixture is buffer gas (N_2), which will reduce the overall electronegativity of the gas mixture, so the SF_6 gas is more likely to corona discharge under the condition of non-uniform electric field. The discharge intensity of $C_5F_{10}O/N_2/O_2$ gas mixture is smaller than that of SF_6 gas under the same conditions when PD occurs in equipment in the process of engineering application, which can reduce the insulation deterioration caused by the decomposition of $C_5F_{10}O/N_2/O_2$ gas mixture in the process of PD and improve the operating stability of equipment.

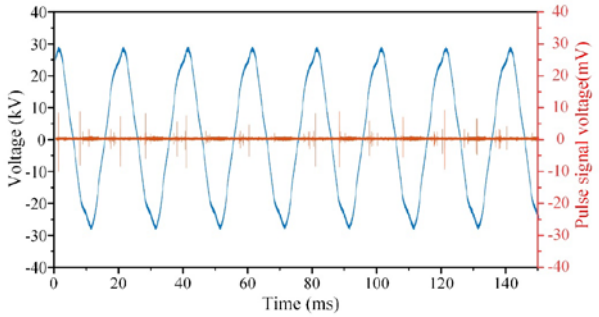

(a) $C_5F_{10}O/N_2/O_2$ gas mixture PD signal

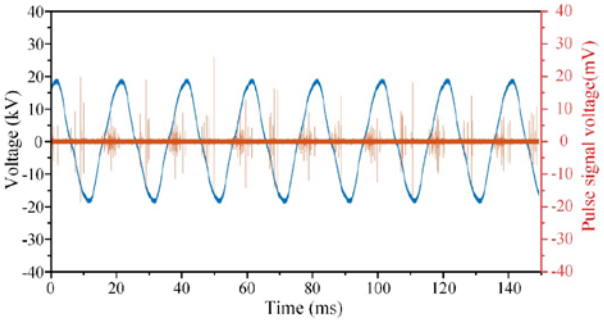

(b) SF_6 gas PD signal

Figure 3.12 Typical PD signal waveforms of $C_5F_{10}O/N_2/O_2$ gas mixture and SF_6 gas

The PDIV with a voltage amplitude of about 1.5 times (17kV) is applied to $C_5F_{10}O/N_2/O_2$ gas mixture with different oxygen contents, which can ensure the stable PD of the gas mixture, and also ensure that the gas mixture will not produce breakdown of the insulating gap. After the PD signal is stabilized, the PD signal is continuously collected for 1 s to record and analyze the information on the number of discharges, discharge phase and discharge magnitude, which is used to explore the effect of oxygen content on the PD characteristics of $C_5F_{10}O/N_2/O_2$ gas mixture. The change rules of three typical characteristic quantities, namely the total discharge times, the cumulative discharge and the average discharge of $C_5F_{10}O/N_2/O_2$ gas mixture under different oxygen contents, are shown in Figure 3.13. When the oxygen content is not more than 8%, the total discharge magnitude and the discharge magnitude in the positive half of the AC voltage gradually grow with the increase of oxygen content, while the discharge magnitude in the negative half remains unchanged. When the oxygen content is from 0 to 12%, the total number of discharge pulses grows gradually, and the number of discharges in the negative half of the AC voltage gradually decreases.

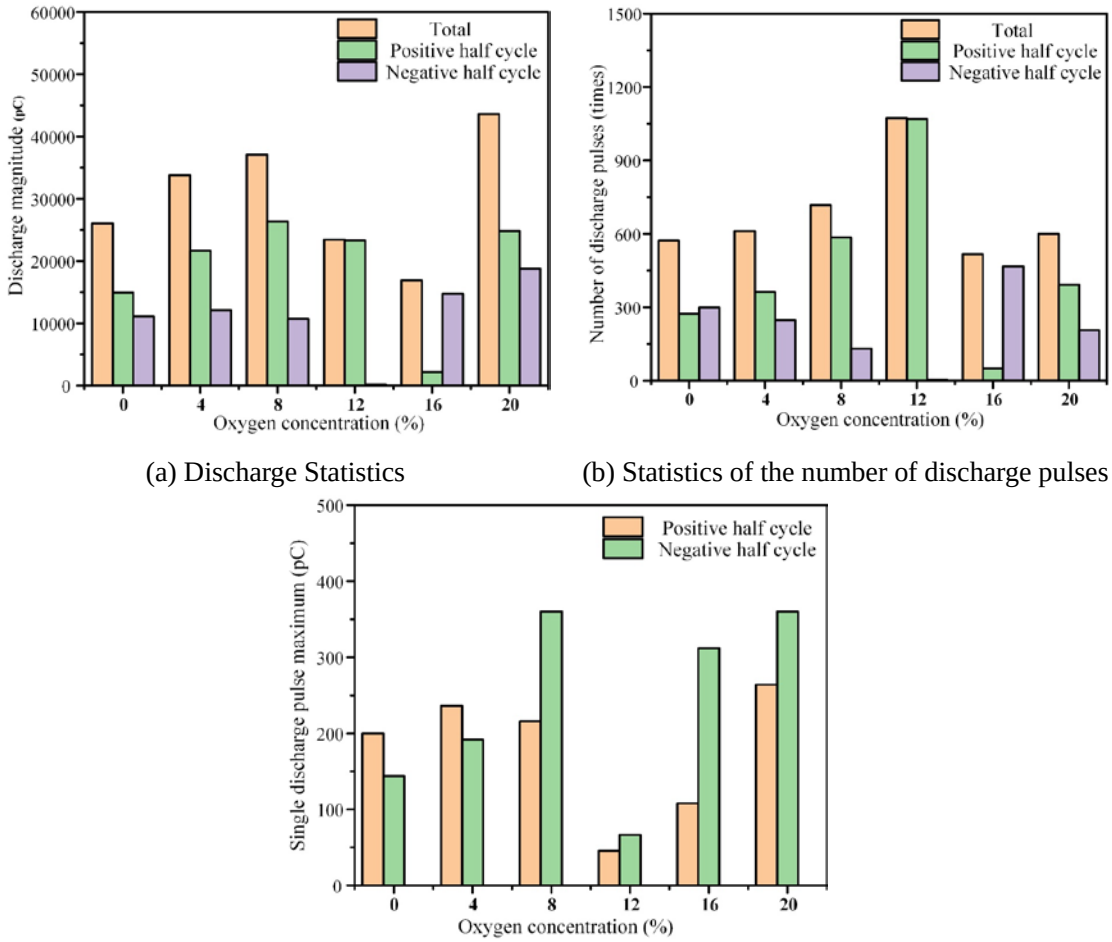

(a) Discharge Statistics (b) Statistics of the number of discharge pulses

(c) Statistics of single-pulse discharge magnitude

Figure 3.13 PD signal statistics of $C_5F_{10}O/N_2/O_2$ gas mixture with different oxygen concentrations

3.2.2 Effect of Oxygen Concentration on the PD Decomposition Characteristics of $C_5F_{10}O/N_2/O_2$

1 Effect of Oxygen Concentration on the Breakdown Products of $C_5F_{10}O/N_2/O_2$ Gas Mixture

The samples of $C_5F_{10}O/N_2/O_2$ gas mixture are collected at the end of the extremely non-uniform electric field breakdown test and the results of gas composition detection using GC-MS are shown in Figure 3.14a. The main decomposition products are CF_4, CO_2, CF_2O, C_2F_6, C_3F_6, C_3F_8, C_4F_{10} and C_3HF_7. In order to analyze the effect of oxygen content on the decomposition products of $C_5F_{10}O/N_2/O_2$ gas mixture, the concentrations of CF_4, CO_2, C_2F_6, C_3F_8 and C_3HF_7, which are more abundant in the decomposition products, are studied quantitatively using standard gases, and the content of CF_2O gas are studied semi-quantitatively using the area external standard method. The change of the content of the above six decomposition products is shown in Figure 3.14b. It can be found that the most abundant gases among the decomposition products are CF_4 and CO_2, which have the simplest structure and are the most stable decomposition products produced by $C_5F_{10}O$. Although only three insulation breakdowns occurr in this section of the test with $C_5F_{10}O$ gas mixture, the content of the decomposition products produced is higher than that in the previous section of the test, which is caused by the difference in discharge energy due to the different length of the gas gap between the electrodes. Since the electronegative gas is more likely to produce corona discharge, in order to prevent the PDIV value close to the breakdown voltage value, making the implementation of the test impossible, the distance between the electrodes used in this section of the test is larger, the voltage value required for insulation breakdown is also higher, and the energy of the discharge channel formed during insulation breakdown is also much higher than AC breakdown test, thus resulting in more decomposition products generated during insulation breakdown. Except for the content of CF_4 gas, the content of the other five decomposition products signifies a trend of decreasing and then increasing with the variation of oxygen concentration, especially when the oxygen concentration is 20%, the content of the above six decomposition products increases significantly. But a local minimum value is observed at 4% oxygen concentration. The above results indicate that oxygen concentration affects the decomposition characteristics of $C_5F_{10}O$ gas, and the addition of low concentration (4% by volume) of oxygen can inhibit the decomposition of $C_5F_{10}O$ gas, while the concentration of oxygen above 4% will promote the decomposition of $C_5F_{10}O$ gas.

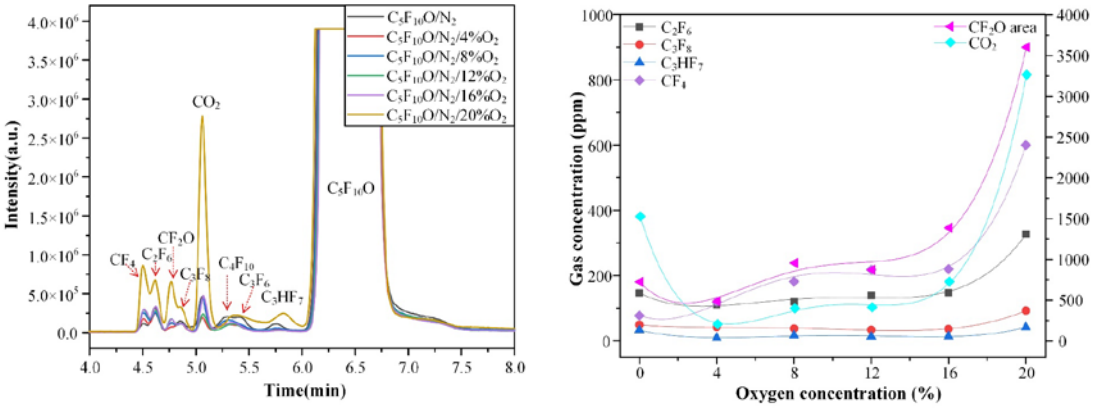

(a) Decomposition products after breakdown

(b) Quantification of decomposition products after breakdown

Figure 3.14 $C_5F_{10}O/N_2/O_2$ gas mixture decomposition products

2 Effect of Oxygen Concentration on the Decomposition Products of Long-term PD of $C_5F_{10}O/N_2/O_2$ Gas Mixture

The early PD inside the equipment is difficult to detect because the discharge intensity is

small. It is often detected only when it has developed into a more serious situation, where the PD may have lasted for a long time. This long time PD will cause the internal insulation gas to decompose. Therefore, clarifying the decomposition rule of $C_5F_{10}O/N_2/O_2$ gas mixture under PD at different times will help to detect the PD caused by insulation defects in time during the operation of GIE and prevent the expansion of hidden dangers leading to equipment failure. In this section, the decomposition of $C_5F_{10}O/N_2/O_2$ gas mixture caused by partial discharge within 96 hours is tested at 12-hour intervals, and quantitative or semi-quantitative analysis of CO, CO_2, CF_4, C_2F_6, C_3F_8, C_3HF_7 and CF_2O, which are more abundant in the decomposition products, is also conducted, and the results are shown in Figure 3.15.

Figure 3.15a shows the concentration of CO gas produced by $C_5F_{10}O/N_2/O_2$ gas mixture when PD occurs at different times, and the CO gas concentration is independent of the PD time. With the increase of oxygen concentration in the gas mixture, the concentration of CO gas produced by PD shows a trend of decreasing first and then increasing. The concentration of CO_2 gas shown in Figure 3.15b gradually increases with the growth of PD time. The change of oxygen concentration in $C_5F_{10}O$ gas mixture has a greater influence on the concentration of CO_2 gas, especially when the oxygen concentration is 20%, the concentration of CO_2 gas produced by PD of $C_5F_{10}O$ gas mixture is higher, and its concentration increases obviously with the PD time. Figure 3.15c shows the trend of the concentration of CF_4 with the PD time. The concentration of CF4 gas grows linearly at a low rate with the PD time when the oxygen concentration is 0%-16%, and the concentration of CF_4 gas produced by different test groups does not differ significantly. The growth rule of CF_4 gas and CO_2 gas is similar, and the concentration of CF_4 gas is significantly higher than that of the other test groups when the oxygen concentration is 20%. The three gases CO, CO_2 and CF_4 produced by PD of $C_5F_{10}O/N_2/O_2$ gas mixture with 4% oxygen concentration are not significantly different from the test group of $C_5F_{10}O/N_2$ gas mixture without oxygen, and significantly lower than the test group of $C_5F_{10}O/N_2/O_2$ gas mixture with 20% oxygen concentration.

Figure 3.15d shows the change of C_2F_6 gas concentration. It can be seen that when the oxygen concentration is 0% and 4%, the C_2F_6 gas concentration generated by the decomposition of $C_5F_{10}O/N_2/O_2$ gas mixture increases linearly with the PD time. The C_2F_6 gas concentration generated by the decomposition of $C_5F_{10}O/N_2$ gas mixture under PD conditions is relatively high, with an average of 4.04ppm per 12 hours. The $C_5F_{10}O/N_2/O_2$ gas mixture with 4% oxygen concentration produced the lowest concentration of C_2F_6 gas by decomposition within the first 48 hours of PD. When the oxygen concentration is greater than 4%, the C_2F_6 gas concentration remains unchanged and low as the PD time increases. Therefore, adding oxygen to $C_5F_{10}O/N_2/O_2$ gas mixture can inhibit the decomposition of $C_5F_{10}O$ during the PD process to generate C_2F_6 gas. In addition, the linear increase of C_2F_6 gas concentration with PD time when the oxygen concentration is 0% and 4% can also be considered as a sign of whether PD occurs in monitoring equipment in engineering applications. Figure 3.15e shows the trend of C_3F_8 gas concentration generated by decomposition with the PD time. The concentration of C_3F_8 gas produced by $C_5F_{10}O/N_2$ gas mixture in PD conditions indicates a trend of saturation growth with time, and the concentration of C_3F_8 gas remains unchanged at about 460 ppm 72 hours after the occurrence of PD. The concentrations of C_3F_8 gas produced at the initial stage of PD are similar in each test group. With the growth of PD time, the concentration of C_3F_8 gas produced by the decomposition of $C_5F_{10}O/N_2/O_2$ gas mixture after

the addition of oxygen gradually increases without the trend of saturation. The trend of the concentration of C_3HF_7 with PD time is shown in Figure 3.15f. With the increase of oxygen concentration, the concentration of C_3HF_7 gas produced by $C_5F_{10}O/N_2/O_2$ gas mixture under PD conditions shows a trend of decreasing first and then increasing. After adding oxygen, the concentration of C_3HF_7 gas generated by the decomposition of $C_5F_{10}O/N_2/O_2$ gas mixture is lower than that of the experimental group without oxygen, especially when the oxygen concentration is 4%-16%. Oxygen can inhibit the decomposition of $C_5F_{10}O$ gas under PD conditions to produce C_3HF_7 gas or cause the further decomposition of C_3HF_7 gas into small molecule gas. The trend of the concentration of CF_2O with PD time is exhibited in Figure 3.15g. The CF_2O gas concentrations produced by each test group containing different oxygen concentrations at the initial stage of PD are similar, and their concentrations gradually increase with the growth of PD time. The concentration of oxygen has almost no effect on the concentration of CF_2O gas produced by the decomposition of $C_5F_{10}O/N_2/O_2$ gas mixture, but the concentration of CF_2O gas produced by the decomposition of $C_5F_{10}O/N_2/O_2$ gas mixture is higher than that of $C_5F_{10}O/N_2$ gas mixture under the same conditions. It is shown that after adding oxygen to $C_5F_{10}O/N_2$ gas mixture, it will decompose to generate more CF_2O gas under PD conditions. But the change of oxygen concentration in the test has no effect on the CF_2O gas concentration.

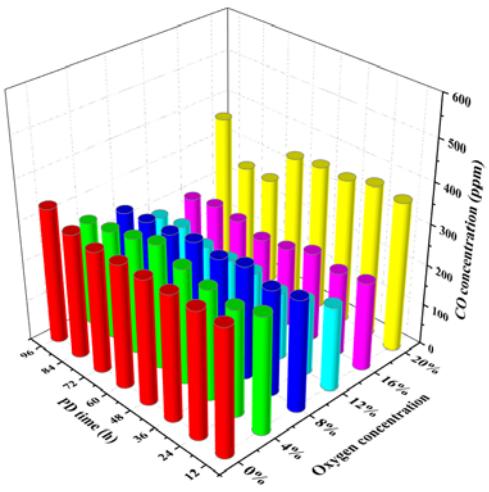

(a) CO

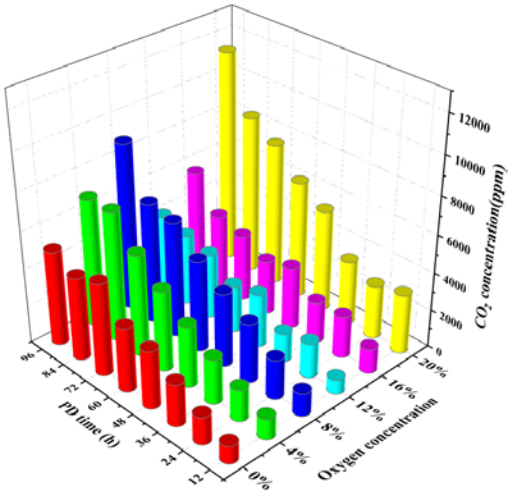

(b) CO_2

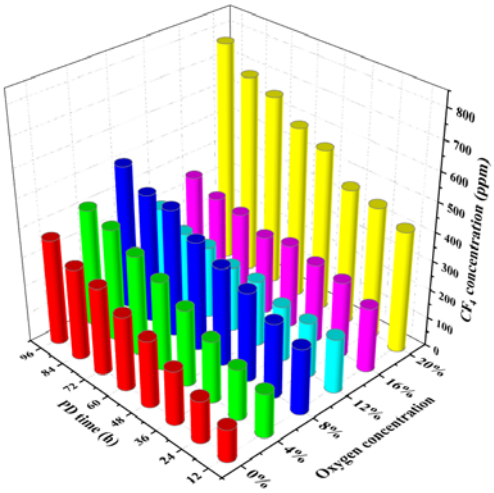

(c) CF_4

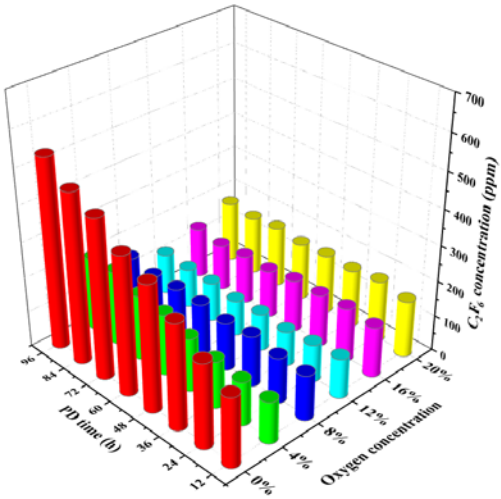

(d) C_2F_6

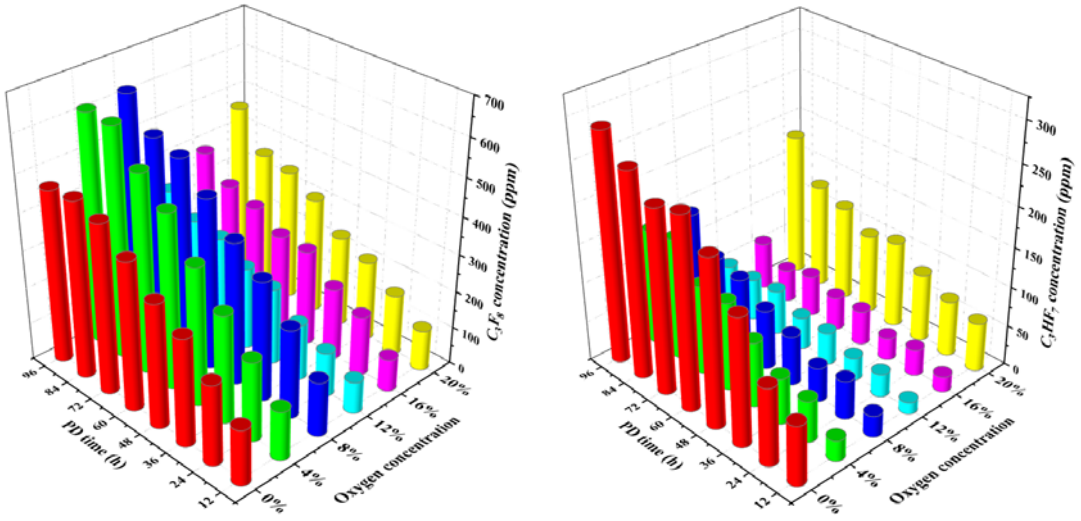

(e) C_3F_8

(f) C_3HF_7

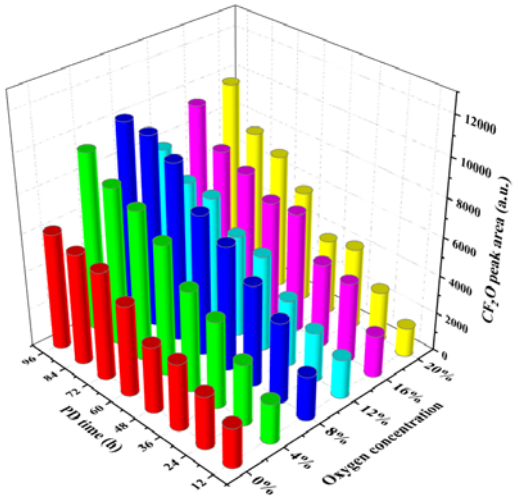

(g) CF_2O

Figure 3.15 Decomposition products of $C_5F_{10}O/N_2/O_2$ gas mixture

3.3 Thermal Decomposition Characteristics of $C_5F_{10}O/N_2/O_2$

POFs are mainly caused by the poor contact of the contacts in GIE. In this case, the heat concentrates at the contact point, which would cause a local temperature increase. POFs develop slowly, in the early stage, the overheating will gradually deteriorate the insulation of the equipment. The deterioration will also further exacerbate the overheating. Eventually, the local overheating faults will cause the insulation breakdown and ablation [98]. However, POFs are very latent in GIE. In order to avoid equipment damage and property loss caused by POFs, the monitoring and issue early warnings of such faults are necessary. Therefore, clarifying the thermal decomposition characteristics and byproducts of the $C_5F_{10}O$ gas mixture is of great significance for the online monitoring of partial overheating in GIE.

3.3.1 Test Platform and Method

We replace a new heat source device and a larger chamber in the test platform in Figure 2.1, Chapter 2. All the tests in this section can be carried out in this adjusted platform. In order

to obtain the decomposition characteristics of $C_5F_{10}O/N_2/O_2$ gas mixture at different heating time, we take gas samples from the chamber at 2, 4, 6, 8, 10 and 12 h of heating. Due to the multiple sampling, the chamber pressure may change obviously. In order to avoid that, we replace the 1L chamber in Figure 2.1 with a 10L one. In addition, the function of heat source in the gas thermal decomposition tests is only heating. The reaction on the interface should be avoided. Hence, we design a new heating source as shown in Figure 3.16. The shell material of the heat source is 2520 type stainless steel material with good corrosion resistance. The heating material is the nickel-chromium alloy wire, and the temperature sensor is a K-type thermocouple. The test temperature can be accurately controlled by the combination of the heating element and the thermocouple. Magnesium oxide powder is filled as insulating medium between the shell and the internal heating material and thermocouple. In order to simulate the POF of metal conductive materials in the equipment, the heat source is placed in the center of the simulated gas chamber.

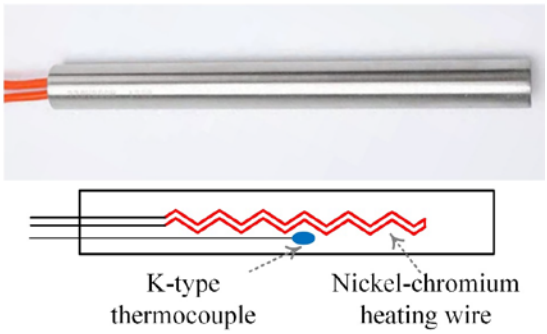

Figure 3.16 Defect model of thermal decomposition test

The test temperatures are set separately at 300 °C, 350 °C, 400 °C, 450 °C, 500 °C and 550 °C, referring to the POF temperature range of SF_6 GIE [99]. First, we test the effect of temperature on the thermal decomposition characteristics of $C_5F_{10}O/N_2$ and $C_5F_{10}O/N_2/O_2$ gas mixtures. Then, the effect of oxygen concentration on the decomposition characteristics of $C_5F_{10}O/N_2/O_2$ gas mixture is tested. The gas mixture composition is the same as the gas conditions used in AC breakdown test in Section 3.1, and the gas composition for each group of tests is shown in Table 3.1. The total gas pressure is 0.14 MPa, the concentration of $C_5F_{10}O$ is fixed at 7.5%, and the concentrations of oxygen are 0, 4%, 8%, 12%, 16% and 20%, respectively. After the start of the test, gas samples are collected every 2 hours for gas composition analysis. One group of tests last for 12 hours.

3.3.2 Effect of Temperature on the Thermal Decomposition Properties of $C_5F_{10}O/N_2/O_2$

The trends of the types and contents of thermal decomposition products of $C_5F_{10}O/N_2$ and $C_5F_{10}O/N_2/O_2$ (the O_2 concentration is 20%) gas mixtures in the temperature range of 300°C-550°C are given in Figure 3.17 and Figure 3.18. It could be found that $C_5F_{10}O/N_2$ gas mixture starts to decompose at 300 °C, and produces the same primary decomposition products as C_3F_6, CHF_3 and C_3HF_7 in the gas-solid interface tests in Chapter 2. When the temperature is above 450 °C, a large number of decomposition products begin to be produced. In the temperature range of 300℃-450℃, $C_5F_{10}O/N_2$ gas mixture is decomposed to produce C_3F_6 gas, and C_3F_6 gas is not detected when the test temperature is 500℃ and 550℃. CHF_3 gas is only produced

at the temperature of 300°C, and no CHF_3 is detected at temperatures of 350°C and above. The above results reveal that $C_5F_{10}O$ gas will generate CHF3 when the temperature is 300 °C, and will decompose to generate C_3F_6 when the temperature is below 450 °C, while the C_3F_6 and CHF_3 gases generated by the decomposition of $C_5F_{10}O$ gas will decompose at higher temperature to generate other more stable decomposition gases. $C_5F_{10}O/N_2/O_2$ gas mixture also began to decompose at 300°C to produce primary decomposition products such as C_3F_6 and C_3HF_7, and a large number of decomposition products began to be produced at temperatures above 400°C. The difference between $C_5F_{10}O/N_2/O_2$ and $C_5F_{10}O/N_2$ gas mixture thermal decomposition products is that $C_5F_{10}O/N_2/O_2$ gas mixture does not decompose to produce CHF_3 gas, and the initial temperature for a large number of decomposition products is lower. In terms of other thermal decomposition products, $C_5F_{10}O/N_2/O_2$ gas mixture decomposes to produce more C_3F_6, C_3HF_7 and CF_2O at 550°C due to the presence of oxygen, while $C_5F_{10}O/N_2$ gas mixture decomposes to produce more C_2F_6.

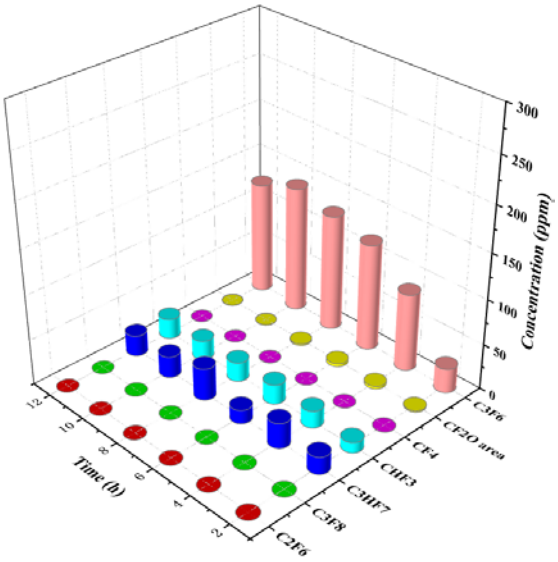

(a) 300℃

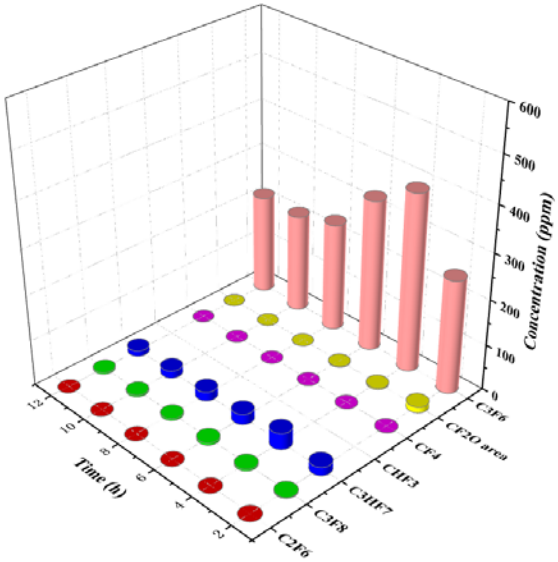

(b) 350℃

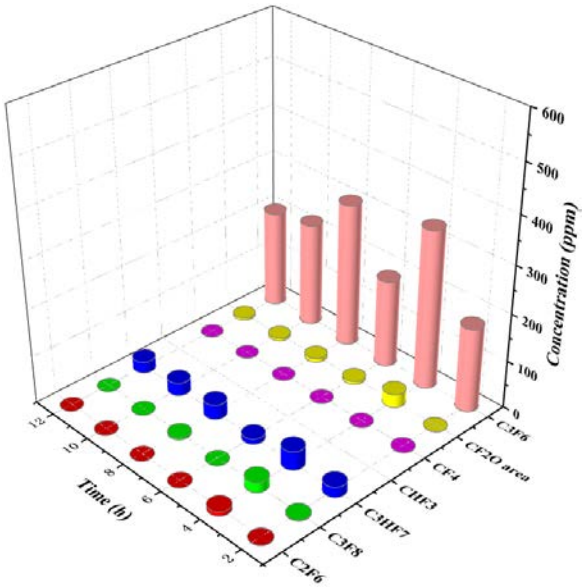

(c) 400℃

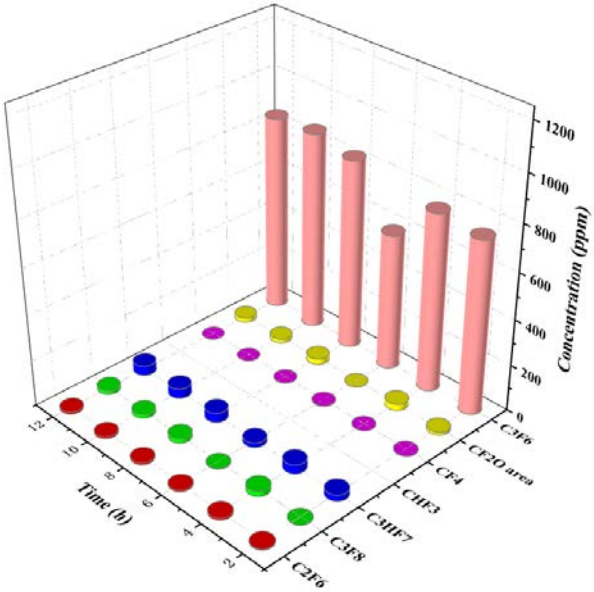

(d) 450℃

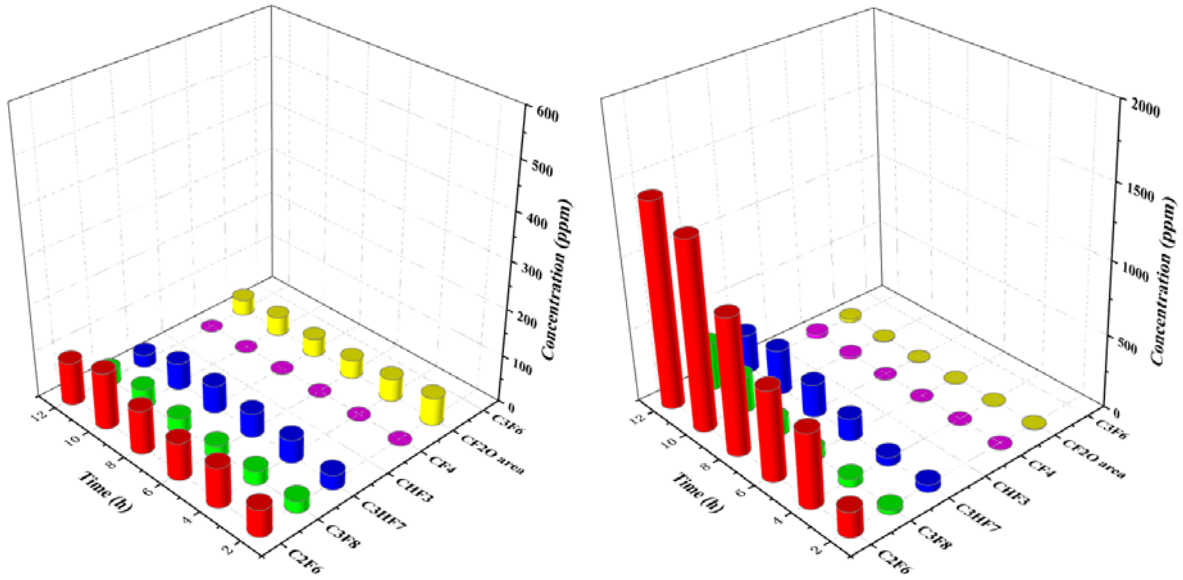

(e) 500℃ (f) 550℃

Figure 3.17 Effect of temperature on the thermal decomposition characteristics of $C_5F_{10}O/N_2$ gas mixture

The trends of thermal decomposition products of $C_5F_{10}O/N_2$ gas mixture in the temperature range of 300°C-550°C are shown in Figure 3.17. Only the concentration of C_3F_6 gas among the primary decomposition products from the decomposition of $C_5F_{10}O/N_2$ gas mixture at 300°C gradually increase during the first 10 hours of the test, and the concentration of C_3F_6 gas slightly decrease at 10-12 hours. The concentrations of CHF_3 and C_3HF_7 gases make no change with the increase of the thermal decomposition time. It shows that CHF_3 and C_3HF_7 gases have reached equilibrium in the first 2 hours of thermal decomposition, which is due to the fact that both CHF_3 and C_3HF_7 gases contain H elements and the formation of H-containing products is limited by the moisture content. The concentration of C_3F_6 gas produced by $C_5F_{10}O/N_2$ gas mixture at the thermal decomposition temperature of 350°C and 400°C also make clear a trend of increasing and then decreasing with the increase of thermal decomposition time, the difference is that the maximum value of C_3F_6 concentration appear earlier with the increase of thermal decomposition temperature. At the temperature of 450°C, the concentration of C_3F_6 gas does not change with the prolongation of thermal decomposition time. When the temperature is higher than 450°C, the thermal decomposition of $C_5F_{10}O/N_2$ gas mixture no longer produces C_3F_6 gas. It's known that $C_5F_{10}O/N_2$ gas mixture does not contain oxygen and only $C_5F_{10}O$ gas decomposition will produce O element. Therefore, only a trace of CF_2O gas is generated during the thermal decomposition of $C_5F_{10}O/N_2$ gas mixture, which is mainly limited by the lack of O element. The decomposition of $C_5F_{10}O/N_2$ gas mixture starts to produce C_2F_6 gas at the test temperature of 500°C, and its generation rate is faster at the temperature of 550°C. The generation of C_3F_8 and CF_4 gases starts at the test temperature of 550°C.

The trends of thermal decomposition products of $C_5F_{10}O/N_2/O_2$ gas mixture in the temperature range of 300°C-550°C are shown in Figure 3.18. The change rule of each primary decomposition product produced by the decomposition of $C_5F_{10}O/N_2/O_2$ gas mixture at 300°C is similar to that of $C_5F_{10}O/N_2$ gas mixture. $C_5F_{10}O/N_2/O_2$ gas mixture starts to produce C_3F_8 and CF_4 gases at the test temperature of 400 ℃, and the concentration of both C_3F_8 and CF_4 gases increase gradually with the increase of the thermal decomposition temperature and time.

The thermal decomposition of $C_5F_{10}O/N_2/O_2$ gas mixture starts to produce C_3F_8 and CF_4 gases at the lower temperature than that of $C_5F_{10}O/N_2$ gas mixture. The decomposition of $C_5F_{10}O/N_2/O_2$ gas mixture begins to produce CF_2O gas at the test temperatures of 500℃ and 550℃, and its concentration increase gradually with the extension of the thermal decomposition time. Meanwhile, the content of CF_2O gas produced by the decomposition of $C_5F_{10}O/N_2/O_2$ gas mixture at 500°C and 550°C is significantly higher than that of $C_5F_{10}O/N_2$ gas mixture due to the sufficient oxygen content. The generation of these characteristic gases can be considered as an indication of different thermal decomposition temperatures, which can be employed to determine the severity of the equipment in the event of POF and provide a reference for online monitoring of POF based on decomposition components.

In summary, the oxygen in $C_5F_{10}O/N_2/O_2$ gas mixture will aggravate the decomposition of $C_5F_{10}O$ gas, which will increase the CF_2O concentration during thermal decomposition and decrease the temperature required for the occurrence of significant decomposition of $C_5F_{10}O$ gas.

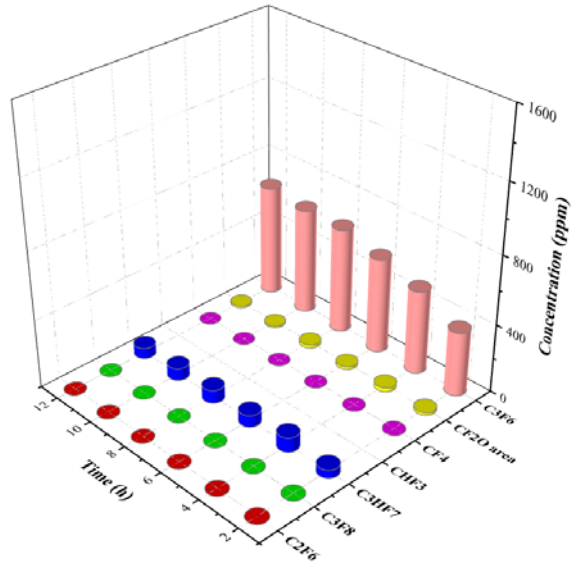

(a) 300℃

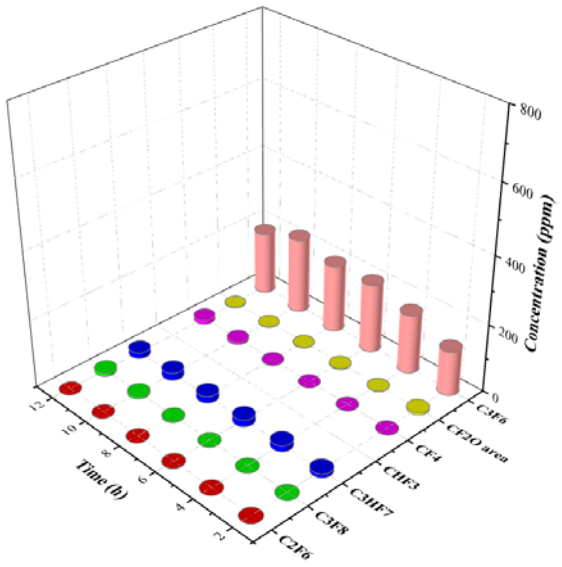

(b) 350℃

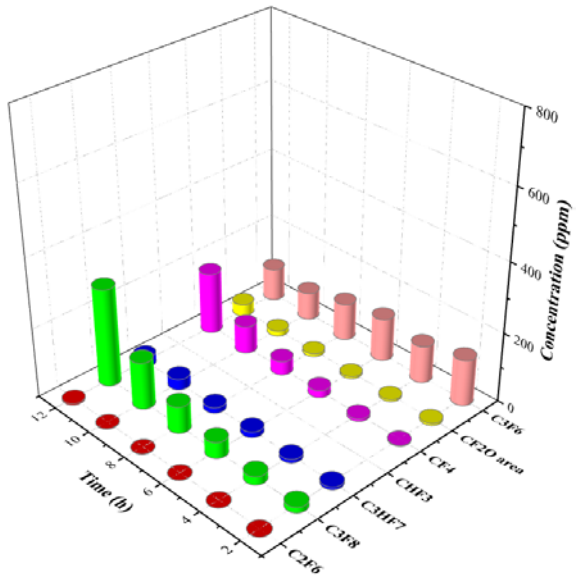

(c) 400℃

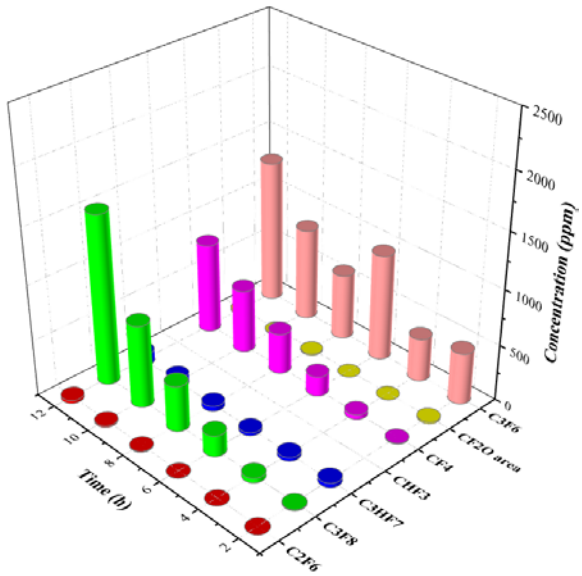

(d) 450℃

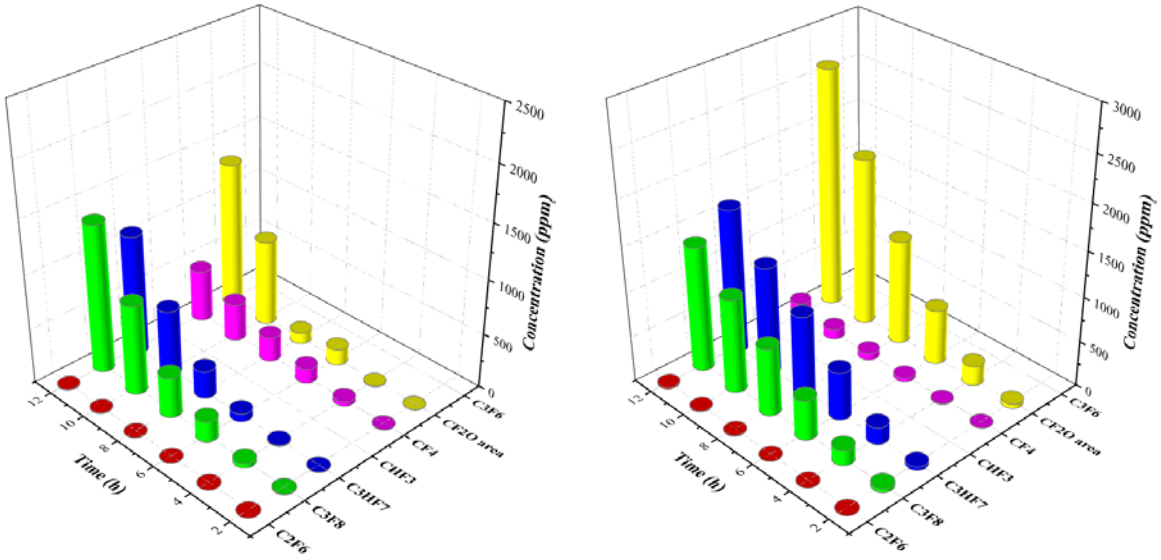

(e) 500℃ (f) 550℃

Figure 3.18 Effect of temperature on the thermal decomposition characteristics of $C_5F_{10}O/N_2/O_2$ gas mixture (the O_2 concentration is 20%)

3.3.3 Effect of Oxygen Concentration on the Thermal Decomposition Properties of $C_5F_{10}O/N_2/O_2$

In the study of the effect of temperature on the thermal decomposition characteristics of $C_5F_{10}O/N_2$ and $C_5F_{10}O/N_2/O_2$ gas mixtures, we find that oxygen promotes the decomposition of $C_5F_{10}O$ gas and reduces the thermal decomposition temperature of $C_5F_{10}O$ gas. To further clarify the effect of oxygen concentration on the thermal decomposition characteristics of $C_5F_{10}O/N_2/O_2$ gas mixture, the thermal decomposition characteristics of $C_5F_{10}O/N_2/O_2$ gas mixture with oxygen content of 0-20% are tested at the temperature of 550°C. Figure 3.19 shows the change of the content of decomposition products in CO_2, CHF_3, CF_2O, C_3HF_7, CF_4, C_2F_6 and C_3F_8 with the thermal decomposition time for $C_5F_{10}O/N_2/O_2$ gas mixture containing different oxygen concentrations at 550°C.

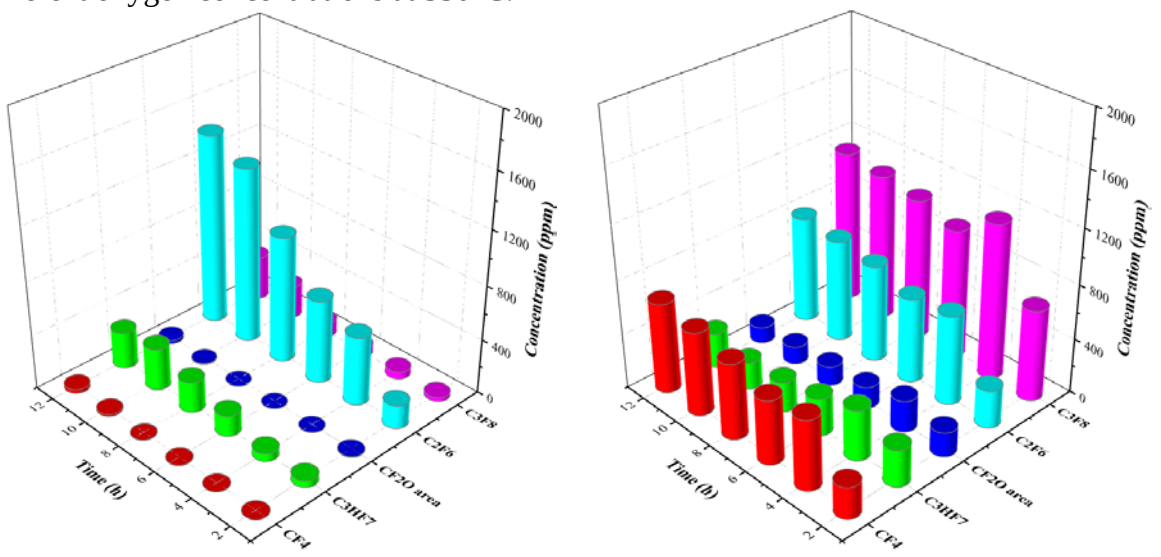

(a) $C_5F_{10}O/N_2$ gas mixture (b) $C_5F_{10}O/N_2/O_2$ gas mixture containing 4% O_2

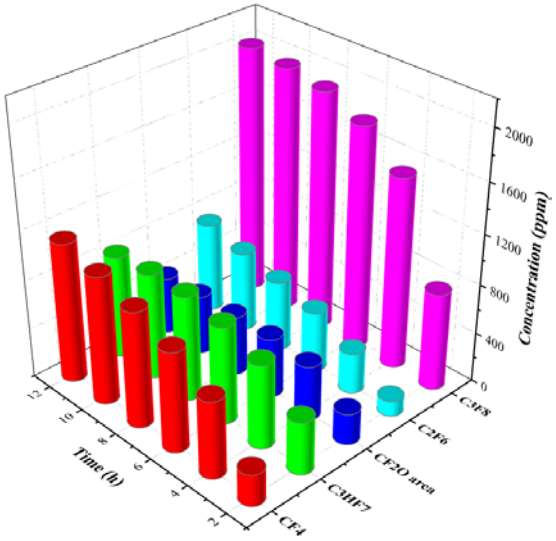

(c) $C_5F_{10}O/N_2/O_2$ gas mixture containing 8% O_2

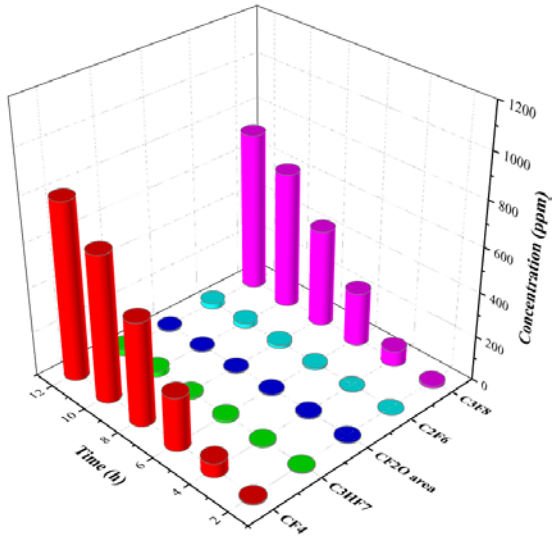

(d) $C_5F_{10}O/N_2/O_2$ gas mixture containing 12% O_2

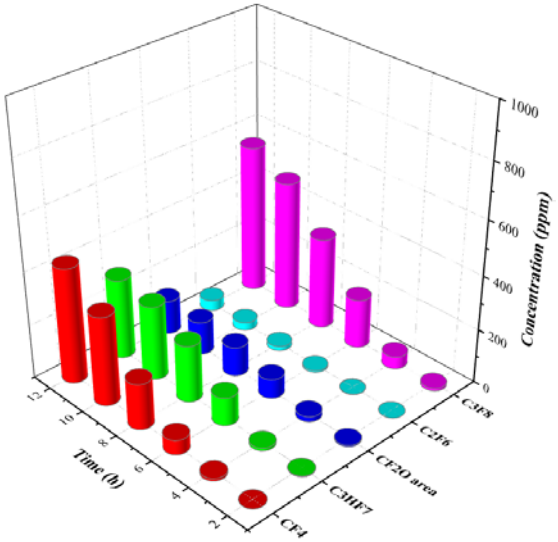

(e) $C_5F_{10}O/N_2/O_2$ gas mixture containing 16% O_2

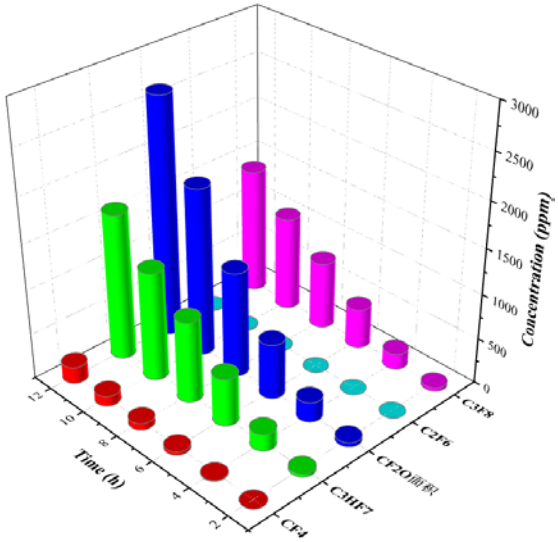

(f) $C_5F_{10}O/N_2/O_2$ gas mixture containing 20% O_2

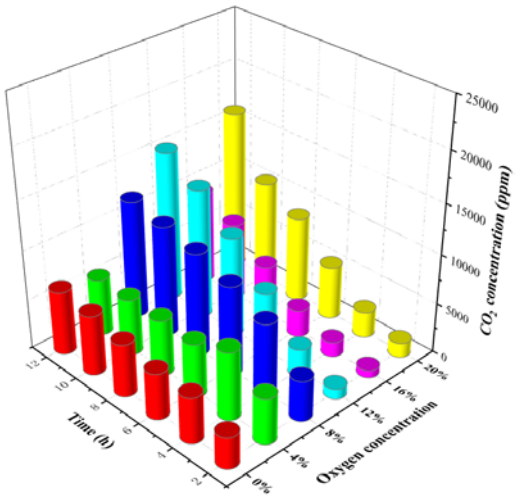

(g) CO_2 concentration from the decomposition of $C_5F_{10}O/N_2/O_2$ gas mixture

Figure 3.19 Effect of oxygen concentration on the thermal decomposition properties of $C_5F_{10}O/N_2/O_2$

The content of all four gas mixtures, CF_4, C_2F_6, C_3F_8 and CO_2, gradually increase with the prolongation of thermal decomposition time. CF_2O gas has a high dependence on oxygen content. When there is low oxygen content, the concentration of CF_2O gas is very low. The oxygen content in the experimental group is 4%, the concentration tends to decrease with the extension of thermal decomposition time. The concentration of CF_2O gas gradually enhances with the increase of thermal decomposition time in the test groups with 16% and 20% oxygen content. In particular, the concentration of CF_2O gas is very high in the 20% oxygen content test group.

In summary, at the temperature of 550°C, $C_5F_{10}O$ gas can decompose continuously to form CF_4, C_2F_6, C_3F_8 and CO_2, and the oxygen content only affects the production rate of these four decomposition products. Oxygen will promote the decomposition of $C_5F_{10}O$ to produce CO_2 gas and inhibit the formation of C_2F_6 gas. When the oxygen concentration in $C_5F_{10}O/N_2/O_2$ gas mixture is less than 8%, the thermal decomposition of $C_5F_{10}O$ will be promoted to produce more CF_4, C_3F_8 and CF_2O gas with the increase of oxygen concentration.

3.4 Similarities and Differences of Discharge and Thermal Decomposition Characteristics of $C_5F_{10}O/N_2/O_2$

In the test of the effect of PD on the decomposition characteristics of $C_5F_{10}O/N_2/O_2$ gas mixture, it is found that in terms of electrical parameters, SF_6 gas is more likely to produce PD than $C_5F_{10}O/N_2/O_2$ gas mixture under the same conditions. The oxygen content in $C_5F_{10}O/N_2/O_2$ gas mixture affects the discharge characteristics parameters such as intensity and frequency of PD, while it has no effect on its PDIV and breakdown voltage values under non-uniform electric field. When the oxygen content is not greater than 8%, with the increase of oxygen content, the total discharge magnitude, the total number of discharge pulses and the positive half of the discharge magnitude in 1 second gradually increase, the negative half of the discharge magnitude remains unchanged and the number of discharge pulses in the negative half cycle gradually decreases. When the oxygen content is 12%, the discharge magnitude generated by a single discharge pulse is the smallest, but its discharge frequency is the highest. As for the decomposition products, the decomposition products produced by PD of $C_5F_{10}O/N_2/O_2$ gas mixture are mainly CF_4, CO, CO_2, CF_2O, C_2F_6, C_3F_6, C_3F_8, C_4F_{10} and C_3HF_7. Since $C_5F_{10}O$ gas contains O element, the types of decomposition products produced by $C_5F_{10}O/N_2/O_2$ gas mixture make no change compared with $C_5F_{10}O/N_2$ gas mixture. With the increase of the PD time, the concentrations of the decomposition products gradually increase, with the exception of the CO gas concentration which remains unchanged. The concentrations of CF_4 and C_2F_6 gases produced by the decomposition of $C_5F_{10}O/N_2/O_2$ gas mixture at 0% and 4% oxygen concentration increase linearly with PD time, and this rule can be considered as the characteristic gas products for PD fault diagnosis of $C_5F_{10}O/N_2/O_2$ insulated equipment. Compared with $C_5F_{10}O/N_2$ gas mixture, $C_5F_{10}O/N_2/O_2$ gas mixture will decompose to produce more CO_2, CF_2O and C_3F_8 during the PD process, but the content of C_2F_6 and C_3HF_7 produced by the decomposition will be reduced.

In the test of the AC breakdown decomposition characteristics of $C_5F_{10}O/N_2/O_2$ gas mixture, it is found that $C_5F_{10}O/N_2$ gas mixture will produce black solids containing simple carbon substances, CuF_2 and CuO during the decomposition process, which will adhere to the electrode surface and distort the electric field in the space around the electrode, and the addition

of oxygen to $C_5F_{10}O/N_2$ gas mixture can inhibit the production of black solids. The dispersion of $C_5F_{10}O/N_2/O_2$ gas mixture will be slightly larger compared to the dispersion of $C_5F_{10}O/N_2$ gas mixture, but its AC breakdown voltage will be slightly increased, which is beneficial to improve its insulation strength. In terms of gas decomposition products, AC breakdown is consistent with the types of decomposition products produced by PD. With the increase of the number of discharges, the content of the six decomposition components, CO, CF_2O, CF_4, C_2F_4, C_2F_6 and C_3F_8, produced in all test groups shows an increasing trend. With the increase of oxygen concentration, the contents of CO, CF_2O and CF_4 produced by the decomposition of $C_5F_{10}O/N_2/O_2$ gas mixture gradually increase, while the contents of C_3F_8, C_3F_6 and C_2F_4 gradually decrease, with the most obvious reduction of C_2F_4.

Figure 3.20 shows the concentrations of CO, CF_4, C_2F_4, C_2F_6, C_3F_8 and C_3F_6 produced by comparing the 20 and 100 breakdowns of $C_5F_{10}O/N_2/O_2$ gas mixture. Compared with the results obtained at other concentrations, addition of 4% oxygen to $C_5F_{10}O/N_2$ gas mixture significantly inhibits the formation of C_2F_4, C_3F_8 and C_3F_6, and produces less decomposition products such as CO and CF_4. Moreover, the content of toxic decomposition products generated after insulation breakdown of $C_5F_{10}O/N_2/O_2$ gas mixture is relatively low. Addition of oxygen could slightly increase the breakdown voltage of $C_5F_{10}O/N_2$ gas mixture and eliminate the generation of black solids during the breakdown of $C_5F_{10}O/N_2$ gas mixture.

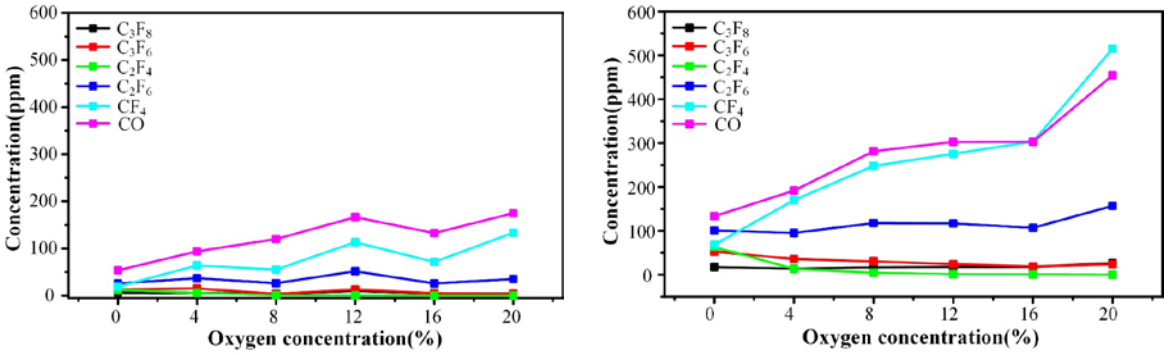

(a) Decomposition products of $C_5F_{10}O/N_2/O_2$ after 20 breakdowns

(b) Decomposition products of $C_5F_{10}O/N_2/O_2$ after 100 breakdowns

Figure 3.20 Effect of oxygen on $C_5F_{10}O/N_2/O_2$ gas mixture decomposition products

In the test of thermal decomposition characteristics of $C_5F_{10}O/N_2/O_2$ gas mixture, it is found that the decomposition of $C_5F_{10}O/N_2$ gas mixture starts at 300°C and produces primary decomposition products such as C_3F_6, CHF_3 and C3HF7, and a large number of decomposition products starts at the temperature above 450°C and produces decomposition products such as CF_2O, C_2F_6, C_3F_8 and CF_4 (the results are shown in Figure 3.21). CHF_3 is only produced when the temperature is 300°C, and C_3F_6 gas is only produced in the range of 300°C-450°C. At higher temperatures, the CHF_3 and C_3F_6 gases generated by the decomposition of $C_5F_{10}O/N_2$ gas mixture will participate in the decomposition reaction and transform into other decomposition products. $C_5F_{10}O/N_2/O_2$ gas mixture also starts to decompose at 300°C to produce primary decomposition products such as C_3F_6 and C_3HF_7, and starts to decompose in large quantities above 400°C. The difference is that $C_5F_{10}O/N_2/O_2$ gas mixture does not produce CHF_3 gas and the temperature required for its significant decomposition is lower than that of $C_5F_{10}O/N_2$ gas mixture. The content of all four gas mixtures, CF_4, C_2F_6, C_3F_8 and CO_2, produced by the decomposition of $C_5F_{10}O/N_2/O_2$ gas mixture gradually increase with the prolongation of the

thermal decomposition time. The concentrations of CF_4 and C_3F_8 gases produced by the thermal decomposition of $C_5F_{10}O/N_2/O_2$ gas mixture shows a trend of increasing and then decreasing with the enhancement of oxygen concentration under the same temperature condition, and the maximum value appears at 8% oxygen concentration, and the concentration of CF_2O gas also has a maximum value when the oxygen concentration is 8%. The concentration of CO_2 gas tends to increase gradually with the increase of oxygen concentration, while the concentration of C_2F_6 gas tends to decrease gradually.

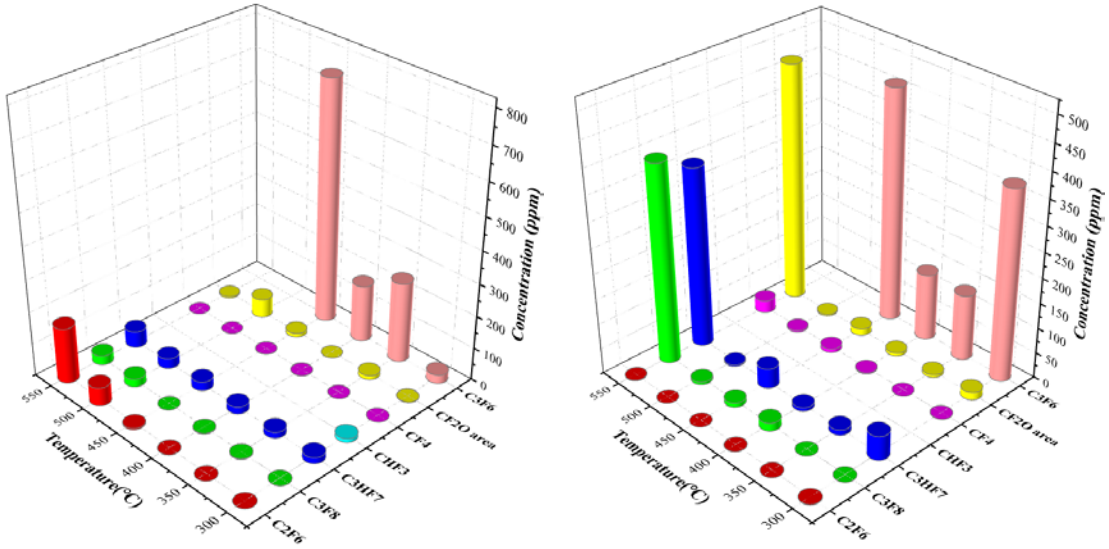

(a) Thermal decomposition products of $C_5F_{10}O/N_2$ gas mixture

(b) Thermal decomposition products of $C_5F_{10}O/N_2/O_2$ gas mixture

Figure 3.21 Decomposition products produced by $C_5F_{10}O/N_2$ and $C_5F_{10}O/N_2/O_2$ gas mixtures at different temperatures

In summary, there is no difference between the decomposition products of $C_5F_{10}O/N_2/O_2$ gas mixture when PD and AC breakdown fault occurs. When POF occurs, due to the low energy at the temperature of 300℃, $C_5F_{10}O/N_2/O_2$ gas mixture first produces primary decomposition products such as C_3F_6 and C_3HF_7. When the temperature rises above 400℃, it will produce decomposition products such as CF_2O, C_2F_6, C_3F_8 and CF_4. Because of the relatively high energy released by the discharge, the types of decomposition products produced by different discharge types do not show the changes in the types of decomposition products caused by the increase in temperature during thermal decomposition. The oxygen content affects the electrical parameters of both PD and AC breakdown characteristics of $C_5F_{10}O/N_2/O_2$ gas mixture. Although the cumulative discharge magnitude and discharge frequency of $C_5F_{10}O/N_2/O_2$ gas mixture per unit time are low when the oxygen content is 16%, the breakdown voltage dispersion of $C_5F_{10}O/N_2/O_2$ gas mixture is larger when AC breakdown occurs. And the content of decomposition products generated at the occurrence of discharge and thermal failure is also higher. Considering the above factors, it is recommended to add 4% oxygen to $C_5F_{10}O/N_2$ gas mixture to inhibit the generation of solid decomposition products during the discharge process. Although the addition of oxygen will promote the decomposition of $C_5F_{10}O/N_2$ gas mixture in the event of discharge and POF, the decomposition products of $C_5F_{10}O/N_2/O_2$ gas mixture containing 4% oxygen are less than those of the test group containing higher oxygen concentration, and the concentration of the decomposition products

is close to that of $C_5F_{10}O/N_2$ gas mixture without oxygen.

3.5 Chapter Summary

In this chapter, the decomposition characteristics of $C_5F_{10}O/N_2/O_2$ gas mixture at the occurrence of three typical discharge and thermal faults, such as AC breakdown, PD and POF, are studied through experiments. And the influence of oxygen concentration on the electrical properties and decomposition characteristics of $C_5F_{10}O/N_2/O_2$ gas mixture is investigated. The following conclusions are obtained based on the experimental results, which suggest the optimal concentration of oxygen addition.

1) Under the discharge condition of $C_5F_{10}O/N_2$ gas mixture, black solids containing simple carbon substances, CuF_2 and CuO will be produced and attached to the electrode surface to distort the electric field in the space around the electrode, and the addition of oxygen to $C_5F_{10}O/N_2$ gas mixture can inhibit the production of black solids. The addition of oxygen can appropriately increase AC breakdown voltage of $C_5F_{10}O/N_2$ gas mixture, which is beneficial to improve its insulation strength.

2) In the extremely non-uniform electric field, SF6 gas is more likely to produce PD than $C_5F_{10}O/N_2/O_2$ gas mixture, and the amplitude and frequency of PD produced by SF_6 gas are higher. The addition of oxygen to $C_5F_{10}O/N_2$ gas mixture affects the frequency and amplitude of PD, and has no significant effect on its PDIV.

3) The gas decomposition products of $C_5F_{10}O$ gas mixture are CO, CO_2, CF_2O, CF_4, C_2F_4, C_2F_6, C_3F_6, C_3F_8, C_4F_{10} and C_3HF_7. The addition of oxygen to the gas mixture will inhibit the production of C_2F_4, C_3F_8 and C_3F_6 and promote the formation of CO, CF_2O and CF_4 when AC breakdown occurs. The addition of 4% oxygen to $C_5F_{10}O/N_2$ gas mixture has a positive effect on inhibiting the decomposition of $C_5F_{10}O$ gas in the process of PD. In addition, the concentration of CF_4 and C_2F_6 gas generated by $C_5F_{10}O$ gas due to PD increases linearly with the PD time, which can also be considered as a sign in engineering applications indicating whether PD occurs in monitoring equipment.

4) Under the POF condition, $C_5F_{10}O/N_2$ gas mixture has higher decomposition temperature and better stability compared with $C_5F_{10}O/N_2/O_2$ gas mixture. Oxygen will promote the decomposition of $C_5F_{10}O$ to produce CO_2 gas and inhibit the production of C_2F_6 gas. When the oxygen concentration is less than 8%, the formation of CF_4, C_3F_8 and CF_2O gas will be promoted with the increase of the oxygen concentration. With the gradual increase of fault temperature from 300°C to 550°C, $C_5F_{10}O/N_2/O_2$ gas mixture first decomposes to produce primary decomposition products such as C_3F_6, CHF_3 and C_3HF_7, and then it will decompose to produce decomposition products such as CF_2O, C_2F_6, C_3F_8 and CF_4, and the different decomposition products can be considered as the characteristic sign products of over-thermal temperature.

5) Considering the decomposition characteristics of $C_5F_{10}O/N_2$ gas mixture in discharge and thermal decomposition tests and the influence of solid decomposition products in the discharge decomposition, it is recommended to add 4% oxygen to $C_5F_{10}O/N_2/O_2$ gas mixture, which can not only adjust its decomposition characteristics, but also inhibit the solid decomposition products produced by the gas mixture in the process of discharge decomposition.

4 Decomposition Mechanism of $C_5F_{10}O/N_2/O_2$ Gas Mixture

The adsorption of $C_5F_{10}O$ gas on the gas-solid interface of the material inside the equipment and the processes of collision ionization and thermal ionization caused by discharge and thermal faults will cause its chemical bonds to break and form free particles. The oxygen and micro-water in the gas mixture will also be decomposed to form active particles. The further reaction of each particle will restore to $C_5F_{10}O$ molecules or generate various decomposition products, resulting in changes in the composition of the mixtures. The research on the decomposition mechanism of $C_5F_{10}O$ gas mixture is helpful to clarify its decomposition characteristics and the correlation characteristics between decomposition products and external conditions.

In this chapter, the decomposition models of $C_5F_{10}O$, O_2, N_2 and H_2O molecules are constructed based on DFT and transition state theory. The microscopic parameters such as the structure, vibration frequency and energy of each particle during the decomposition of $C_5F_{10}O$ are obtained by calculation, and the thermodynamic parameters such as enthalpy and activation energy of the decomposition path of $C_5F_{10}O/N_2/O_2$ gas mixture and the composite path of decomposition products are solved, and the decomposition mechanism and product formation mechanism of $C_5F_{10}O$ gas mixture are studied. Finally, the decomposition mechanism of $C_5F_{10}O/N_2/O_2$ gas mixture is revealed by combining gas-solid interface decomposition test and discharge and thermal decomposition test.

4.1 Construction of $C_5F_{10}O$ Decomposition System

4.1.1 Density Functional Theory

The classical electronic structure theory methods (such as the Hartree-Fock (HF) method) are based on the wave function as the basic quantity to describe the system. When the classical electronic structure theory method deals with multi-electron systems, the energy and electronic structure of the multi-electron system can be obtained by solving the Schrödinger equation for any multi-electron system (ignoring the motion of the nucleus, as shown in Equation 4.1) [100]. The wave function of each electron needs 3 space variables for description, so the wave function variables are three times the number of electrons when dealing with multi-electron systems, which considerably increases the computational volume and difficulty.

$$\begin{aligned}\hat{H}\psi &= \left[\hat{T}+\hat{U}+\hat{V}\right]\psi \\ &= \left[\sum_i^N\left(-\frac{\hbar^2}{2m}\nabla_i^2\right)+\sum_i^N V(\vec{r}_i)+\sum_i^N U(\vec{r}_i,\vec{r}_j)\right]\psi \\ &= E\psi\end{aligned} \tag{4.1}$$

where, $\hat{H}$ is the Hamiltonian operator, $\hat{T}$ is the kinetic energy operator of the particles in the system, $\hat{U}$ is the interaction potential energy operator between electrons in the system, and $\hat{V}$ is the potential energy operator of the nuclear electric field.

Density functional theory (DFT) studies the ground state properties of multi-electron architectures through electron density. And there are only three variables in the electron density

function, which is very convenient in both theoretical and practical calculations. Thomas and Fermi proposes the Thomas-Fermi model (uniform electron gas model) to express the kinetic energy of electrons in terms of electron density, and the kinetic energy of multi-electron systems in the form of electron density functionals, and the interaction kinetic energy in the multi-electron system is described by using the uniform electron gas composed of the steady-state electron density without interaction [101, 102]. The Hohenberg-Kohn theorem puts forward the theory of non-uniform electron gas and lays the theoretical foundation for the development of density functional theory, which can be summarized as two fundamental theorems [103]:

1) The ground state electron density $\rho(\boldsymbol{r})$ of the multi-electron system in the external field V determines its ground state properties, and the ground state energy of the multi-electron system is the only functional of its electron density.

2) Assuming that the energy of the multi-electron system is the only functional of the electron density, under the condition of constant electron density, the minimum value of the ground state energy functional can be obtained by minimizing the energy of the multi-electron system.

Based on the above two fundamental theorems, the core problem of DFT is to solve the energy functional E. Kohn and Sham in 1965 proposed a solution to obtain information about the interaction system by solving a series of single-particle equations, called the Kohn-Sham (KS) equation, which is solved iteratively by the self-consistent field method. The KS equation is shown as follows:

$$\left\{-\frac{\hbar^2}{2m}\nabla^2 + V_{KS}[\rho(\vec{r})]\right\}\varphi_i(\vec{r}) = E[\rho(\vec{r})]\varphi_i(\vec{r}) \tag{4.2}$$

$$\rho(\vec{r}) = \sum_{i=1}^{N}\left|\varphi_i(\vec{r})\right|^2 \tag{4.3}$$

The second term of Equation 4.2 is the potential energy of the KS equation:

$$\begin{aligned} V_{KS}[\rho(\vec{r})] &= V(\vec{r}) + V_H[\rho(\vec{r})] + V_{xc}[\rho(\vec{r})] \\ &= V(\vec{r}) + \int d\vec{r}' \frac{\rho(\vec{r}')}{\left|\vec{r} - \vec{r}'\right|} + \frac{\delta E_{xc}[\rho(\vec{r})]}{\delta\rho(\vec{r})} \end{aligned} \tag{4.4}$$

where, $V(\boldsymbol{r})$ is the Coulomb potential generated by the atom, V_H is the Coulomb interaction between electrons, and V_{xc} is the exchange correlation potential, which is the first derivative of the exchange correlation energy.

In the actual solution process, the density functional form of the exchange correlation potential V_{xc} is unknown, and an approximate method needs to be employed to solve it. Local Density Approximation (LDA) and Generalized Gradient Approximation (GGA) are the most frequently used methods to calculate V_{xc}. GGA introduces the first-order gradient of electron density on the basis of LDA to describe the change of electron cloud, and GGA can calculate the energy of the system with fast electron density variation more accurately [104]. The GGA-Perdew-Berke-Ernzerhof (PBE) functional has been widely used in the calculation of solid interface properties.

4.1.2 Time-dependent Density Functional Theory

In 1984, Runge and Gross proved that the time-dependent electron density can determine the physical quantity of the system singly, and extended the ground state DFT calculation to the system whose physical properties change with time, namely, the time-dependent density

functional theory (TDDFT) [105, 106], TDDFT can be employed to calculate the energies of excited states. Similar to DFT, a series of one-electron time-dependent Kohn-Sham (TDKS) equations can be obtained from the time-dependent Schrodinger equation in TDDFT as follows:

$$i\hbar\frac{\partial}{\partial t}\varphi_i(\vec{r},t) = H_S(\vec{r},t)\varphi_i(\vec{r},t) \tag{4.5}$$

$$\rho(\vec{r},t) = \sum_{i=1}^{N}\left|\varphi_i(\vec{r},t)\right|^2 \tag{4.6}$$

The form of the Hamiltonian quantity $H_S(\vec{r},t)$ is similar to Equation 4.2:

$$\begin{aligned} H_S(\vec{r},t) &= -\frac{\hbar^2}{2m}\nabla^2 + V_{KS}[\rho(\vec{r},t)] \\ &= -\frac{\hbar^2}{2m}\nabla^2 + V(\vec{r},t) + V_H[\rho(\vec{r},t)] + V_{xc}[\rho(\vec{r},t)] \end{aligned} \tag{4.7}$$

The TDKS equation can be solved by the linear response mechanism or the real-time evolution of the TDKS equation. The properties of the linear response system can be obtained by Fourier transforming from the time domain space to the frequency domain space to obtain the frequency information such as the optical absorption spectrum and the strength of electric dipole oscillations of the molecule. The excited state properties such as the polarization intensity, the position of the optical absorption peak and the forbidden band width of the molecule can be better described. This method is only suitable for weak external fields, and the nonlinear effects in strong fields need to be solved by using the real-time evolution method of the TDKS equation [107, 108].

4.1.3 Transition State Theory

The transition state theory holds that a chemical reaction is composed of multiple elementary reactions, and in each primitive reaction, instead of direct conversion of reactants to intermediate products, the reactants first absorb energy to form an unstable transition state structure between reactants and products, as shown in Figure 4.1. The vibrational frequency of the transition state has one and only one imaginary frequency, and the vibrational tendency of the imaginary frequency vibrates between the reactant and the product. The energy of the transition state is higher than that of the reactants and products, and the energy absorbed from the reactants to the transition state is called the activation energy ΔE^* of the elementary reaction. Transition state theory has been widely used in the calculation of transition state structures and chemical reaction mechanisms of elementary reactions.

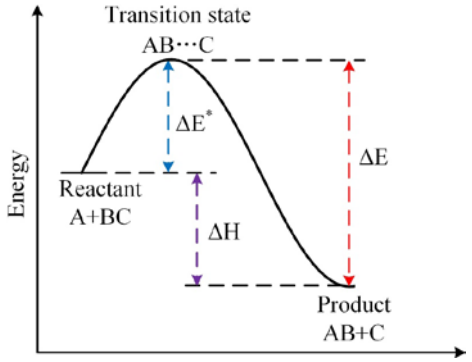

Figure 4.1 Schematic diagram of transition state reaction

Transition states can be calculated with application of the synchronous transfer method and the perturbation method. Synchronous transfer method is used to search for transition states by inserting a reaction path between reactants and products, and is classified as Linear Synchronous Transit (LST) [109] and Quadratic Synchronous Transit (QST) [110]. The LST method constructs the reaction path by interpolating between the reactant and product atoms, and the ideal structure set of the transition state can be obtained as follows:

$$r_{ab}(i) = (1-f)r_{ab}^{R} + fr_{ab}^{P} \tag{4.8}$$

where, f is the interpolation parameter, r_{ab}^{R} and r_{ab}^{P} are the internuclear distances between reactants and products determined by the least square method.

The minimum value of the objective function is solved by adjusting an initial set of linearly interpolated Cartesian coordinates obtained from the coordinates of the reactants and products at the maximum coincidence:

$$S = \sum_{a>b}^{N} \frac{[r_{ab}(c) - r_{ab}(i)]^2}{[r_{ab}(i)]^4} + 10^{-6} \sum_{\omega=x,y,z} \sum_{a}^{N} [\omega_a(c) - \omega_a(i)]^2 \tag{4.9}$$

where, (c) and (i) represent the computational and interpolated quantities measured in atomic units, respectively.

The QST method requires interpolation between three points, and a third intermediate point in addition to the reactants and generators. In the calculation the QST method starts the transition state search from the intermediate point, thus avoiding the situation that the transition state structure in some of the calculations is the same as the reactants and products. The LST and QST can be used together in the calculation, and the transition state structure obtained from the LST calculation is used as the intermediate point needed in the QST calculation to obtain a more accurate transition state structure.

4.1.4 Molecular Structural Properties of $C_5F_{10}O$, N_2 and O_2

1 Molecular Structure Characteristics of $C_5F_{10}O$

$C_5F_{10}O$, a new insulating gas that has only been widely noticed in recent years, has a molecular structure that varies in the relevant literature due to the existence of numerous isomers of the $C_5F_{10}O$ molecule. The main difference in molecular configuration is in the dihedral angle O-C2-C3-F1 in the $C_5F_{10}O$ molecule shown in Figure 4.2, where the O and F1 atoms are located on the same side or on the opposite side of the C2-C3 axis, which is mainly caused by the rotation of functional groups inside the $C_5F_{10}O$ molecule. When the molecule is subjected to disturbing factors such as collision, it may produce partial group rotation to form an unstable structure. In order to accurately determine the configuration of the $C_5F_{10}O$ molecule, the stable structure with the lowest energy is determined by scanning the energy change of the $C_5F_{10}O$ molecule during the 360° rotation of the dihedral angle. Figure 4.3 shows the energy change surface during the rotation of C_3F_7- and CF_3- groups around the dihedral angle O-C2-C3-F1. It could be found that the energy of $C_5F_{10}O$ molecule changes 3 periods during the 360° rotation of the CF_3- group around the dihedral angle O-C2-C3-F1, and the change period is 120°. This is because the CF_3- has 3 identical C-F bonds, the structure is rotationally symmetric at 120°. The energy of the $C_5F_{10}O$ molecule changes by 1 cycle during the 360° rotation of the C_3F_7- group around the dihedral angle O-C2-C3-F1. The energy change of the $C_5F_{10}O$ molecule during the rotation process is symmetrical with the O and F1 atoms located on the same side

of the C2-C3 axis as the symmetry axis, and the $C_5F_{10}O$ molecular energy surface appears as a minimal value at that point. There are also multiple minimal value points on the energy surface of $C_5F_{10}O$ molecule. In the process of constructing the structure of $C_5F_{10}O$ molecule if the initial angle of the internal group is not reasonable, it will converge to a minimal value point during the optimization of the structure and get a wrong structure, which is the reason why different $C_5F_{10}O$ molecular structures appear in the literature. The structure corresponding to the minimum value of the $C_5F_{10}O$ molecular energy surface is when the O and F1 atoms are located on opposite sides of the C2-C3 axis, as shown in Figure 4.2.

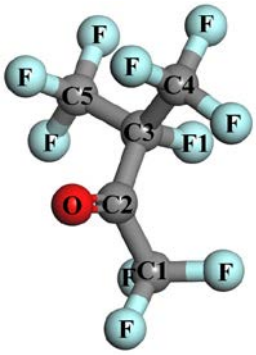

Figure 4.2 The calculation model of the $C_5F_{10}O$ molecule

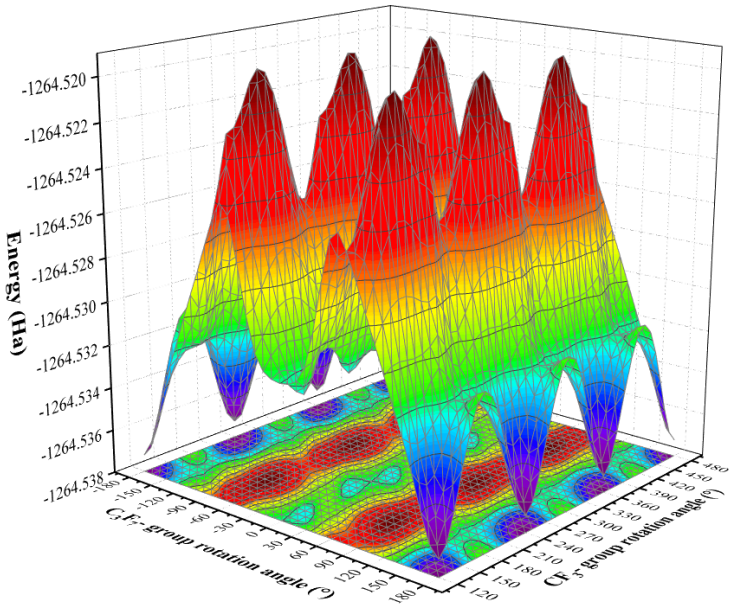

Figure 4.3 Potential energy surface during rotation of C_3F_7- and CF_3- groups in the $C_5F_{10}O$ molecule

Figure 4.4 shows the bond length and bond angle parameters of the $C_5F_{10}O$ molecule after relaxation based on the Triple Numeric with Polarization (TNP)-B3LYP method. The carbon atom sp2 on the carbonyl group of $C_5F_{10}O$ molecule is hybridized and then bonded to the sp3 hybridized CF_3- and C_3F_7-groups to form $C_5F_{10}O$ molecule, which is of a certain symmetric structure. Among them, the carbonyl C=O double bond has the shortest bond length of 1.190 Å. The CF bond length in the CF_3- group is between 1.331-1.344 Å, and the C-F bond on the central carbon atom of the C_3F_7- group is 1.372 Å. The bond length of C-C bond is longer than that of C-F bond and C=O double bond, and the bond length of C-C bond is between 1.560-1.565 Å. The bond length of two C-C bonds in C_3F_7-group is shorter, and the bond length is about 1.560 Å. The bond length of the C-C bond attached to the carbonyl carbon atom is around

1.565 Å.

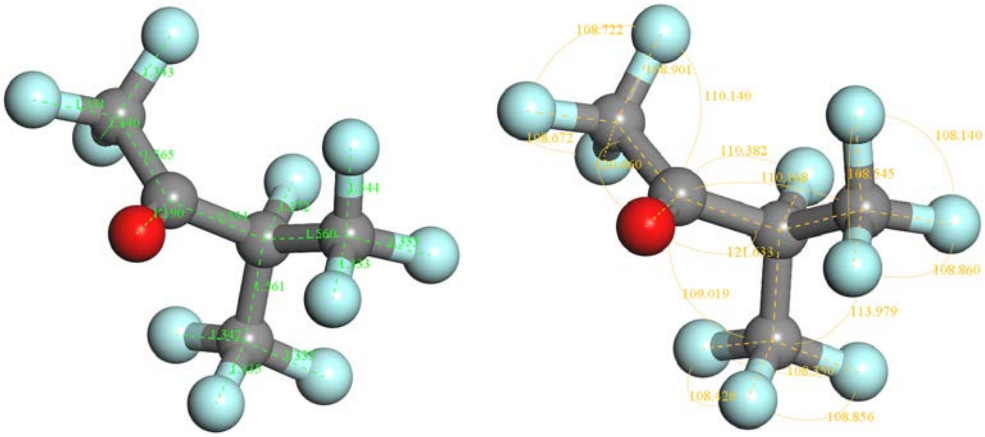

(a) Bond length of the $C_5F_{10}O$ molecule (b) Bond angle of the $C_5F_{10}O$ molecule

Figure 4.4 Bond lengths and bond angles of $C_5F_{10}O$ molecules

To further evaluate the strength of each chemical bond in the $C_5F_{10}O$ molecule, the Mayer bond orders (MBO) [111] of each chemical bond in the $C_5F_{10}O$ molecule is calculated by DFT, and the results are shown in Figure 4.5. The highest MBO value (1.9993) for the carbonyl C=O double bond in the $C_5F_{10}O$ molecule indicates that the C=O double bond is the strongest. The MBO value for the C-F bond in the CF_3-group is between 0.9589 and 1.0326, which is higher than that of the C-F bond on the central carbon atom of the C_3F_7-group (0.9527). The MBO values of the C-C bonds in the CF_3- and C_3F_7-groups attached to the carbonyl carbon atom are respectively 0.7362 and 0.7527, which are lower than the MBO value of the C-C bond in the C_3F_7-group. The C-C bond formed by the CF_3- group and the carbonyl carbon atom has the smallest MBO value, followed by the C-C bond formed by the C_3F_7- group and the carbonyl carbon atom, indicating that the C-C bond formed by the carbon atom attached to the carbonyl carbon atom at the α-position has the lowest strength and the chemical bond is most likely to be broken and dissociated into ionic fragments under the conditions of electron collision and high temperature.

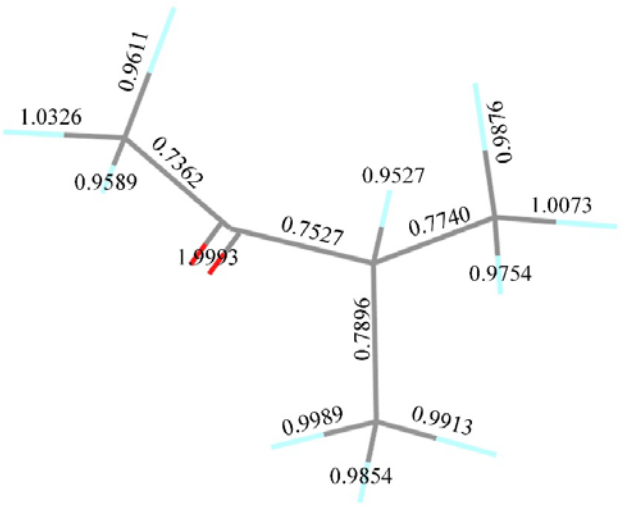

Figure 4.5 MBO values of $C_5F_{10}O$ molecule

The energy band gap of $C_5F_{10}O$ molecule can be calculated using the TDDFT method [112, 113], and the obtained energy levels of $C_5F_{10}O$ molecule and the wave function distribution of

frontline molecular orbitals of $C_5F_{10}O$ are shown in Figure 4.6. The energy of Lowest Unoccupied Molecular Orbital (LUMO) of $C_5F_{10}O$ molecule is mainly distributed on the carbonyl group and its two connected α-position carbon atoms, the LUMO has the ability to accommodate electrons, and the region where the wave function of LUMO is concentrated has stronger electron affinity. The energy of Highest Occupied Molecular Orbital (HOMO) of $C_5F_{10}O$ molecule is mainly distributed on the carbonyl and fluorine atoms, and the outer valence electrons of the molecule are inside the HOMO. Considering that the nucleus has a weak binding ability to the electrons in the HOMO and the HOMO is easy to lose electrons in strong electric field, the carbonyl and fluorine atoms in $C_5F_{10}O$ molecule are ionization sites. The HOMO energy of $C_5F_{10}O$ molecule is -7.722 eV, the LUMO energy is -4.120 eV, and the energy band gap is 3.642 eV, indicating that at least 3.642 eV energy is required to make the $C_5F_{10}O$ molecule in the ground state transition to the excited state.

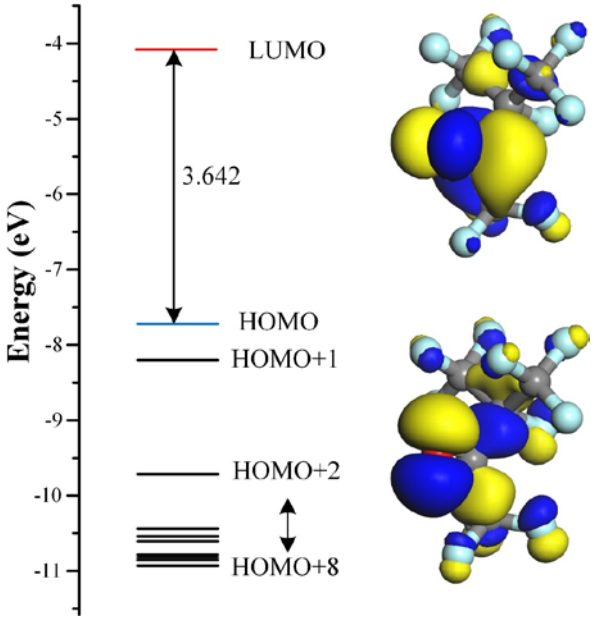

Figure 4.6 The triplet state energy level diagram and band gap (eV) of $C_5F_{10}O$ molecule

In summary, the C-C bond between the carbonyl group and the α-position carbon atom in $C_5F_{10}O$ molecule is the weakest, and the chemical bond is easily broken on both sides of the carbonyl group under the conditions of electron collision and high temperature. The electrophilic region of $C_5F_{10}O$ molecule is also concentrated in this region, while the ionization sites are mainly distributed on the carbonyl and fluorine atoms.

2 Ionization Parameters of $C_5F_{10}O$, N_2 and O_2 Molecules

In order to study the ionization parameters of $C_5F_{10}O/N_2/O_2$ gas mixture in electric field, the ionization parameters of $C_5F_{10}O$, N_2 and O_2 molecules, including ionization energy (IE) and electron affinity (EA), are calculated based on DFT. The vertical ionization parameter of the molecule represents the minimum energy required for the molecule in the ground state to form ions, ie *IE(V)=E(optimized positive anion)-E(optimized neutral) or EA(V)=E(optimized negative anion)-E(optimized neutral)*. The adiabatic ionization parameter of the molecule represents the energy required to form positive and negative ions of the molecular structure that satisfies the principle of minimum energy, ie, *IE(A)=E(positive anion at optimized neutral geometry)-E(optimized neutral)* or *EA(A)=E(negative anion at optimized neutral geometry)-E(optimized neutral)*. All energies are corrected with zero-point vibrational energy (ZPVE) at

298.15K. The ionization parameters of $C_5F_{10}O$, N_2 and O_2 molecules are shown in Table 4.1.

Table 4.1 Ionization parameters of molecules in $C_5F_{10}O$ gas mixture

Gas	*IE(V)* (eV)	*IE(A)* (eV)	*EA(V)* (eV)	*EA(A)* (eV)
$C_5F_{10}O$	10.52	10.95	-1.51	-0.81
N_2	15.32	15.34	2.20	2.75
O_2	12.12	12.49	-0.17	0.41

From the results in Table 4.1, it can be seen that among the three gas molecules, $C_5F_{10}O$, N_2 and O_2, the adiabatic ionization energies of $C_5F_{10}O$ and O_2 are 10.95 eV and 12.49 eV, respectively, while the adiabatic ionization energy of N_2 is the highest at 15.34 eV, indicating that N_2 is the most difficult to be ionized to form positive ions among the three gas molecules. The adiabatic ionization energy values of all three gas molecules are large, and all of them are not easily ionized in the electric field to form positive ions. While the adiabatic electron affinity energy of all three gas molecules, $C_5F_{10}O$, N_2 and O_2, are small.

The vertical ionization energies of the three gas molecules, $C_5F_{10}O$, N_2 and O_2, are 10.52 eV, 15.32 eV and 12.12 eV, respectively. All three gas molecules are difficult to form positive ions. However, the vertical electron affinity energies of the three gas molecules, $C_5F_{10}O$, N_2 and O_2, are very low. The electron affinity energies of $C_5F_{10}O$ and O_2 are both negative, the electron affinity energy of $C_5F_{10}O$ is -1.51 eV, indicating that the $C_5F_{10}O$ molecule has a strong ability to adsorb free electrons. Figure 4.7 shows the charge distribution after the formation of positive and negative ions for each of the three gas molecules, and it can be seen that the charge of positive and negative ions formed by $C_5F_{10}O$ molecules is mainly distributed on the O and F atoms. When O_2 molecules form negative ions, the charges on the O_2^- ions are evenly distributed on both ends of the two atoms. N_2 and O_2, as nonpolar molecules, have overlapping positive and negative charge centers, and therefore, the charge distribution of positive and negative ions formed by these two molecules also has symmetry.

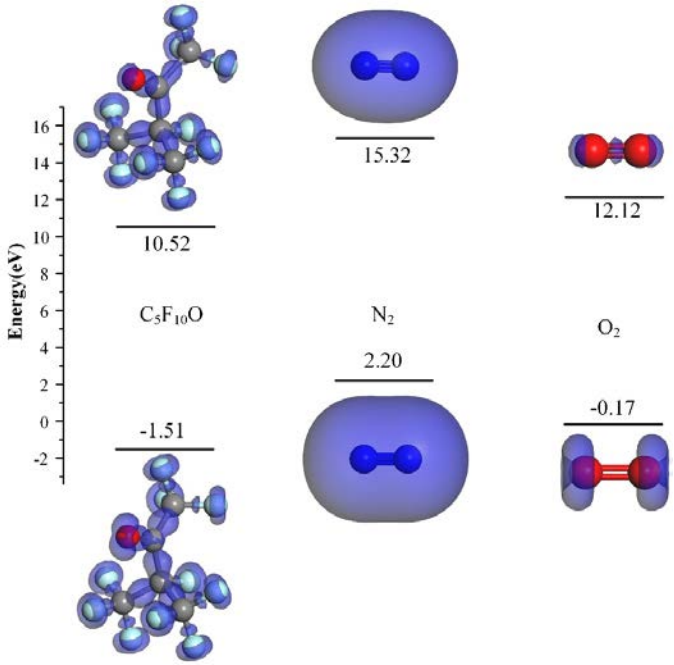

Figure 4.7 The charge distributions of the positive and negative ions of $C_5F_{10}O$, N_2 and O_2 molecules

The bond lengths of $C_5F_{10}O$, N_2 and O_2 and their positive and negative ions are shown in

Table 4.2 and Figure 4.8. Due to the repulsive effect of the same charge, the length of the chemical bond after the three gas molecules form positive and negative ions also changes. The C=O bond, N≡N bond and O=O bond in the negative ions formed by the three gas molecules of $C_5F_{10}O$, N_2 and O_2 are all elongated by about 0.1 Å. The bond energy decreases after the chemical bonds are elongated, resulting in higher chemical reactivity.

Table 4.2 The bond lengths of N_2 and O_2 molecules and ions

Gas	Bond length of neutral molecule(Å)	Bond length of negative ions (Å)	Bond length of positive ion(Å)
N_2	1.104	1.202	1.113
O_2	1.224	1.373	1.124

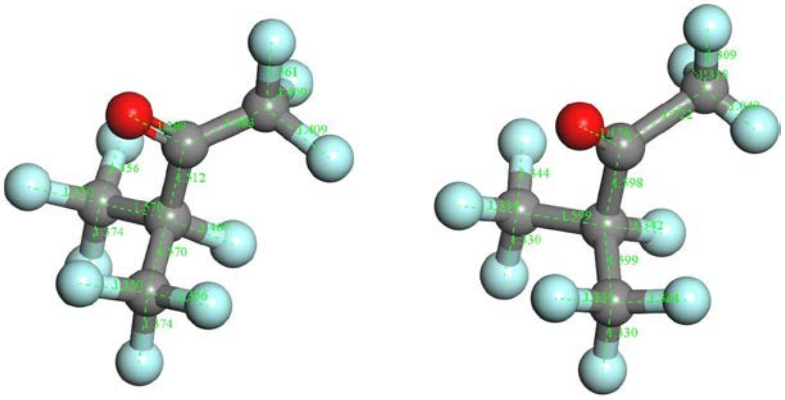

(a) Bond length of $C_5F_{10}O$ negative ion

(b) Bond length of $C_5F_{10}O$ positive ion

Figure 4.8 Bond length of $C_5F_{10}O$ ion

The bond length of the carbonyl C=O double bond in the negative ion formed by the $C_5F_{10}O$ molecule is elongated to 1.289 Å, the C-α1C bond is shortened to 1.483 Å, and the C-α2C bond is shortened to 1.512 Å. The bond lengths of other bonds change very little. However, the bond length of the positive ionic carbonyl C=O double bond formed by the $_C5F_{10}O$ molecule is shortened to 1.176 Å, the bond length of the C-α1C bond is elongated to 1.722 Å, and the bond length of the C-α2C bond is elongated to 1.598 Å.

The above study shows that $C_5F_{10}O$ is a strongly electronegative gas, and its molecular structure contains O atoms and a large number of F atoms, which are very easy to adsorb free electrons to form negative ions in the plasma region generated by strong electric field. This process greatly reduces the probability of collisional ionization of free electrons, which gives $C_5F_{10}O$ molecules high insulating properties. The electron affinity energy of O_2 molecule is -0.17 eV, indicating that the formation of negative ions from O_2 molecules is also an exothermic process, and it is also easy to form negative ions. While the electron affinity energy of N_2 molecule is 2.20 eV, it is more difficult for N_2 molecule to form negative ions.

4.2 Mechanism of Gas-solid Interface Interaction Between $C_5F_{10}O$ and Copper

4.2.1 Interaction Model

The atoms on the solid surface will be packed with unsaturated bonds, so the presence of

some dangling bonds causes the chemical properties of the solid surface to be more active than the internal atoms. When the gas is in contact with the solid surface for a long time, adsorption will occur on the surface. The adsorption of gases on solid surfaces can be divided into physical adsorption and chemical adsorption. Physical adsorption is mainly caused by van der Waals forces, which are generated by electrostatic interactions between molecules or atoms. Physical adsorption is ubiquitous at the gas-solid interaction interface. Due to the small activation energy, both adsorption and desorption are relatively easy, and it is generally a reversible process. Adsorption due to the formation of chemical bonds between molecules is called chemisorption. Chemisorption is selective and has a large activation energy. Both adsorption and desorption are difficult, and higher reaction temperatures are often required. The actual adsorption model may have both physisorption and chemisorption. Therefore, by calculating whether the adsorption of $C_5F_{10}O$ gas on the gas-solid interface on the surface of the copper material is physical adsorption or chemical adsorption, people can judge whether the $C_5F_{10}O$ gas has chemically reacted with the copper material so as to obtain the stability of the gas-solid interaction.

In order to explore the gas-solid interface interaction mechanism between $C_5F_{10}O$ and copper materials, this manuscript uses the DMol3 module of Materials Studio to construct a gas-solid interface interaction model for copper materials based on density functional theory [114, 115]. The most stable surface structure of face-centered cubic metal crystal materials is (1 1 1) surface. Therefore, this chapter constructs the Cu(1 1 1) metal interface system to study the interaction between $C_5F_{10}O$ and copper. The structure of the Cu(1 1 1) surface and the active adsorption sites are shown in Figure 4.9a. The Cu(1 1 1) surface mainly contains four active sites: Top site (point a), Hexagonal-close-packed (Hcp) site (point b), Face-centered cubic (Fcc) site (point c) and Bridge site (point d).

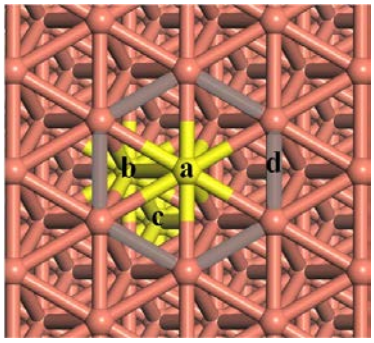

Figure 4.9 Cu(1 1 1) surface structure

In all calculations in this chapter, the $C_5F_{10}O$ molecules and the outer atoms of the metal material are allowed to relax, while the fractional coordinates of the bottommost atoms of the metal material are fixed. According to the structural characteristics of the $C_5F_{10}O$ molecule and the Cu(1 1 1) surface, 13 initial structures of the interaction between the $C_5F_{10}O$ molecule and the Cu(1 1 1) surface are constructed, as shown in Figure 4.10. The thickness of the vacuum layer above the periodic system is set to 20 Å. In the process of calculation, the DNP basis set is selected to expand the wave function, and the GGA-PBE method is used to process the exchange correlation functional. An all-electron model is used to deal with electrons inside atoms, and DFT-based relativistic semi-core pseudopotential (DSPP) are employed to describe electron-ion interactions on gas-solid surfaces, and Grimme methods are adopted to describe

weak interactions such as van der Waals forces. The convergence parameters of geometric optimization are: Energy change convergence accuracy 1.0×10-5Ha, SCF tolerance 1.0×10^{-6}, maximum force 0.002Ha/Å, and maximum displacement 0.005Å.

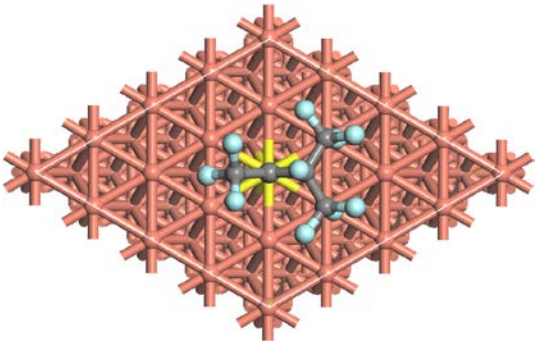

(a) O-Top

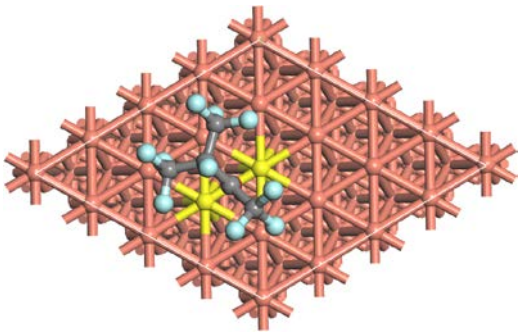

(b) O-Bridge

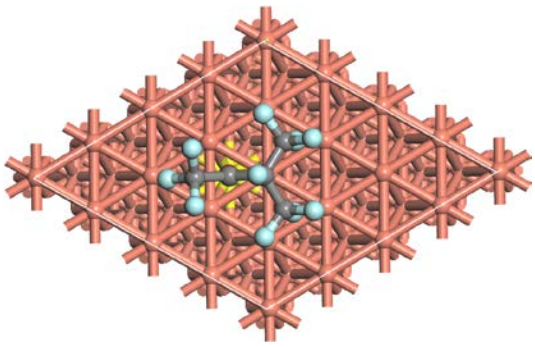

(c) O-Hcp

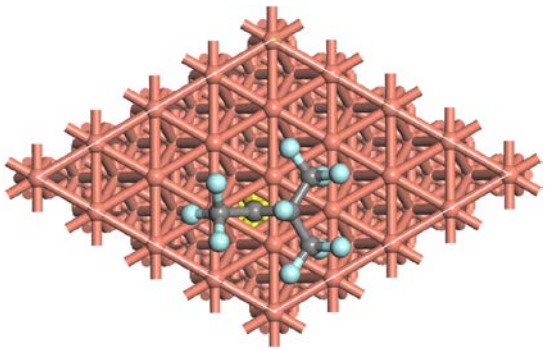

(d) O-Fcc

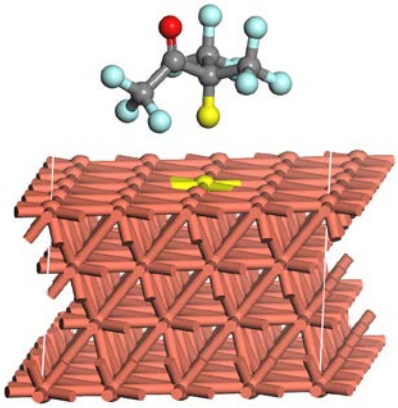

(e) α1-F-Top

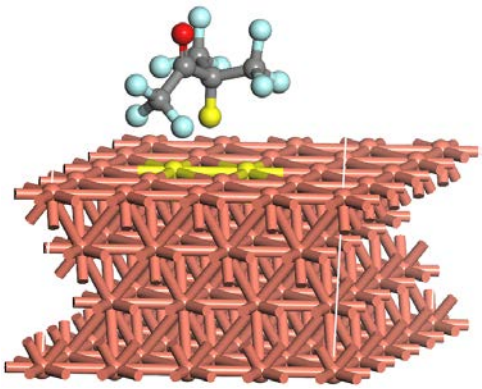

(f) α1-F-Bridge

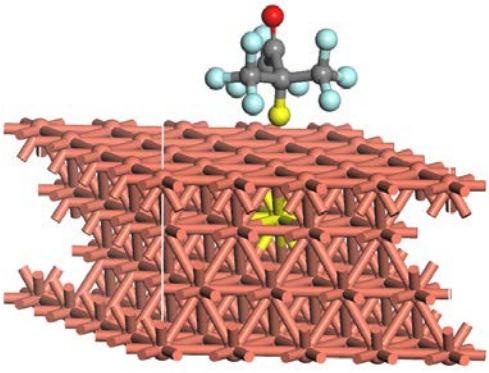

(g) α1-F-Hcp

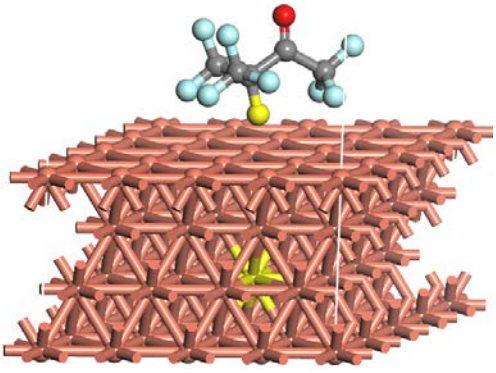

(h) α1-F-Fcc

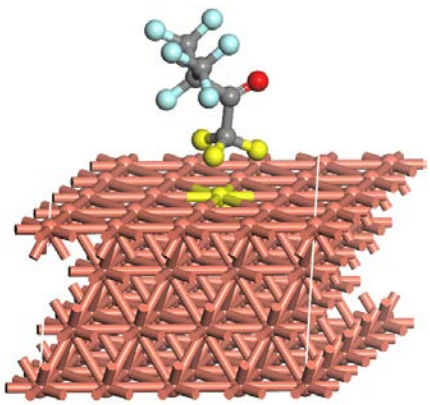

(i) α2-F3-Top

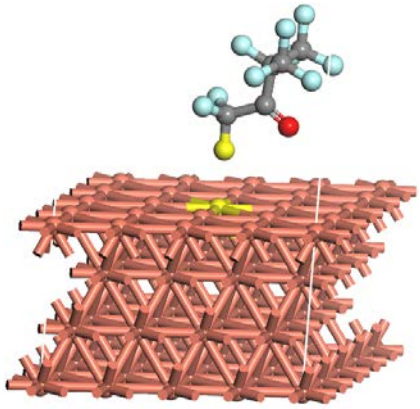

(j) α2-F-Top

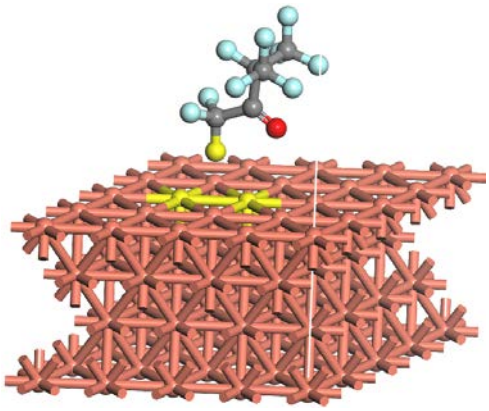

(k) α2-F-Bridge

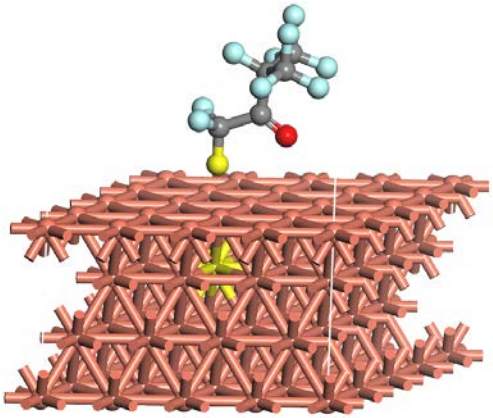

(l) α2-F-Hcp

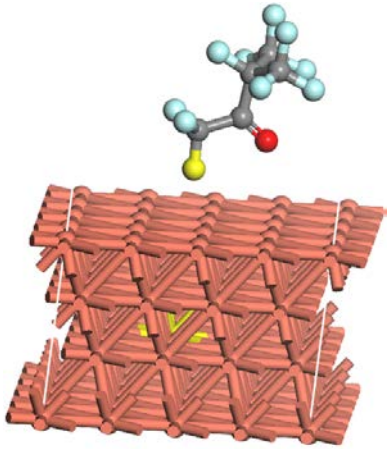

(m) α2-F-Fcc

Figure 4.10 Initial adsorption structure of $C_5F_{10}O$ on Cu(1 1 1) surface

In this manuscript, the interaction mechanism of gas-solid interface between $C_5F_{10}O$ and metal materials copper, aluminum and silver is mainly studied from the two dimensions of adsorption energy and microstructure. The calculations are focused on the parameters of adsorption energy, charge transfer, electronic density of states distribution and differential charge density distribution for gas-solid interaction.

(1) Adsorption energy (Ea)

The adsorption energy is used to describe the energy change of the $C_5F_{10}O$ molecule-metal

surface interaction system before and after the interaction. The adsorption energy can reflect the strength of the interaction of $C_5F_{10}O$ molecules at the metal gas-solid interface, which is defined as follows:

$$E_a = E_{gas\_metal} - \left(E_{gas} + E_{metal}\right) \tag{4.10}$$

where, E_a is the adsorption energy of $C_5F_{10}O$ molecules on the metal surface. E_{gas_metal} is the total energy of the system after the $C_5F_{10}O$ molecule interacts with the metal surface. E_{gas} is the steady-state energy of the $C_5F_{10}O$ gas structure after optimization. E_{metal} is the steady-state energy of the metal surface structure after optimization.

(2) Charge transfer(q_t)

Charge transfer is used to describe the charge change of the $C_5F_{10}O$ molecule-metal surface interaction system before and after the interaction, and it is defined as follows:

$$q_t = q_{gas\_metal} - q_{gas} \tag{4.11}$$

where, q_t is the charge transferred during the interaction between the $C_5F_{10}O$ molecule and the metal surface. q_{gas_metal} is the total charge carried by the $C_5F_{10}O$ molecule after the interaction between the $C_5F_{10}O$ molecule and the metal surface. q_{gas} is the total charge carried by the $C_5F_{10}O$ molecule before it interacts with the metal surface.

(3) Density of electronic states

The density of electronic states is used to indicate the number of electronic states per unit energy interval in the case of a quasi-continuous distribution of electron energy levels. The density of electronic states is closely related to the energy band structure and can be considered as a visualization result of the energy band structure.

(4) Difference charge density ($\Delta\rho_q$)

The difference charge density is used to describe the difference in charge density between the $C_5F_{10}O$ molecule and the metal surface interaction system before and after bonding, and can be employed to reflect the transfer and distribution of charges during the formation of chemical bonds. It is defined as follows:

$$\Delta\rho_q = \rho_{gas\_metal} - \rho_{gas} - \rho_{metal} \tag{4.12}$$

where, $\Delta\rho_q$ is the difference charge density of $C_5F_{10}O$ molecules after interaction with the metal surface. ρ_{gas_metal} is the charge density distribution of $C_5F_{10}O$ molecules after interaction with the metal surface. ρ_{gas} is the charge density distribution of the $C_5F_{10}O$ molecule. ρ_{metal} is the charge density distribution of the metal crystal.

4.2.2 Adsorption Energy and Charge Transfer

Table 4.3 lists the adsorption energies and charge transfer of the previously constructed $C_5F_{10}O$ molecules on the Cu(1 1 1) surface after relaxation of the 13 adsorbed initial structures. The adsorption energies of $C_5F_{10}O$ molecules interacting with the four initial structures, O-Top, O-Bridge, α2-F-Top and α2-F-Fcc, on the Cu(1 1 1) surface are -0.762 eV, -0.770 eV, -0.750 eV and -0.782 eV, respectively, which are higher than the other initial adsorption structure models. In terms of charge transfer, the adsorption of carbonyl oxygen atoms in $C_5F_{10}O$ molecule on the Cu(1 1 1) surface has more charge transfer in all four active sites, -0.223 e, -0.213 e, -0.223 e and -0.231 e, respectively. In addition, the α2-F-Top and α2-F-Fcc sites with higher adsorption energy also have more charge transfer, -0.227 e and -0.215 e, respectively,

indicating that electrons from the Cu(1 1 1) surface are transferred to the $C_5F_{10}O$ molecule during the interaction. The charge transfer of other adsorption structure models are all around -0.06 e, and it can be considered that there is no charge transfer during the interaction.

Table 4.3 Adsorption energy and charge transfer of $C_5F_{10}O$ interaction with Cu(1 1 1) surface

Adsorption structure	Adsorption energy (eV)	Charge transfer (e)
O-Top	**-0.762**	**-0.223**
O-Bridge	**-0.770**	**-0.213**
O-Hcp	-0.667	**-0.223**
O-Fcc	-0.662	**-0.231**
α1-F-Top	-0.680	-0.064
α1-F-Bridge	-0.683	-0.063
α1-F-Hcp	-0.701	-0.061
α1-F-Fcc	-0.706	-0.068
α2-F3-Top	-0.444	-0.047
α2-F-Top	**-0.750**	**-0.227**
α2-F-Bridge	-0.442	-0.071
α2-F-Hcp	-0.521	-0.091
α2-F-Fcc	**-0.782**	**-0.215**

The adsorption models formed by the six structures with larger adsorption energy and charge transfer during the interaction between the $C_5F_{10}O$ molecule and the Cu(1 1 1) surface are shown in Figure 4.11, and Table 4.4 lists the structural parameters of the six adsorption structures. It can be seen that the carbonyl oxygen atoms in the $C_5F_{10}O$ molecule in the two initial structures of O-Top and O-Bridge form chemical bonds with the copper atoms on the Cu(1 1 1) surface, and the bond lengths are 2.091 Å and 2.111 Å, respectively. The carbonyl oxygen atom in the $C_5F_{10}O$ molecule can only interact with one copper atom on the Cu(1 1 1) surface to form a chemical bond. When a carbonyl oxygen atom interacts with two adjacent copper atoms, it is biased towards one of the copper atoms to form a chemical bond during structural relaxation. In the Hcp site and the Fcc site, although the interaction between the $C_5F_{10}O$ molecule and the Cu(1 1 1) surface undergoes charge transfer, the carbonyl oxygen atom is located in the geometric center of the three copper atoms, and the interaction between the atoms forms a relatively stable structure, so that the carbonyl oxygen atom cannot be biased towards one of the copper atoms to form a chemical bond like the Bridge site. During the interaction between $C_5F_{10}O$ molecules and the Cu(1 1 1) surfaces in α2-F-Top and α2-F-Fcc sites, the fluorine atoms and the copper surface are far away from each other, while the oxygen atoms gradually approach the copper surface and form the same adsorption structure as O-Top and O-Bridge. Therefore, the interaction process between $C_5F_{10}O$ molecules and the Cu(1 1 1) surface mainly forms a stable adsorption structure at the O-Top site. During the interaction between the carbonyl oxygen atom in the $C_5F_{10}O$ molecule and the Cu(1 1 1) surface, the $C_5F_{10}O$ molecule gains electrons, which leads to the lengthening of the C=O double bond of the carbonyl group to about 1.244 Å, and the bond length of the C-C bond between the carbon atom of the carbonyl group of the $C_5F_{10}O$ molecule and the two α carbon atoms is slightly shortened. This is consistent with the change rule of bond length after $C_5F_{10}O$ molecules form

negative ions. In other adsorption models, the bond length and bond angle of $C_5F_{10}O$ molecules do not change significantly, which belongs to physical adsorption.

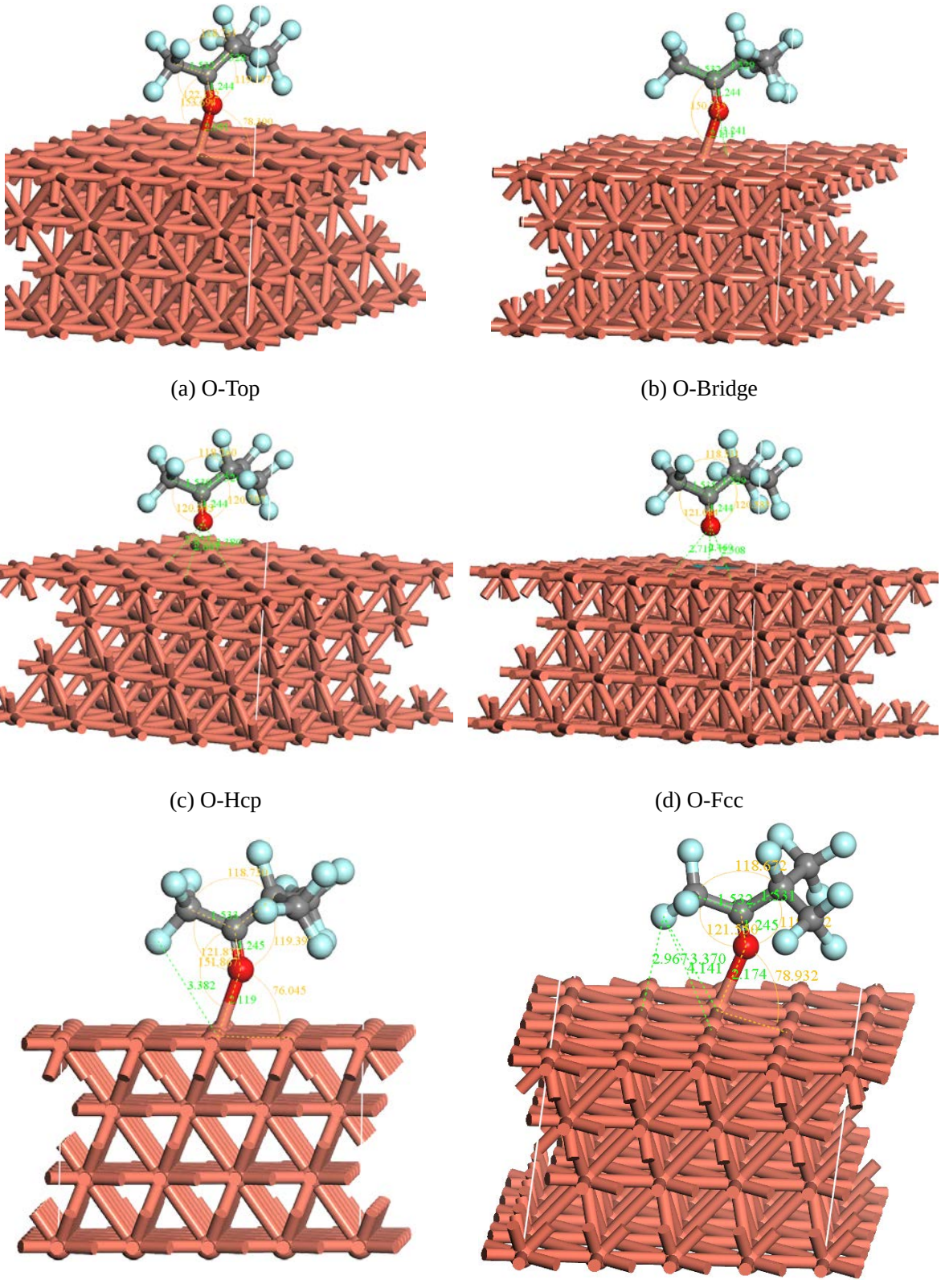

(a) O-Top (b) O-Bridge

(c) O-Hcp (d) O-Fcc

(e) α2-F-Top (f) α2-F-Fcc

Figure 4.11 Stable adsorption structures formed by $C_5F_{10}O$ on Cu(1 1 1) surface

Table 4.4 Parameters of stable adsorption structures formed by $C_5F_{10}O$ on Cu(1 1 1) surface

Adsorption structure	Bond length (Å)		Bond angle(°)		Charge transfer (e)
O-Top	Cu-O	2.091	O-Cu-Cu	78.300	-0.223
	C-O	1.244	Cu-O-C	153.694	
	C-α1C	1.532	O-C-α1C	122.132	
	C-α2C	1.528	O-C-α2C	119.137	
O-Bridge	Cu-O	2.111	O-Cu-Cu	77.607	-0.213
	C-O	1.244	Cu-O-C	150.735	
	C-α1C	1.532	O-C-α1C	122.125	
	C-α2C	1.529	O-C-α2C	119.434	
α2-F-Top	Cu-O	2.119	O-Cu-Cu	76.045	-0.227
	C-O	1.245	Cu-O-C	151.867	
	C-α1C	1.533	O-C-α1C	121.873	
	C-α2C	1.530	O-C-α2C	119.397	
α2-F-Fcc	Cu-O	2.174	O-Cu-Cu	78.932	-0.215
	C-O	1.245	Cu-O-C	143.012	
	C-α1C	1.532	O-C-α1C	121.550	
	C-α2C	1.531	O-C-α2C	119.712	

4.2.3 Density of Electronic States and Difference Charge Density

The density of electronic states and difference charge density are analyzed for the typical stable adsorption structure formed by the carbonyl oxygen atom of the $C_5F_{10}O$ molecule and the Cu(1 1 1) surface, as shown in Figure 4.12 and Figure 4.13. Figure 4.12 shows the distribution of the partial density of states (PDOS) after the interaction between the carbonyl oxygen atom of the $C_5F_{10}O$ molecule and the copper atom at the O-Top site and the O-Fcc site, respectively. It can be seen that the 4s orbital of the copper atom at the O-Top site and the 2p orbital of the carbonyl oxygen atom of the $C_5F_{10}O$ molecule have obvious overlaps near -9eV and -10eV, and the 3d orbital of the copper atom and the 2p orbital of the carbonyl oxygen atom of the $C_5F_{10}O$ molecule have obvious overlaps around -3.5 eV and 0.3 eV. It is shown that the 3d and 4s orbitals of copper atoms are hybridized with the 2p orbitals of carbonyl oxygen atoms of $C_5F_{10}O$ molecules, which confirms the strong interaction between copper atoms and carbonyl oxygen atoms. However, the 2p orbital of the carbonyl oxygen atom of the $C_5F_{10}O$ molecule at the O-Fcc site has less overlap with the PDOS of the 4s and 3d orbitals of the copper atom around -9eV and 0.3eV, respectively. It shows that the chemical bonds formed by the carbonyl oxygen atoms of $C_5F_{10}O$ molecules are mainly the 2p orbitals of the oxygen atoms and the 4s and 3d orbitals of the copper atoms to form chemical bonds near -9eV and 0.3eV.

Figure 4.13 shows the difference charge density distribution of $C_5F_{10}O$ molecule carbonyl oxygen atoms interacting with copper atoms at O-Top site and O-Fcc site. The red area represents an increase in charge density, and the blue area represents a decrease in charge density. During the interaction between the carbonyl oxygen atom of the $C_5F_{10}O$ molecule and the copper atom, electrons are transferred from the copper atom to the $C_5F_{10}O$ molecule, and

the transferred electrons are mainly distributed on the carbonyl group. The charge density in the region between the copper atom and the oxygen atom at the O-Top site varies significantly, and the copper atoms near the bonding copper atoms also undergo charge transfer. As the atoms between the Cu-O bonds have opposite polar charges at the O-Top site and the copper atom will attract the charge carried in the $C_5F_{10}O$ molecule to the oxygen atom, the charge density around the oxygen atom at the O-Top site is higher than that at the O-Fcc site.

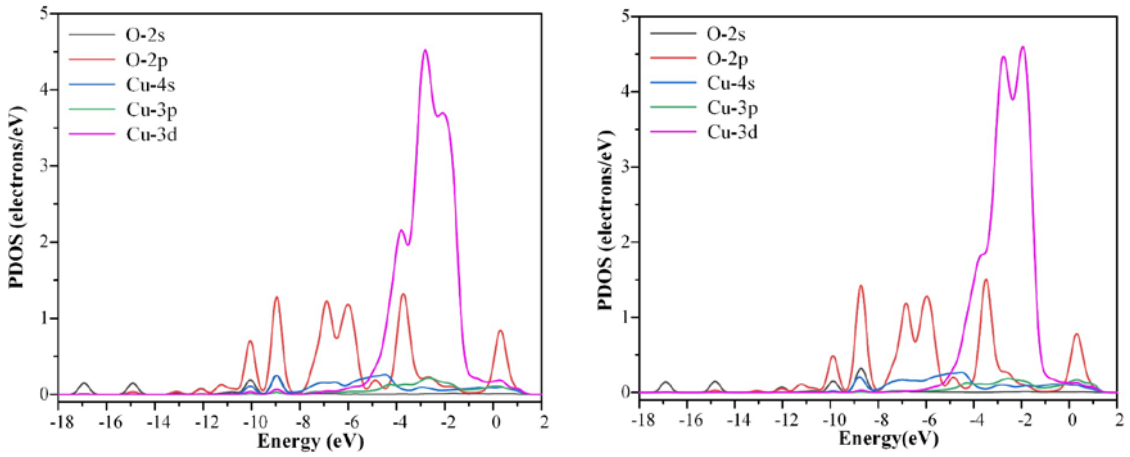

(a) O-Top (b) O-Fcc

Figure 4.12 PDOS after interaction of $C_5F_{10}O$ with Cu(1 1 1) surface

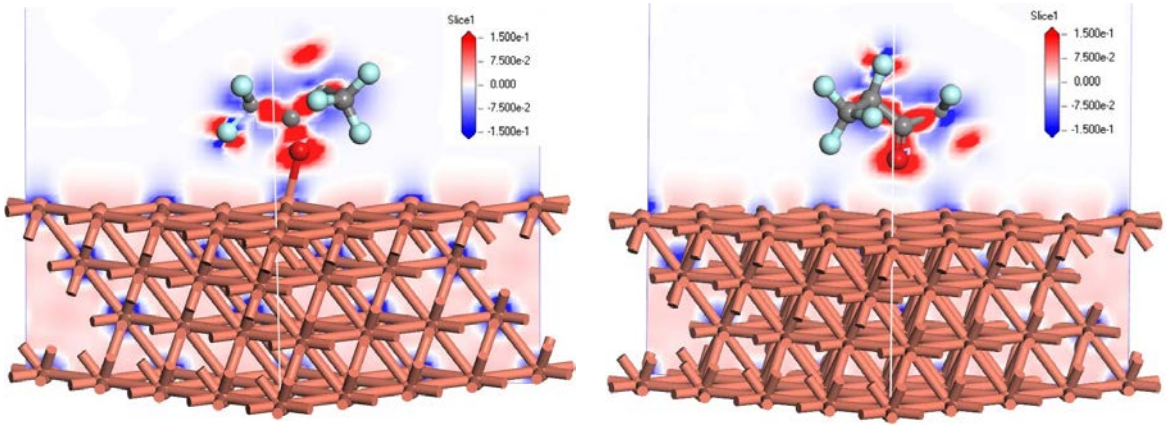

(a) O-Top (b) O-Fcc

Figure 4.13 Difference charge density after interaction of $C_5F_{10}O$ with Cu(1 1 1) surface

In conclusion, the carbonyl oxygen atom of $C_5F_{10}O$ molecule has high chemical reactivity, and the charge is transferred from the copper surface to the $C_5F_{10}O$ molecule during the interaction with the Cu(1 1 1) surface. The electrons obtained by $C_5F_{10}O$ molecules are mainly distributed near the carbonyl group with a strong electrophilic region, which leads to the elongated C=O double bond length of the carbonyl group, and the bond length of the two α carbon-carbon single bonds connected to the carbonyl group is slightly shortened. The $C_5F_{10}O$ molecule forms a chemical bond on the Cu(1 1 1 1) surface mainly in the Top site by hybridizing the 3d and 4s orbitals of the copper atom with the 2p orbitals of its carbonyl oxygen atom, and forms a stable adsorption structure. The adsorption of $C_5F_{10}O$ molecule carbonyl oxygen atom and Cu(1 1 1) surface will cause the dissociation of $C_5F_{10}O$ molecule in the process of desorption, and the Cu(1 1 1) surface will also be oxidized to form CuO and Cu_2O.

4.3 Mechanism of Gas-solid Interface Interaction Between $C_5F_{10}O$ and Silver

4.3.1 Interaction Model

In order to clarify the stability of the interaction between silver and $C_5F_{10}O$ gas after the silver-plated protective layer on the copper surface, the interaction model of Ag(1 1 1) surface and $C_5F_{10}O$ molecules is constructed in this manuscript. The Ag(1 1 1) surface is similar in structure to the Cu(1 1 1) surface (as shown in Figure 4.14), and also mainly includes four active sites: Top site (point a), Hcp site (point b), Fcc site (point c) and bridge site (point d). According to the structural characteristics of the $C_5F_{10}O$ molecule and the Ag(1 1 1) surface, 13 interaction initial structures are constructed in the same way as in the study of the Cu(1 1 1) surface, which will not be listed here.

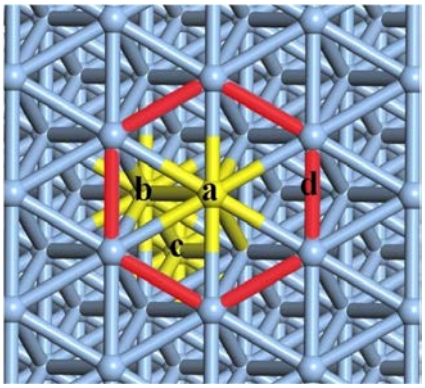

Figure 4.14 Ag(1 1 1) surface structure

4.3.2 Adsorption Energy and Charge Transfer

Table 4.5 lists the adsorption energy and charge transfer after the initial structural relaxation of the interaction between $C_5F_{10}O$ molecule and Ag(1 1 1) surface. The maximum adsorption energy of $C_5F_{10}O$ molecules on the Ag (1 1 1) surface is -0.783 eV, and the minimum adsorption energy is -0.464 eV. In terms of charge transfer, the adsorption of carbonyl oxygen atoms in the $C_5F_{10}O$ molecule on the four active sites on the Ag(1 1 1) surface also has high charge transfer, which are -0.229 e, -0.222 e, -0.215 e and -0.212 e, respectively, indicating that the electrons on the Ag(1 1 1) surface are transferred to the $C_5F_{10}O$ molecule during the interaction. The charge transfer of other adsorbed structural models is lower. In terms of adsorption energy and charge transfer, the results of the interaction process between carbonyl oxygen atoms in $C_5F_{10}O$ molecules and Ag(1 1 1) and Cu(1 1 1) surfaces are similar.

Figure 4.15 shows the Top site adsorption model of the carbonyl oxygen atom and the fluorine atom on the α2 carbon atom in the $C_5F_{10}O$ molecule on the Ag(1 1 1) surface, and Table 4.6 lists the relevant structural parameters. It can be seen that the bond length of the carbonyl C=O bond of the $C_5F_{10}O$ molecule in the O-Top site is slightly increased, but it is less than the bond length after the interaction with the Cu(1 1 1) surface. There is no chemical bond between the carbonyl oxygen atom in the $C_5F_{10}O$ molecule and the silver atom on the Ag(1 1 1) surface, and the interatomic distance is 2.567 Å, which is much larger than that of the Cu-O bond. In the α2-F-Top site, the change of bond length and bond angle of $C_5F_{10}O$ molecules

before and after adsorption are small, and the distance between $C_5F_{10}O$ molecules and Ag(1 1 1) surface after interaction is 2.796 Å. The interaction between $C_5F_{10}O$ molecule and Ag(1 1 1) surface is weak, which belongs to physical adsorption.

Table 4.5 Adsorption energy and charge transfer of $C_5F_{10}O$ interaction with Ag(1 1 1) surface

Adsorption structure	Adsorption energy (eV)	Charge transfer (e)
O-Top	-0.775	-0.229
O-Bridge	-0.763	-0.222
O-Hcp	-0.750	-0.215
O-Fcc	-0.748	-0.212
α1-F-Top	-0.705	-0.114
α1-F-Bridge	-0.773	-0.114
α1-F-Hcp	-0.783	-0.119
α1-F-Fcc	-0.783	-0.119
α2-F3-Top	-0.464	-0.097
α2-F-Top	-0.749	-0.117
α2-F-Bridge	-0.486	-0.097
α2-F-Hcp	-0.498	-0.100
α2-F-Fcc	-0.508	-0.098

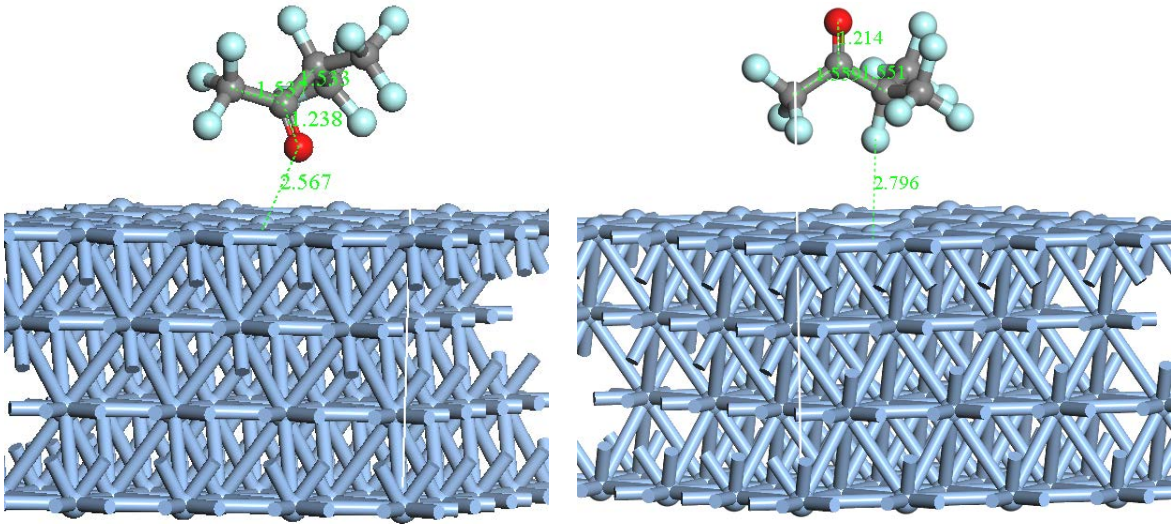

(a) O-Top (b) α2-F-Top

Figure 4.15 Stable adsorption structures formed by $C_5F_{10}O$ on Ag(1 1 1) surface

Table 4.6 Parameters of stable adsorption structures formed by $C_5F_{10}O$ on Ag(1 1 1) surface

Adsorption structure	Bond length (Å)	Bond angle(°)	Charge transfer (e)
O-Top	C-O 1.238 C-α1C 1.537 C-α2C 1.533	O-C-α1C 121.448 O-C-α2C 120.258	-0.229
α2-F-Top	C-O 1.214 C-α1C 1.559 C-α2C 1.551 F-α2C 1.391	O-C-α1C 121.650 O-C-α2C 121.575	-0.117

4.3.3 Density of Electronic States and Difference Charge Density

Figure 4.16 shows the PDOS distribution of $C_5F_{10}O$ molecules after the interaction of Top sites on the Ag(1 1 1) surface. It can be seen that there is no obvious overlap between the 4s orbital of silver atom and the orbital of carbonyl oxygen atom of $C_5F_{10}O$ molecule in the O-Top adsorption structure. The 2p orbital of the carbonyl oxygen atom of the $C_5F_{10}O$ molecule slightly overlaps with the 3p and 3d orbitals of the silver atom in the electronic density of states around -3.5eV and 0.3eV, respectively. The differential charge density shown in Figure 4.17a shows that the electrons of the $C_5F_{10}O$ molecule are mainly distributed near the carbonyl group, while there is no obvious increase or decrease in the charge density on the silver surface, indicating that no chemical bonds are formed during the interaction process. The difference charge density shown in Figure 4.17a shows that the electrons of the $C_5F_{10}O$ molecule are mainly distributed near the carbonyl group, while there is no obvious increase or decrease in the charge density on the silver surface, indicating that no chemical bonds are formed during the interaction process. The 2p orbital of fluorine atom in the α2-F-Top adsorption structure slightly overlaps with the 3d orbital of silver atom around -5eV. The difference charge density shown in Figure 4.17b shows that the region between the fluorine and silver atoms has a small amount of negative charges of the same polarity, which will cause the $C_5F_{10}O$ molecule and the Ag(1 1 1) surface to move away from each other during the interaction process, and finally form a relatively stable adsorption structure.

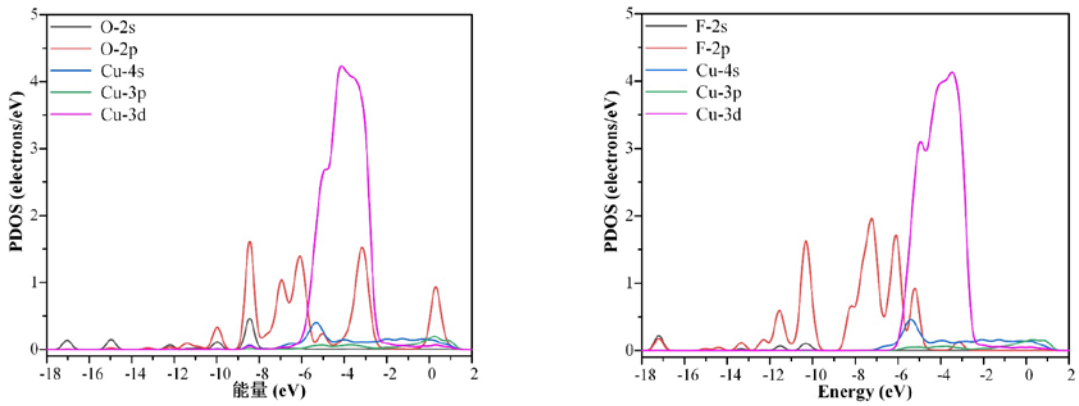

(a) O-Top (b) α2-F-Top

Figure 4.16 PDOS after interaction of $C_5F_{10}O$ with Ag(1 1 1) surface

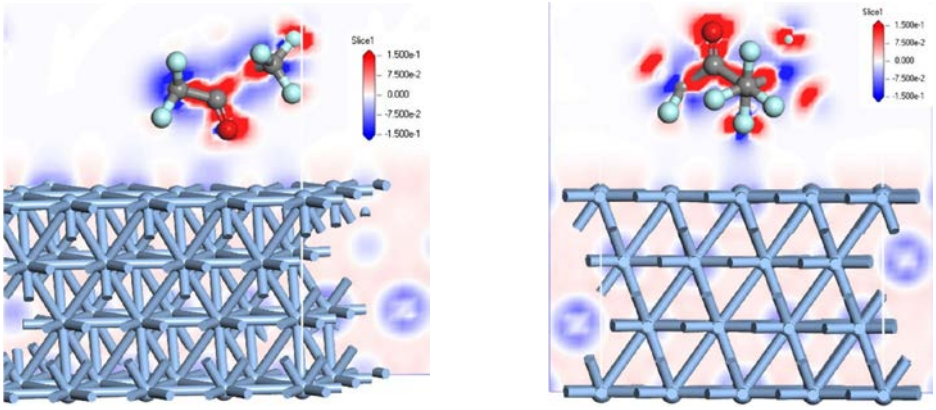

(a) O-Top (b) α2-F-Top

Figure 4.17 Difference charge density after interaction of $C_5F_{10}O$ with Ag(1 1 1) surface

In summary, the interaction process between $C_5F_{10}O$ molecules and Ag(1 1 1) surface will have a small amount of charge transfer from the silver surface to $C_5F_{10}O$ molecules, but the adsorption distance between the $C_5F_{10}O$ molecule and the stable adsorption structure formed on the Ag(1 1 1) surface is relatively large, and no chemical bond is formed, which belongs to physical adsorption.

4.4 Mechanism of Gas-solid Interface Interaction Between $C_5F_{10}O$ and Aluminum

4.4.1 Interaction Model

Since the aluminum material is easily oxidized in the air to form a dense Al_2O_3 oxide layer to protect the internal aluminum material from oxidation and corrosion, the gas-solid interface interaction between $C_5F_{10}O$ and aluminum is actually the contact between Al_2O_3 and $C_5F_{10}O$ molecules, which has also been confirmed in the previous experiments. Therefore, the research on the gas-solid interface mechanism of $C_5F_{10}O$ and aluminum takes Al_2O_3 as the main research object, and the Al_2O_3(1 1 1) surface is shown in Figure 4.18. The Al_2O_3(1 1 1) surface mainly contains four kinds of atoms with different chemical properties. Oxygen vacancies (point c) are generated on the Al_2O_3(1 1 1) surface after removing the top atoms, and the aluminum atoms on the surface (point a) are connected with three oxygen vacancies to form coordinately unsaturated aluminum atoms, and the oxygen vacancy is connected to one coordinatively unsaturated aluminum atom and two 6-coordinated aluminum atoms (point b). The d atom in Figure 4.18 is an oxygen atom in a quadruple coordination on the subsurface of Al_2O_3(1 1 1). The oxygen vacancy *c* and the aluminum atom *a* are the adsorption active sites on the Al_2O_3(1 1 1) surface.

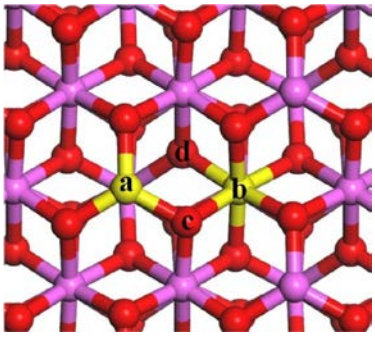

Figure 4.18 Al_2O_3(1 1 1) surface structure

According to the structural characteristics of the $C_5F_{10}O$ molecule and the Al_2O_3(1 1 1) surface and the previous research results of the gas-solid interface interaction between the $C_5F_{10}O$ gas and copper materials, this manuscript constructs four initial interaction structures shown in Figure 4.19.

4.4.2 Adsorption Energy and Charge Transfer

Table 4.7 lists the adsorption energies and charge transfer after relaxation of the four adsorbed initial structures of the $C_5F_{10}O$ molecules constructed in this manuscript on the Al_2O_3(1 1 1) surface. The adsorption energies of $C_5F_{10}O$ molecules on the O-Al-Top site and O-O-Top site on the Al_2O_3(1 1 1) surface are respectively -0.949 eV and -1.013 eV, which are higher than the other two initial adsorption structure models. However, the charge transfer of

the four adsorption initial structure models of the $C_5F_{10}O$ molecule and the Al_2O_3(1 1 1) surface in the interaction process is all lower than 0.1e, which can be considered as no charge transfer.

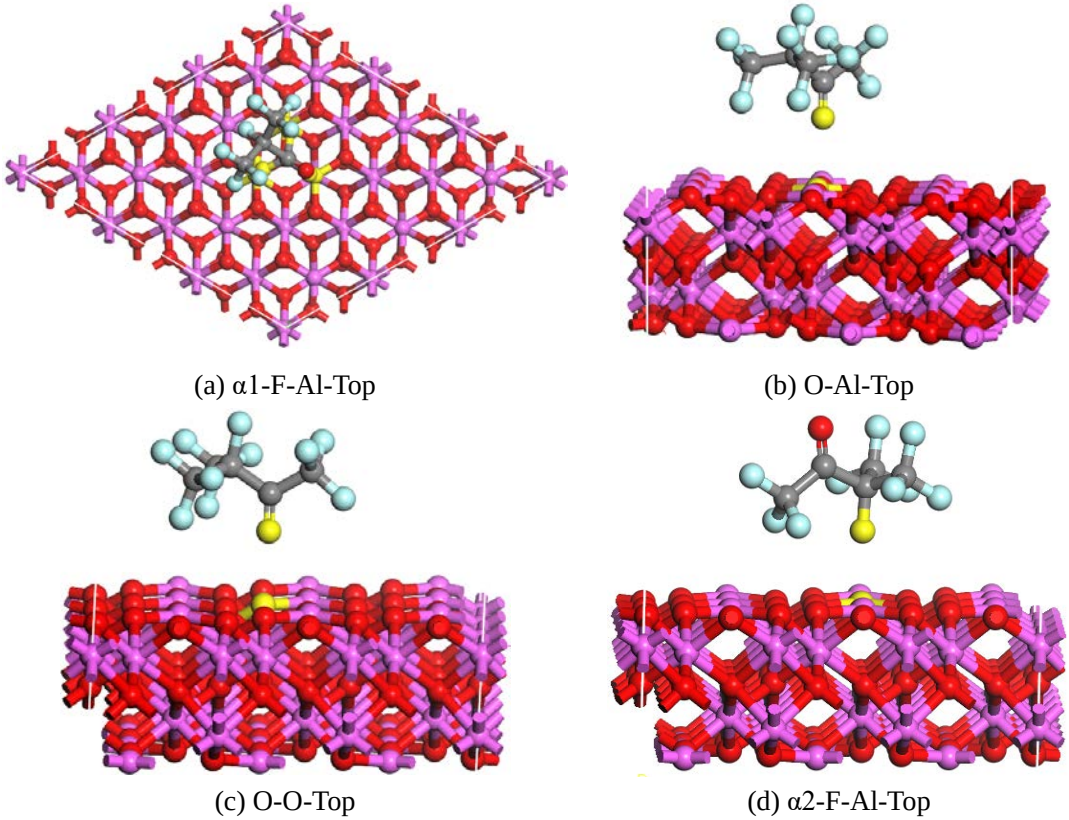

(a) α1-F-Al-Top (b) O-Al-Top

(c) O-O-Top (d) α2-F-Al-Top

Figure 4.19 Initial adsorption structure of $C_5F_{10}O$ on Al_2O_3(1 1 1) surface

Table 4.7 Adsorption energy and charge transfer of $C_5F_{10}O$ interaction with Al_2O_3(1 1 1) surface

Adsorption structure	Adsorption energy (eV)	Charge transfer (e)
α1-F-Al-Top	-0.439	-0.057
O-Al-Top	-0.949	-0.092
O-O-Top	-1.013	-0.063
α2-F-Al-Top	-0.565	0.018

The four stable adsorption structures of $C_5F_{10}O$ molecule and Al_2O_3(1 1 1) surface are shown in Figure 4.20, and the parameters of these four adsorption structures are listed in Table 4.8. The optimized structures show that the carbonyl oxygen atoms of the $C_5F_{10}O$ molecule in the two initial structures, O-Al-Top and O-O-Top, form chemical bonds with the aluminum atoms on the Al_2O_3(1 1 1) surface with bond lengths of 1.928 Å and 1.968 Å, respectively. The Al-O bond length on the Al_2O_3(1 1 1) surface is 1.706 Å, and the length of the Al-O bond formed by the carbonyl oxygen atoms in the $C_5F_{10}O$ molecule and the aluminum atoms on the Al_2O_3(1 1 1) surface is significantly larger than this value. In the O-O-Top site, the carbonyl oxygen atom in the $C_5F_{10}O$ molecule and the oxygen atom on the surface of Al_2O_3(1 1 1) both have negative charges of the same polarity and repel each other when the distance is short. The interaction force causes the rotation of the $C_5F_{10}O$ molecule away from the original position, resulting in a similar result to the O-Al-Top site. In the O-Al-Top and O-O-Top sites, the bond length of the carbonyl group of the $C_5F_{10}O$ molecule is elongated to about 1.23 Å after the interaction of the $C_5F_{10}O$ molecule with the Al_2O_3(1 1 1) surface. There is no change in the bond angles of the $C_5F_{10}O$ molecule. At the α1-F-Al-Top and α2-F-Al-Top sites, the C-F bond

length of the $C_5F_{10}O$ molecule is elongated to about 1.41 Å, and other bond lengths and bond angles do not change significantly.

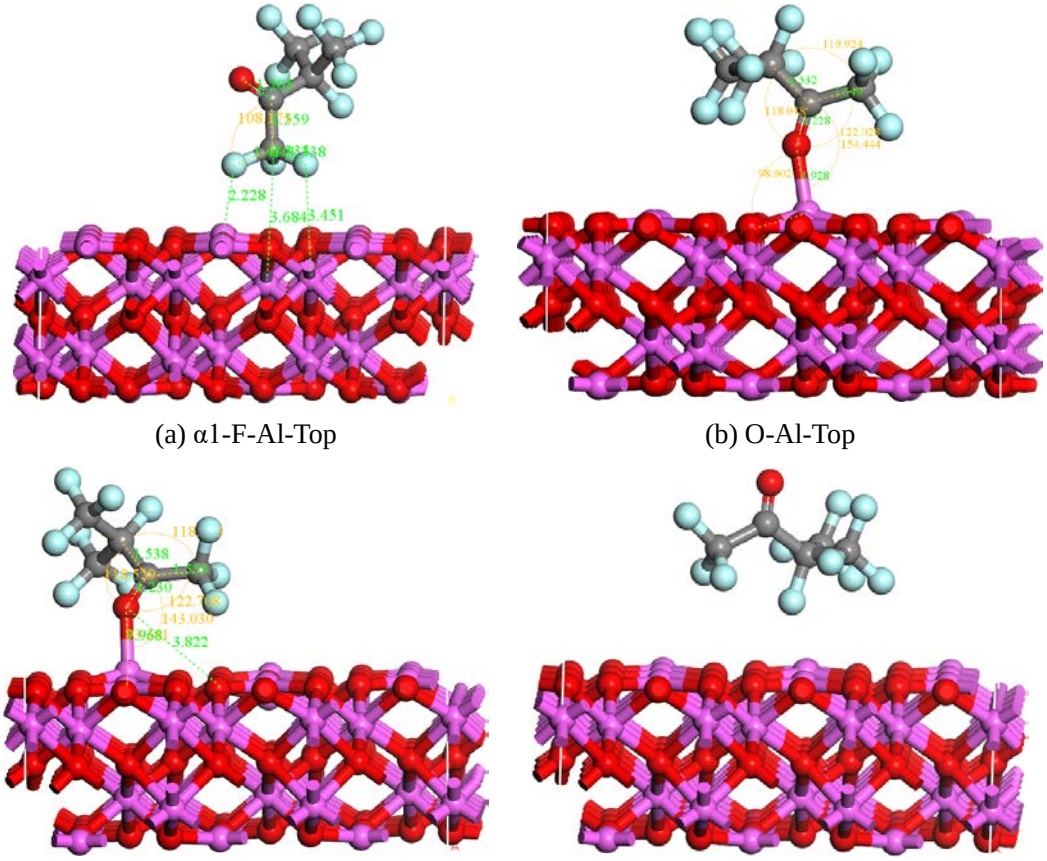

(a) α1-F-Al-Top (b) O-Al-Top

(c) O-O-Top (d) α2-F-Al-Top

Figure 4.20 Stable adsorption structures formed by $C_5F_{10}O$ on Al_2O_3(1 1 1) surface

Table 4.8 Parameters of stable adsorption structures formed by $C_5F_{10}O$ on Al_2O_3(1 1 1) surface

Adsorption structure	Bond length (Å)	Bond angle(°)	Charge transfer (e)
α1-F-Al-Top	α1C-F 1.410 C-O 1.205 C-α1C 1.559 C-α2C 1.560	O-C-α1C 122.481 O-C-α2C 122.520 C-α1C-F 108.171	-0.057
O-Al-Top	Al-O 1.982 C-O 1.228 C-α1C 1.549 C-α2C 1.532	O-Al-O 98.602 Al-O-C 154.444 O-C-α1C 122.028 O-C-α2C 118.048	-0.057
O-O-Top	Al-O 1.968 C-O 1.230 C-α1C 1.553 C-α2C 1.538	O-Al-O 93.341 Al-O-C 143.030 O-C-α1C 122.708 O-C-α2C 118.529	-0.063
α2-F-Al-Top	α2-F 1.412 C-O 1.206 C-α1C 1.565 C-α2C 1.554	O-C-α1C 122.156 O-C-α2C 120.516 C-α2C-F 109.420	0.018

4.4.3 Density of Electronic States and Difference Charge Density

Figure 4.21 shows the PDOS distribution of $C_5F_{10}O$ molecules after the interaction between the $C_5F_{10}O$ molecule and Al_2O_3(1 1 1) surface. It can be seen that the 2s and 2p orbitals of the fluorine atom of the $C_5F_{10}O$ molecule in the α1-F-Al-Top site slightly overlap with the 3p and 4s orbitals of the aluminum atom around 4.7eV and 5.7eV, respectively, and the 3d orbitals of the aluminum atoms also overlap slightly around 5.7 eV. In the O-Al-Top and O-O-Top sites, the 2s and 2p orbitals of the carbonyl oxygen atoms of the $C_5F_{10}O$ molecule slightly overlap with the 3p and 4s orbitals of the aluminum atoms around -9.4eV and -8.2eV. The 2p orbital of carbonyl oxygen atom also has a slight overlap with the 3p and 3d orbital of aluminum atom around 1eV. In the α2-F-Al-Top site, the 2s and 2p orbitals of fluorine atoms of $C_5F_{10}O$ molecules slightly overlap with the 3p, 3d and 4s orbitals of aluminum atoms around 4eV.

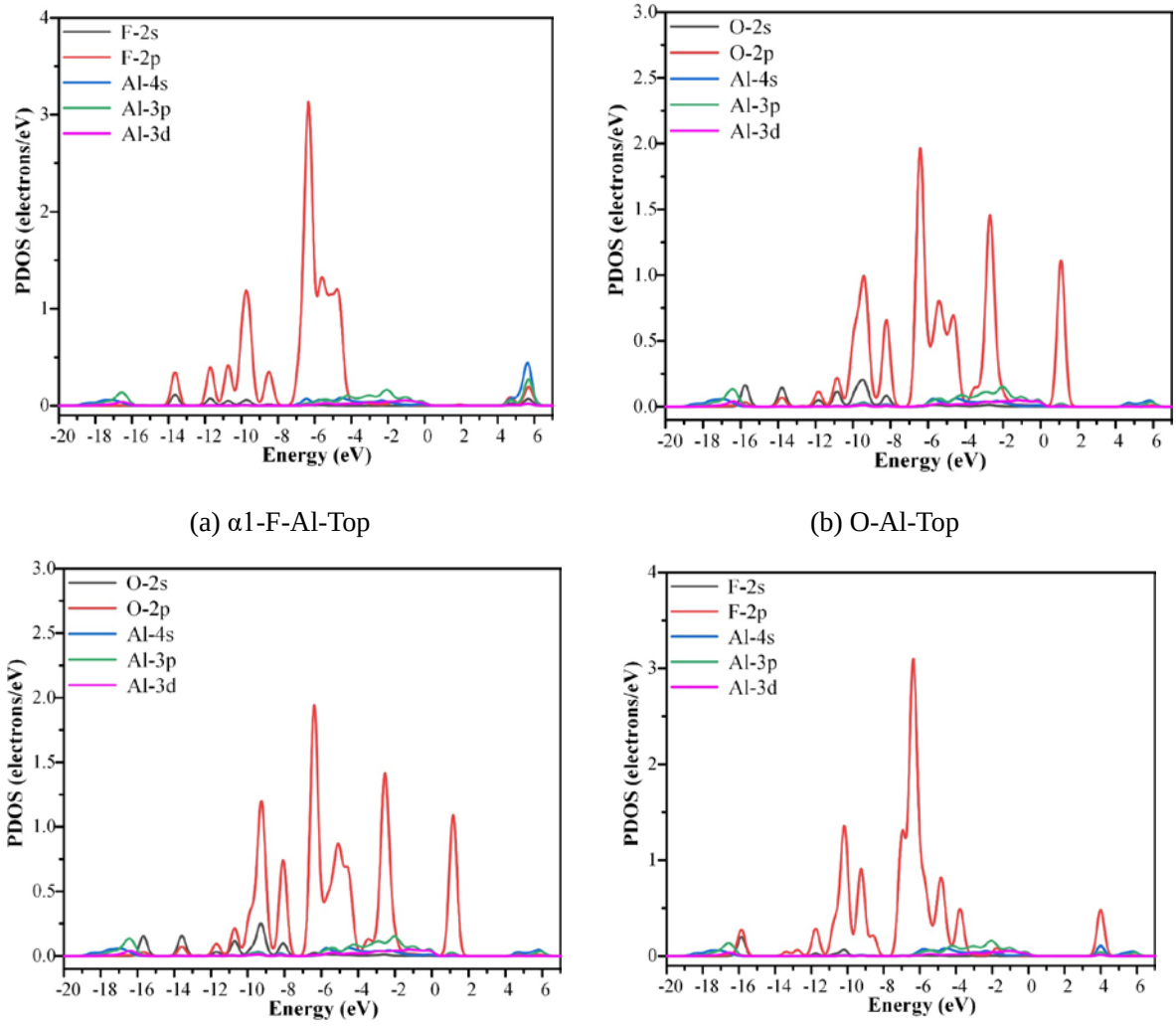

(a) α1-F-Al-Top

(b) O-Al-Top

(c) O-O-Top

(d) α2-F-Al-Top

Figure 4.21 PDOS after interaction of $C_5F_{10}O$ with Al_2O_3(1 1 1) surface

Figure 4.22 shows the difference charge density distribution after the interaction between $C_5F_{10}O$ molecule and Al_2O_3(1 1 1) surface. In the $C_5F_{10}O$ molecule, the charge is mainly distributed around the carbonyl group, while the aluminum atom with unsaturated coordination

on the Al_2O_3(1 1 1) surface is positively charged, and the oxygen atom in the oxygen vacancy is negatively charged. During the interaction process, the aluminum atom will attract the carbonyl oxygen atom of the $C_5F_{10}O$ molecule, resulting in the adsorption of the $C_5F_{10}O$ molecule on the surface of the Al_2O_3(1 1 1) to form a relatively stable structure. This result is consistent with the conclusion that $C_5F_{10}O$ gas will adsorb on the aluminum surface at high temperature in the experiments in Chapter 2. The fluorine atoms in the $C_5F_{10}O$ molecule are positively charged in the direction of the C-F bond and negatively charged in the direction of the perpendicular C-F bond due to electron orbital hybridization. During the interaction with Al_2O_3(1 1 1), the molecule is deflected due to the repulsive force of the same charge.

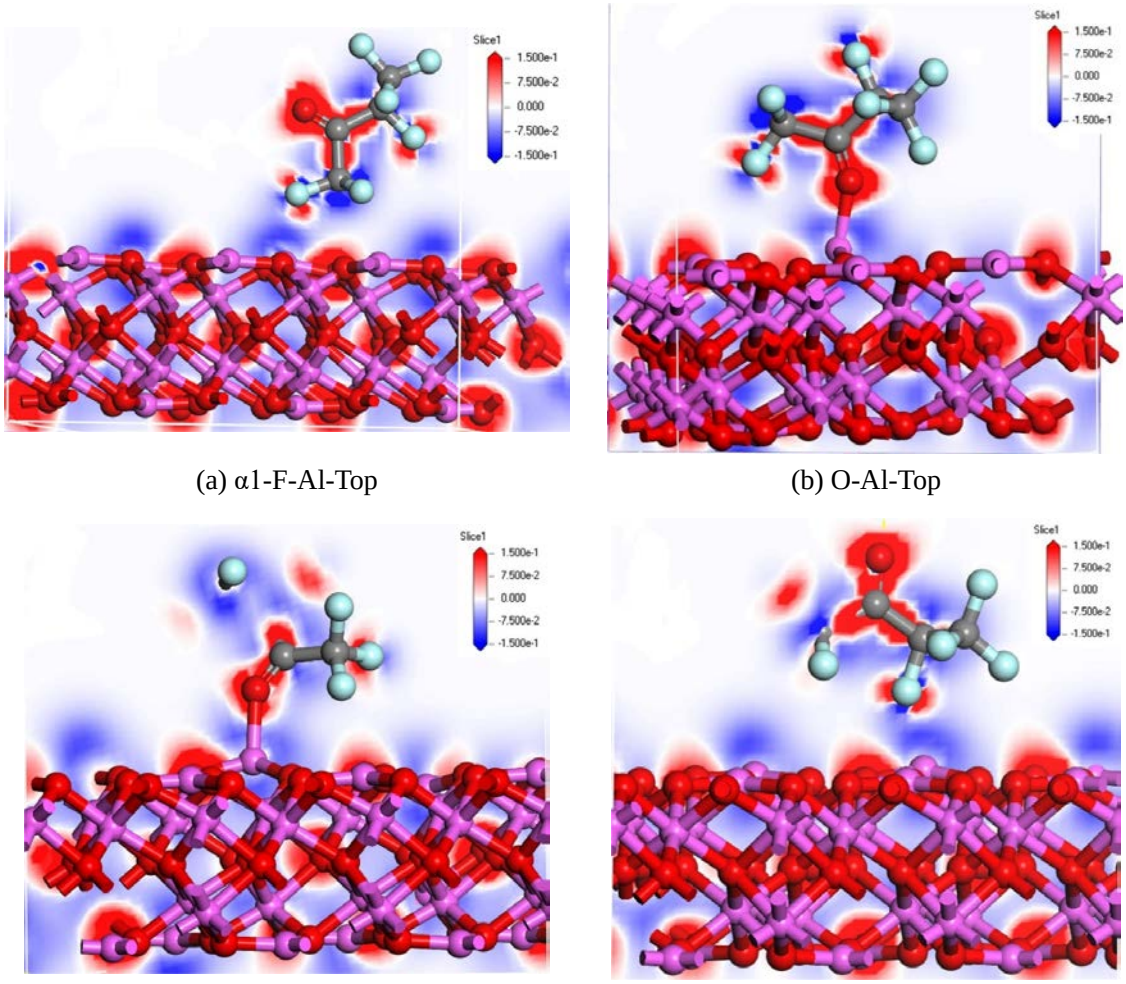

(a) α1-F-Al-Top (b) O-Al-Top

(c) O-O-Top (d) α2-F-Al-Top

Figure 4.22 Difference charge density after interaction of $C_5F_{10}O$ with Al_2O_3(1 1 1) surface

In conclusion, during the interaction between the $C_5F_{10}O$ molecule and Al_2O_3(1 1 1), the aluminum atom will attract the carbonyl oxygen atom of the C5F10O molecule and repel the fluorine atom. Therefore, the interaction between the carbonyl oxygen atom of the $C_5F_{10}O$ molecule and Al_2O_3(1 1 1) produces a large adsorption energy, but does not cause charge transfer. The interaction process between the $C_5F_{10}O$ molecule and Al_2O_3(1 1 1) belongs to physical adsorption.

4.5 Discharge and Thermal Decomposition Mechanism of $C_5F_{10}O/N_2/O_2$ Gas Mixture

4.5.1 Decomposition Path and Products Generation Path Model of $C_5F_{10}O/N_2/O_2$

The decomposition of $C_5F_{10}O$ gas mixture under discharge and thermal faults is determined by the dissociation mechanism of its molecule itself, while the exterior conditions such as discharge, over-thermal are only the induced factors of $C_5F_{10}O$ gas molecules. Therefore, the dissociation of $C_5F_{10}O$ gas molecules and the recombination process among the particles after dissociation are of great significance to the study of the decomposition mechanism of $C_5F_{10}O$ gas. In this section, based on DFT and transition state theory, the paths of dissociation of $C_5F_{10}O$ gas mixture and the paths of recombination of various particles generated by dissociation are firstly constructed by combining the structural properties of $C_5F_{10}O$, O_2 and H_2O molecules. Then, relaxation and vibrational frequency calculations are performed for the dissociation of $C_5F_{10}O$, O_2 and H_2O molecules and the structures of the substances involved in the composite path between each particle after their dissociation, and the stable geometric structure configuration and energy of each substance satisfying the energy minimum principle are obtained, and the energy of each particle at 298.15 K (room temperature 25°C) is also corrected, and the enthalpy of the constructed reaction path is calculated. Next, the reaction path is performed on the reaction path based on the transition state theory, and parameters such as the structure and activation energy of the transition state are obtained. Finally, the energy results of each dissociation path and composite path are analyzed.

The molecular decomposition system of $C_5F_{10}O$, O_2 and H_2O constructed in this manuscript is shown in Figure 4.23.

The calculations in this section are based on the Dmol^3 toolkit of Materials Studio. The TNP-B3LYP method is used to relax the structure of each particle and the LST-QST algorithm is used to search for transition states. Considering the structural characteristics of $C_5F_{10}O$ molecules and its possible chemical bond breaking sites, 7 possible primary decomposition paths are listed, and the decomposition path of particles generated by each primary decomposition path is calculated. The final $C_5F_{10}O$ decomposes into multiple simple particle structures. Considering also the influence of micro-water and oxygen in $C_5F_{10}O$ gas mixture in the actual operation of GIE, and this manuscript constructs 87 dissociation paths to reveal the decomposition mechanism of $C_5F_{10}O/N_2/O_2$ gas mixture. In addition, Figure 4.24 constructs 23 decomposition product generation pathways for revealing the generation mechanism of $C_5F_{10}O/N_2/O_2$ gas mixture decomposition products.

The $C_5F_{10}O$ gas discharge decomposition mechanism and the decomposition path depend on the associated reaction mechanism, and is independent of the type of discharge. The energy of moving particles such as electrons in different discharge types or different strength electric fields varies, resulting in different temperatures and collision energies in the discharge channels. Therefore, different types of discharge affect the decomposition path of $C_5F_{10}O$ gas, causing differences in the types and content of the decomposition product, which has also been confirmed in previous experiments. In addition, the structure of $C_5F_{10}O$ molecule is more complicated, and the research on its dissociation and composite path is still not comprehensive. This section mainly studies the generation mechanism of various types of neutral particles and

decomposition products produced by $C_5F_{10}O$, O_2 and H_2O molecular decomposition. The mechanism of the decomposition of $C_5F_{10}O/N_2/O_2$ gas mixture under different conditions is obtained by calculating the conditions for the generation of each particle and decomposition product.

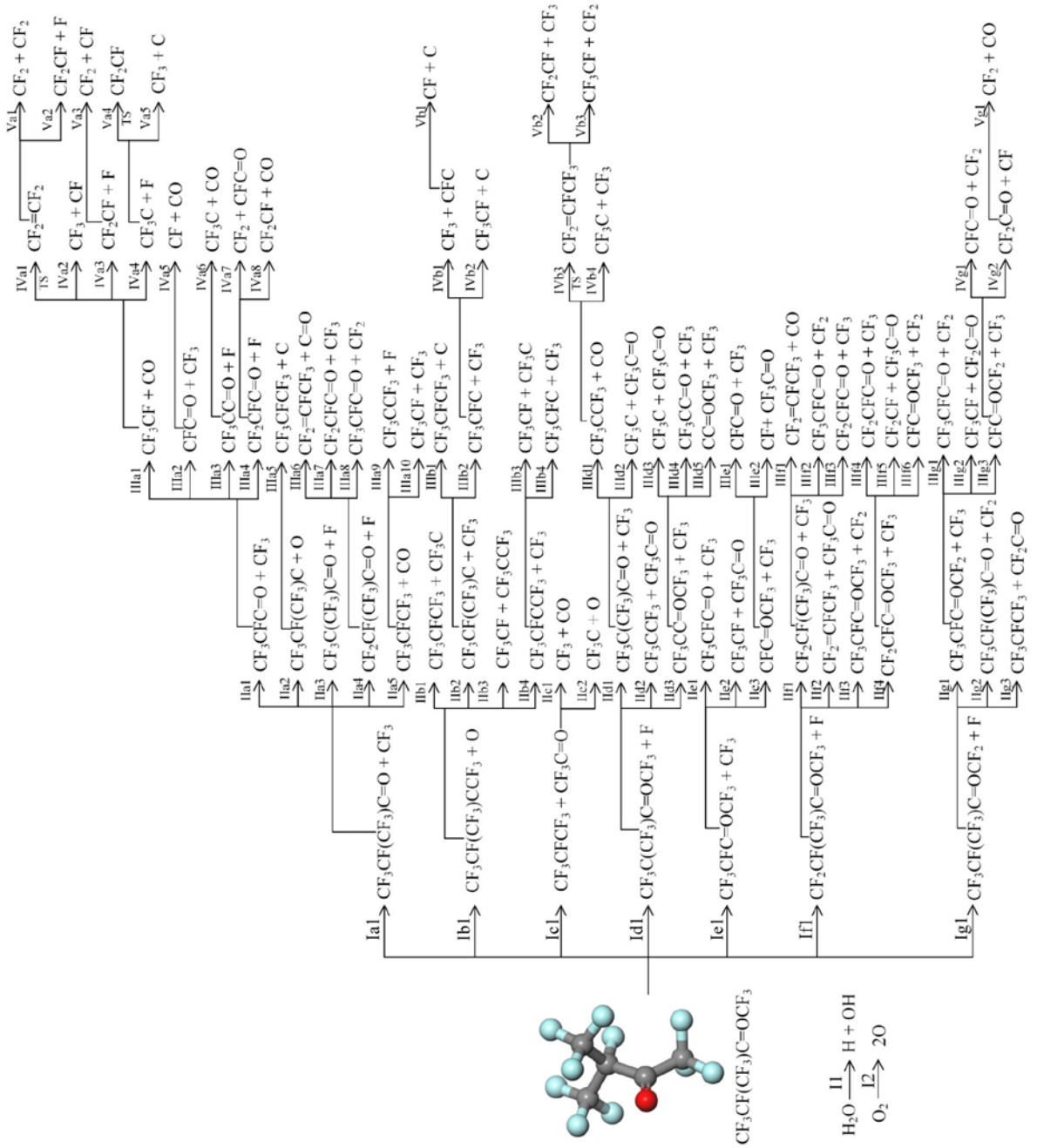

Figure 4.23 $C_5F_{10}O$, O_2 and H_2O molecular dissociation paths

4.5.2 Decomposition Mechanism of $C_5F_{10}O$ Gas Mixture

In order to clarify the decomposition mechanism of $C_5F_{10}O$ gas, this section calculates the energy of $C_5F_{10}O$ molecule dissociation to generate each particle and composite to form each decomposition product, and the enthalpy and activation energy of each dissociation reaction and recombination reaction are obtained after correcting the ZPVE of the reaction at a

temperature of 298.15K. The enthalpy of reaction can be calculated by the following formula:

$$E = \left(E_{ptotal} + G_{ptotal}\right) - \left(E_{rtotal} + G_{rtotal}\right) \quad (4.13)$$

where E is the enthalpy of the chemical reaction. E_{ptotal} and E_{rtotal} are the total energy of the products and reactants of the chemical reaction, respectively. G_{ptotal} and G_{rtotal} are the corrections for the products and reactants of this chemical reaction containing zero-point energy at a temperature of 298.15 K, respectively.

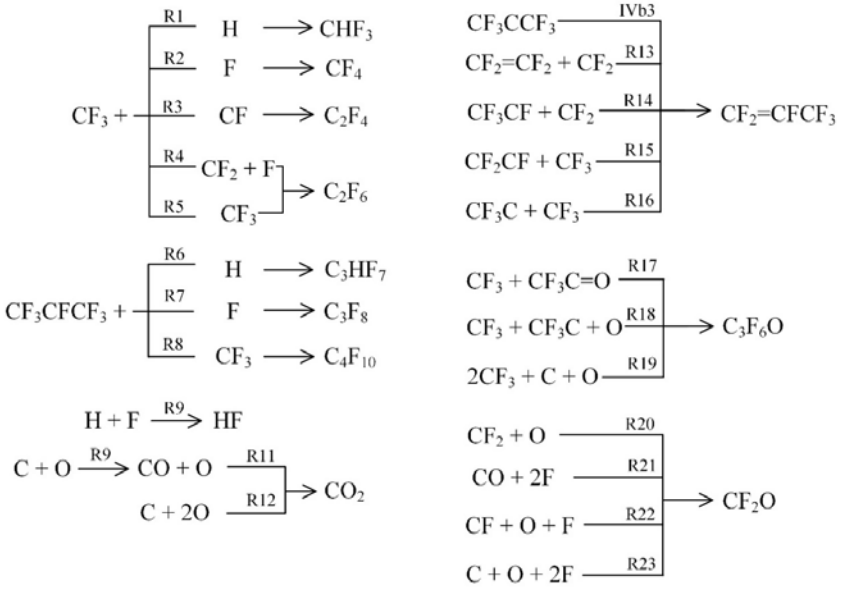

Figure 4.24 Decomposing product generation path

Table 4.9 shows the enthalpy and activation energy of the $C_5F_{10}O$ molecular dissociation pathway considered in this manuscript at a temperature of 298.15K.

Table 4.9 Main dissociation reactions of $C_5F_{10}O$ molecule and its enthalpy and activation energy (T=298.15K)

No.	Chemical reaction	Enthalpy (kcal/mol)	Activation energy (kcal/mol)
Ia1	$C_5F_{10}O \rightarrow CF_3CF(CF_3)C{=}O + CF_3$	58.63	-
Ib1	$C_5F_{10}O \rightarrow CF_3CF(CF_3)CCF_3 + O$	193.13	-
Ic1	$C_5F_{10}O \rightarrow CF_3CFCF_3 + CF_3C{=}O$	51.09	-
Id1	$C_5F_{10}O \rightarrow CF_3C(CF_3)C{=}OCF_3 + F$	125.92	-
Ie1	$C_5F_{10}O \rightarrow CF_3CFC{=}OCF_3 + CF_3$	51.10	-
If1	$C_5F_{10}O \rightarrow CF_2CF(CF_3)C{=}OCF_3 + F$	143.37	-
Ig1	$C_5F_{10}O \rightarrow CF_3CF(CF_3)C{=}OCF_2 + F$	132.12	-
I1	$H_2O \rightarrow H + OH$	136.21	-
I2	$O_2 \rightarrow 2O$	182.29	-
IIa1	$CF_3CF(CF_3)C{=}O \rightarrow CF_3CFC{=}O + CF_3$	19.16	-
IIa2	$CF_3CF(CF_3)C{=}O \rightarrow CF_3CF(CF_3)C + O$	205.72	-
IIa3	$CF_3CF(CF_3)C{=}O \rightarrow CF_3C(CF_3)C{=}O + F$	68.54	-
IIa4	$CF_3CF(CF_3)C{=}O \rightarrow CF_2CF(CF_3)C{=}O + F$	144.71	-
IIa5	$CF_3CF(CF_3)C{=}O \rightarrow CF_3CFCF_3 + CO$	-10.87	-

IIb1	$CF_3CF(CF_3)CCF_3 \rightarrow CF_3CFCF_3 + CF_3C$	67.42	-
IIb2	$CF_3CF(CF_3)CCF_3 \rightarrow CF_3CF(CF_3)C + CF_3$	71.21	-
IIb3	$CF_3CF(CF_3)CCF_3 \rightarrow CF_3CF + CF_3CCF_3$	74.74	-
IIb4	$CF_3CF(CF_3)CCF_3 \rightarrow CF_3CFCCF_3 + CF_3$	9.07	-
IIc1	$CF_3C=O \rightarrow CF_3 + CO$	-3.33	-
IIc2	$CF_3C=O \rightarrow CF_3C + O$	209.47	-
IId1	$CF_3C(CF_3)C=OCF_3 \rightarrow CF_3C(CF_3)C=O + CF_3$	1.25	-
IId2	$CF_3C(CF_3)C=OCF_3 \rightarrow CF_3CCF_3 + CF_3C=O$	82.68	-
IId3	$CF_3C(CF_3)C=OCF_3 \rightarrow CF_3CC=OCF_3 + CF_3$	73.75	-
IIe1	$CF_3CFC=OCF_3 \rightarrow CF_3CFC=O + CF_3$	26.69	-
IIe2	$CF_3CFC=OCF_3 \rightarrow CF_3CF + CF_3C=O$	70.94	-
IIe3	$CF_3CFC=OCF_3 \rightarrow CFC=OCF_3 + CF_3$	80.00	-
IIf1	$CF_2CF(CF_3)C=OCF_3 \rightarrow CF_2CF(CF_3)C=O + CF_3$	59.97	-
IIf2	$CF_2CF(CF_3)C=OCF_3 \rightarrow CF_2=CFCF_3(C_3F_6) + CF_3C=O$	0.71	-
IIf3	$CF_2CF(CF_3)C=OCF_3 \rightarrow CF_3CFC=OCF_3 + CF_2$	22.59	-
IIf4	$CF_2CF(CF_3)C=OCF_3 \rightarrow CF_2CFC=OCF_3 + CF_3$	6.40	-
IIg1	$CF_3CF(CF_3)C=OCF_2 \rightarrow CF_3CFC=OCF_2 + CF_3$	55.06	-
IIg2	$CF_3CF(CF_3)C=OCF_2 \rightarrow CF_3CF(CF_3)C=O + CF_2$	41.37	-
IIg3	$CF_3CF(CF_3)C=OCF_2 \rightarrow CF_3CFCF_3 + CF_2C=O$	52.87	-
IIIa1	$CF_3CFC=O \rightarrow CF_3CF + CO$	40.92	-
IIIa2	$CF_3CFC=O \rightarrow CFC=O + CF_3$	75.45	-
IIIa3	$CF_3CFC=O \rightarrow CF_3CC=O + F$	127.56	-
IIIa4	$CF_3CFC=O \rightarrow CF_2CFC=O + F$	133.22	-
IIIa5	$CF_3CF(CF_3)C \rightarrow CF_3CFCF_3 + C$	88.14	-
IIIa6	$CF_2CF(CF_3)C=O \rightarrow CF_2=CFCF_3(C_3F_6) + CO$	-62.59	-
IIIa7	$CF_2CF(CF_3)C=O \rightarrow CF_2CFC=O + CF_3$	7.67	-
IIIa8	$CF_2CF(CF_3)C=O \rightarrow CF_3CFC=O + CF_2$	-10.69	-
IIIa9	$CF_3CFCF_3 \rightarrow CF_3CCF_3 + F$	157.51	-
IIIa10	$CF_3CFCF_3 \rightarrow CF_3CF + CF_3$	70.95	-
IIIb1	$CF_3CF(CF_3)C \rightarrow CF_3CFCF_3 + C$	88.14	-
IIIb2	$CF_3CF(CF_3)C \rightarrow CF_3CFC + CF_3$	13.15	-
IIIb3	$CF_3CFCCF_3 \rightarrow CF_3CF + CF_3C$	129.30	-
IIIb4	$CF_3CFCCF_3 \rightarrow CF_3CFC + CF_3$	75.29	-
IIId1	$CF_3C(CF_3)C=O \rightarrow CF_3CCF_3 + CO$	78.10	-
IIId2	$CF_3C(CF_3)C=O \rightarrow CF_3C + CF_3C=O$	145.06	-
IIId3	$CF_3CC=OCF_3 \rightarrow CF_3C + CF_3C=O$	72.55	-
IIId4	$CF_3CC=OCF_3 \rightarrow CF_3CC=O + CF_3$	5.67	-
IIId5	$CF_3CC=OCF_3 \rightarrow CC=OCF_3 + CF_3$	62.76	-
IIIe1	$CFC=OCF_3 \rightarrow CFC=O + CF_3$	22.14	-
IIIe2	$CFC=OCF_3 \rightarrow CF+ CF_3C=O$	56.24	-
IIIf1	$CF_2CF(CF_3)C=O \rightarrow CF_2=CFCF_3(C_3F_6) + CO$	-62.59	-
IIIf2	$CF_2CF(CF_3)C=O \rightarrow CF_3CFC=O + CF_2$	-10.69	-
IIIf3	$CF_2CF(CF_3)C=O \rightarrow CF_2CFC=O + CF_3$	7.67	-
IIIf4	$CF_2CFC=OCF_3 \rightarrow CF_2CFC=O + CF_3$	61.23	-

IIIf5	$CF_2CFC=OCF_3 \rightarrow CF_2CF + CF_3C=O$	82.77	-
IIIf6	$CF_2CFC=OCF_3 \rightarrow CFC=OCF_3 + CF_2$	96.18	-
IIIg1	$CF_3CFC=OCF_2 \rightarrow CF_3CFC=O + CF_2$	5.47	-
IIIg2	$CF_3CFC=OCF_2 \rightarrow CF_3CF + CF_2C=O$	68.76	-
IIIg3	$CF_3CFC=OCF_2 \rightarrow CFC=OCF_2 + CF_3$	77.47	-
IVa1	$CF_3CF \rightarrow CF_2=CF_2(C_2F_4)$	-41.36	30.96
IVa2	$CF_3CF \rightarrow CF_3 + CF$	65.30	-
IVa3	$CF_3CF \rightarrow CF_2CF + F$	110.51	-
IVa4	$CF_3CF \rightarrow CF_3C + F$	150.19	-
IVa5	$CFC=O \rightarrow CF + CO$	30.77	-
IVa6	$CF_3CC=O \rightarrow CF_3C + CO$	63.55	-
IVa7	$CF_2CFC=O \rightarrow CF_2 + CFC=O$	57.09	-
IVa8	$CF_2CFC=O \rightarrow CF_2CF + CO$	18.21	-
IVb1	$CF_3CFC \rightarrow CF_3 + CFC$	57.64	-
IVb2	$CF_3CFC \rightarrow CF_3CF + C$	145.94	-
IVb3	$CF_3CCF_3 \rightarrow CF_2=CFCF_3(C_3F_6)$	-64.51	14.31
IVb4	$CF_3CCF_3 \rightarrow CF_3C + CF_3$	63.63	-
IVg1	$CFC=OCF_2 \rightarrow CFC=O + CF_2$	3.44	-
IVg2	$CFC=OCF_2 \rightarrow CF_2C=O + CF$	56.59	-
Va1	$CF_2=CF_2(C_2F_4) \rightarrow CF_2 + CF_2$	58.11	-
Va2	$CF_2=CF_2(C_2F_4) \rightarrow CF_2CF + F$	151.87	-
Va3	$CF_2CF \rightarrow CF_2 + CF$	69.65	-
Va4	$CF_3C \rightarrow CF_2CF$	-39.68	15.66
Va5	$CF_3C \rightarrow CF_3 + C$	91.93	-
Vb1	$CFC \rightarrow CF + C$	153.60	-
Vb2	$CF_2=CFCF_3(C_3F_6) \rightarrow CF_2CF + CF_3$	88.46	-
Vb3	$CF_2=CFCF_3(C_3F_6) \rightarrow CF_3CF + CF_2$	92.81	-
Vg1	$CF_2C=O \rightarrow CF_2 + CO$	-22.37	-

It can be seen from Table 4.9 that some of the reaction enthalpies involving the breaking of the C-C bond at the α-position of the carbonyl group are negative, indicating that the breaking reaction of the C-C bond at the α-position of the carbonyl group in these reactions is exothermic and proceeds spontaneously at room temperature. Therefore, the reaction pathways in the dissociation pathway of the $C_5F_{10}O$ molecule in Figure 4.23 juxtaposed with the reaction pathways IIa5, IIc1, IIIa6, IIIf1 and Vg1 will not occur in the actual decomposition process. And the $CF_3CF(CF_3)C=O$ particles produced by the reaction pathway Ia1 will directly decompose through the reaction pathway IIa5 to generate CF_3CFCF_3 and CO. The $CF_3C=O$ particles generated by the reaction pathway Ic1 will directly decompose through the reaction pathway IIc1 to generate CF_3 and CO. Reaction paths Ia and Ic produce identical dissociated particles via the break of the C-C bond.

Figure 4.25 shows the enthalpy of the primary dissociation reaction of the $C_5F_{10}O$ molecule. Among the seven primary dissociation paths listed in this manuscript, the enthalpies of four dissociation paths, Ib1, Id1, If1 and Ig1, are significantly higher than those of the other three paths. Among them, the dissociation of carbonyl group in the Ib1 path is the most difficult, and the C=O double bond breaking requires an energy of 193.13 kcal/mol. The enthalpies of

the three dissociation paths, Ia1, Ic1 and Ie1, are lower, and the calculated results are basically consistent with the literature [70]. $C_5F_{10}O$ molecules decomposed through paths Ia1 and Ic1 and spontaneously reacted to generate CF_3CFCF_3, CF_3 and CO three particles. The total energy required for this process is only 47.76kcal/mol, which is the path with the lowest energy among all decomposition reactions. During the dissociation process of $C_5F_{10}O$ molecules, the decomposition of $C_5F_{10}O$ molecules will mainly form decomposition products through these two paths when the external electric field strength or temperature is low, and $C_5F_{10}O$ molecules can undergo hydrolysis reactions with water at room temperature through this path. This is also verified by the fact that the decomposition products C_3HF_7, C_3F_6O and CHF_3 containing CF_3CFCF_3, CF_3 and CO particles are first detected in the previous stability experiment of the interaction of $C_5F_{10}O$ gas with metal materials.

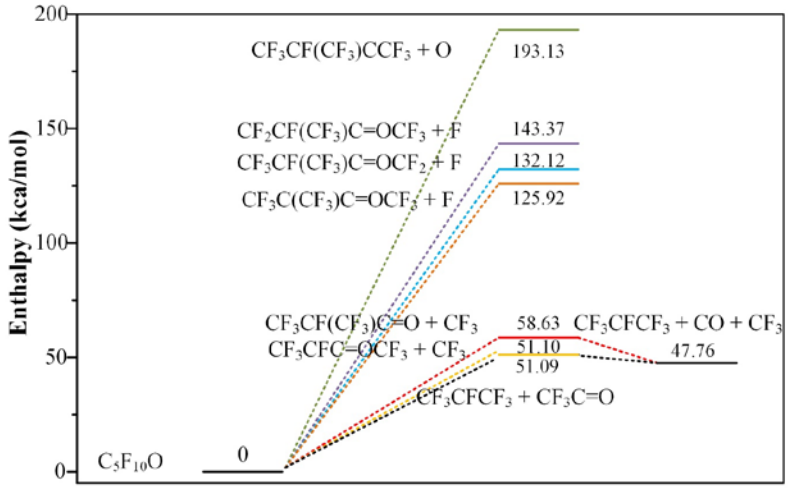

Figure 4.25 The enthalpy of the primary dissociation reaction of the $C_5F_{10}O$ molecule (T=298.15K)

Due to the large size of $C_5F_{10}O$ molecules, the main particles generated through the primary dissociation path are still macromolecules, and further dissociation reactions will occur under conditions such as discharge and high temperature. Therefore, this manuscript discusses the re-dissociation process of the primary particles generated by the primary dissociation of the $C_5F_{10}O$ molecule. Figure 4.26 shows the enthalpy of the dissociation reaction of the most easily generated CF_3CFCF_3 particles in the primary dissociation process of the $C_5F_{10}O$ molecule. It can be seen that the dissociation of CF_3CFCF_3 particles via path IIIa10 to form CF_3CF and CF_3 particles only needs to absorb 70.95 kcal/mol of energy, which is the lowest among the three dissociation paths. CF_3CF particles can also continue to dissociate to form smaller particles or to form the isomer C_2F_4 through the transition state reaction of pathway IVa1. The enthalpy of CF_3CFCF_3 particles dissociating to form C_2F_4 gas and CF_3 particles is only 29.59 kcal/mol. Therefore, C_2F_4 gas is also an important intermediate product of $C_5F_{10}O$ molecule decomposition. The enthalpy of CF_3CFCF_3 particles to form CF_3CCF_3 particles and F through IIIa9 is 157.51 kcal/mol, which is the most difficult dissociation reaction for CF_3CFCF_3 particles. The enthalpy of CF_3CFCF_3 particles to directly dissociate to form CF_2CFCF_3 (C_3F_6) gas and F is 93.00 kcal/mol, which is much lower than the energy absorbed by CF_3CFCF_3 particle through IIIa9 to form CF_3CCF_3 particle and F, and then through the transition state reaction IVb3 to cross the energy barrier of 14.31 kcal/mol to form the isomer CF_2CFCF_3 (C_3F_6).

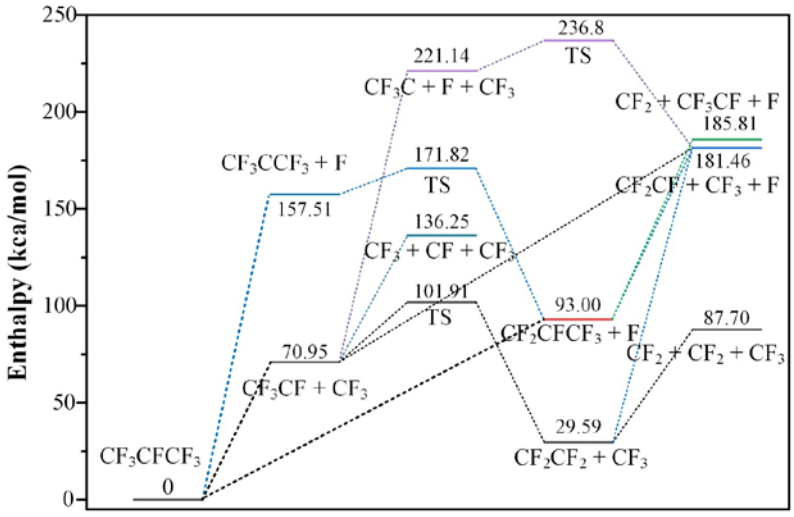

Figure 4.26 Enthalpy of dissociation reaction of CF_3CFCF_3 particle (T=298.15K)

Figure 4.27 shows the enthalpy of the re-dissociation reaction of $CF_3CFC=OCF_3$ particle generated by the dissociation pathway of Ie1. It can be seen that $CF_3CFC=OCF_3$ particle will dissociate by absorbing 70.94 kcal/mol of energy through path IIe2 to generate CF_3CF and CF3C=O particles. $CF_3C=O$ particle is unstable and will decompose into CF_3 and CO particles and release 3.33 kcal/mol of energy. $CF_3CFC=OCF_3$ particle will also dissociate by absorbing 26.69 kcal/mol of energy through path IIe3 to generate $CF_3CFC=O$ and CF_3 particles, and $CF_3CFC=O$ particle absorb 40.92 kcal/mol of energy to dissociate to generate CF_3CF and CO particles. $CF_3CFC=OCF_3$ particle will dissociate through paths IIe2 and IIe3 to obtain the same particles, but the energy absorbed during the dissociation process is different, and the energy absorbed by the dissociation path IIe3 is lower.

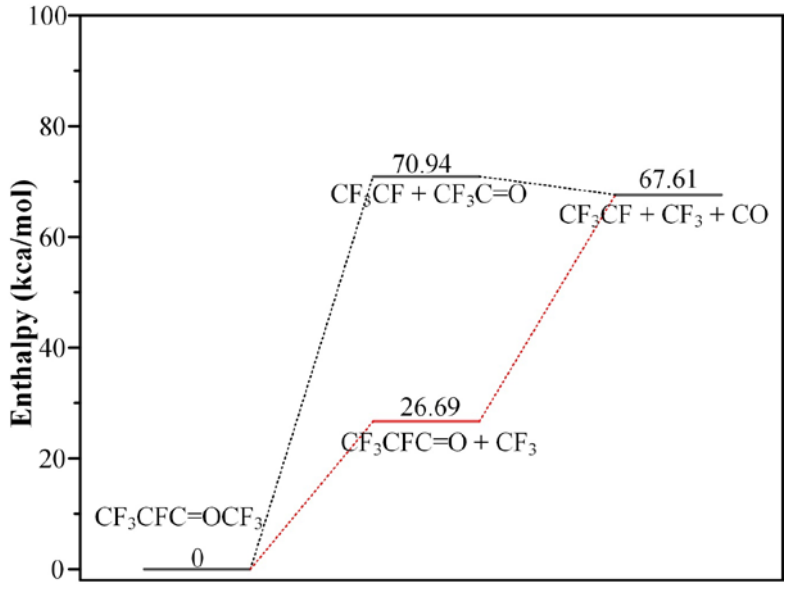

Figure 4.27 Enthalpy of dissociation reaction of Ie1-$CF_3CFC=OCF_3$ particle (T=298.15K)

Figure 4.28 shows the enthalpy of the re-dissociation reaction of $CF_3C(CF_3)C=OCF_3$ particle generated by the dissociation pathway of Id1. $CF_3C(CF_3)C=OCF_3$ particle will dissociate through path IId1 to generate $CF_3C(CF_3)C=O$ and CF_3 particles, which only need to absorb 1.25 kcal/mol of energy, which is the lowest dissociation path among all paths. In the

actual decomposition process, $CF_3C(CF_3)C=OCF_3$ particle is easily decomposed by IId1. The dissociation of $CF_3C(CF_3)C=O$ particle to form CF_3CCF_3 and CO particles also requires only 78.10 kcal/mol of energy. The continuous decomposition of $CF_3C(CF_3)C=OCF_3$ particle to form CF_3CCF_3, CF_3 and CO particles requires only 79.35 kcal/mol of energy, which is the path with the lowest energy among all dissociation paths.

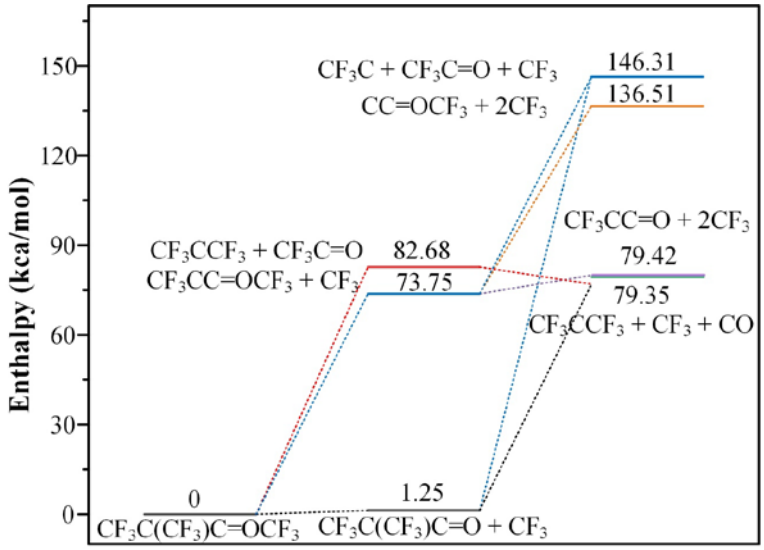

Figure 4.28 Enthalpy of dissociation reaction of Id1-$CF_3C(CF_3)C=OCF_3$ particle (T=298.15K)

Figure 4.29 shows the enthalpy of the re-dissociation reaction of $CF_3CF(CF_3)CCF_3$ particle generated by the dissociation pathway of Ib1. It can be seen that the energy required for the dissociation of $CF_3CF(CF_3)CCF_3$ particle through pathways IIb1, IIb2 or IIb3 is about 70 kcal/mol, while the energy required for the dissociation of CF_3CFCCF_3 and CF_3 particles through pathway IIb4 is only 9.07 kcal/mol, which is the lowest among all pathways. The energy required to generate CF_3CFCF_3, C and CF_3 particles is the highest among the particles produced by the re-decomposition of $CF_3CF(CF_3)CCF_3$, reaching 159.35 kcal/mol. The energy required for the reaction of IIIb1, IVb2, Va5 and Vb1 to generate carbon element is also about 100 kcal/mol or even higher, which is generally higher than the energy required for dissociation to form CF_x particles, indicating that the energy required for $C_5F_{10}O$ molecules to dissociate to form carbon element is higher. Therefore, the conditions required for the decomposition of $C_5F_{10}O$ molecules to produce simple carbon substances are relatively harsh, and only in the event of a serious discharge and thermal faults could lead to the decomposition of $C_5F_{10}O$ molecules to produce simple carbon substances. The decomposition of $C_5F_{10}O/N_2$ gas mixture produced simple carbon substances in the previous AC breakdown experiment, while the decomposition of $C_5F_{10}O/N_2$ gas mixture do not produce simple carbon substances during the corona discharge due to the low discharge energy.

Figure 4.30 shows the enthalpy of the re-dissociation reaction of the $CF_2CF(CF_3)C=OCF_3$ particle produced by the If1 dissociation pathway. It can be seen that the dissociation of $CF_2CF(CF_3)C=OCF_3$ particle through the path IIf2 to form CF_2CFCF_3 and $CF_3C=O$ particles only requires 0.71 kcal/mol. $CF_3C=O$ particle will also release energy at room temperature to re-decompose to generate CF_3 and CO particles. Therefore, $CF_2CF(CF_3)C=OCF_3$ particle will decompose through this path to form CF_2CFCF_3, CO and CF3 particles in the actual decomposition process.

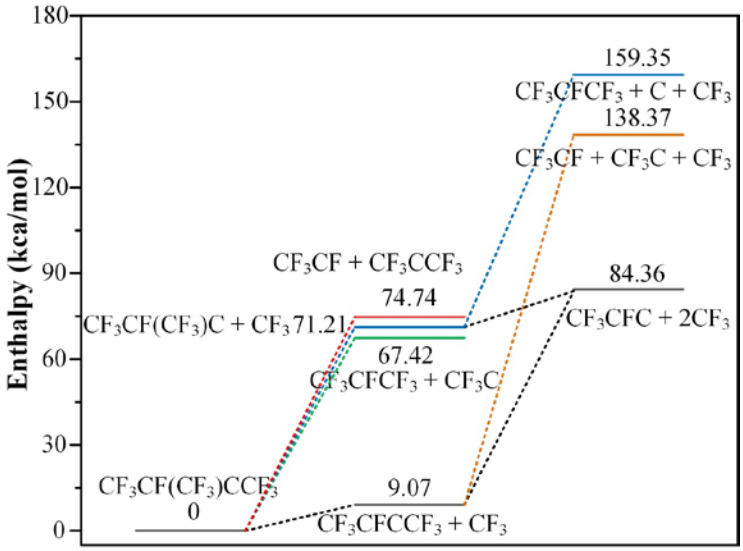

Figure 4.29 Enthalpy of dissociation reaction of Ib1- $CF_3CF(CF_3)CCF_3$ particle (T=298.15K)

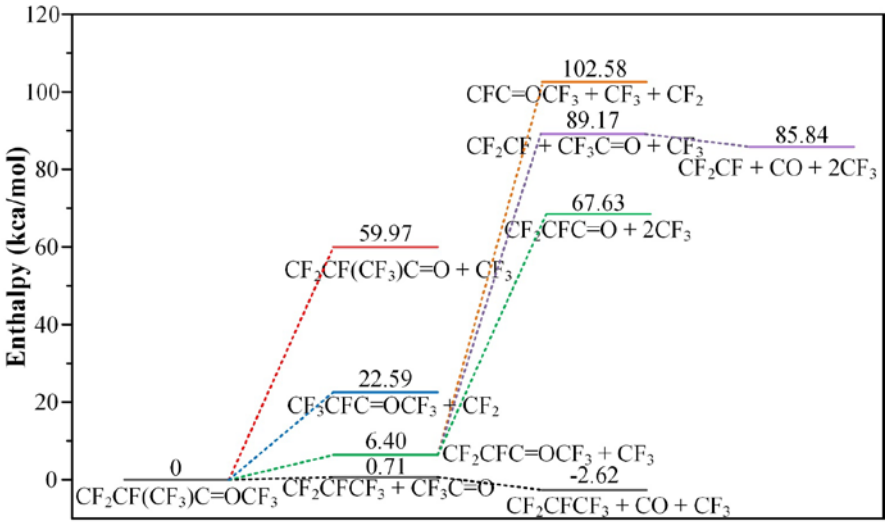

Figure 4.30 Enthalpy of dissociation reaction of If1- $CF_2CF(CF_3)C=OCF_3$ particle (T=298.15K)

Figure 4.31 shows the enthalpy of the re-dissociation reaction of $CF_3CF(CF_3)C=OCF_2$ particle generated by the dissociation pathway of Ig1. It can be seen that the energy required for dissociation of $CF_3CF(CF_3)C=OCF_2$ particle through paths IIg1 and IIg3 are similar(55.06 kcal/mol and 52.87 kcal/mol, respectively), and slightly higher than that required for dissociation through path IIg2 (41.37 kcal/mol). The energy required for the dissociation of CF3CF(CF3)C=OCF2 particle through path IIIg1 to produce CF3CFC=O and CF2 particles (41.37 kcal/mol) is significantly lower than that of the other two paths (77.47 kcal/mol and 68.76 kcal/mol, respectively). However, the energy required for the dissociation of $CF_3CF(CF_3)C=OCF_2$ particle through path IIg2 to generate $CF_3CF(CF_3)C=O$ and CF_2 particles is only 41.37 kcal/mol, and the dissociated $CF_3CF(CF_3)C=O$ particle can release 10.87 kcal/mol of energy through spontaneous reaction IIa5 to generate CF_3CFCF_3 and CO. The dissociation of $CF_3CF(CF_3)C=OCF_2$ particle to form CF_3CFCF_3, CO and CF_2 particles requires only 30.50 kcal/mol of energy, which is the lowest energy path in all reactions. Therefore, it is easier to form CF_3CFCF_3, CO, and CF_2 particles when $CF_3CF(CF_3)C=OCF_2$ particle undergo continuous decomposition.

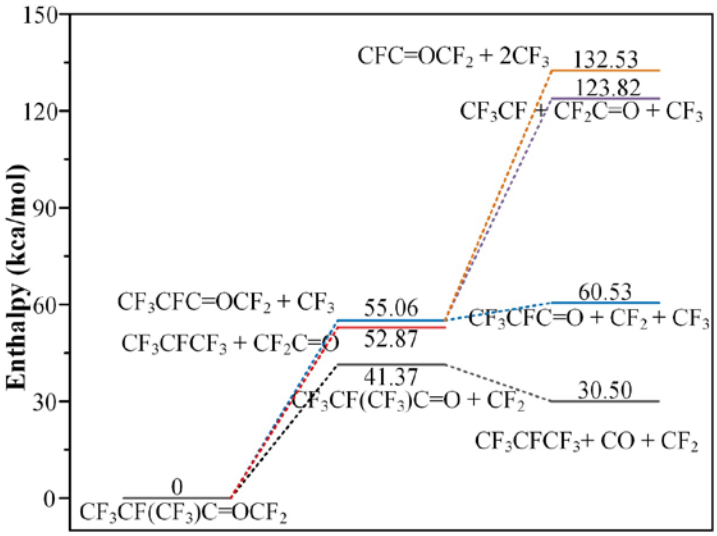

Figure 4.31 Enthalpy of dissociation reaction of Ig1- $CF_3CF(CF_3)C=OCF_2$ particle (T=298.15K)

In summary, CF_3, CO, CF_3CFCF_3, $CF_3CFC=OCF_3$ and $CF_3C(CF_3)C=OCF_3$ are generated when the decomposition of $C_5F_{10}O$ molecule occurs, in which the energy required for the decomposition of the $C_5F_{10}O$ molecule through paths Ia1 and Ic1 to produce the three particles CF_3CFCF_3, CF_3 and CO is the lowest among all paths. The energy required for C-F bond or C=O bond breakage in $C_5F_{10}O$ molecule to form F and O is significantly greater than the energy required for C-C bond breakage. Therefore, in the actual decomposition process, the $C_5F_{10}O$ molecule is more likely to break the α-position C-C bond through the paths Ia1 and Ic1, and the break of the C-F bond or the C=O double bond will only occur when the external electric field strength or temperature is high.

4.5.3 Formation Mechanism of $C_5F_{10}O$ Gas Mixture Decomposition Products

Table 4.10 lists the enthalpy and activation energy of the composite reaction of small particles such as F, C, O, CF_3, and H formed by the dissociation of $C_5F_{10}O$, O_2 and H_2O molecules.

Table 4.10 Generation paths of the main decomposition products of $C_5F_{10}O$

No.	Chemical reaction	Enthalpy (kcal/mol)	Activation energy (kcal/mol)
R1	$CF_3 + H \rightarrow CHF_3$	-104.93	-
R2	$CF_3 + F \rightarrow CF_4$	-151.98	-
R3	$CF_3 + CF \rightarrow CF_2{=}CF_2(C_2F_4)$	-106.66	30.96
R4	$CF_3 + CF_2 + F \rightarrow C_2F_6$	-189.08	-
R5	$2CF_3 \rightarrow C_2F_6$	-74.22	-
R6	$CF_3CFCF_3 + H \rightarrow C_3HF_7$	-98.53	-
R7	$CF_3CFCF_3 + F \rightarrow C_3F_8$	-137.36	-
R8	$CF_3CFCF_3 + CF_3 \rightarrow C_4F_{10}$	-60.58	-
R9	$H + F \rightarrow HF$	-174.99	-
R10	$C + O \rightarrow CO$	-304.73	-
R11	$CO + O \rightarrow CO_2$	-154.06	-

R12	$C + 2O \rightarrow CO_2$	-458.78	-
IVb3	$CF_3CCF_3 \rightarrow CF_2{=}CFCF_3(C_3F_6)$	64.51	14.31
R13	$CF_2{=}CF_2(C_2F_4) + CF_2 \rightarrow CF_2{=}CFCF_3(C_3F_6)$	-51.45	1.64
R14	$CF_3CF + CF_2 \rightarrow CF_2{=}CFCF_3(C_3F_6)$	-92.81	-
R15	$CF_2CF + CF_3 \rightarrow CF_2{=}CFCF_3(C_3F_6)$	-88.46	-
R16	$CF_3C + CF_3 \rightarrow CF_2{=}CFCF_3(C_3F_6)$	-128.14	14.31
R17	$CF_3 + CF_3C{=}O \rightarrow C_3F_6O$	-60.46	-
R18	$CF_3 + CF_3C + O \rightarrow C_3F_6O$	-269.92	-
R19	$2CF_3 + C + O \rightarrow C_3F_6O$	-361.86	-
R20	$CF_2 + O \rightarrow CF_2O$	-181.79	-
R21	$CO + 2F \rightarrow CF_2O$	-217.29	-
R22	$CF + O + F \rightarrow CF_2O$	-345.20	-
R23	$C + O + 2F \rightarrow CF_2O$	-522.02	-

The CF_3 group is the most common group in $C_5F_{10}O$ molecule and fluorocarbon organic molecules, and a large number of CF_3 particle will be generated during the dissociation of $C_5F_{10}O$ molecule. The CF and CF_2 particles produced by the dissociation of $C_5F_{10}O$ molecule release more than 100 kcal/mol of energy by combining with F to form CF_3 particle. Figure 4.32 shows the enthalpy and activation energies of CF_3 particle combined with F, H, CF, and CF_3 to produce CF_4, CHF_3, C_2F_4, and C_2F_6, respectively. The process of compounding CF_3 and CF particles to form C_2F_4 needs to first release 65.30 kcal/mol of energy to form CF_3CF, and then cross the energy barrier of 30.96 kcal/mol. The enthalpy of other compound reactions are all negative, which proceed spontaneously. The recombination of CF_3 particle with F to form CF_4 is the lowest energy recombination pathway among all pathways, and this process releases 151.98 kcal/mol of energy. In addition, the energy released by $C_5F_{10}O$ molecule to generate HF, CO and CO_2 through the reaction paths R9-R12 is also above 150 kcal/mol. Therefore, the simple molecules formed by the composite of these small particles will be the final decomposition products formed by the complete decomposition of $C_5F_{10}O$ molecule. However, it should also be noted that the conditions for the dissociation of $C_5F_{10}O$ molecule to form small particles such as C, F and O are relatively harsh, and the decomposition to form small molecular decomposition products often requires a strong electric field or high temperature to achieve.

Figure 4.33 gives the enthalpy of the primary dissociation of $C_5F_{10}O$ molecule involving the most readily produced CF_3CFCF_3 particle to combine with CF_3, H and F to produce C_4F_{10}, C_3HF_7 and C_3F_8, respectively. The recombination of CF_3CFCF_3 and CF_3 particles through the path R6 to form C_4F_{10} gas released the least energy (-60.58 kcal/mol). The energy released by the recombination of CF_3CFCF_3 particle and H to form C_3HF_7 gas through the path R8 is second (-98.53 kcal/mol). The energy released by the recombination of CF_3CFCF_3 particle and H to form C_3HF_7 gas through the path R8 is second (-98.53 kcal/mol). CF_3CFCF_3 particles recombine with F through path R7 to generate C_3F_8 gas releases 137.36 kcal/mol of energy, which is the path with the highest energy release among the three reaction paths. However, the energy required for the dissociation of $C_5F_{10}O$ molecule to generate CF_3CFCF_3 particle is low, which is not enough to dissociate $C_5F_{10}O$ molecule to generate F. Although the path to generate C_3F_8 gas through R7 recombination releases the most energy, it is more difficult to generate F, which is more difficult to occur in the actual process than the paths R6 and R8 that produce

C_4F_{10} and C_3HF_7. Therefore, the generation of C_3HF_7 by CF_3CFCF_3 particles through the path R8 is the most likely reaction among all paths, and the gas decomposition product of C_3HF_7 is also detected first in the previous experiments.

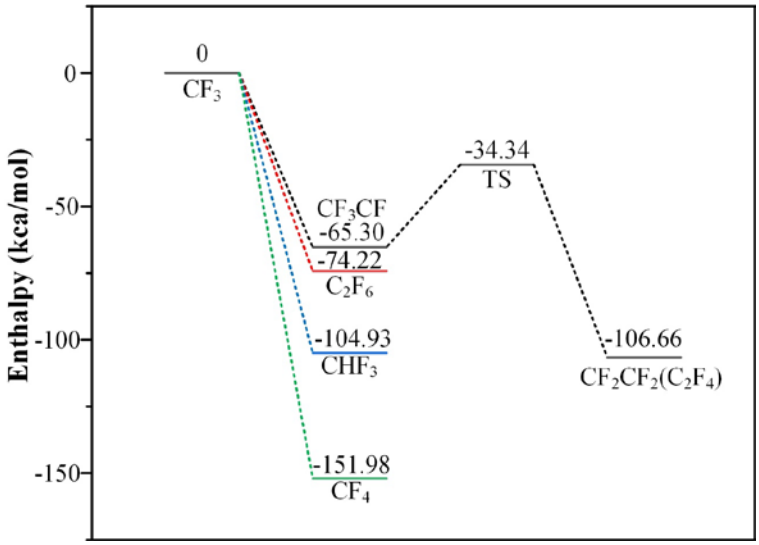

Figure 4.32 The enthalpy of the main composite reaction involving CF_3 particle (T=298.15K)

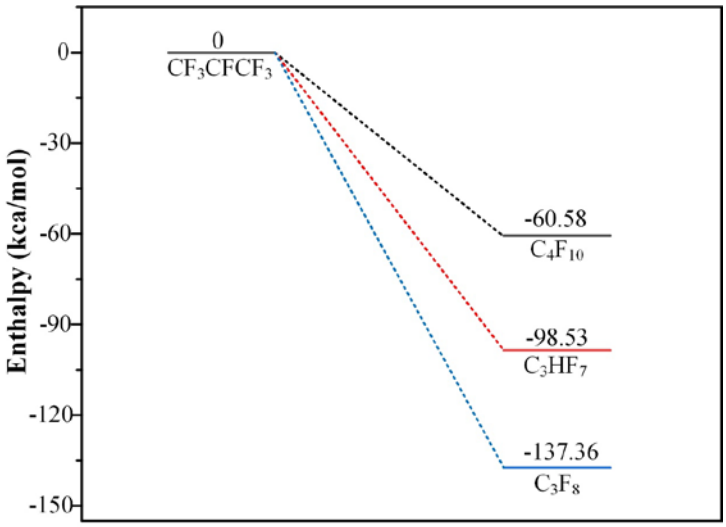

Figure 4.33 The enthalpy of the main composite reaction involving CF_3CFCF_3 particle (T=298.15K)

Figure 4.34 shows the enthalpy and activation energy of C_3F_6 formed by the dissociation of $C_5F_{10}O$ molecule through different pathways. In the previous study on the dissociation pathways of $C_5F_{10}O$ molecule, the pathways of CF_3CFCF_3 and CF_3CCF_3 particles to generate C_3F_6 through dissociation or transition state reaction has been studied. The pathways to C_3F_6 through recombination reactions are also listed here, in which the recombination of CF_3CF and CF_2 particles to form C_3F_6 through path R14 releases the most energy (-92.81 kcal/mol). The energy released by the recombination of CF_2CF and CF_3 particles to form C_3F_6 through path R15 is 88.46 kcal/mol, which is slightly lower than that of path R14. In the process of compounding C_2F_4 and CF_2 particles to generate C_3F_6 gas, it will first absorb 10.54 kcal/mol of energy to form $CF_2CF_2CF_2$, and then cross the energy barrier of 1.64 kcal/mol to convert into C_3F_6 gas.

Figure 4.35 shows the paths and enthalpy of C_3F_6O formed by the recombination of particles generated by the dissociation of $C_5F_{10}O$ molecule. The enthalpy of CF_3 and $CF_3C{=}O$

particles to form C_3F_6O through the path R17 is -60.46 kcal/mol, but the $CF_3C{=}O$ particle is unstable and spontaneously decompose to generate CF_3 and CO. Therefore, the path of the decomposition of $C_5F_{10}O$ molecule to C_3F_6O is closely related to the external conditions. When the external electric field strength or temperature is high, the particles forming C_3F_6O molecules will dissociate to form smaller particles.

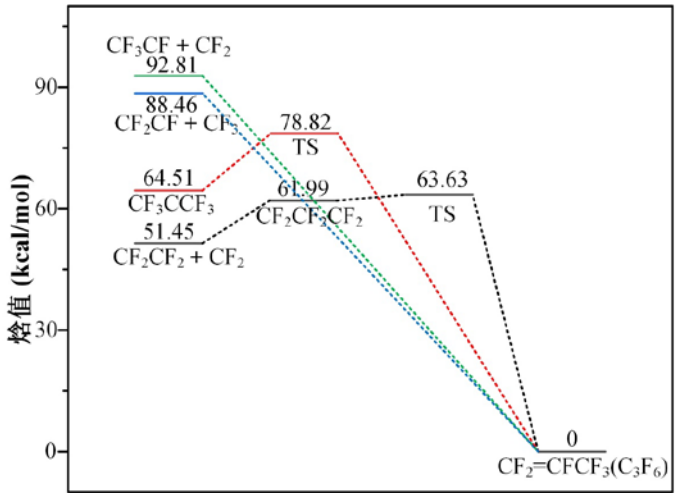

Figure 4.34 Enthalpy of the main generation paths of CF_2CFCF_3 (C_3F_6) (T=298.15K)

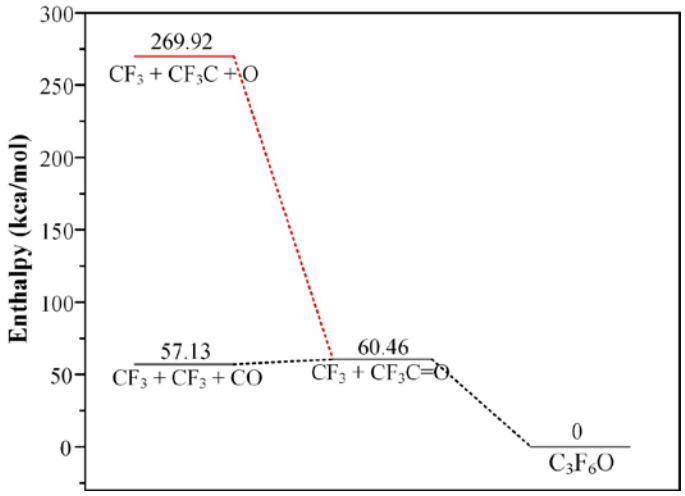

Figure 4.35 Enthalpy of the main generation paths of C_3F_6O (T=298.15K)

Figure 4.36 shows the paths and enthalpy of the particles generated by the dissociation of $C_5F_{10}O$ molecule to form CF_2O. The enthalpy of CF_2 and O through the path R20 or CO and F through the path R21 to generate CF_2O is about 200 kcal/mol, which is greater than that the enthalpies of most composite reactions. However, since CF_2O molecule contains oxygen atom, the generation of CF_2O molecule is closely related to oxygen. O and F required to generate CF_2O cannot be formed when the gas mixture does not contain oxygen or the external electric field strength is low, while the CO required to form CF_2O will undergo oxidation reaction to form CO_2 when oxygen is sufficient and the external electric field strength is high. The pathway for recombination to form CF_2O will be mainly the path R20.

In summary, the reactions of F, CF, CF_2 and CF_3 particles generated by the dissociation of $C_5F_{10}O$ molecules and H and O particles formed by the dissociation of H_2O and O_2 to form characteristic decomposition products such as HF, CO, CO_2, CF_4, CHF_3, C_2F_4, C_2F_6, C_4F_{10}, C_3HF_7, C_3F_8, C_3F_6O and CF_2O will all proceed spontaneously. The energy released by the

compound reaction to generate the gas with larger molecular weight is generally lower than that of the compound reaction of the small molecule gas, but the generation conditions of the reaction particles required to generate the small molecule gas are also higher. Therefore, macromolecular gas products such as C_4F_{10}, C_3HF_7, C_3F_8 and C_3F_6O are the primary products of the decomposition of $C_5F_{10}O$ molecule. When the external conditions can provide more energy, the decomposition of $C_5F_{10}O$ molecule will be more thorough and form small molecular gas products such as HF, CO, CO_2, CF_4.

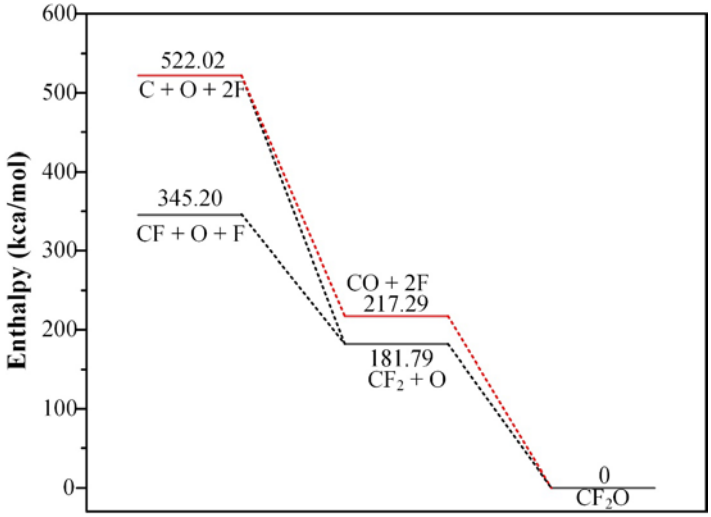

Figure 4.36 Enthalpy of the main generation paths of CF_2O (T=298.15K)

4.6 Chapter Summary

In this chapter, based on the structural characteristics of $C_5F_{10}O$, N_2 and O_2 molecules, the molecular structural properties of the $C_5F_{10}O/N_2/O_2$ gas mixture are first studied. Then, the interaction mechanism between $C_5F_{10}O$ and metal materials is studied by constructing the gas-solid interface interaction model between $C_5F_{10}O$ and metal materials copper, aluminum and silver. Finally, the decomposition mechanism and product generation mechanism of $C_5F_{10}O/N_2/O_2$ gas mixture are investigated by constructing the dissociation and decomposition product composite paths of $C_5F_{10}O$ molecules considering the effects of micro-water and oxygen in the equipment, and the following conclusions are obtained.

1) The bond energy of the carbonyl C=O double bond of $C_5F_{10}O$ molecule is the largest, while the strength of the two C-C bonds connected to the carbonyl group is the weakest, which is most likely to break during the decomposition of $C_5F_{10}O$. The electrophilic region of $C_5F_{10}O$ molecule is also mainly concentrated around the carbonyl group.

2) The carbonyl oxygen atom of the $C_5F_{10}O$ molecule has high chemical reactivity, and the electron orbital overlap and charge transfer occur during the interaction with the Cu(1 1 1) surface. During the interaction process, the 3d and 4s orbitals of the copper atom and the 2p orbital of the carbonyl oxygen atom of the $C_5F_{10}O$ molecule are hybridized and formed chemical bonds mainly in the Top position. The interaction of $C_5F_{10}O$ molecule with Cu_2O(1 1 1) formed by oxidation of copper also forms chemical bonds mainly by the hybridization of the Top site with the 3d orbital of the unsaturated coordination Cu+ cation. The adsorption of $C_5F_{10}O$ molecule and Ag(1 1 1) surface belongs to physical adsorption, and the interaction stability of $C_5F_{10}O$ and Ag is more stable.

3) During the interaction between the $C_5F_{10}O$ molecule and Al_2O_3 (1 1 1), the positive charge of the aluminum atom will attract the carbonyl oxygen atom of the $C_5F_{10}O$ molecule and repel the fluorine atom. In the interaction process, a large adsorption energy is generated due to the interaction of positive and negative charges, but no charge transfer occurs. The interaction between $C_5F_{10}O$ molecule and Al_2O_3(1 1 1) belongs to physical adsorption.

4) When the decomposition of $C_5F_{10}O$ molecule occurs, the two α-position C-C bonds connected with the carbonyl group will be the first to break to form particles such as CF_3, CO and CF_3CFCF_3, and react with the micro-water inside the equipment to form primary decomposition products such as C_4F_{10}, C_3HF_7 and C_3F_6O. The further dissociation of $C_5F_{10}O$ molecules will produce F, CF, CF_2 and CF_3 particles and composite to form C_3F_8 and small molecular gas products such as HF, CO, CO_2 and CF_4. The formation rules of each decomposition product are consistent with the experimental results.

5 Application Safety Assessment Considering $C_5F_{10}O/N_2/O_2$ Gas Mixture Decomposition and Biosafety

IEC62271-200 [116] stipulates that the annual gas leakage rate of GIE should be no more than 0.1%, while some low- and medium-voltage gas-insulated equipment such as LBS are usually used in an indoor environment, which may cause the gas leakage of GIE to gather if the indoor ventilation is poor. In addition, PD, POF and insulation breakdown of GIE can cause the decomposition of internal insulation gas, which may even lead to serious accidents of internal gas leakage. Therefore, evaluating the biosafety of $C_5F_{10}O$ and its decomposition products before the large-scale application of $C_5F_{10}O$ GIE is essential to safeguard the health and lives of workers.

This chapter considers the biosafety of $C_5F_{10}O$ gas and its decomposition products under the action of arc, and firstly studies and analyzes the biosafety of $C_5F_{10}O$ gas. Then, the arc characteristics of $C_5F_{10}O/N_2/O_2$ gas mixture are studied using LBS, and the gaseous and solid decomposition products under the action of the arc are analyzed. Finally, the biosafety of the gaseous decomposition gas produced by $C_5F_{10}O$ under the action of arc is studied, and the feasibility and safety of $C_5F_{10}O$ gas mixture engineering application are evaluated based on the electrothermal decomposition characteristics and biosafety results of $C_5F_{10}O$ gas, and relevant safety protection measures and suggestions are put forward.

5.1 Biosafety of pure $C_5F_{10}O$ gas

5.1.1 Biosafety test platform

The acute inhalation toxicity test platform for $C_5F_{10}O$ was shown in Figure 5.1. The exposure chamber is a cube (40cm×30cm×20cm) sealed by a transparent Acrylic board with a circular observation window set on the front. A gas recovery device is installed at the outlet to collect exhaust gas. The dynamic gas sample compounder was used to prepare $C_5F_{10}O$ gas mixture with different concentration and flow rate in real time for exposure based on the mass flow conversion method.

Relevant tests were conducted in accordance with the standard for gas acute inhalation tests in the Organization for Economic Cooperation and Development (OECD, 2009) Guideline 403 and “Biotoxication tests by Sulphur hexafluoride” (DL/T 921-2005) [117]. Briefly, mice (5 mice per group) were selected as the test animal and the acute toxicity inhalation exposure period was set at 4h. The content of $C_5F_{10}O$ for engineering application gas mixture is in the range of 5~13.6% considering the working temperature of GIE, while the concentration around the equipment surrounding environment depends on the severity of gas leakage fault. Herein, we conducted acute inhalation test for gas mixture with 0.6%~1% (6000-10000ppm) $C_5F_{10}O$ based on the data disclosed in Reference and relevant test conditions were given in Table 5.1. During the experiment, the flow rate of $C_5F_{10}O$ gas mixture was set to 3000mL·min^{-1} to ensure the inflation volume not less than 1/8 of the exposure chamber. After exposure, the samples were transferred to the animal room for 14 days observation and their health status were recorded. The sample that died during the 14-day observation period was dissected immediately and the target organs including heart, liver, spleen, lung, kidney, brain, intestine,

skin, eye were collected for further analysis. All the samples were euthanized at the end of observation period.

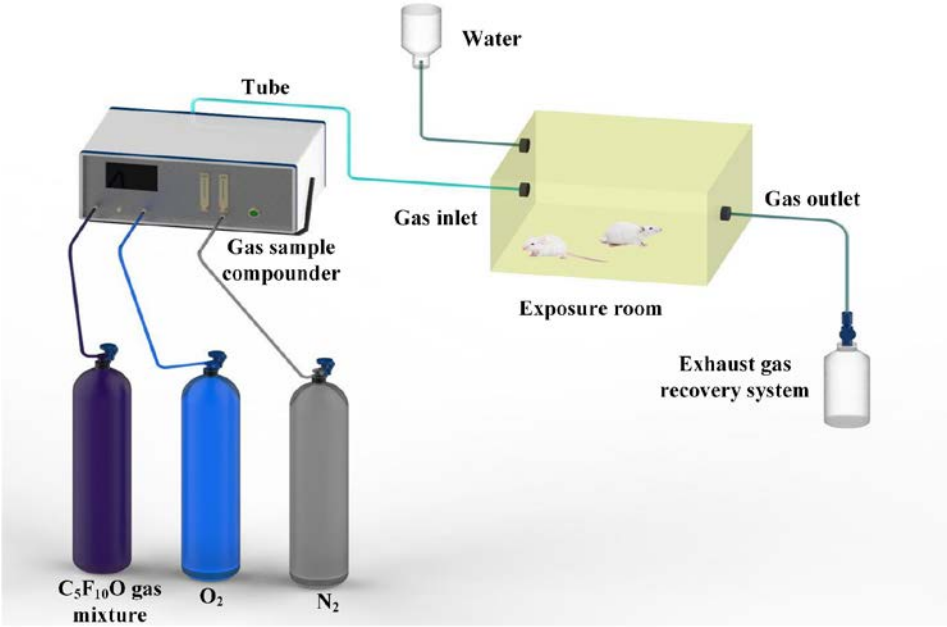

Figure 5.1 Schematic of acute inhalation toxicity test platform

The inbred mice were provided by Hubei Provincial Animal Experimental Center, which were quarantined by Guangdong Provincial Animal Quality Monitoring Institute and belonged to Specific pathogen Free (SPF) animals. All mice are 8 weeks old with the weight 20-22g (male) and 20-22g (female). The $C_5F_{10}O$ used was provided by 3M with a purity ⩾99.5%. And high-purity oxygen and nitrogen are provided by Wuhan Niuride Special Gas Co., Ltd with purity 99.999%. The LC50 of $C_5F_{10}O$ gas were calculated based on the straight-line interpolation method [118]. The collected organs and tissues were observed under an optical microscope (Microscope model: NIKON Eclipse ci, imaging system: NIKON digital sight DS-FI2, MADE IN JAPAN) after dehydration, embedding, preparation and hematoxylin-eosin staining (HE), and the main lesions were photographed for pathological section analysis. The experiment was carried out with the assistance of the Medical Science Research Center of Zhongnan Hospital, Wuhan University.

Table 5.1 Acute inhalation toxicity test conditions of $C_5F_{10}O$ gas

No.	$C_5F_{10}O$ concentration (ppm)	Sample composition	$C_5F_{10}O$ concentration (ppm)	Sample composition	Background gas content	Exposure period
1	0	5 female mice	0	5 male mice	N_2+21%O_2	4h
2	6000	5 female mice	7000	5 male mice	N_2+21%O_2	4h
3	7000	5 female mice	8000	5 male mice	N_2+21%O_2	4h
4	7300	5 female mice	8500	5 male mice	N_2+21%O_2	4h
5	7400	5 female mice	8600	5 male mice	N_2+21%O_2	4h
6	7500	5 female mice	8800	5 male mice	N_2+21%O_2	4h
7	8000	5 female mice	9000	5 male mice	N_2+21%O_2	4h
8	10000	5 female mice	10000	5 male mice	N_2+21%O_2	4h

5.1.2 Biosafety test results

1 Health status and body weight change after acute inhalation of $C_5F_{10}O$

We firstly conducted acute inhalation toxicity tests and no sample was died during 4h exposure in all the test groups. However, we found that samples exposed to low concentration of $C_5F_{10}O$ (female less than 7400ppm, male less than 8600ppm) were particularly sensitive to external stimuli. The mice will be extremely excited when contacted with each other, screaming and jumping up or down in the animal cage, accompanied by clinical manifestations such as increased heartbeat and respiratory rate. This may due to the nervous system injury caused by acute inhalation of $C_5F_{10}O$. The above abnormal behavior disappeared within 5 hours and the mice can drink or eat normally during the 14-day observation period without any dead individuals.

The samples exposed to higher concentration of $C_5F_{10}O$ (higher than 8000ppm for females, 9000ppm for males) for 4 hours demonstrated a paralyzed state (The clinical symptoms of mice are recorded as shown in Table 5.2). The mice hardly respond to external stimuli, showing low heartbeat and breathing rates and cannot eat or drink spontaneously. Dead samples were found within the first three days of the observation period. For example, female mice exposed to 7500ppm $C_5F_{10}O$ died (#1 and #3 sample) on the third day, male mice exposed to 8800 ppm $C_5F_{10}O$ (#5 sample) died on the second day and the remaining samples died within 24 hours (Day 1) of the observation period. The above-mentioned phenomena indicate that $C_5F_{10}O$ has neurotoxicity, which causes loss of athletic ability, mobility disorder and even death.

Table 5.2 Clinical symptoms of mice after acute inhalation of $C_5F_{10}O$

	Very sensitive, nervous, screaming (+)	Autonomous activity (*)	Terrified hair	Increased breathing and pulse
Compare group	-	-	-	+
6000 ppm (Female)	-	+	-	+
7000ppm (Female)	+ +	+	-	+
7300ppm (Female)	+	+	-	+
7400ppm (Female)	+ +	+	+	+ +
7500ppm (Female)	+	+	+	+ +
8000ppm (Female)	-	-	+	-
10000ppm (Female)	- -	- -	+ +	-
7000ppm (Male)	+	+	-	+
8000ppm (Male)	+	+	-	+
8500ppm (Male)	-	+	+	+ +
8600ppm (Male)	-	-	+	+ +
8800ppm (Male)	+	-	+	+
9000ppm (Male)	- -	-	+ +	-
10000ppm (Male)	- -	- -	+ +	-

The change of body weight during the test period is an important indicator to reflect the health condition of mice after $C_5F_{10}O$ exposure. As shown in Figure 5.2, the body weight of mice decreased after 4h acute inhalation toxicity test, which is due to its defecation, urination and no food supply during the exposure (OECD 403 recommends only provide water during exposure). During observation period, all the surviving samples were able to move and eat. The body weight for samples in the female 7500ppm exposure group and male 8800ppm exposure group began to increase after a continuous decline during the two days observation. And the body weight of the other test groups started to increase on the first day after 4h exposure and returned to the pre-test level quickly. In addition, the body weight loss of all the samples did not exceed 20% of their initial value and all surviving samples exceeded their pre-test weight at the end of observation period.

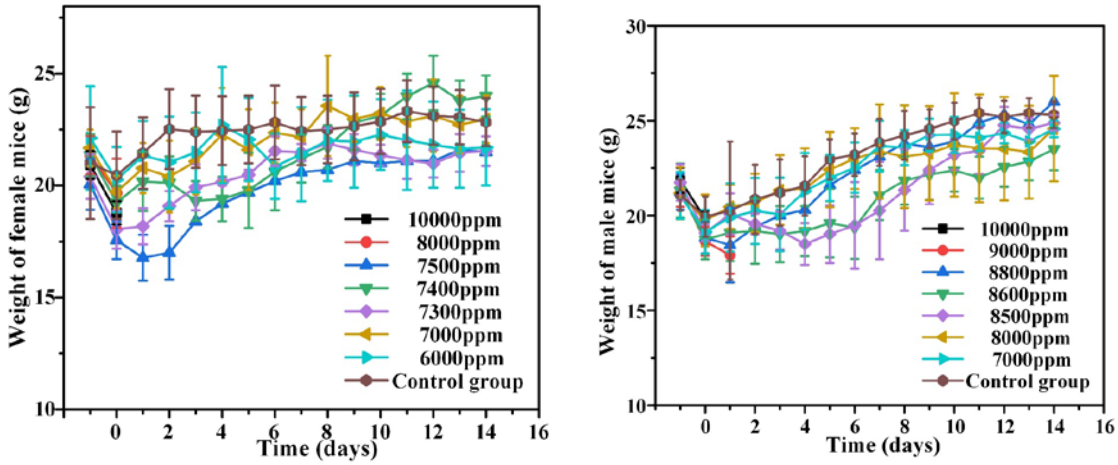

(a) Body weight change of female mice (b) Body weight change of male mice

Figure 5.2 Body weight change of mice after $C_5F_{10}O$ exposure

Gender differences in the weight change during the observation period can be found. Male mice showed a continuous increase in weight during the 14-day observation period, while the weight changes of all female mice stabilized after the 6th day. Actually, the male, female samples used for test is similar and the weight of adult male mice was generally heavier than that of female ones. At the end of observation period, the body weight of male mice was higher than that of female ones and the body weight of female ones reached to its normal value after 6th day. Thus, acute inhalation of $C_5F_{10}O$ haven't show long-term effects on mice.

2 LC50 of $C_5F_{10}O$

The survival status of mice after the end of observation period is shown in Figure 5.3. For female groups, the survival rate was 100% when the exposure concentration is lower than 7400ppm. When the $C_5F_{10}O$ concentration reaches 7500ppm, 4 mice died within 3 days and only one mouse safely passed the 14-day observation period. For higher exposure conditions (7600 ppm), all the mice died within 24h after 4h acute inhalation.

As to male samples, we found that the survival rate was 100% when $C_5F_{10}O$ concentration is lower than 8600 ppm. When the exposure concentration reaches to 8800 ppm, only one mouse passed the 14-day observation period safely. For higher exposure content ($\geqslant$9000 ppm), all mice died within 24h after 4h acute inhalation of $C_5F_{10}O$.

Based on the above-mentioned results, we calculated and obtained the LC50 value of $C_5F_{10}O$ [118]. Briefly, the 4h acute inhalation toxicity LC50 of $C_5F_{10}O$ gas was 7461ppm (female)

and 8724ppm (male). And the tolerance of male mice to $C_5F_{10}O$ is stronger than that of female ones.

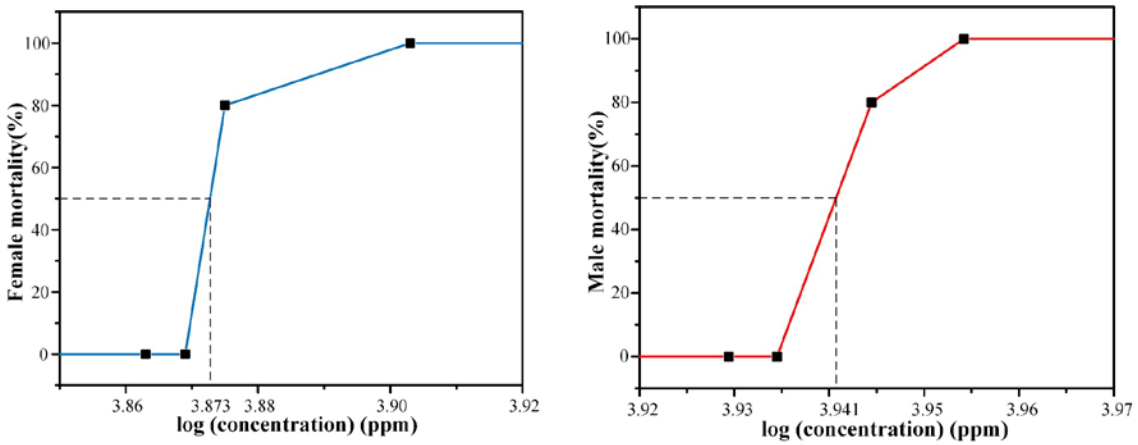

(a) The LC50 of female mice (b) The LC50 of male mice

Figure 5.3 The LC50 value of $C_5F_{10}O$

3 Analysis of results of blood and organ tissue samples

In order to further reveal the effect of $C_5F_{10}O$ on physiological indicators and vital organs of mice, we dissected the mice and extracted blood and organ samples for further analysis. Table 5.3 demonstrates blood analysis results. It can be seen that multiple routine blood test indicators of the dead mice were abnormal after acute inhalation of $C_5F_{10}O$, especially related parameters that related to red blood cell (oxygen transportation) deviated from the normal value seriously, which led to low oxygen concentration in the blood rapidly death due to acute hypoxia. The surviving samples also has high hemoglobin (HGB) and red blood cell pressure (HCT) after 4h acute inhalation of $C_5F_{10}O$ and their value returned to normal at the end of observation period. Erythrocytes are the main transport carriers for oxygen transportation and hemoglobin is deeply involved in the aerobic respiration of cells. Therefore, $C_5F_{10}O$ demonstrates acute injury to the heart and lung function (clinical manifestations: rapid breathing and increased heart rates).

Table 5.3 Blood routine examination results before and after acute inhalation of $C_5F_{10}O$ gas in mice

Parameter	Control group	Live (day 0)	Live (day 14)	Died	Unit	Reference value
WBC	5.8	8.4	9.5	13.7	10^9/L	0.8-6.8
Lymph#	4.7	5.7	7.7	10.4	10^9/L	0.7-5.7
Mon#	0.1	0.7	0.2	0.5	10^9/L	0.0-0.3
Gran#	1	2	1.6	2.8	10^9/L	0.1-1.8
RBC	8.03	10.02	8.9	3.32	10^{12}/L	6.36-9.42
HGB	132	158	138	167	g/L	110-143
HCT	41.7	51.7	43.1	16.1	%	34.6-44.6
MCV	52	51.6	48.5	48.6	fL	48.2-58.3
MCH	16.4	15.7	15.5	50.3	pg	15.8-19
MCHC	316	305	320	1037	g/L	302-353
RDW	13.1	14.5	13.1	34.4	%	13-17
PLT	539	970	619	586	10^9/L	450-1590
MPV	6.8	8.4	6.7	5.5	fL	3.8-6.0

The number of white blood cell (WBC) in the surviving mice was higher than the reference value, mainly originate from the number of monocytes (Mon#) and neutrophils (Gran#). Considering the important role of monocytes and neutrophils in the immune system, their high counts indicate that inhalation of $C_5F_{10}O$ triggers acute inflammation in mice and the immune protection mechanism produces a response. After the 14-day observation period, WBC in the test groups were still high, which is mainly because the lymphocytes (Lymph#) was higher than the reference range (0.7-5.7). The counts of Mon# and Gran# returned to normal at the end of observation period. The high concentration of lymphocytes implies to the specific immune system was triggered and induced the body to produce an immune response, thereby enhancing the mice's immune function. In addition, the mean platelet volume (MPV) was also higher than the normal reference range (3.8-6.0) after exposure. Considering the control group also has the same phenomenon, the abnormal value may due to the physique of mice.

On the whole, the mice have acute inflammation after acute inhalation of $C_5F_{10}O$, which is manifested by an increase of white blood cells related to the immune system (Mon# and Gran#) and red blood cells related to the respiratory system (HGB and HCT). During the 14-day observation period, the mice had basically returned to normal various functions through self-regulation. While the number of white blood cells in the body was still high, indicating that the inflammation caused by $C_5F_{10}O$ still exists.

Table 5.4 shows the autopsy results of mice that died within the 14-day observation period. The dead samples in 7500ppm female test group had excrement in their intestines (with no fluid accumulation) as well as slight bloating in the stomach and bleeding in the lungs. Female mice exposed to 8000 ppm, 10000 ppm $C_5F_{10}O$ for 4h all suffered from intestinal effusion, accompanied by flatulence and pulmonary hemorrhage. For male groups, the dead mice exposed to 8800ppm, 9000ppm and 10000ppm $C_5F_{10}O$ also had intestinal effusion, flatulence and pulmonary hemorrhage. Actually, intestinal effusion could cause dehydration, diarrhea as well as excessive water loss in plasma, resulting in increased red blood cell and hemoglobin count. In addition, the mice that survived 14-day observation period revealed no obvious abnormalities in all organs. Overall, inhaling a lethal dose $C_5F_{10}O$ (higher than LC50) could cause intestinal effusion, flatulence and pulmonary hemorrhage. Although male mice can tolerate higher $C_5F_{10}O$ than female ones, the severity of clinical symptoms were basically the same.

Table 5.4 Autopsy results of the dead mice after acute inhalation of $C_5F_{10}O$

	Intestinal effusion or gaseous distention	Gastric distention	Pulmonary hemorrhage
Control group (Female & Male)	-	-	-
Surviving mice	-	-	-
7500ppm (Female)	-	+	+
8000ppm (Female)	+	+ +	+
10000ppm (Female)	+ +	+ +	+ +
8800ppm (Male)	+	+ +	+
9000ppm (Male)	+	+ +	+ +
10000ppm (Male)	+	+ +	+ +

Further analysis on the toxicity mechanism of $C_5F_{10}O$ on mice organs was conducted based on the pathological section. Organ tissue slices of the control group and test group were divided into three categories. The first category belongs to the control group or the test group with 7400ppm $C_5F_{10}O$ for female group (or 8600ppm for male group). All samples were survived and no significant difference was observed in the pathological section results. (label as low concentration test group or control group). The second category denotes the test female test group with 7500ppm $C_5F_{10}O$ (or 8800ppm for male group) and the surviving mice showed lesions in their organs (label as medium concentration test group). The third category refers the mice that died within the 14-day observation period (label as high-concentration test group).

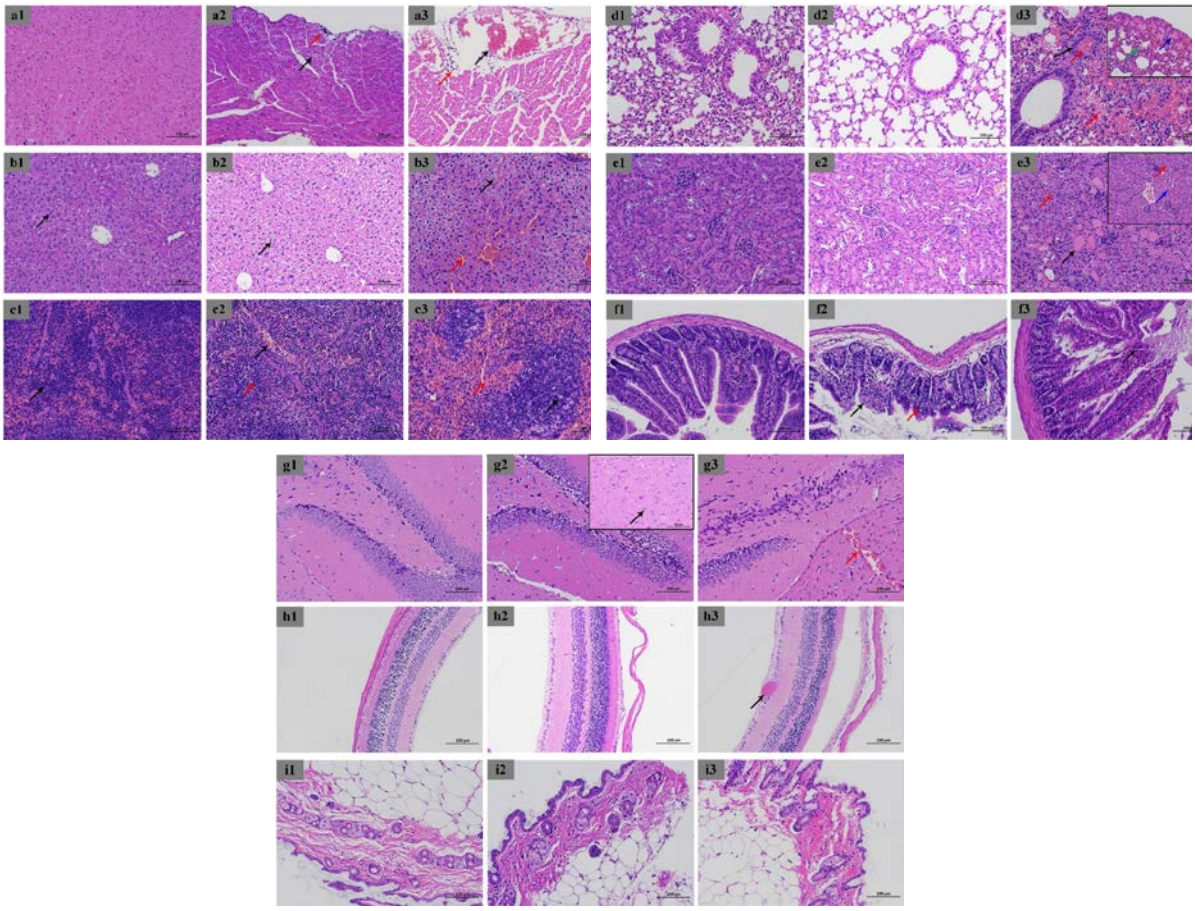

Figure 5.4 Pathological section results of mice

As shown in Figure 5.4a, the cardiomyocytes of mice in the low concentration test group are tightly arranged with normal cell morphology and no obvious abnormalities were found. Although most of cardiomyocytes exposed to the medium concentration $C_5F_{10}O$ are tightly arranged, some loosen and lightly stained cells were found (See black arrow). And calcium salt deposits exists in the local epicardium (See red arrow). For the high concentration test group, a small amount of vasodilation and congestion (black arrow) as well as lymphocyte infiltration (red arrow) can be found. Thus, $C_5F_{10}O$ exposure below LC50 has little affect to the heart tissue. As the exposure concentration close to LC50, $C_5F_{10}O$ could cause slight injury to the heart, and higher concentration exposure results in blood vessel dilation and congestion in the heart. This is consistent well with the clinical manifestations of increased heartbeat and respiratory rate before death.

Figure 5.4b demonstrates the pathological sections of liver. Tightly arranged cells can be

found for the low concentration exposure group, the hepatocytes are widely seen to be loose or vacuolated (black arrow) without other obvious abnormalities. The liver tissue lobules in the medium concentration test group were intact, and the liver cells were swollen with cytoplasmic loose or vacuolated (black arrow). The liver sinusoids were squeezed and disappeared, indicating $C_5F_{10}O$ injury the liver. As for the high concentration exposure, the liver cells showed vacuolar degeneration with tiny round vacuoles (black arrow) in the cell cytoplasm and hepatic sinus congestion (red arrow) can be found locally. Considering liver is the main organ for toxins metabolism in animals, inhaling $C_5F_{10}O$ exceed LC50 will cause liver injury and hard detoxification.

The pathological sections of spleen are given in Figure 5.4c. The demarcation of red and white pulp in the spleen is clear for most of the low concentration exposure group. The number of white pulps is abundant with lymphocytes closely arranged and their shape is regular. The red pulp lymphocytes are also abundant while a large number of extramedullary hematopoietic cells are visible (See black arrow). For the medium concentration exposure (some low concentration exposure), local congestion in the red pulp (See red arrow) exists. In addition, there were a few apoptotic cells in the spleen after high concentration exposure (See black arrow), and extensive congestion (red arrow) exists in the red pulp. Thus, the acute inhalation of $C_5F_{10}O$ will cause a series of immune responses considering spleen is an important lymphatic organ.

Figure 5.4d shows the pathological sections of lung after exposure. There is no significant difference for all surviving mice in the control group and low or medium concentration test group. The structure of alveoli and bronchi is clear. The alveolar wall is thin without obvious thicken, the bronchial structure is intact and the epithelial cell morphology is normal. For the high concentration test group, amounts of alveolar walls capillary congestion or local hemorrhage were found (See black arrows). In addition, the red blood cells exuded in the alveolar cavity or bronchi (See red arrow) and the bronchial epithelial cells arranged irregularly. There exists pulmonary edema at the edge and the alveolar cavity is filled with eosinophilic protein fluid (See green arrow). Therefore, acute inhaling high concentration $C_5F_{10}O$ is harmful to lung, causing rupture or bleeding of capillaries in the alveolar wall and pulmonary edema. During the autopsy process, we also found that the mice had severe lung bleeding and the direct reason for death may due to the respiratory disorder caused by acute heart and lung injury. It should be noted that the lung injury caused by $C_5F_{10}O$ is reversible according to the low or medium concentration exposure results.

As shown in Figure 5.4e, there is no significant difference in the kidney tissue of all surviving mice in the control and test groups. The demarcation of the cortex and medulla is clear. Cortical renal tubules are abundant and arranged closely with clear boundaries. The morphology of epithelial cells was normal and glomerular capillaries were clear. For the high concentration exposure, a large number of renal tubules in the cortex were expanded and filled with eosinophilic protein fluid (See black arrow). Amounts of renal tubular epithelial cells have vacuolar degeneration with tiny circular vacuoles formed in the cytoplasm (See red arrow). A small number of renal tubular epithelial cells were necrotic, some nucleus was fragmented and dissolved, accompanying by the enhanced eosinophilic cytoplasm (See blue arrow). The above results indicate that acute inhalation of low content $C_5F_{10}O$ will not cause irreversible injury to the kidney. Excessive inhalation of $C_5F_{10}O$ will result in acute liver and kidney failure.

Figure 5.4f shows the pathological section of intestinal. We can find that the demarcation of intestinal layers after low concentration exposure is clear. The intestinal villi, glands were abundant and arranged regularly without mucosal epithelial fallen off. Some mice demonstrate a small amount of swollen mucosal epithelial cells and loose cytoplasm. For the medium concentration exposure, amounts of mucosal epithelial cells fall off (black arrow) and intestinal gland epithelial cells are swollen. The cytoplasm was loose and lightly stained (See red arrow). As to high concentration exposure, a small number of epithelioid cells were shed in the intestinal lumen (See black arrow). Actually, intestinal mucosal epithelial cells play an important role in the immune defense or tolerance and are responsible for digestion or absorption of systemic nutrients [119]. Therefore, the intestinal mucosal epithelial cells also responded after acute inhalation of $C_5F_{10}O$.

The pathological sections of brain, eye and skin are given in Figure 5.4g-i, respectively. We found that the brain cells are tightly structured after low concentration exposure. Cortical neuron cells are abundant in number and evenly distributed, with obvious nucleoli and normal cell morphology. While a small number of pyramidal cells in the hippocampus are constricted and deeply stained with irregular shapes. For medium concentration exposure, there were more gaps (See black arrows) around the neuronal cells in the brain. After high concentration exposure, a small number of pyramidal cells in the hippocampus are pyknotic and deeply stained with irregular shapes and local vascular congestion, indicating $C_5F_{10}O$ could injury the brain of mice.

In addition, there was no significant difference in the eye for all surviving mice. The structure of cornea and retina is clear and the cell morphology is normal. As to the high concentration exposure, there exists local vascular congestion (See black arrow) in the retinal ganglion cell layer. The skin tissue after exposure demonstrates clear epidermis and dermis structure. The dermis is rich in collagen and the hair follicle structure, as well as sebaceous glands, is clearly visible. Overall, $C_5F_{10}O$ did not cause serious injury to the brain, eye and skin of mice.

Combining the clinical symptoms, blood routine examination and pathological section results, we can conclude that acute inhalation low concentration of $C_5F_{10}O$ (< 7400ppm for female, < 8600 ppm male) did not cause irreversible injury to the organs and functions of mice considering the toxins can be excreted through metabolism during the 14-day observation period. Acute inhalation medium concentration of $C_5F_{10}O$ (7500ppm for female, 8800 ppm male) caused some injury to the heart, liver, spleen, kidney and intestine of mice and the effects on other organs could return to normal during the 14-day observation period. High concentration inhalation of $C_5F_{10}O$ will cause capillary rupture and hemorrhage, affecting the heart, lung, liver and kidney that related to respiration and metabolism. Due to impaired cardiopulmonary function, the organism cannot normally supply oxygen, and the liver, kidneys cannot metabolize toxins. The direct reason for the death is the impairing of heart and lung, leading to the failure of multiple organs such as the liver, kidney. The concentration that could not cause permanent injury to the mice health is 7400ppm for female and 8600ppm for male.

5.2 Arc decomposition products of $C_5F_{10}O/N_2/O_2$ gas mixture and its biosafety

Although some decomposition products were detected from the decomposition of

$C_5F_{10}O/N_2/O_2$ gas mixture in the previous gas-solid interface stability and discharge and thermal decomposition tests, only trace amounts of decomposition components were present in the gas mixture at the end of the tests. In order to comprehensively investigate the biosafety of $C_5F_{10}O/N_2/O_2$ gas mixture decomposition products, this section firstly uses LBS to conduct load current breaking tests. The purpose of the arc test is to use the discharge and thermal effects of the arc to fully decompose $C_5F_{10}O/N_2/O_2$ gas mixture to obtain its arc decomposition products, and then use the decomposed gas to conduct an acute inhalation test to evaluate the biosafety of the decomposition products of $C_5F_{10}O/N_2/O_2$ gas mixture.

5.2.1 Arc characteristics of $C_5F_{10}O/N_2/O_2$ gas mixture

1 Synthetic test circuit platform and test method

The schematic diagram of the synthetic test circuit platform used is shown in Figure 5.5a. The current source circuit has four branches with the same structure that includes an C_1=16.8 mF capacitor, L_1=0.603 mH inductor. The maximum charging voltage of each capacitor group is 5 kV and the maximum output current is 20 kA. The energy of the current source is charged by the grids, and the LBS is discharged according to the test requirements. LBS are commonly used in medium-voltage distribution networks to break currents of several hundred amperes. Therefore, the arc in the LBS is generally free burning or has very weak arc blowing performance, mainly relying on the inherent physical properties of the dielectric to quench the arc [61].

The LBS used in the test was an SF_6 gas insulated LBS produced by Schneider Electric, and its rated working condition is 24kV/630A (Figure 5.5b). The gas chamber is a cavity with a volume of about 11 L made of epoxy resin. The gas chamber was filled with 17.7kPa $C_5F_{10}O$-112.3 kPa N_2/O_2 gas mixture (the $C_5F_{10}O$ gas concentration of 13.6%) with the liquefaction temperature of -15°C. The usage of air as the buffer gas mainly considers that the oxygen can inhibit the generation of solid by-products. The $C_5F_{10}O$ gas concentration used in this test is 13.6%, which is higher than the $C_5F_{10}O$ concentration used in the previous tests because the pressure and volume of LBS gas chamber are both small (gas pressure is 0.13MPa, volume is about 11L), in order to ensure a sufficient amount of decomposed gas to carry out the biosafety research of $C_5F_{10}O$ gas decomposition products, more gas can be obtained by increasing the concentration of $C_5F_{10}O$ under the premise that the gas pressure and volume cannot be changed.

The LBS was first subjected to the withstanding voltage test of 42 kV min^{-1} phase to phase and 48 kV min^{-1} phase to ground after filled with $C_5F_{10}O/N_2/O_2$ gas mixture in accordance with IEC 622271-103. The LBS passed all the withstanding voltage tests, indicating that the insulation strength of the $C_5F_{10}O/N_2/O_2$ based LBS meets the relevant standard requirements. Due to the internal resistance of the synthetic test circuit platform, the current will decay in the LC oscillation circuit during the actual test and the recorded short-circuit waveform is shown in Figure 5.5c. The current in the loop was lower than 100 A after decayed for about 7 cycles (140 ms) and the average current decay is about 14% per cycle. Therefore, the time difference between the CB action time t of the synthetic test circuit platform and the LBS action time $t+\delta t$ should be adjusted with the δt<40 ms to ensure the LBS will act within two cycles after the CB is closed, and the current flowing through the fracture is about 630 A. After 200 arc extinguishing tests, gas sample was collected from the arc extinguishing chamber of the LBS and the gas composition was detected using GC-MS.

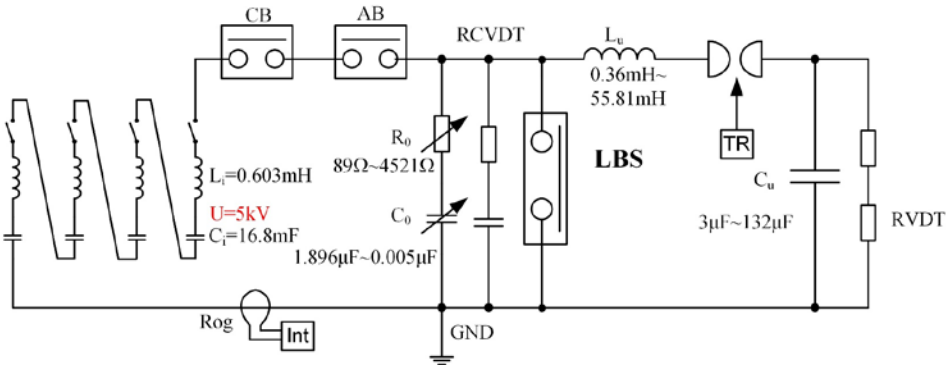

(a) The schematic diagram of the synthetic test circuit platform

(b) Structure of the LBS

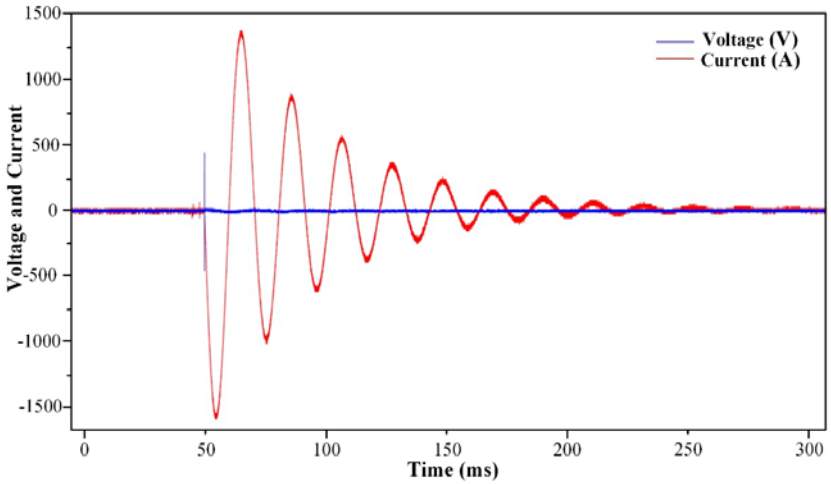

(c) The short-circuit waveform of the test platform

Figure 5.5 synthetic test circuit platform

2 Arc extinguishing characteristics of $C_5F_{10}O/N_2/O_2$ gas mixture LBS

The typical voltage and current waveforms of $C_5F_{10}O/N_2/O_2$ gas mixture during the arc extinguishing process are shown in Figure 5.6a, and the arcing time distribution is shown in Figure 5.6b and 5.6c. It can be seen that the arcing time of $C_5F_{10}O/N_2/O_2$ gas mixture is distributed between 1-16 ms, with an average of 7.68ms and a median of 8 ms. The standard deviation of the arcing time is 3.42 ms and the 95% confidence interval is in the range of 0.99-14.38 ms.

According to the relationship between the gas pressure and the number of arcing shown

in Figure 5.6d, the gas pressure rises rapidly with the arcing number during the early test stage (before 60 number), and the growth rate slows down to an approximately linear growth. The gas pressure increased by 19.1 kPa after 60 times of tests, which is mainly ascribed to the decomposition of $C_5F_{10}O$ in the gas mixture. Then the pressure increases by ~0.144 kPa for each arc extinguishing operation. At this time, the amount of $C_5F_{10}O$ that decomposed during each test reaches to a constant value. The totally increase of 39.1 kPa was detected after 200 times of breaking.

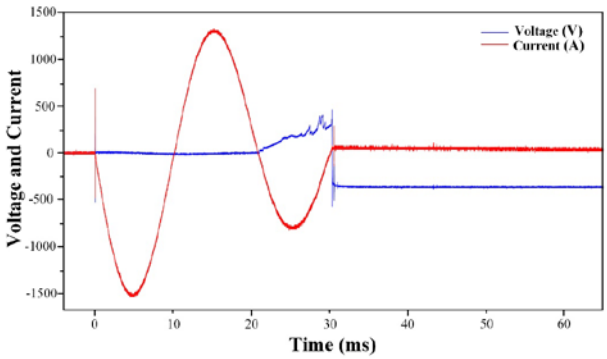

(a) Typical waveform of $C_5F_{10}O/N_2/O_2$ gas mixture during the arc extinguishing

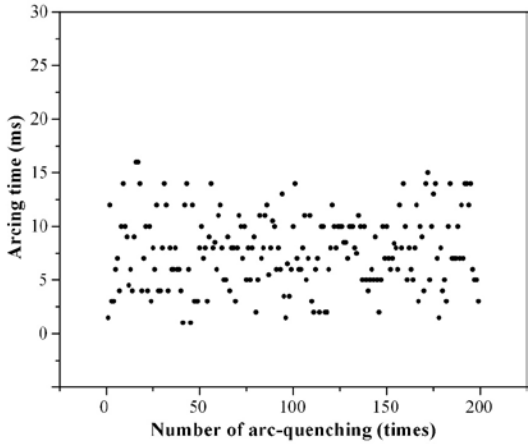

(b) Arcing time

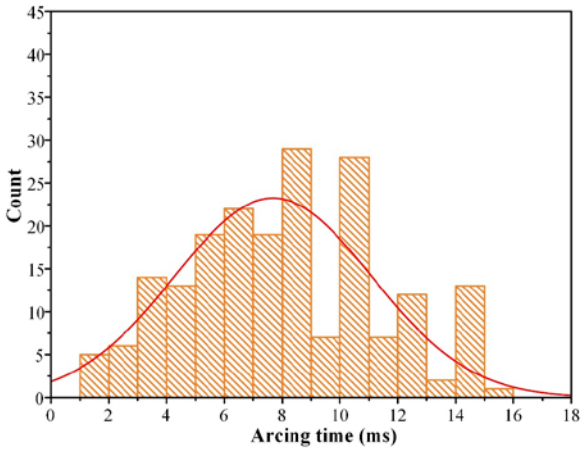

(c) Arcing time distribution curve

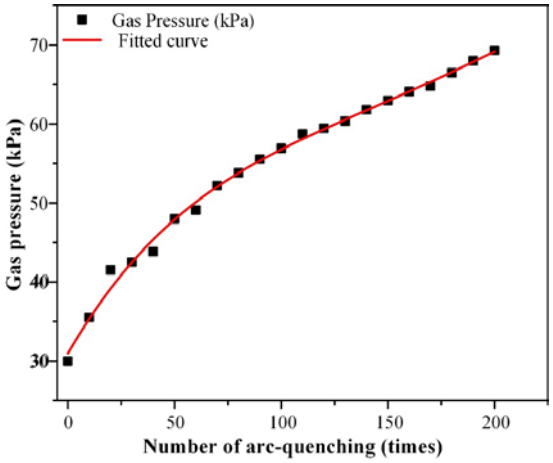

(d) Gas pressure change curve

Figure 5.6 Arc extinguishing characteristics of $C_5F_{10}O/N_2/O_2$ gas mixture LBS

5.2.2 Arc decomposition characteristics of $C_5F_{10}O/N_2/O_2$ gas mixture

The gas components in the gas chamber were further analyzed (as shown in Figure 5.7a). The decomposition of $C_5F_{10}O/N_2/O_2$ after arc extinguishing includes CF_4, C_2F_6, C_3F_6, C_3F_8, CO_2, C_4F_{10}, C_3HF_7 and $C_2H_6F_2Si$. CF_4 reaches the highest content among all by-products, followed by CO_2. Moreover, some by-products including CO, CF_2O and C_2F_4 that produced during the power frequency breakdown of $C_5F_{10}O$ gas mixture were not detected [9.11], which is mainly due to the CO and CF_2O will be produced when the O_2 involved in the reaction is insufficient, as shown in equation (5.1). In the case of sufficient O_2, the CO gas generated by

the decomposition of $C_5F_{10}O$ can further react with O_2 to produce CO_2. In addition, C_2F_4 and CF_2O gas can also be converted to CO_2 and CF_4 according to equations (5.2) and (5.3). Considering CO and CF_2O has the LC50 of 1807 ppm (4h rat) and 92 ppm (4h rat), the addition of excessive O_2 to prevent the generation of CO and CF_2O in the $C_5F_{10}O$ gas mixture can effectively improve its application safety.

$$C + CO_2 \rightarrow 2CO \quad (5.1)$$

$$2CF_2O \rightarrow CO_2 + CF_4 \quad (5.2)$$

$$C_2F_4 + O_2 \rightarrow CO_2 + CF_4 \quad (5.3)$$

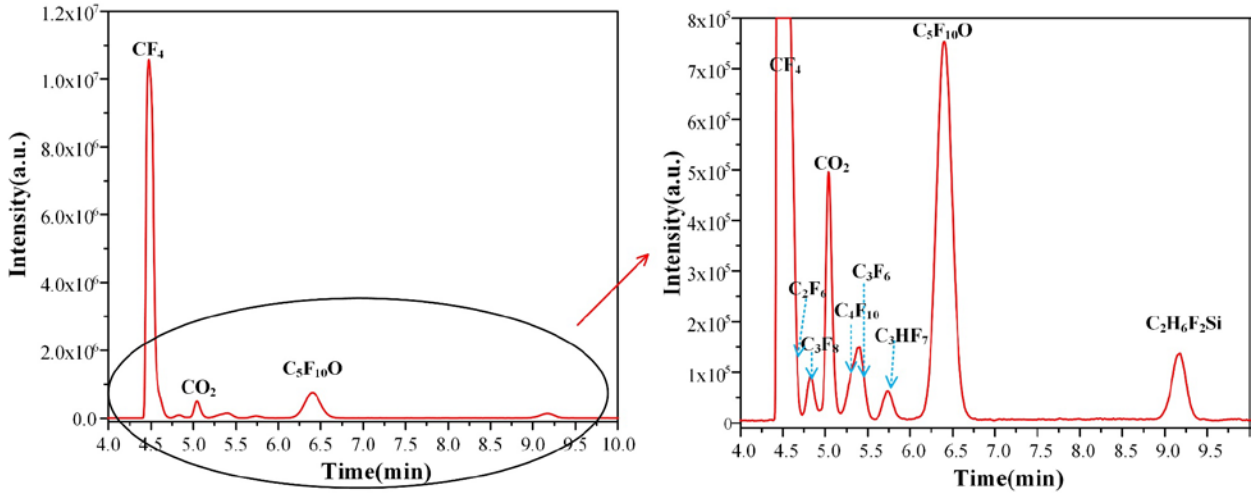

(a) Types of $C_5F_{10}O/N_2/O_2$ gas mixture arc decomposition products

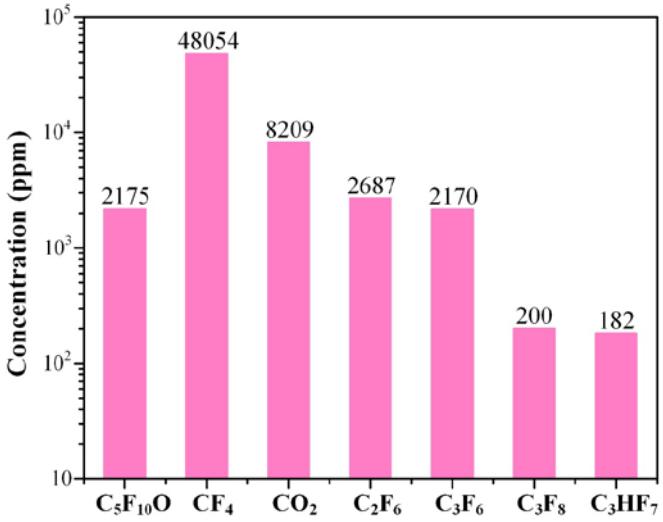

(b) Concentration of decomposition products of $C_5F_{10}O/N_2/O_2$ gas mixture

Figure 5.7 Gas decomposition products of $C_5F_{10}O/N_2/O_2$ gas mixture

Besides, the $C_5F_{10}O$ inside the gas chamber was 13.6% (v/v) before the test and finally decreased to 2175 ppm (about 0.22% v/v) (Figure 5.7b), indicating that most of the $C_5F_{10}O$ gas was decomposed during the 200 times of arc extinguishing processes. The highest content of gaseous decomposition product is CF_4, with the final content of 48054 ppm (4.8%), followed by CO_2 of 8209 ppm. And the above two substances have relatively low acute inhalation toxicity (LC50 values of 895,000 ppm (15 min rat) and >470000 ppm (30 min rat)) (as shown

in Table 5.5). The content of C_2F_6, C_3F_6, C_3F_8 and C_3F_7H were 2687 ppm, 2170 ppm, 200 ppm and 182 ppm, respectively. Overall, the main decomposition products of $C_5F_{10}O$ are saturated fluorocarbons with low toxicity, and C_3F_6 demonstrates the highest toxicity with the LC50 of 1672 ppm (4h, rat).

Table 5.5 Acute inhalation toxicity of characteristic decomposition products of $C_5F_{10}O$

Gas	LC50 (rat)
$C_5F_{10}O$	20000ppm/4h
CF_4	895000ppm/15min
CO_2	>470000ppm/30min
C_2F_6	>20000ppm/2h
C_3F_6	1672ppm/4h
C_3F_8	90000ppm/4h
C_3HF_7	>50000ppm/2h
CO	1807ppm/4h
C_2F_4	19561ppm/4h
CF_2O	92 ppm/4h

The inner structure of the gas chamber after 200 times of arc extinguishing arc extinguishing tests is shown in Figure 5.8a. The structure of the arc extinguishing chamber has a double fracture (shown in the bottom right of Figure 5.5b) that can increase the fracture distance during LBS operation. Due to the excessive O_2 mixed in the $C_5F_{10}O$ gas mixture, only trace amounts of black solids were generated inside the gas chamber (shown in Figure 5.8b), which was mainly adsorbed near the fracture contacts. This is ascribed to the high temperature burning contact produced solid particles that adhered to the surrounding epoxy surface (red circle in the picture). We also collected trace amounts of black solids inside the gas chamber for energy dispersive spectroscopy (EDS) analysis, as shown in Figure 5.8c and Table 5.6. The black solid covered by the epoxy resin surface mainly contains C, O, F, Si, Cu, Ag, Fe, Cr, Mo that contained in the copper alloy. The copper alloy contact surface is silver-plated to protect the inner conductor, while the peeling off of Ag is inevitable during the arc extinguishing, resulting in the exposure of Fe, Cr, Mo in the purple copper alloy. The Si element originates from the silicone grease coated on the sealing rubber. The more abundant C, O and F elements are mainly produced by the decomposition of $C_5F_{10}O$ gas mixture, which account for about 62.91% (Weight percentage) of the whole surface element content. In addition, the distribution patterns of O, F and Cu on the solid surface are similar, and the C element is mainly distributed around O and F elements. The large surface particles demonstrated in the SEM are mainly composed of CuO and CuF_2.

Overall, the trace black solids formed by $C_5F_{10}O/N_2/O_2$ gas mixture after load current breaking are mainly produced by the contact ablation and a small amount of sealing silicone grease coated on the surface of the sealing material. This is very different from the solid carbon produced by the decomposition of $C_5F_{10}O$ gas during the power frequency breakdown process. Excess oxygen in the arc burning process can react with the carbon generated by the decomposition of $C_5F_{10}O$ to generate CO_2 that inhibits the formation of solid carbon.

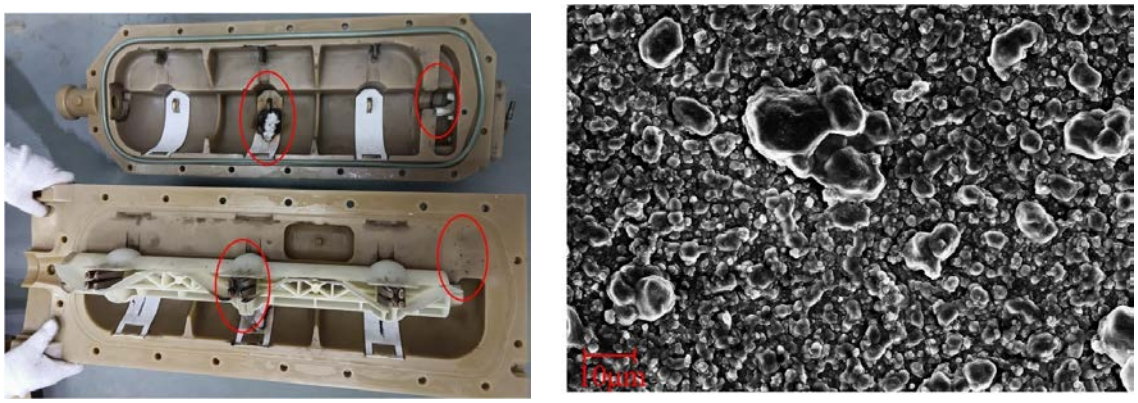

(a) The internal structure of the gas chamber (b) Microscopic morphology of black solids

(c) Elemental distribution of black solids

Figure 5.8 Solid decomposition products of $C_5F_{10}O/N_2/O_2$ gas mixture

Table 5.6 The composition of trace amounts of black solids produced after arc extinguishing of the LBS

Element	Weight percentage (Wt%)	Element	Weight percentage (Wt%)
C	21.16	Al	0.34
O	19.16	Ag	1.72
F	22.15	Cr	0.53
Si	20.24	Fe	1.43
Cu	12.08		

5.2.3 Biosafety of $C_5F_{10}O/N_2/O_2$ gas mixture arc decomposition products

1 LC50 of $C_5F_{10}O/N_2/O_2$ gas mixture arc decomposition products

The acute inhalation toxicity test for the $C_5F_{10}O/N_2/O_2$ after arc extinguishing shows that the test group with a concentration of 3000 ppm was unable to complete the 4h exposure test. The mice in other test groups (1200-2400 ppm) were survived at the end of 4h exposure. For the exposure of 2400 ppm, the mice were in poor condition at the end of the test, lying on the exposure chamber in a limp state and losing their ability to move. One female mouse firstly died within 1 h after exposure test, and all samples died within 7h after exposure (the survival sample at the end of the test is shown in Table 5.7). The mice exposed in the 1200, 2000 and 2200 ppm $C_5F_{10}O/N_2/O_2$ after arc extinguishing showed the similar clinical symptoms to the

control group mice at the end of the test, and showed no obvious symptoms of toxicity, abnormal symptoms or death during the 14-day observation. Furtherly, the LC50 value of the $C_5F_{10}O/N_2/O_2$ gas mixture after arc extinguishing was calculated with the value of 2300 ppm(as shown in Figure 5.9) based on the straight-line interpolation. The tolerance of mice to $C_5F_{10}O/N_2/O_2$ gas mixture after arc extinguishing is similar for the male and female samples, which is clear difference to that of pure $C_5F_{10}O$.

Table 5.7 Acute inhalation toxicity test results of $C_5F_{10}O$ gas decomposition products

No.	$C_5F_{10}O$ concentration(ppm)	Number of dead mice	Mortality rate
1	0	0 female mice+0 male mice	0
2	1200	0 female mice+0 male mice	0
3	2000	0 female mice+0 male mice	0
4	2200	0 female mice+0 male mice	0
5	2400	5 female mice+5 male mice	100%
6	3000	5 female mice+5 male mice	100%

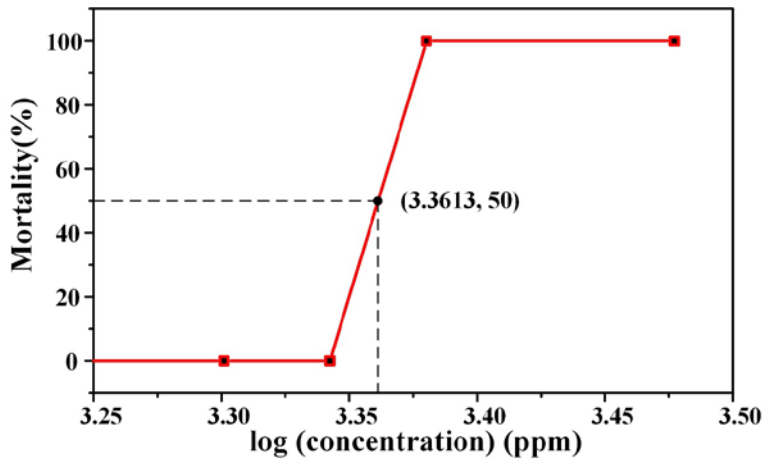

Figure 5.9 The LC50 value of the decomposition products of $C_5F_{10}O/N_2/O_2$ gas mixture inhaled by mice

2 Analysis of blood and organ pathological sections

The effects of $C_5F_{10}O/N_2/O_2$ gas decomposition products on the physiological indicators and vital organ tissues of mice were further explored by extraction of blood and pathological section analysis of organs.

The blood test results presented in Table 5.8 indicates that the number of white blood cell (WBC) was relatively high owing to the number of neutrophil granulocyte (Gran#) in the WBC was higher than the reference range, indicating that inhalation of $C_5F_{10}O$ gas mixture after arc discharge triggered acute inflammation and the immune protection mechanism in the body produces an immune response. The WBC count of mice in the test groups had returned to normal at the end of the 14-day observation period with the Gran# count also changed within the reference range. The hemoglobin (HGB), hematocrit (Hct) and mean corpuscular hemoglobin concentration (MCHC) of dead mice were higher than the normal reference range. Red blood cells are the primary transport vehicle for oxygen delivery to cells by peripheral blood in animals, and HGB is deeply involved in the interior of cells for the body's aerobic respiration, thus the increase of HGB and red blood cells in mice after inhalation of $C_5F_{10}O$ gas

mixture after arc discharge are associated with acute injury of lung function in mice. The blood test results of all mice showed that mean platelet volume (MPV) was higher than the normal reference range (3.8-6.0), and the same phenomenon was observed in unexposed blank control mice, which might related to the physical condition of the same batch of mice. Overall, the routine blood results confirmed that the mice developed acute inflammation after inhalation of $C_5F_{10}O$ gas mixture after arc extinguishing, which was manifested as an increase in WBC count (rapid increase in Gran# count) related to the immune system (rapid increase in Gran# count). During the 14-day observation period, the mice returned to normal through self-regulation, indicating that the gas mixture would not cause irreversible injury to the blood indicators of the mice.

Tanle 5.8 Routine blood tests before and after acute inhalation of $C_5F_{10}O$ gas decomposition products in mice

Parameter	Control group	Live (day 0)	Live (day 14)	Died	Unit	Reference value
WBC	5.8	7.1	3.6	3.1	10^9/L	0.8-6.8
Lymph#	4.7	3.8	2.9	2.1	10^9/L	0.7-5.7
Mon#	0.1	0.2	0.0	0.1	10^9/L	0.0-0.3
Gran#	1	3.1	0.7	0.9	10^9/L	0.1-1.8
RBC	8.03	8.61	8.09	8.96	10^{12}/L	6.36-9.42
HGB	132	137	128	164	g/L	110-143
HCT	41.7	44.3	39.2	45.7	%	34.6-44.6
MCV	52	51.5	48.5	51.1	fL	48.2-58.3
MCH	16.4	15.9	15.8	18.3	pg	15.8-19
MCHC	316	309	326	358	g/L	302-353
RDW	13.1	14.3	13.1	14.5	%	13-17
PLT	539	667	596	497	10^9/L	450-1590
MPV	6.8	6.5	6.1	6.6	fL	3.8-6.0

The pathological sections of major organ tissues of mice inhaled $C_5F_{10}O$ gas decomposition products are shown in Figure 5.10. The liver tissue structure of the high concentration test group (exposed to 2400ppm and 3000ppm) was slightly abnormal with a small number of liver cells showed fatty degeneration, and round vacuoles of different sizes (yellow arrows) can be seen in the cytoplasm. The liver tissue structure of the mice in the other test groups was normal (as shown in Figure 5.10a). The spleen pathology section shown in Figure 5.10b were normal in structure and no significant abnormalities were observed in the low (1200 ppm and 2000 ppm) and high concentration groups. While multinucleated giant cells increased (yellow arrow) accompanied by a small amount of cell necrosis as well as nuclear fragmentation or pyknosis (red arrow) can be found for the samples exposed to the 2200 ppm of $C_5F_{10}O$ gas mixture. No abnormality for the high concentration test group is ascribed to the mice were died soon after exposure. The lung tissue of the mice exposed to 2400ppm and 3000ppm $C_5F_{10}O$ gas mixture demonstrates unclear structure of the alveolar wall. A a large amount of cellulose can be observed (blue arrow) accompanied by a small amount of cell necrosis and nuclei fragmentation (red arrow). The lung tissue structure of the mice in the other test groups was normal. Moreover, the pathological section of heart, kidney, intestine and eye kept normal after exposure (detail explanation given in Figure 5.10c-h).

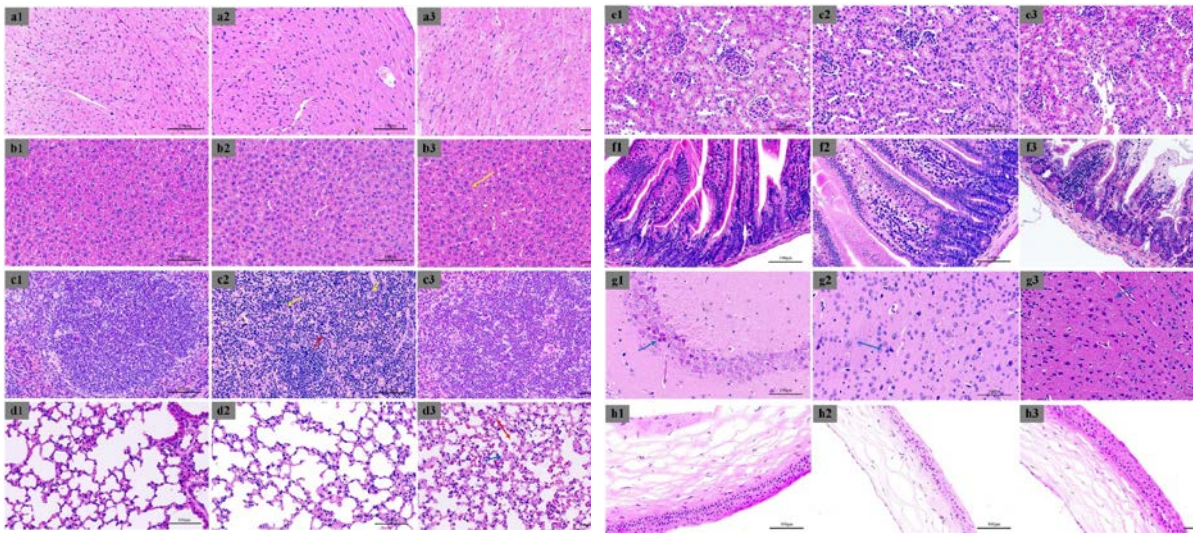

Figure 5.10 Pathological section results of mice organ specimens

In summary, there is no highly toxic gas by-products in the $C_5F_{10}O/N_2/O_2$ gas mixture after arc extinguishing tests. Mice inhaling the arc decomposed $C_5F_{10}O$ mainly cause acute injury to their lungs and liver. Slightly abnormal for the spleen tissue was also found for the samples exposed to 2200 ppm of $C_5F_{10}O$ gas mixture at the end of the 14-day observation period, indicating that excessive inhalation of $C_5F_{10}O$ gas decomposition products would cause injury to the spleen. Besides, it is reported that some injury to the heart, liver, spleen, kidney and intestine of mice was found for the samples acutely inhaled pure $C_5F_{10}O$ gas at concentrations close to LC50. While the samples inhaled $C_5F_{10}O$ gas with decomposition products at concentrations close to LC50 caused slight injury to the spleen and almost no effect on other organs.

5.3 Application Safety Assessment of $C_5F_{10}O/N_2/O_2$ and Its Decomposition Products

Overall, we have revealed the acute inhalation toxicity of pure $C_5F_{10}O$ based on the above-mentioned results. For related research and engineering application, $C_5F_{10}O/N_2/O_2$ gas mixture with 5%-13.6% $C_5F_{10}O$ is widely used. Therefore, we convert the biological toxicity of $C_5F_{10}O/N_2/O_2$ gas mixture according to the proportion of $C_5F_{10}O$ and relevant results are shown in Table 5.9.

Table 5.9 Comparison of biological toxicity of $C_5F_{10}O/N_2/O_2$ gas mixture at different concentrations

Type	LC50(4-h) on mice (ppm)	No harm concentration on mice (ppm)	TLV-TWA
$C_5F_{10}O$	7461-8724	7400-8600	225ppm
5%$C_5F_{10}O/N_2/O_2$	149220-174480	148000-172000	4500ppm
7.5%$C_5F_{10}O/N_2/O_2$	99480-116320	98666-114666	3000ppm
13.6%$C_5F_{10}O/N_2/O_2$	54860-64147	54411-63235	1654ppm

Considering the $C_5F_{10}O$ components in $C_5F_{10}O/N_2/O_2$ gas mixture is lower than air, its acute inhalation toxicity is significantly lower than pure $C_5F_{10}O$. For example, the acute inhalation toxicity of $C_5F_{10}O$ (mice, 4 h) reaches 5.4% and the TLV-TWA for long-term safe exposure is 1654 ppm (higher than 1000ppm of SF_6) for the 13.6% $C_5F_{10}O/N_2/O_2$ gas mixture.

In terms of long-term toxicity, the toxicity of 13.6% $C_5F_{10}O/N_2/O_2$ gas mixture (the highest $C_5F_{10}O$ in $C_5F_{10}O/N_2/O_2$ gas mixture for engineering application) is lower than that of SF_6. And the toxicity of gas mixture will be further reduced when the content of $C_5F_{10}O$ gas is lower than 13.6%. The concentration of $C_5F_{10}O/N_2/O_2$ gas mixture used in the previous test is 7.5%, for this application scheme, the acute inhalation toxicity (mice, 4h) is higher than 9.8%. Actually, the exposure concentration in serious equipment accidents including gas leakage is difficult for the exposure concentration in the air around the equipment to achieve this value (exceed 9.8%).

For normal operating conditions, the IEC62271-200 [116] standard stipulates that the annual gas leakage rate of GIE is <0.1%, and $C_5F_{10}O/N_2/O_2$ gas mixture RMUs are usually used in indoor spaces. Assuming that 10 LBS are installed in a room with a volume of 54 m^3 (5.0×3.6×3.0), the volume of the gas chamber in each equipment is about 11L (gas pressure is 130 kPa). Taking the maximum leakage rate of 0.1% as an example, there will be 0.14L $C_5F_{10}O/N_2/O_2$ gas mixture leaked into the room area within a year. The concentration of $C_5F_{10}O$ gas leaked into the indoor environment by LBS (13.6% $C_5F_{10}O/N_2/O_2$) is 0.36ppm, which is much lower than the TLV-TWA value (225ppm) of $C_5F_{10}O$ gas. In the actual situation, considering the indoor ventilation and actual leakage rate, the concentration of $C_5F_{10}O$ gas in the air will be reduced by 10-100 times [15].

The $C_5F_{10}O$ gas leaked by GIE will not cause potential harm to the health of scientific researcher and technical personnel. For sudden accidents, Christophe et al. simulated the diffusion process after accidental gas leakage in the GIE chamber [118]. Relevant results indicate that the concentration of gas (or gas mixture) at a distance of 0.8 m from the equipment is about 6000 ppm considering a quickly leakage of 0.9 m^3 in GIE. For 13.6% $C_5F_{10}O/N_2/O_2$ gas mixture, the concentration of $C_5F_{10}O$ at a distance of 0.8 m from the equipment is about 816 ppm, which is also an order of magnitude lower than its LC50 value. Thus, accidental leakage of $C_5F_{10}O/N_2/O_2$ gas mixture from GIE will not cause acute injury to technical personnel.

Moreover, Christophe et al. simulated the diffusion process of gas in GIE after accidental leakage and estimated the gas concentration in the surrounding space [118]. Relevant results show that the concentration at 0.8 m from the equipment after a rapid leak of 0.9 m^3 of gas (or gas mixture) from GIE into the surrounding space is about 6000 ppm. Assuming that the gas concentration inside the LBS is 13.6% $C_5F_{10}O/N_2/O_2$, the content of leaking gases at 0.8m from the equipment is about 13ppm, which is less than two magnitude orders of the LC50 value. Thus, the accidental leakage of $C_5F_{10}O/N_2/O_2$ gas mixture after arc decomposition will cause little acute injury.

Table 5.10 lists the toxicity of arc decomposition products of $C_5F_{10}O$ and SF_6 gases, and LC50 values are given for some of the decomposed gases. The highest content of $C_5F_{10}O$ gas decomposition products are CF_4 and CO_2 gas, both of which have low acute inhalation toxicity, with LC50 values of 895000ppm (15min rat) and >470000ppm (30min rat), respectively. The main decomposition products of $C_5F_{10}O$ gas under the action of arc are CF_4, C_2F_6, C_3F_6, C_3F_8, CO_2, C_4F_{10} and C_3HF_7 with low toxicity, which is another advantage of its use as an eco-friendly insulating gas. Although the LC50 value of SF_6 gas is as high as 800000ppm (4h rat), its decomposition products such as SO_2, H_2S, SOF_2 and SO_2F_2 are all highly toxic. The toxicity of SF_6 gas decomposition products is much higher than that of $C_5F_{10}O$ gas decomposition products. Once the decomposed SF_6 gas in the equipment leaks into the surrounding

environment, it will bring security risks.

Table 5.10 Toxicity comparison of arc decomposition products of $C_5F_{10}O$ and SF_6

$C_5F_{10}O$ decomposition products	LC50 (Rat)	SF_6 decomposition products	LC50 (Rat)
$C_5F_{10}O$	20000ppm/4h	SF_6	>80%
CF_4	895000ppm/15min	$SF_5(S_2F_{10})$	Easily decomposed to produce SF_4, extremely toxic
CO_2	>470000ppm/30min	SF_4	19ppm
C_2F_6	>20000ppm/2h	SOF_4	Injury the lungs
C_3F_6	1672ppm/4h	SOF_2	Lung hemorrhage due to inhalation
C_3F_8	90000ppm/4h	SO_2F_2	Toxic by inhalation, very toxic to aquatic life
C_3HF_7	>50000ppm/2h	SO_2	2520ppm/1h
CO	1807ppm/4h	CO	1807ppm/4h
C_2F_4	19561ppm/4h	CF_4	895000ppm/15min
CF_2O	92 ppm/4h	CS_2	25mg/m^3 2h

The above analysis shows that $C_5F_{10}O/N_2/O_2$ gas mixture and its decomposition products have high biosafety and will not be life-threatening to the workers in practical applications. However, relevant workers and researchers should also take protective and preventive measures to prevent accidents at work (as shown in Figure 5.11).

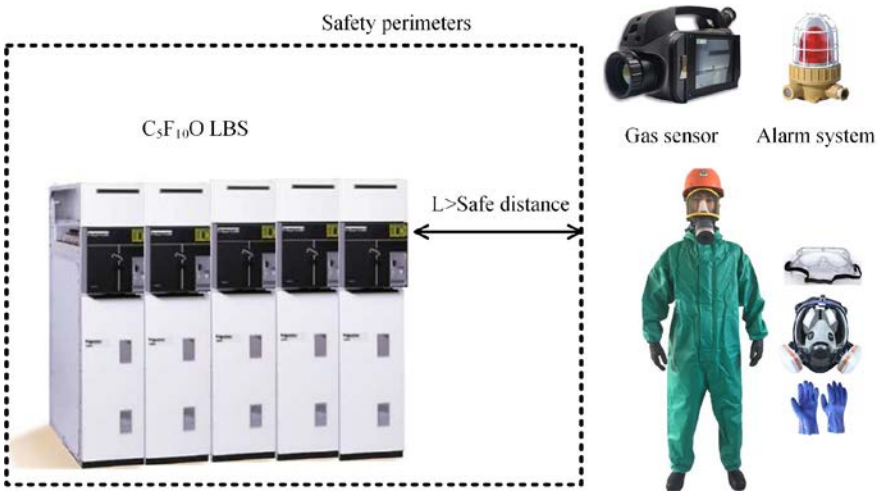

Figure 5.11 Safety protective measures based on $C_5F_{10}O$ gas mixture LBS

1) Operators need to conduct safety training and safety clearance.

2) The same protection precautions as SF_6 GIE can be taken during normal operation of the equipment.

3) Appropriate personal protective equipment (protective gloves, goggles, gas mask, self-contained breathing apparatus etc.) should be provided in the case of possible exposure to high concentration $C_5F_{10}O$ gas, such as sub-assembly, filling process.

At the same time, the following suggestions should be taken around the workplace.

1) Post clear hazard notices around the equipment (including high voltage hazards, leakage hazards, safety perimeters, safety instructions and recommendations etc.).

2) Install gas sensors in the workplace for leakage detection of $C_5F_{10}O$.

3) Be equipped with facilities to extract or channel leaked gas to a safe location.

4) The exhaust gas generated by GIE due to maintenance and other reasons cannot be directly discharged into the atmosphere, which needs to be recycled and treated in a harmless manner.

On the whole, relevant scientific researchers and technical personnel should pay attention to protection during work although $C_5F_{10}O$ demonstrates high biosafety. The characteristic phenomenon that acute inhalation of $C_5F_{10}O$ results in particularly sensitive to external stimuli can be considered as an early symptom signal for judging the acute inhalation poisoning occurrence of $C_5F_{10}O$. Once the above-mentioned symptoms appear during work, the staff should evacuate to a ventilated or open outdoor environment in time, and seek medical treatment if they still feel uncomfortable.

5.4 Chapter Summary

This chapter firstly test the biosafety of $C_5F_{10}O$ gas, and reveal the toxic mechanism of $C_5F_{10}O$ gas combined with routine blood and organ tissue section analysis. Then, the arc decomposition characteristics of $C_5F_{10}O/N_2/O_2$ gas mixture are tested by LBS, and the biosafety and toxicity mechanism of its arc decomposition products are tested, and the application safety of $C_5F_{10}O/N_2/O_2$ gas mixture is evaluated. The following conclusions are obtained.

1) The LC50(mice, 4h) of $C_5F_{10}O$ is 7461ppm for female and 8724ppm for male. The harmless concentration of is $C_5F_{10}O$ 7400ppm for female and 8600ppm for male. Low concentration inhalation (< LC50) of $C_5F_{10}O$ leads to excessive excitement of mice with increasing heartbeat and breath rate. These clinical symptoms could disappear within 5h after exposure, and the organs of the mice would not be injured.

2) The median arcing time for the rated current (630 A) of $C_5F_{10}O/N_2/O_2$ gas mixture is 8 ms. The gas pressure in the LBS chamber increase by 39.1 kPa (23.1%) after 200 times of tests. Arc decomposition of $C_5F_{10}O/N_2/O_2$ gas mixture mainly produces CF_4, C_2F_6, C_3F_6, C_3F_8, CO_2, C_4F_{10}, C_3HF_7 and $C_2H_6F_2Si$. Sufficient oxygen will inhibit the decomposition of $C_5F_{10}O$ to form solid carbon and the formation of toxic products CO and CF_2O.

3) The LC50 (4h, mice) of $C_5F_{10}O/N_2/O_2$ gas mixture after arc decomposition is 2300 ppm. Injury to the lungs, liver and spleen can be observed for the mice exposed to 2400 ppm mixture. Considering the annual leakage rate and gas leakage failure of LBS, $C_5F_{10}O$ gas decomposition products demonstrate little potential health hazards to technical personnel, while protective measures are recommended during the work.

6 Conclusion and Prospect

6.1 Main Conclusions

In this manuscript, systematic experimental and theoretical researches are carried out on the decomposition characteristics and biosafety of $C_5F_{10}O/N_2/O_2$ mixed insulating gas at gas-solid interface and under discharge and thermal effects. The decomposition of $C_5F_{10}O/N_2/O_2$ gas mixture with metal materials under gas-solid interface interaction and discharge and thermal effects is tested to clarify the decomposition characteristics of $C_5F_{10}O/N_2/O_2$ gas mixture under different conditions. The decomposition path and product generation system of $C_5F_{10}O/N_2/O_2$ and the gas-solid interface interaction model of $C_5F_{10}O$ molecules with metal materials copper, aluminum and silver are constructed to reveal the decomposition mechanism of $C_5F_{10}O/N_2/O_2$ gas mixture in discharge and thermal effects and metal interfaces. Finally, the biosafety of $C_5F_{10}O$ gas and $C_5F_{10}O/N_2/O_2$ decomposition products are tested, and suggestions are provided for the development of early warning and protective measures for relevant workplaces and workers. The main conclusions of this manuscript are as follows.

1) Through the built gas-solid interface interaction test platform, the gas-solid interface decomposition characteristics of $C_5F_{10}O/N_2/O_2$ and metal copper, aluminum and silver at different temperatures are tested, and the decomposition of $C_5F_{10}O$ and the surface morphology and elemental composition and valence state changes of metal materials are analyzed. It is found that the gas-solid interface stability of $C_5F_{10}O/N_2/O_2$ gas mixture with copper material is poor, which will cause corrosion of copper surface at high temperature to generate CuO and Cu_2O, etc.. Therefore, it is necessary to do anti-corrosion treatment on the copper surface, and it is found that the silver-plated protective layer on the copper surface can protect the copper material. In order to prolong the service life of the equipment and operational stability, in engineering applications need to pay attention to the integrity of the silver protective layer, such as the need for timely maintenance of any damage. The surface of the aluminum material will naturally oxidize to form Al_2O_3 oxide layer to protect the internal aluminum material, thus showing high gas-solid interface stability. The decomposition of $C_5F_{10}O$ gas is mainly caused by the hydrolysis reaction with the micro-water contained in the materials inside the equipment, and the formed decomposition products are mainly C_3HF_7, C_3F_6O, C_3F_6 and CHF_3.

2) The gas-solid interface interaction model between $C_5F_{10}O$ molecule and three metal materials is constructed, and the microscopic parameters such as adsorption energy, charge transfer and difference charge density of the interaction system between $C_5F_{10}O$ and metal interface are analyzed. The calculation shows that the carbonyl oxygen atom of $C_5F_{10}O$ molecule has high reactivity, and electron orbital overlap and charge transfer occur during the interaction with Cu(1 1 1) surface. The $C_5F_{10}O$ molecule and Cu(1 1 1) surface mainly form chemical bonds in the Top site through the hybridization of the 3d and 4s orbitals of the copper atom with the 2p orbital of the carbonyl oxygen atom of $C_5F_{10}O$ molecule. The adsorption of $C_5F_{10}O$ molecules and Ag(1 1 1) surface belongs to physical adsorption, which has high interaction stability. During the interaction between $C_5F_{10}O$ molecules and Al_2O_3(1 1 1), the aluminum atoms with positive charges attract the carbonyl oxygen atoms of $C_5F_{10}O$ molecules and repel the fluorine atoms. The interaction of positive and negative charges produces a large adsorption energy, but no charge transfer occurs. Therefore, the interaction between $C_5F_{10}O$

molecule and Al_2O_3(1 1 1) belongs to physical adsorption.

3) The typical discharge and thermal faults decomposition characteristics of $C_5F_{10}O/N_2/O_2$ gas mixture containing different concentrations of oxygen are revealed, and the composition and generation rules of the decomposition products of the gas mixture under the faults of AC breakdown, PD and POF are obtained. It is found that $C_5F_{10}O/N_2$ gas mixture will decompose under the discharge condition and produce black solids contain some simple carbon substances, CuF_2 and CuO, etc. to attach to the electrode surface, and the addition of oxygen to the gas mixtures will inhibit the production of black solids. The gas decomposition products generated by $C_5F_{10}O/N_2/O_2$ gas mixture when AC breakdown or PD occurs are mainly CO, CO_2, CF_2O, CF_4, C_2F_4, C_2F_6, C_3F_6, C_3F_8, C_4F_{10} and C_3HF_7. In case of POF, with the gradual increase of fault temperature from 300°C to 550°C, $C_5F_{10}O/N_2/O_2$ gas mixture first decomposes to produce primary decomposition products such as C_3F_6, CHF_3 and C_3HF_7, and then it will decompose to produce decomposition products such as CF_2O, C_2F_6, C_3F_8 and CF4, and the different decomposition products can be considered as the characteristic sign products of over-thermal temperature. It is recommended to add 4% volume fraction of oxygen to $C_5F_{10}O/N_2$ gas mixture, which can regulate the decomposition characteristics of $C_5F_{10}O/N_2$ gas mixture and also inhibit the generation of solid decomposition products during the discharge decomposition of $C_5F_{10}O$ gas.

4) The discharge and thermal failure-induced $C_5F_{10}O/N_2/O_2$ gas dissociation and product generation systems are constructed, and the thermal and kinetic parameters of the relevant reaction paths and the effects of oxygen and micro-water on the decomposition reactions are obtained based on DFT and transition state theory. The calculation shows that the bond energy of the carbonyl C=O double bond of the $C_5F_{10}O$ molecule is the largest, while the strength of the two C-C bonds connected to the carbonyl group is the weakest, and the energy required for breaking is the lowest. The electrophilic region of the $C_5F_{10}O$ molecule is also mainly concentrated around the carbonyl group. When the $C_5F_{10}O$ molecule is decomposed, the two C-C bonds connected to the carbonyl group will be broken first to generate particles such as CF_3, CO and CF_3CFCF_3, which will react with the micro-water inside the equipment to form primary decomposition products such as CHF_3, C_4F_{10}, C_3HF_7 and C_3F_6O. Further dissociation of $C_5F_{10}O$ molecule will generate F, CF, CF_2 and CF_3 particles and compound to form C_3F_8 and small molecule gas products such as HF, CO, CO_2 and CF_4. The formation rules of each decomposition product are consistent with the experimental results.

5) In terms of biosafety, the LC50 concentrations of $C_5F_{10}O$ gas for acute inhalation in mice are 7461 ppm (female) and 8724 ppm (male). Arc decomposition of $C_5F_{10}O/N_2/O_2$ gas mixture mainly produced CF_4, C_2F_6, C_3F_6, C_3F_8, CO_2, C_4F_{10}, C_3HF_7 and $C_2H_6F_2Si$, among which CF_4 and CO_2 have the highest content, and the toxicity of the main decomposition products is low, and its LC50 concentration is 2300ppm. Low concentration inhalation (< LC50) of $C_5F_{10}O$ leads to excessive excitement of mice with increasing heartbeat and breath rate. These clinical symptoms could disappear within 5h after exposure, and the organs of the mice would not be injured. However, acute inhalation of high concentrations of $C_5F_{10}O$ gas decomposition products in mice can cause injury to the lungs, liver and spleen of mice. Although $C_5F_{10}O$ gas and its decomposition products have high biosafety, relevant personnel should also take the recommended protective measures to avoid threats to life safety.

6.2 Prospects for Follow-up Research

This manuscript analyzes and evaluates the feasibility and safety of $C_5F_{10}O/N_2/O_2$ mixed insulating gas applications in terms of gas-solid interface stability, discharge and thermal decomposition characteristics and biosafety, and obtains the characteristic decomposition particles and product generation laws of $C_5F_{10}O/N_2/O_2$ gas mixture under different conditions, and initially clarifies the decomposition mechanism of $C_5F_{10}O/N_2/O_2$ gas mixture and biosafety. However, there are still many problems that need to be further studied before the application of $C_5F_{10}O/N_2/O_2$ mixed insulating gas.

1) This manuscript mainly studies the gas-solid interface interaction process between $C_5F_{10}O/N_2/O_2$ gas mixture and the commonly used metal materials inside the equipment, and the equipment also contains some non-metallic materials such as rubber sealing rings, epoxy resin insulators, and silicone grease. It is necessary to carry out experimental research on the interaction mechanism of $C_5F_{10}O/N_2/O_2$ gas mixture with various non-metallic materials in the equipment and the stability of gas-solid interface before the engineering application of $C_5F_{10}O/N_2/O_2$ gas mixture.

2) This manuscript mainly analyzes the dissociation and recombination reaction of neutral particles generated by $C_5F_{10}O/N_2/O_2$, without considering the chemical reaction involving positive and negative ions formed during the actual discharge decomposition due to the process of free electron collision and electron attachment. It is necessary to carry out research on the decomposition mechanism of $C_5F_{10}O/N_2/O_2$ gas mixture with the participation of various types of charged anions and free electrons in the future.

3) Due to the limitation of gas and solid detection techniques and methods and the unavailability of standard gases for some gases, quantitative study of all products could not be achieved in this manuscript. In the future, it is necessary to accurately quantify the products that cannot be quantitatively studied at present and obtain their concentration change rules after the detection technology is improved or standard gases are obtained.

4) The biosafety assessment of $C_5F_{10}O$ gas and $C_5F_{10}O/N_2/O_2$ decomposition products in this manuscript only tests its acute inhalation toxicity. In recent history, there are many examples of serious biosafety problems caused by commercial application of chemicals without fully clarifying the properties of chemicals. We should learn from the experience and comprehensively investigate the biosafety of $C_5F_{10}O$ gas mixture before its large-scale engineering application, including acute toxicity, chronic toxicity, carcinogenicity and potential genetic mutagenicity, to avoid biosafety hazards.

References

[1] Xianglian, Yan, et al. "Modeling of the relation between SF_6 decomposition products and interior faults in gas insulated equipment." Transactions of China Electrotechnical Society 30.22 (2015): 231-238.

[2] Xiaoxing, Zhang, Xiao Hanyan, and Huang Yangjue. "A review of degradation of SF_6 waste by low temperature plasma." Transactions of China Electrotechnical Society 31.24 (2016): 16-24.

[3] Stocker, Thomas, ed. Climate change 2013: the physical science basis: Working Group I contribution to the Fifth assessment report of the Intergovernmental Panel on Climate Change. Cambridge university press, 2014.

[4] Nechmi, Houssem Eddine, et al. "Fluoronitriles/CO_2 gas mixture as promising substitute to SF_6 for insulation in high voltage applications." IEEE Transactions on Dielectrics and Electrical Insulation 23.5 (2016): 2587-2593.

[5] Rogelj, Joeri, et al. "Paris Agreement climate proposals need a boost to keep warming well below 2 °C." Nature 534.7609 (2016): 631-639.

[6] Xin, M. A., et al. "Key issues for negotiation of Adaptation Committee under UNFCCC." Advances in Climate Change Research 8.2 (2012): 144.

[7] Global Monitoring Laboratory Earth System Research Laboratories https://gml.noaa.gov/hats/combined/SF6.html

[8] Rabie, Mohamed, and Christian M. Franck. "Assessment of eco-friendly gases for electrical insulation to replace the most potent industrial greenhouse gas SF_6." Environmental science & technology 52.2 (2018): 369-380.

[9] China Energy Research Society. Research Report on Alternative Technology of Sulfur Hexafluoride in Power Industry. Beijing, 2019.

[10] European Commission Joint Research Centre (JRC)/Netherlands Environmental Assessment Agency (PBL). Emission Database for Global Atmospheric Research (EDGAR), release version 4.2. 2010; http://edgar.jrc.ec.europa.eu.

[11] Fluorinated greenhouse gases; https://ec.europa.eu/clima/eu-action/fluorinated-greenhouse-gases_en

[12] Stiglitz, Joseph E., et al. "Report of the high-level commission on carbon prices." (2017): 1-61.

[13] http://www.chinatpg.com/home/news/pages/n_id/119482.html

[14] Owens, John, Ang Xiao, and Jason Bonk. "Emission Reductions through use of Sustainable SF_6 Alternatives." (2019).

[15] Diggelmann, T., D. Tehlar, and P. Müller. "170 kV pilot installation with a ketone based insulation gas with first experience from operation in the grid." Cigre, Paris (2016): 105-113.

[16] https://www.hitachiabb-powergrids.com/news/global-news/press-releases/abb-wins--40-million-order-for-eco-efficient-substation-in-germa

[17] Sheet, Safety Data. 3M™ Novec™ 5110 Insulating Gas, 3M Company, St. Paul, MN (2015).

[18] Tang, Ju, et al. "Partial discharge recognition through an analysis of SF_6 decomposition products part 1: decomposition characteristics of SF 6 under four different partial discharges." IEEE Transactions on Dielectrics and Electrical Insulation 19.1 (2012): 29-36.

[19] Cheng, Lin, et al. "Action Mechanism of Trace O_2 on Characteristic Components of SF_6 Thermal Decomposition." High Voltage Engineering 41.12 (2015): 4105-4112.

[20] Metwally, I. A. "Status review on partial discharge measurement techniques in gas-insulated switchgear/lines." Electric Power Systems Research 69.1 (2004): 25-36.

[21] Zhang, Xiaoxing, et al. "Actuality and perspective of proximate analysis of SF_6 decomposed products under partial discharge." High Voltage Engineering 34.4 (2008): 664-669.

[22] Tang, Ju, et al. " Feature extraction of SF_6 thermal decomposition characteristics to diagnose overheating fault." IET Science, Measurement & Technology 9.6 (2015): 751-757.

[23] Tang, Ju, et al. "Correlation analysis between formation process of SF_6 decomposed components and partial discharge qualities." IEEE Transactions on Dielectrics and Electrical Insulation 20.3 (2013): 864-875.

[24] Chu, F. Y. "SF_6 decomposition in gas-insulated equipment." IEEE Transactions on Electrical Insulation 5 (1986): 693-725.

[25] Devins, J. C. "Replacement gases for SF_6." IEEE Transactions on Electrical Insulation 2 (1980): 81-86.

[26] Zhang, Xiaoxing, et al. "Reactive molecular dynamics study of the decomposition mechanism of the environmentally friendly insulating medium C_3F_7CN." RSC advances 7.80 (2017): 50663-50671.

[27] Li, Xingwen, et al. "Calculation of thermodynamic properties and transport coefficients of $C_5F_{10}O$-CO_2 thermal plasmas." Journal of Applied Physics 122.14 (2017): 143302.

[28] Linteris, Gregory T., et al. "Unwanted combustion enhancement by $C_6F_{12}O$ fire suppressant." Proceedings of the Combustion Institute 34.2 (2013): 2683-2690.

[29] Zhang, Xiaoxing, et al. "A Review Study of SF_6 Substitute Gases." Transactions of China Electrotechnical Society 33.12 (2018): 2883-2893.

[30] Koch, Hermann, and Mel Hopkins. "Overview of gas insulated lines (GIL)." IEEE Power Engineering Society General Meeting, 2005. IEEE, 2005.

[31] Gao, K., X. Yan, and Y. Liu. "Progress of technology for environment-friendly gas insulated transmission line." Transactions of China Electrotechnical Society 35.1 (2020): 3-20.

[32] Li, Bing, Y. K. Deng, and D. M. Xiao. "Insulation characteristics of C_3F_8 and C_3F_8-N_2 gas mixture using Boltzmann equation method." High Voltage Engineering 41.12 (2015): 4150-4157.

[33] Wu, Bian-Tao, et al. "Analysis of insulation characteristics of c-C_4F_8 and N_2 gas mixtures by the Monte Carlo method." Journal of Physics D: Applied Physics 39.19 (2006): 4204.

[34] Okabe, Shigemitsu, Junichi Wada, and Genyo Ueta. "Dielectric properties of gas mixtures with C_3F_8/C_2F_6 and N_2/CO_2." IEEE Transactions on Dielectrics and Electrical Insulation 22.4 (2015): 2108-2116.

[35] Wang, Xiaohua, et al. "Investigation of dielectric properties of cold C_3F_8 mixtures and hot C_3F_8 gas as Substitutes for SF_6." The European Physical Journal D 69.10 (2015): 1-7.

[36] Zhang Xiaoxing, Zhou Junjie, Tang Ju, and Zhuo Ran Chen Yang. "Experimental Study of Partial Discharge Insulating Properties for CF_3I-CO_2 Mixtures under Needle-Plate Electrode." Transactions of China Electrotechnical Society (2013).

[37] Zhang, Xiaoxing, et al. "Experimental analysis of the feasibility of CF_3I/CO_2 substituting SF_6 as insulation medium using needle-plate electrodes." IEEE Transactions on Dielectrics and Electrical Insulation 21.4 (2014): 1895-1900.

[38] Taki, M., et al. "Interruption capability of CF_3I Gas as a substitution candidate for SF_6 gas." IEEE Transactions on Dielectrics and Electrical Insulation 14.2 (2007): 341-346.

[39] Chachereau, Alise, Andreas Hösl, and Christian M. Franck. "Electrical insulation properties of the perfluoronitrile C_4F_7N." Journal of Physics D: Applied Physics 51.49 (2018): 495201.

[40] Li, Yi, et al. "Decomposition properties of C_4F_7N/N_2 gas mixture: an environmentally friendly gas to replace SF_6." Industrial & Engineering Chemistry Research 57.14 (2018): 5173-5182.

[41] Li, Yi, et al. "Assessment on the toxicity and application risk of C_4F_7N: A new SF_6 alternative gas." Journal of hazardous materials 368 (2019): 653-660.

[42] Stoller, P. C., et al. "Mixtures of CO_2 and $C_5F_{10}O$ perfluoroketone for high voltage applications." IEEE Transactions on Dielectrics and Electrical Insulation 24.5 (2017): 2712-2721.

[43] Li, Yi, et al. "Insight into the compatibility between $C_6F_{12}O$ and metal materials: Experiment and theory." IEEE Access 6 (2018): 58154-58160.

[44] Zhang, Xiaoxing, et al. "Insulation strength and decomposition characteristics of a $C_6F_{12}O$ and N_2 gas mixture." Energies 10.8 (2017): 1170.

[45] Zongkai, J. I. A., et al. "Study of partial discharge characteristics in HFO-1234ze (E)/N_2 mixtures." Plasma Science and Technology 22.11 (2020): 115403.

[46] Liu, Jie, et al. "Theoretical study of the decomposition mechanism of a novel eco-friendly insulation medium HFO-1336mzz (E) considering the effect of trace humidity." Journal of Physics D: Applied Physics 55.4 (2021): 045201.

[47] Mantilla, J. D., et al. "Investigation of the insulation performance of a new gas mixture with extremely low GWP." 2014 IEEE Electrical Insulation Conference (EIC). IEEE, 2014.

[48] Simka, Philipp, and N. Ranjan. "Dielectric strength of C5 perfluoroketone." 19th International Symposium on High Voltage Engineering. 2015.

[49] Zhong, Jianying, et al. "Insulation performance and liquefaction characteristic of $C_5F_{10}O/CO_2$ gas mixture." 2017 4th International Conference on Electric Power Equipment-Switching Technology (ICEPE-ST). IEEE, 2017.

[50] Wu, Junhui, et al. "Experiment of dielectric strength of $C_5F_{10}O$ gas mixture and calculation of stratification." 2017 4th International Conference on Electric Power Equipment-Switching Technology (ICEPE-ST). IEEE, 2017.

[51] Wang, X., et al. "Insulation performance of $C_5F_{10}O/CO_2$ gas mixture." High Voltage Engineering 43.3 (2017): 715-720.

[52] Zhang, Yue, et al. "AC breakdown and decomposition characteristics of environmental friendly gas $C_5F_{10}O$/Air and $C_5F_{10}O/N_2$." IEEE Access 7 (2019): 73954-73960.

[53] Chachereau, Alise, Andreas Hösl, and C. M. Franck. "Electrical insulation properties of the perfluoroketone $C_5F_{10}O$." Journal of Physics D: Applied Physics 51.33 (2018): 335204.

[54] Illenberger, Eugen, and Martina C. Meinke. "Reactions in acetone, perfluoroacetone and acetylene triggered by low energy (0–15 eV) electrons." International Journal of Mass Spectrometry 365 (2014): 80-85.

[55] Wang, Feng, et al. "Calculations of total electron impact ionization cross sections for fluoroketone and fluoronitrile." IEEE Transactions on Dielectrics and Electrical Insulation 26.5 (2019): 1693-1700.

[56] Xiong, Jiayu, et al. "Calculations of total electron-impact ionization cross sections for Fluoroketone $C_5F_{10}O$ and Fluoronitrile C_4F_7N using modified Deutsch–Märk formula." Journal of Physics D: Applied Physics 50.44 (2017): 445206.

[57] Zhong, Linlin, et al. "Electron-impact ionization cross sections of new SF_6 replacements: A method of combining Binary-Encounter-Bethe (BEB) and Deutsch-Märk (DM) formalism." Journal of Applied Physics 126.19 (2019): 193302.

[58] Aints, Märt, et al. "Effective ionization coefficient of C5 perfluorinated ketone and its mixtures with air." Journal of Physics D: Applied Physics 51.13 (2018): 135205.

[59] Egüz, Eda A., et al. "Measurements of Swarm Parameters in C_4F_7N: O_2: CO_2, $C_5F_{10}O$: O_2: CO_2 and $C_5F_{10}O$: O_2: N_2 Mixtures." The International Symposium on High Voltage Engineering. Springer,

Cham, 2019.

[60] Hyrenbach, Maik, et al. "Alternative gas insulation in medium-voltage switchgear." Proceedings of the 23rd International Conference on Electricity Distribution, Lyon, France. 2015.

[61] Ranjan, N., J. Carstensen, and S. Scheel. "Interruption of weakly cooled arcs in air and airplus." PLASMA PHYSICS AND TECHNOLOGY 4.2 (2017): 194-197.

[62] Saxegaard, Magne, et al. "Low-current interruption in SF_6-alternatives." CIRED-Open Access Proceedings Journal 2017.1 (2017): 286-288.

[63] Tatarinov, A. V., et al. "Dielectric barrier discharge processing of trans-CF_3CH=CHF and $CF_3C(O)CF(CF_3)_2$, their mixtures with air, N_2, CO_2 and analysis of their decomposition products." Plasma Chemistry and Plasma Processing 35.5 (2015): 845-862.

[64] Tatarinov, A. V., et al. "Comparative study of degradation of trans-1,3,3,3-trifluoropropene, 2,3,3,3-tetrafluoropropene, perfluoro-3-methylbutanone-2, and sulfur hexafluoride in dielectric-barrier discharge." High Energy Chemistry 50.1 (2016): 64-70.

[65] Li, Yi, et al. "Study on the Discharge Decomposition Characteristics of an Environmental-friendly Insulating Medium $C_5F_{10}O$." Proceedings of the CSEE 38.14 (2018): 4298-4306.

[66] Zhang, Xiaoxing, et al. " Decomposition mechanism of the $C_5F_{10}O/CO_2$, gas mixture as an alternative gas for SF_6." Chemical Engineering Journal 336 (2017): 36-48.

[67] Li, Yi, et al. "Decomposition characteristics of $C_5F_{10}O$/air mixture as substitutes for SF_6 to reduce global warming." Journal of Fluorine Chemistry 208 (2018): 65-72.

[68] Xiao, Song, et al. "Effects of micro-water on decomposition of the environment-friendly insulating medium $C_5F_{10}O$." AIP Advances 7.6 (2017): 065017.

[69] Li, Yingwen, et al. "Influence of Trace Water on Decomposition of Environmental Insulating Medium $C_5F_{10}O$." High Voltage Apparatus 55.8(2019): 10-15.

[70] Fu, Yuwei, et al. "Theoretical study of the decomposition pathways and products of C5-perfluorinated ketone (C5 PFK)." Aip Advances 6.8 (2016): 085305.

[71] Fu, Yuwei, Xiaohua Wang, and Jiandong Duan. "Calculated rate constants of main C5 PFK ($C_5F_{10}O$) decomposition reactions: an environmental-friendly alternative gas in electrical equipment." 2018 13th IEEE Conference on Industrial Electronics and Applications (ICIEA). IEEE, 2018.

[72] Zhou, Z., D. Han, and M. Zhao. "Decomposition characteristics of $C_5F_{10}O$ mixtures under corona discharge." Transactions of China Electrotechnical Society 36.2 (2020): 407.

[73] Zhang, Xiaoxing, et al. "Decomposition mechanism of the C5-PFK/CO_2 gas mixture as an alternative gas for SF6." Chemical Engineering Journal 336 (2018): 38-46.

[74] Zeng, Fuping, et al. "Over thermal decomposition characteristics of $C_5F_{10}O$: An environmental friendly insulation medium." IEEE Access 7 (2019): 62080-62086.

[75] Chen, Li, et al. "Chemical kinetics analysis of two C5-perfluorinated ketone (C5 PFK) thermal decomposition products: C_4F_7O and C_3F_4O." Journal of Physics D: Applied Physics 51.43 (2018): 435202.

[76] Chen, Li, Boya Zhang, and Xingwen Li. "Decomposition pathway and kinetic analysis of perfluoroketone $C_5F_{10}O$." Journal of Physics D: Applied Physics 53.41 (2020): 415502.

[77] Liu, Yue, et al. "Development and application of a ReaxFF reactive force field for molecular dynamics of perfluorinatedketones thermal decomposition." Chemical Physics 538 (2020): 110888.

[78] Fu, Yuwei, et al. "The varying characteristics of $C_5F_{10}O$ decomposition components at 300 K-3500 K with a chemical kinetic model." AIP Advances 9.1 (2019): 015318.

[79] Fu, Yuwei, et al. "Rate constants of $C_5F_{10}O$ decomposition reactions at temperatures of 300–3500 K."

Journal of Physics D: Applied Physics 52.3 (2018): 035202.
[80] Deng, Yunkun, et al. "Calculation and analysis of the thermophysical properties of $C_5F_{10}O$-N_2 mixtures." AIP Advances 9.10 (2019): 105019.
[81] Li, Yalong, et al. "Study on the Reaction Mechanism of Ethylene Propylene Diene Monomer Sealing Material and $C_5F_{10}O$–CO_2 Gas Mixture." ACS omega 6.43 (2021): 28770-28778.
[82] Zhang, Boya, et al. "Thermal and electrical decomposition products of C5F10O and their compatibility with Cu (1 1 1) and Al (1 1 1) surfaces." Applied Surface Science 513 (2020): 145882.
[83] Owens, John, Ang Xiao, and Jason Bonk. "Emission Reductions through use of Sustainable SF6 Alternatives." (2019).
[84] Castonguay, Jacques. "In-situ measurements of SF 6 leak rates in indoor gas-insulated switchgears (GIS)." Gaseous Dielectrics IX. Springer, Boston, MA, 2001. 549-554.
[85] Preve, Christophe, et al. "Validation method and comparison of SF6 alternative gases." CIGRE. 2016.
[86] Hyrenbach, Maik, Thomas A. Paul, and John Owens. "Environmental and safety aspects of AirPlus insulated GIS." CIRED-Open Access Proceedings Journal 2017.1 (2017): 132-135.
[87] Chenet, Luciano, et al. "An Enel-ABB partnership to develop an eco-sustainable alternative to SF_6 for MV switchgears, dimensionally compatible with existent apparatus using SF_6." (2019).
[88] Kristoffersen, Martin, et al. "RMU with Eco-Efficient Gas Mixture: Evaluation after 3 years of Field Experience." (2019).
[89] Chu, F. Y. "SF_6 decomposition in gas-insulated equipment." IEEE Transactions on Electrical Insulation 5 (1986): 693-725.
[90] Maik, H., and S. Zache. "Alternative gas insulation in medium-voltage switchgear." Proceedings of the 23rd International Conference on Electricity Distribution 2015.
[91] Muniz-Miranda, Maurizio, Francesco Muniz-Miranda, and Stefano Caporali. "SERS and DFT study of copper surfaces coated with corrosion inhibitor." Beilstein Journal of Nanotechnology 5.1 (2014): 2489-2497.
[92] Bazelyan, Eduard Meerovič, and Yu P. Raizer. Spark discharge. Routledge, 2017.
[93] Hikita, Masayuki, et al. "Insulation characteristics of gas mixtures including perfluorocarbon gas." IEEE Transactions on Dielectrics and Electrical Insulation 15.4 (2008): 1015-1022.
[94] Li, Yalong, et al. "Detection of ozone and nitric oxide in decomposition products of air-insulated switchgear using ultraviolet differential optical absorption spectroscopy (UV-DOAS)." Applied Spectroscopy 72.8 (2018): 1244-1251.
[95] Radisavljevic, B., et al. "Switching performance of alternative gaseous mixtures in high-voltage circuit breakers." Int. Symp. High Vol. Eng.(ISHVE). Vol. 1. 2017.
[96] Niemeyer, Lutz. "A generalized approach to partial discharge modeling." IEEE transactions on Dielectrics and Electrical insulation 2.4 (1995): 510-528.
[97] Stone, G. C., Meredith KW Stranges, and Donald G. Dunn. "Common questions on partial discharge testing: a review of recent developments in IEEE and IEC standards for offline and online testing of motor and generator stator windings." IEEE Industry Applications Magazine 22.1 (2015): 14-19.
[98] Hou, Niancang. "The infrared thermography diagnostic technique of high-voltage electrical equipments with internal faults." POWERCON'98. 1998 International Conference on Power System Technology. Proceedings (Cat. No. 98EX151). Vol. 1. IEEE, 1998.
[99] Zeng, Fuping, et al. "Decomposition characteristics of SF_6 under thermal fault for temperatures below 400 C." IEEE Transactions on Dielectrics and Electrical Insulation 21.3 (2014): 995-1004.
[100] Combes, Jean-Michel, Pierre Duclos, and Ruedi Seiler. "The born-oppenheimer approximation."

Rigorous atomic and molecular physics. Springer, Boston, MA, 1981. 185-213.
[101] Fermi, Enrico. "Un metodo statistico per la determinazione di alcune priorieta dell'atome." Rend. Accad. Naz. Lincei 6.602-607 (1927): 32.
[102] Thomas, Llewellyn H. "The calculation of atomic fields." Mathematical proceedings of the Cambridge philosophical society. Vol. 23. No. 5. Cambridge University Press, 1927.
[103] Hohenberg, Pierre, and Walter Kohn. "Inhomogeneous electron gas." Physical review 136.3B (1964): B864.
[104] Perdew, John P., et al. "Atoms, molecules, solids, and surfaces: Applications of the generalized gradient approximation for exchange and correlation." Physical review B 46.11 (1992): 6671.
[105] Runge, Erich, and Eberhard KU Gross. "Density-functional theory for time-dependent systems." Physical Review Letters 52.12 (1984): 997.
[106] Onida, Giovanni, Lucia Reining, and Angel Rubio. "Electronic excitations: density-functional versus many-body Green's-function approaches." Reviews of modern physics 74.2 (2002): 601.
[107] Baroni, Stefano, et al. "Phonons and related crystal properties from density-functional perturbation theory." Reviews of modern Physics 73.2 (2001): 515.
[108] Sternheimer, R. "On nuclear quadrupole moments." Physical Review 84.2 (1951): 244.
[109] Halgren, Thomas A., and William N. Lipscomb. "The synchronous-transit method for determining reaction pathways and locating molecular transition states." Chemical Physics Letters 49.2 (1977): 225-232.
[110] Govind, Niranjan, et al. "A generalized synchronous transit method for transition state location." Computational materials science 28.2 (2003): 250-258.
[111] Mayer, I. "Bond orders and valences from ab initio wave functions." International Journal of Quantum Chemistry 29.3 (1986): 477-483.
[112] Hirata, So, Timothy J. Lee, and Martin Head-Gordon. "Time-dependent density functional study on the electronic excitation energies of polycyclic aromatic hydrocarbon radical cations of naphthalene, anthracene, pyrene, and perylene." The Journal of chemical physics 111.19 (1999): 8904-8912.
[113] Van Gisbergen, S. J. A., et al. "Time-dependent density functional calculations on the electronic absorption spectrum of free base porphin." The Journal of chemical physics 111.6 (1999): 2499-2506.
[114] Delley, Bernard. "From molecules to solids with the $DMol^3$ approach." The Journal of chemical physics 113.18 (2000): 7756-7764.
[115] Zhang, Xiaoxing, et al. "Dissociative adsorption of environment-friendly insulating medium C_3F_7CN on Cu (111) and Al (111) surface: A theoretical evaluation." Applied Surface Science 434 (2018): 549-560.
[116] Switchgear, High-Voltage. "Controlgear–Part 200: AC Metal-Enclosed Switchgear and Controlgear for Rated Voltages Above 1 kV and Up to and Including 52 kV." IEC Standard (2003): 298-1994.
[117] 《Biotoxication tests by sulphur hexafluoride》(DL/T 921-2005)
[118] Preve, Christophe, et al. "Hazard study of medium-voltage switchgear with SF 6 alternative gas in electrical room." CIRED-Open Access Proceedings Journal 2017.1 (2017): 198-201.
[119] Peterson, Lance W., and David Artis. "Intestinal epithelial cells: regulators of barrier function and immune homeostasis." Nature Reviews Immunology 14.3 (2014): 141-153.

Research achievements during PhD studies

[1] **Li Yalong**, Zhang Xiaoxing, Li Yi, Wei Zhuo, Fanchao Ye, Xiao Song, Wang Yi. "Effect of oxygen on power frequency breakdown characteristics and decomposition properties of C5-PFK/CO_2 gas mixture." IEEE Transactions on Dielectrics and Electrical Insulation 28.2 (2021): 373-380.

[2] **Li Yalong**, Li Yi, Wei Zhuo, Zhang Xiaoxing, Chen Weijiang, Xiao Song, Bauchire Jean-Marc, Hong Dunpin, Tang Ju. "Quantification of C5-PFK Gas Mixture Based on Ultraviolet Differential Optical Absorption Spectroscopy (UV-DOAS)." IEEE Transactions on Dielectrics and Electrical Insulation, 29.2 (2022): 394-402.

[3] **Li Yalong**, Zhang Xiaoxing, Wang Yi, Li Yi, Zhang Yue, Wei Zhuo, Xiao Song. "Experimental study on the effect of O_2 on the discharge decomposition products of C5-PFK/N_2 mixtures." Journal of Materials Science: Materials in Electronics 30.21 (2019): 19353-19361.

[4] **Li Yalong**, Zhang Yue, Li Yi, Tang Feng, Lv Qishen, Zhang Ji, Xiao Song, Tang Ju, Zhang Xiaoxing. "Experimental study on compatibility of eco-friendly insulating medium $C_5F_{10}O/CO_2$ gas mixture with copper and aluminum." IEEE Access 7 (2019): 83994-84002.

[5] **Li Yalong**, Zhang Xiaoxing, Xie Cheng, Wei Zhuo, Xiao Song, Tang Ju. "Study on the Reaction Mechanism of Ethylene Propylene Diene Monomer Sealing Material and $C_5F_{10}O–CO_2$ Gas Mixture." ACS omega 6.43 (2021): 28770-28778.

[6] **Li Yalong**, Zhang Xiaoxing, Wei Zhuo, Wang Yi, Li Yi, Xiao Song. "Quantitative Detection on the Concentration of Eco-Friendly Insulating Medium $C_5F_{10}O$ Gas Mixture Concentration." Transactions of China Electrotechnical Society, 37.8 (2022):2117-2125. DOI: 10.19595/j.cnki.1000-6753.tces.201160.

[7] **Li Yalong**, Zhang Xiaoxing, Cui Zhaolun, Xiao Hanyan, Zhang Guozhi. "Experiment of Effect of Ammonia on Degradation of Sulfur Hexafluoride by Dielectric Barrier Discharg." Transactions of China Electrotechnical Society, 34.24 (2019): 5262-5269.

[8] **Li Yalong**, Zhang Xiaoxing, Bauchire Jean-Marc, Hong Dunpin, Xiao Song. "Effect of arc on the decomposition characteristics of eco-friendly insulating medium $C_5F_{10}O$." XVème Colloque sur les Arcs Electriques. 2021.

[9] **Li Yalong**, Zhang Xiaoxing, Wei Zhuo, Wang Yi, Li Yi, Xiao Song. "Study on the Acute Inhalation Toxicity of Eco-friendly Gas Insulating Medium C5-PFK." 22nd International Symposium on High Voltage Engineering, ISH 2021. 2021.

Recherche sur les caractéristiques de décomposition et la biosécurité du gaz isolant mixte $C_5F_{10}O/N_2/O_2$

Résumé long

L'hexafluorure de soufre (SF_6) possède d'excellentes propriétés physico-chimiques et électriques. Ses performances en matière d'isolation sont environ 2,5 fois supérieures à celles de l'air à la pression atmosphérique, et ses performances en matière d'extinction d'arc sont environ 100 fois supérieures à celles de l'air dans les mêmes conditions. En outre, il possède des propriétés chimiques extrêmement stables et constitue un gaz diélectrique idéal pour l'isolation et l'extinction des arcs électriques. Cependant, le gaz SF_6 a un effet de serre très important et une durée de vie extrêmement longue dans l'atmosphère. Son potentiel de réchauffement global (PRG) est 23 500 fois supérieur à celui du CO_2 (en 100 ans), et sa durée de vie naturelle dans l'atmosphère est d'environ 3 200 ans. Par conséquent, le SF_6 émis dans l'atmosphère s'accumulera progressivement. La concentration moyenne mondiale de SF_6 a atteint plus de 10,89 ppt. Le taux de croissance annuel, d'environ 0,24 ppt par an, n'est pas stable et tend à croître. La concentration moyenne mondiale de SF_6 dans l'atmosphère a par exemple augmenté de 44,49 % au cours des dix dernières années. Actuellement, plus de 80 % du SF_6 produit annuellement dans le monde est utilisé dans l'industrie énergétique. L'utilisation du SF_6 dans les principaux équipements électriques chinois a atteint à elle seule 7000 tonnes par an et continuera d'augmenter. L'utilisation à grande échelle du gaz SF_6 produira inévitablement une grande quantité de gaz de fuite SF_6, ce qui entraînera des dangers cachés majeurs pour l'environnement. Certains pays et organisations ont mis en place de nombreuses politiques et mesures visant à réduire l'utilisation du gaz SF_6 et à limiter ses

émissions directes. Le protocole de Kyoto, signé dès 1997, a identifié le SF_6 comme l'une des six catégories de gaz à effet de serre dont les émissions doivent être limitées.

En réponse à l'appel aux économies d'énergie et à la réduction des émissions, les chercheurs du secteur de l'énergie du monde entier travaillent également sur des solutions pour réduire l'effet de serre causé par les émissions de gaz SF_6 dans différentes directions. À l'heure actuelle, l'idée de réduire les émissions de gaz SF_6 dans l'industrie électrique tourne principalement autour du recyclage du gaz d'échappement SF_6 (en vue de sa purification et de sa réutilisation), de sa dégradation et de sa transformation, de l'utilisation de gaz d'isolation de remplacement, à faible effet de serre, pour réduire ou interdire à terme l'utilisation du gaz SF_6.

L'utilisation d'un gaz isolant écologique à faible effet de serre pour remplacer le gaz SF_6 comme diélectrique d'isolation peut résoudre l'effet de serre provoqué par le SF_6 depuis la source. Ces dernières années, le perfluoropentanone ($C_5F_{10}O$) a susciter l'intérêt des chercheurs grâce à ses excellentes propriétés environnementales et d'isolation. Il est considéré comme une alternative prometteuse au gaz SF_6 en tant que diélectrique d'isolation dans les équipements électriques de basse et moyenne tension. Le PRG du $C_5F_{10}O$ est inférieur à 1, le potentiel d'appauvrissement de la couche d'ozone (PAO) est de 0, et la durée de vie dans l'atmosphère est d'environ 15 jours. Le gaz $C_5F_{10}O$ possède également des propriétés d'isolation élevées, et sa rigidité diélectrique relative est 1,4 fois supérieure à celle du SF_6. En raison de sa température de liquéfaction élevée (26,9 °C sous pression normale), il est nécessaire de le mélanger à des composants de l'air (CO_2, N_2 ou air sec) ayant une température de liquéfaction plus basse pour réduire la température du point de rosée du mélange afin de répondre aux exigences de température dans les applications d'ingénierie. L'utilisation du mélange gazeux $C_5F_{10}O$ comme diélectrique isolant pour les équipements électriques peut ainsi réduire de plus de 99,99 % l'effet de serre causé par l'utilisation du SF_6 dans l'industrie énergétique.

Bien que le gaz $C_5F_{10}O$ possède d'excellentes propriétés de protection de l'environnement et d'isolation, l'évaluation de la fiabilité de son utilisation doit également inclure la stabilité de l'interface gaz-matériau solide, la stabilité électrothermique, la performance d'extinction de l'arc, les caractéristiques de décomposition, la biosécurité et bien d'autres aspects.

Le diélectrique isolant idéal doit être capable de maintenir l'équipement électrique stable dans des conditions de fonctionnement complexes et même dans des conditions de défaillance, sans décomposition importante. Le GIE (Gas Insulated Equipment) a une tension de fonctionnement élevée et fonctionne dans un environnement électromagnétique fort pendant une longue période, ce qui est susceptible de provoquer des défauts cachés tels que des décharges partielles (DP) et des défauts de surchauffe partielle (DSP). Parallèlement, les équipements électriques peuvent avoir des défauts d'isolation tels que des bavures au cours de la production, de l'installation, de l'exploitation et de la maintenance, et peuvent provoquer des DP pendant le fonctionnement de l'équipement. La DP est un processus à long terme qui se développe lentement. Si le défaut potentiel ne peut être détecté à temps, les particules à haute énergie générées par l'ionisation de la DP se diffuseront dans le gaz environnant et subiront des processus physiques et chimiques tels que l'ionisation par collision et l'adsorption avec d'autres molécules, aggravant encore l'intensité de la DP, ce qui entraînera la décomposition du diélectrique à l'intérieur du GIE et conduira finalement à un accident dû à la défaillance de l'isolation. En outre, la résistance de contact entre les contacts haute tension à l'intérieur de l'équipement peut augmenter en raison d'un mauvais contact, de l'endommagement et de l'oxydation de la couche argentée à la surface, ce qui peut entraîner un échauffement anormal pendant le fonctionnement en raison de l'effet thermique du courant. Le GIE ne peut dissiper la chaleur que par échange avec le de gaz interne, alors que le fonctionnement normal de l'équipement peut également générer des augmentations de température allant jusqu'à 70 °C sur le jeu de barres. Lorsque la DSP se produit à l'intérieur de l'équipement, la température à l'intérieur de l'équipement s'élève à un niveau plus élevé. Une température élevée peut entraîner la décomposition du gaz isolant et la corrosion de la surface du conducteur métallique. Le contact à long terme entre le gaz isolant et le conducteur métallique, et la réaction chimique à l'interface gaz-solide, lorsque la température augmente, peuvent conduire à la décomposition du gaz isolant, ce qui menace la durée de vie et la stabilité opérationnelle de l'équipement. En outre, les caractéristiques de récupération de la rigidité diélectrique du gaz après sa décomposition et la biosécurité du gaz lui-même et de ses produits de décomposition sont également essentielles pour déterminer si le gaz isolant est adapté à l'application.

A l'heure actuelle, les recherches sur la stabilité de l'interaction gaz-matériau solide, sur les caractéristiques de décomposition électrothermique et sur la biosécurité du $C_5F_{10}O$ dans des conditions de fonctionnement normales et dans des conditions de défaillance du GIE sont encore insuffisantes. Les caractéristiques macroscopiques ne sont pas entièrement comprises et le mécanisme de réaction microscopique n'est pas clair. Il est donc nécessaire de mener des recherches systématiques sur les caractéristiques et le mécanisme de décomposition du mélange gazeux $C_5F_{10}O$, d'évaluer de manière exhaustive la faisabilité et le potentiel de son application technique en combinaison avec la biosécurité, ainsi que de fournir des données de base de référence pour la technologie d'exploitation et de maintenance basée sur la méthode d'analyse des composants, de manière à promouvoir la modernisation écologique et le développement sain de l'industrie chinoise des équipements d'isolation des gaz de transmission et de distribution.

Le GIE a une longue durée de vie et une longue période de maintenance. La pression de fonctionnement du gaz y est également élevée, et le gaz isolant est en contact direct avec les matériaux à l'intérieur de l'équipement pendant une longue période dans des conditions de fonctionnement normales. Les propriétés physico-chimiques $C_5F_{10}O$ sont très différentes de celles du gaz SF_6. L'interaction de l'interface gaz-solide entre le mélange gazeux $C_5F_{10}O/N_2/O_2$ et les matériaux de l'équipement accompagne l'ensemble du cycle de vie du GIE, ce qui impose des exigences plus élevées en matière de compatibilité avec les matériaux, ce qui constitue également une condition préalable à son application technique. Par rapport aux matériaux isolants non métalliques tels que les matériaux d'étanchéité en caoutchouc et les résines époxy dans l'équipement, les propriétés chimiques des matériaux conducteurs métalliques sont plus actives, et l'augmentation maximale de la température causée par l'effet thermique du courant pendant le fonctionnement normal de l'équipement peut conduire les barres conductrices métalliques à travailler dans un environnement de température de 100~120 °C (la température de travail est beaucoup plus élevée que celle du matériau isolant de l'enveloppe de l'équipement). Par conséquent, cette thèse a d'abord consisté à la réalisation d'expériences pour déterminer les caractéristiques de décomposition de l'interface du mélange gazeux $C_5F_{10}O/N_2/O_2$ et des matériaux métalliques (cuivre, aluminium et argent) dans l'équipement à différentes températures (120 ~ 220 °C), et pour obtenir des informations

sur la stabilité de l'interaction gaz-solide dans des conditions de vieillissement thermiquement accéléré.

Les résultats obtenus indiquent que la stabilité gaz-solide du mélange gazeux $C_5F_{10}O$ avec le cuivre est médiocre, ce qui entraîne la corrosion de la surface du cuivre pour former du CuO et du Cu_2O à des températures élevées. L'oxygène dans le mélange gazeux aggravera la corrosion de la surface du cuivre à des températures élevées, alors que l'oxygène a l'effet inverse à des températures expérimentales plus basses. La surface du cuivre doit donc être traitée avec un produit anticorrosion. Les propriétés chimiques du matériau argenté sont stables, et la couche protectrice argentée sur la surface du cuivre peut protéger le matériau cuivreux. Ceci est dû au fait que l'atome d'oxygène carbonique de la molécule $C_5F_{10}O$ a une réactivité chimique élevée, et que le chevauchement des orbitales électroniques et le transfert de charge se produisent lors de l'interaction avec la surface de Cu(111). Au cours du processus d'interaction, les orbitales 3d et 4s de l'atome de cuivre et l'orbitale 2p de l'atome d'oxygène carbonyle de la molécule $C_5F_{10}O$ sont hybridées et forment des liaisons chimiques principalement en position supérieure. L'interaction de la molécule de $C_5F_{10}O$ avec le Cu_2 O(111) produit par l'oxydation du cuivre forme également des liaisons chimiques, principalement par l'hybridation du site supérieur avec l'orbitale 3d du cation Cu^+ de coordination insaturée. L'adsorption de la molécule $C_5F_{10}O$ et de la surface Ag(111) relève de l'adsorption physique, et la stabilité de l'interaction entre $C_5F_{10}O$ et Ag est meilleure. La surface du matériau en aluminium s'oxyde naturellement pour former une couche d'oxyde Al_2O_2 afin de protéger le matériau en aluminium interne, montrant ainsi une grande stabilité de l'interface gaz-solide. Lors de l'interaction entre la molécule $C_5F_{10}O$ et l'Al_2O_3 (111), la charge positive de l'atome d'aluminium attire l'atome d'oxygène carbonique de la molécule $C_5F_{10}O$ et repousse l'atome de fluor. Dans le processus d'interaction, une grande énergie d'adsorption est générée en raison de l'interaction des charges positives et négatives, mais aucun transfert de charge ne se produit. L'interaction entre la molécule de $C_5F_{10}O$ et l'Al_2O_3 (111) relève de l'adsorption physique. Par conséquent, afin de prolonger la durée de vie et la stabilité de fonctionnement de l'équipement, la surface du cuivre dans le GIE doit être traitée par argenture, tandis que l'aluminium n'a pas besoin de traitement spécial. Il est nécessaire de prêter attention à l'intégrité de la couche protectrice d'argent dans les applications techniques, et si elle est endommagée, elle doit être entretenue à temps.

Dans des conditions de fonctionnement à long terme, des défauts peuvent apparaître liés à des DSP, des DP ou claquages AC. Lorsqu'un défaut se produit, une série de réactions chimiques peuvent avoir lieu dans le gaz isolant sous l'effet de la décharge et des effets thermiques, et divers produits de décomposition peuvent être produits. Comme la structure moléculaire du SF_6 est simple et que le gaz isolant est un composant unique, la plupart de ses produits de décomposition sont des gaz sulfuriques. En revanche, la structure moléculaire du gaz $C_5F_{10}O$ est plus complexe et il doit être mélangé à un gaz tampon, ce qui rend son processus de décomposition plus compliqué. En outre, la stabilité de l'interaction entre le mélange gazeux $C_5F_{10}O/N_2$ et le cuivre s'est avérée meilleure que celle du mélange gazeux $C_5F_{10}O/N_2/O_2$ dans l'étude de la stabilité de l'interaction entre le gaz et l'interface solide. Lorsque le mélange gazeux ne contient pas d'oxygène, il est bénéfique pour la stabilité de l'interaction gaz-solide, mais le mélange gazeux $C_5F_{10}O/N_2$ créera des produits de décomposition solides noirs lors de la décomposition par décharge, ce qui affectera sérieusement la fiabilité opérationnelle de l'équipement. Par conséquent, dans cette thèse, l'expérience sur les caractéristiques de décomposition du mélange gazeux $C_5F_{10}O/N_2/O_2$ a été réalisée en construisant une plate-forme expérimentale dédiée de simulation de décharge et de défauts thermiques. L'étude sur l'influence de la concentration d'oxygène sur ses caractéristiques de décomposition a été étudiée.

Le test de l'effet de la DP sur les caractéristiques de décomposition du mélange gazeux $C_5F_{10}O/N_2/O_2$ a révélé qu'en termes de paramètres électriques, le gaz SF_6 est plus susceptible de produire une DP que le mélange gazeux $C_5F_{10}O/N_2/O_2$ dans les mêmes conditions. La teneur en oxygène du mélange gazeux $C_5F_{10}O/N_2/O_2$ affecte les caractéristiques de la décharge, tels que l'intensité et la fréquence de la DP, alors qu'elle n'a aucun effet sur les valeurs de la tension d'amorçage de la décharge partielle (PDIV) et de la tension de claquage dans un champ électrique non uniforme. Lorsque la teneur en oxygène est inférieure ou égale à 8 %, avec l'augmentation de la teneur en oxygène, l'amplitude totale de la décharge, le nombre total d'impulsions de décharge et la partie positive de l'amplitude de la décharge en 1 seconde augmentent progressivement. La partie négative de l'amplitude de la décharge reste inchangée et le nombre d'impulsions de décharge dans la demi-alternance négative diminue progressivement.

Lorsque la teneur en oxygène est de 12 %, l'amplitude de la décharge générée par une seule impulsion de décharge est plus faible, mais sa fréquencede décharge est la plus élevée. En ce qui concerne les produits de décomposition, les produits de décomposition générés par la DP du mélange gazeux $C_5F_{10}O/N_2/O_2$ sont principalement le CF_4, le CO, le CO_2 , le CF_2O, le C_2F_6 , le C_3F_6 , le C_3F_8 , le C_4F_{10} et le C_3 HF_7. Étant donné que le gaz $C_5F_{10}O$ contient l'élément O, les types de produits de décomposition créés par le mélange gazeux $C_5F_{10}O/N_2/O_2$ ne changent pas par rapport au mélange gazeux $C_5F_{10}O/N_2$. Avec l'augmentation du temps de DP, les concentrations des produits de décomposition augmentent progressivement, à l'exception de la concentration du gaz CO qui reste inchangée. Les concentrations des gaz CF_4 et C_2F_6 produits par la décomposition du mélange gazeux $C_5F_{10}O/N_2/O_2$ à une concentration d'oxygène de 0 % et 4 % augmentent linéairement avec le temps de DP, et cette règle peut être considérée comme caractéristique pour le diagnostic des défauts de DP d'équipements isolés $C_5F_{10}O/N_2/O_2$. Comparé au mélange gazeux $C_5F_{10}O/N_2$, le mélange gazeux $C_5F_{10}O/N_2/O_2$ se décomposera pour produire plus de CO_2 , CF_2 O et C_3F_8 pendant le processus de DP, mais la teneur en C_2F_6 et C_3HF_7 produite par la décomposition sera réduite.

Lors de l'essai des caractéristiques de décomposition par claquage en courant alternatif du mélange gazeux $C_5F_{10}O/N_2/O2$, il a été constaté que le mélange gazeux $C_5F_{10}O/N_2$ produira des solides noirs contenant des substances carbonées simples, CuF_2 et CuO pendant le processus de décomposition, qui adhéreront à la surface de l'électrode et fausseront le champ électrique dans l'espace autour de l'électrode, et que l'ajout d'oxygène au mélange gazeux $C_5F_{10}O/N_2$ peut inhiber la production de ces solides noirs. La dispersion du mélange gazeux $C_5F_{10}O/N_2/O_2$ sera légèrement plus importante que celle du mélange gazeux $C_5F_{10}O/N_2$, mais sa tension de claquage en courant alternatif sera légèrement plus élevée, ce qui est positif pour améliorer sa résistance d'isolation. En ce qui concerne les produits de décomposition du gaz, la décomposition en courant alternatif est cohérente avec les types de produits de décomposition produits par la DP. Avec l'augmentation du nombre de décharges, la teneur des six composants de décomposition, CO, CF_2 O, CF_4, $C2F_4$, C_2F_6 et C_3F_8 , produits dans tous les groupes de test montre une tendance à la hausse. la réduction la plus évidente étant celle de C_2F_4.

Le test des caractéristiques de décomposition thermique du mélange gazeux $C_5F_{10}O/N_2/O_2$ a révélé que la décomposition du mélange gazeux $C_5F_{10}O/N_2$ commence à 300°C et crée des produits de décomposition primaires tels que C_3F_6 , CHF_3 et C_3HF_7. Un grand nombre de produits de décomposition apparaissent à une température supérieure à 450°C et créent à leur tour des produits de décomposition tels que CF_2O, C_2F_6, C_3F_8 et CF_4. Le CHF_3 n'est produit qu'à une température de 300°C, et le gaz C_3F_6 n'est produit qu'à une température comprise entre 300°C et 450°C. A des températures plus élevées, les gaz CHF_3 et C_3F_6 générés par la décomposition du mélange gazeux $C_5F_{10}O/N_2$ participent aux réactions de décomposition et se transformeront également. Le mélange gazeux $C_5F_{10}O/N_2/O2$ commence aussi à se décomposer à 300°C pour créer des produits de décomposition primaires tels que C_3F_6 et C_3HF_7, qui commencent à se décomposer en grandes quantités au-dessus de 400°C. La différence est que le mélange de gaz $C_5F_{10}O/N_2/O_2$ ne produit pas de gaz CHF_3 et que la température requise pour sa décomposition significative est inférieure à celle du mélange de gaz $C_5F_{10}O/N_2$. La teneur des quatre gaz, CF_4, $C2F_6$, $C3F_8$ et CO_2, produits par la décomposition du mélange gazeux $C_5F_{10}O/N_2/O_2$ augmente progressivement avec le temps de décomposition thermique. Les concentrations des gaz CF_4 et C_3F_8 produits par la décomposition thermique du mélange de gaz $C_5F_{10}O/N_2/O_2$ ont tendance à augmenter puis à diminuer avec l'augmentation de la concentration d'oxygène dans les mêmes conditions de température, et la valeur maximale apparaît à une concentration d'oxygène de 8 %. La concentration du gaz CF_2O a également une valeur maximale lorsque la concentration d'oxygène est de 8 %. La concentration du gaz CO_2 tend à augmenter progressivement avec l'augmentation de la concentration d'oxygène, tandis que la concentration du gaz $C2F_6$ tend à diminuer progressivement.

Les voies de dissociation du gaz $C_5F_{10}O/N_2/O_2$ induits par la décharge et la thermique, les paramètres thermiques et cinétiques des voies de réaction pertinentes ainsi que les effets de l'oxygène et de l'eau sur les réactions de décomposition sont obtenus sur la base de la théorie DFT et de la théorie des états de transition. Les calculs montrent que l'énergie de liaison de la double liaison carbonyle C=O de la molécule $C5F_{10}O$ est la plus importante, tandis que la force des deux liaisons C-C reliées au groupe carbonyle est

la plus faible et que l'énergie requise pour la rupture est la plus basse. La région électrophile de la molécule $C_5F_{10}O$ est aussi principalement concentrée autour du groupe carbonyle. Lorsque la molécule $C_5F_{10}O$ est décomposée, les deux liaisons C-C reliées au groupe carbonyle sont rompues en premier pour générer des particules telles que CF_3, CO et CF_3CFCF_3, qui réagissent avec la faible quantité d'eau à l'intérieur de l'équipement pour former des produits de décomposition primaires tels que CHF_3, C_4F_{10}, C_3HF_7 et C_3F_6O. La dissociation ultérieure de la molécule $C_5F_{10}O$ génère des particules F, CF, CF_2 et CF_3 et se compose pour former C_3F_8 et des produits gazeux à petites molécules tels que HF, CO, CO_2 et CF_4. Les règles de formation de chaque produit de décomposition sont cohérentes avec les résultats expérimentaux.

Il n'y a pas de différence entre les produits de décomposition du mélange gazeux $C_5F_{10}O/N_2/O_2$ lorsque des défauts type PD et AC se produisent. Lorsque le DSP se produit, en raison de la faible énergie à la température de 300°C, le mélange gazeux $C_5F_{10}O/N_2/O_2$ produit d'abord des produits de décomposition primaires tels que C_3F_6 et C_3HF_7. Lorsque la température dépasse 400°C, il se forme des produits de décomposition tels que CF_2 O, C_2F_6, C_3F_8 et CF_4. En raison de l'énergie relativement élevée libérée par la décharge, les types de produits de décomposition créés par les différents types de décharge ne montrent pas de changements dans les types de produits de décomposition causés par l'augmentation de la température pendant la décomposition thermique. La teneur en oxygène affecte les paramètres électriques des caractéristiques de décomposition en DP et en claquage AC du mélange gazeux $C_5F_{10}O/N_2/O_2$. Bien que l'ampleur et la fréquence des décharges cumulées du mélange gazeux $C_5F_{10}O/N_2/O_2$ par unité de temps soient faibles lorsque la teneur en oxygène est de 16 %, la dispersion de la tension de claquage du mélange gazeux $C_5F_{10}O/N_2/O_2$ est plus importante lorsque le claquage AC se produit. La teneur en produits de décomposition générés lors de la décharge et de la défaillance thermique est également plus élevée. Après réflexion, il est recommandé d'ajouter 4 % d'oxygène au mélange gazeux $C_5F_{10}O/N_2$ afin d'empêcher la génération de produits de décomposition solides au cours du processus de décharge. Bien que l'ajout d'oxygène favorise la décomposition du mélange gazeux $C_5F_{10}O/N_2$ en cas de décharge et de DSP, les produits de décomposition du mélange gazeux $C_5F_{10}O/N_2/O_2$ contenant 4 % d'oxygène sont inférieurs à ceux du groupe d'essai contenant une concentration d'oxygène plus élevée,

et la concentration des produits de décomposition est proche de celle du mélange gazeux $C_5F_{10}O/N_2$ sans oxygène.

La norme IEC62271-200 stipule que le taux annuel de fuite de gaz des GIE ne doit pas dépasser 0,1 %, alors que certains équipements isolés au gaz (GIE) à basse et moyenne tension, tels que les interrupteurs de charge (LBS), sont généralement utilisés dans un environnement intérieur, ce qui peut entraîner une augmentation des fuites de gaz des GIE si la ventilation intérieure est médiocre. En outre, les PD, les DSP et les ruptures d'isolation des GIE peuvent entraîner la décomposition du gaz d'isolation interne, ce qui peut même conduire à des accidents graves de fuite de gaz interne. Par conséquent, il est essentiel d'évaluer la biosécurité du $C_5F_{10}O$ et de ses produits de décomposition avant l'application à grande échelle du GIE $C_5F_{10}O$ afin de préserver la santé et la vie des travailleurs.

Dans cette thèse, des souris ont été utilisées comme animaux de laboratoire pour tester la toxicité aiguë par inhalation du gaz $C_5F_{10}O$. Les résultats ont montré que la concentration létale à 50 % (LC50) (souris, 4h) du $C_5F_{10}O$ est de 7461ppm pour la femelle et de 8724ppm pour le mâle. La concentration inoffensive de $C_5F_{10}O$ est de 7400 ppm pour la femelle et de 8600 ppm pour le mâle. L'inhalation de faibles concentrations (< LC50) de $C_5F_{10}O$ entraîne une excitation excessive des souris avec une augmentation du rythme cardiaque et respiratoire. Ces symptômes cliniques peuvent disparaître dans les 5 heures suivant l'exposition et les organes des souris ne sont pas endommagés. Ces réactions physiologiques cliniques peuvent servir de signal d'alerte précoce pour évaluer les premiers symptômes d'un empoisonnement aigu par inhalation de gaz $C_5F_{10}O$ chez les travailleurs concernés, et des mesures doivent être prises en temps utile pour éviter de mettre leur vie et leur santé en danger. La CL50 (4h, souris) du mélange de gaz $C_5F_{10}O/N_2/O_2$ après décomposition à l'arc est de 2298 ppm. Des lésions des poumons, du foie et de la rate peuvent être observées chez les souris exposées à un mélange de 2400 ppm. Compte tenu du taux de fuite annuel et des défauts de fuite de gaz du LBS, les produits de décomposition du gaz $C_5F_{10}O$ présentent peu de risques potentiels pour la santé du personnel technique, mais des mesures de protection sont recommandées pendant le travail.

En résumé, cette thèse a d'abord évalué la stabilité de l'interaction gaz-solide du mélange gazeux $C_5F_{10}O/N_2/O_2$ avec le cuivre, l'aluminium et l'argent, qui sont des matériaux métal-

-liques couramment utilisés dans les équipements électriques. Elle a permis de clarifier le mécanisme de l'interaction de l'interface gaz-solide entre le mélange gazeux $C_5F_{10}O$ et les matériaux métalliques, et de proposer un schéma d'optimisation de la stabilité de la couche protectrice plaquée argent sur la surface du matériau métallique en cuivre ayant une mauvaise stabilité gaz--solide. Ceci résout de manière préliminaire la durée de vie et la stabilité de fonctionnement du GIE. Le mécanisme de décomposition du mélange gazeux $C_5F_{10}O/N_2/O_2$ a été étudié au travers d'expériences et de simulation. Les caractéristiques de décomposition des défauts électriques et thermiques typiques du mélange gazeux $C_5F_{10}O/N_2/O_2$ contenant différentes concentrations d'oxygène ont été obtenues. La composition et les voies chimiques de génération des produits de décomposition du mélange gazeux en cas de calquage en courant alternatif, de décharge partielle et de surchauffe partielle ont été obtenues, et la corrélation entre les types et les contenus des produits de décomposition caractéristiques et les types de panne, ainsi que la régulation de l'oxygène dans les produits de décomposition du mélange gazeux $C_5F_{10}O$ ont été analysés, ainsi que le mécanisme d'inhibition de la précipitation des produits solides. Les produits caractéristiques de la décharge et du défaut thermique du mélange gazeux $C_5F_{10}O/N_2/O_2$ ont été déduits, ce qui a permis de fournir une référence pour la surveillance en ligne des défauts basée sur les éléments de décomposition. Enfin, afin de garantir la sécurité de l'application du GIE $C_5F_{10}O$, la biosécurité du $C_5F_{10}O$ et de ses produits de décomposition par l'arc a été étudié. Les données de toxicité aiguë par inhalation du gaz $C_5F_{10}O$ et de ses produits de décomposition ont été obtenues, et leur effets sur divers organes et signes vitaux des souris ont été clarifiés par des expériences et des analyses pathologiques et hématologiques. Un ratio du mélange gazeux $C_5F_{10}O/N_2/O_2$ adapté aux applications techniques a été proposé, et des suggestions ont été faites pour les mesures de protection des travailleurs concernés. Les résultats de ces recherches constituent une référence importante pour l'application technique, l'exploitation et la maintenance du mélange gazeux $C_5F_{10}O/N_2/O_2$.

Yalong LI

Recherche sur les caractéristiques de décomposition et la biosécurité du gaz isolant mixte $C_5F_{10}O/N_2/O_2$

Dans ce travail de thèse de doctorat, des études expérimentales et théoriques sont réalisées sur les caractéristiques de décomposition du mélange gazeux $C5F_{10}O/N_2/O_2$ à l'interface gaz-solide de matériaux métalliques et sous l'action d'une décharge électrique dans un appareil de coupure électrique. La faisabilité et la sécurité de son utilisation sont évaluées en combinaison avec la biosécurité du gaz $C_5F_{10}O$ et des produits de décomposition du gaz plasmagène. Compte tenu du contact long entre le mélange gazeux $C_5F_{10}O/N_2/O_2$ et les matériaux internes de l'équipement de coupure électrique pendant son fonctionnement, la stabilité de l'interaction gaz-solide du mélange gazeux avec les métaux couramment utilisés (cuivre, aluminium et argent), à l'intérieur de l'équipement est caractérisé, et le mécanisme d'interaction gaz-solide entre le mélange gazeux $C_5F_{10}O$ et les matériaux métalliques est précisé. Un défaut thermique peut également se produire pendant le fonctionnement de l'équipement. Les caractéristiques typiques de la décharge et de la décomposition par défaut thermique du mélange gazeux $C_5F_{10}O/N_2/O_2$ contenant différentes concentrations d'oxygène sont identifiées. La composition et les processus de création des produits de décomposition du mélange gazeux sont obtenues, et la corrélation entre les types et le contenu des produits de décomposition caractéristiques et les types de défaut, ainsi que la réaction de l'oxygène vers les produits de décomposition du mélange gazeux $C_5F_{10}O$ et le mécanisme d'inhibition de la précipitation des produits solides sont analysés. Sur la base de ce travail, nous proposons un schéma d'optimisation de la stabilité de la couche protectrice argentcuivre est proposé pour le cuivre avec une faible stabilité gaz-solide du gaz $C_5F_{10}O/N_2/O_2$. Nous avons défini les produits caractéristiques de la décharge et du défaut thermique du mélange gazeux, ce qui constitue une référence pour la surveillance en ligne des défauts. Nous avons testé la biosécurité du $C_5F_{10}O$ et des produits de décomposition par arc. Sa sécurité d'application a été évaluée en fonction des caractéristiques de décharge et de décomposition thermique du mélange gazeux, et des mesures et de protection ciblées et des suggestions sont proposées.

Mots clés : Mélange gazeux $C_5F_{10}O/N_2/O_2$, gaz isolant écologique, stabilité de l'interface gaz-solide, décomposition par décharge, décomposition thermique, biosécurité

Research on the Decomposition Characteristics and Biosafety of $C_5F_{10}O/N_2/O_2$ Mixed Insulating Gas

In this doctoral thesis work, experimental and theoretical studies are carried out on the decomposition characteristics of $C_5F_{10}O/N_2/O_2$ gas mixture at the gas-solid interface of metal materials and under the discharge and thermal action, and the feasibility and safety of its application are evaluated in combination with the biosafety of $C_5F_{10}O$ gas and arc decomposition products of $C_5F_{10}O/N_2/O_2$. Considering the long-term contact between $C_5F_{10}O/N_2/O_2$ gas mixture and the internal materials of the equipment during normal operation, the gas-solid interaction stability of $C5F_{10}O/N_2/O_2$ gas mixture with commonly used metal copper, aluminum and silver inside the equipment is evaluated, and the mechanism of gas-solid interface interaction between $C_5F_{10}O$ gas mixture and metal materials is clarified. Discharge and thermal fault may also occur during the long-term operation of the equipment. The failure decomposition mechanism of $C_5F_{10}O/N_2/O_2$ gas mixture is studied through experiments and simulations. The typical discharge and thermal fault decomposition characteristics of $C_5F_{10}O/N_2/O_2$ gas mixture containing different concentrations of oxygen are revealed. The composition and generation rules of decomposition products of the gas mixture under the faults are obtained, and the correlation between the types and contents of characteristic decomposition products and the fault types, as well as the regulation of oxygen to $C_5F_{10}O$ gas mixture decomposition products and the inhibition mechanism of solid product precipitation are analyzed. In conclusion, based on the simulation and experimental results, we proposed the stability optimization scheme of silver-plated protective layer on copper surface for metal copper material with poor gas-solid stability of $C_5F_{10}O/N_2/O_2$ gas. We extracted the characteristic products characterizing the discharge and thermal fault of $C_5F_{10}O/N_2/O_2$ gas mixture, which provided a reference for the on-line fault monitoring based on the decomposition components. We tested the biosafety of $C_5F_{10}O$ and its arc decomposition products, and evaluated its application safety based on the discharge and thermal fault decomposition characteristics of $C_5F_{10}O/N_2/O_2$ gas mixture, and proposed targeted safety protection measures and suggestions.

Keywords: $C_5F_{10}O/N_2/O_2$ gas mixture, Eco-friendly insulating gas, Gas-solid interface stability, Discharge decomposition, Thermal decomposition, Biosafety

Groupe de Recherche sur l'Energétique des Milieux Ionisés, Université d'Orléans, 14 Rue d'Issoudun, 45067 Orléans Cedex 2

School of Electrical and Automation, Wuhan University, Wuhan, 430068 China